Spring 2024

Gems & Gemology

90th ANNIVERSARY

VOLUME LX

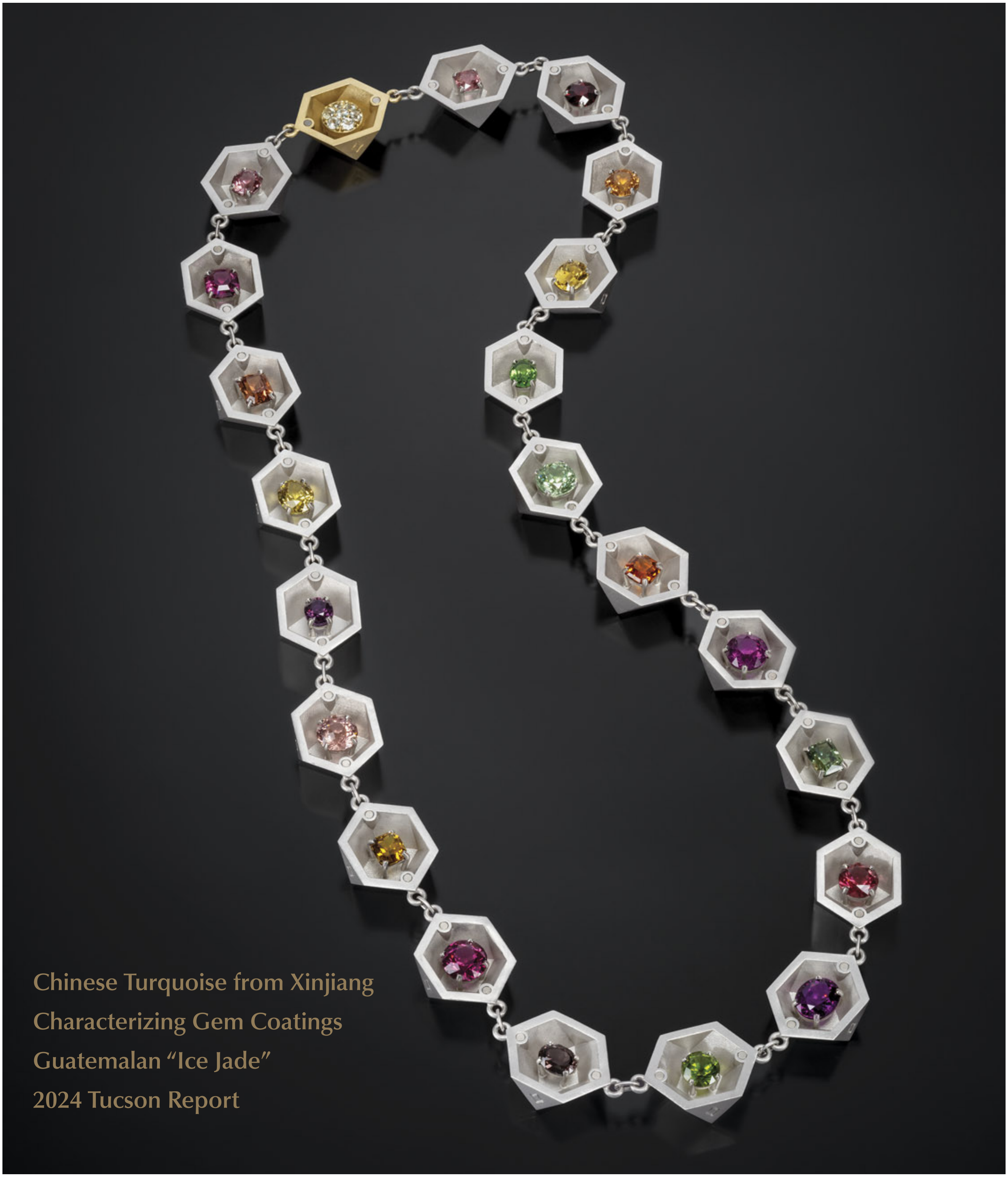

Chinese Turquoise from Xinjiang

Characterizing Gem Coatings

Guatemalan “Ice Jade”

2024 Tucson Report

The Quarterly Journal of the Gemological Institute of America

GEMS & GEMOLOGY®

Spring 2024
VOLUME 60, No. 1


p. 4


p. 43


p. 60

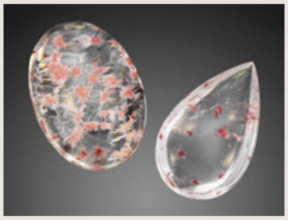
p. 77


p. 118


p. 142

EDITORIAL

FEATURE ARTICLES

REGULAR FEATURES

Editorial Staff

Editor-in-Chief
Duncan Pay

Managing Editor
Stuart D. Overlin
soverlin@gia.edu

Editor
Brooke Goedert

Associate Editor
Erica Zaidman

Senior Technical Editor
Jennifer Stone-Sundberg

Technical Editor
Tao Z. Hsu

Editors, Lab Notes
Thomas M. Moses
Shane F. McClure
Sally Eaton-Magaña

Editors, Micro-World
Nathan Renfro
John I. Koivula
Tyler Smith

Editors, Gem News
Gagan Choudhary
Christopher M. Breeding
Guanghai Shi

Editors, Colored Stones Unearthed
Aaron C. Palke
James E. Shigley

Editor, Diamond Reflections
Evan M. Smith

Contributing Editors
James E. Shigley
Raquel Alonso-Perez

Editor-in-Chief Emerita
Alice S. Keller

Assistant Editor
Erin Hogarth

Production Staff

Creative Director
Faizah Bhatti

Production and Multimedia Specialist
Michael Creighton

Photo/Video Producer
Kevin Schumacher

Photographer
Robert Weldon

Multimedia Associate
Christopher Bonine

Video Production
Albert Salvato

GEMS & GEMOLOGY®
gia.edu/gems-gemology

Customer Service
(760) 603-4200
gandg@gia.edu

Subscriptions
Copies of the current issue may be purchased for $29.95 plus shipping. Subscriptions are $79.99 for one year (4 issues) in the U.S. and $99.99 elsewhere. Canadian subscribers should add GST. Discounts are available for renewals, group subscriptions, GIA alumni, and current GIA students. To purchase print subscriptions, visit store.gia.edu or contact Customer Service. For institutional rates, contact Customer Service.

Database Coverage
Gems & Gemology's impact factor is 2.6, according to the 2022 Journal Citation Reports by Clarivate Analytics (issued June 2023). *G&G* is abstracted in Thomson Reuters products (Current Contents: Physical, Chemical & Earth Sciences and Science Citation Index—Expanded, including the Web of Knowledge) and other databases. For a complete list of sources abstracting *G&G*, go to gia.edu/gems-gemology, and click on "Publication Information."

Manuscript Submissions
Gems & Gemology, a peer-reviewed journal, welcomes the submission of articles on all aspects of the field. Please see the Author Guidelines at gia.edu/gems-gemology or contact the Managing Editor. Letters on articles published in *G&G* are also welcome. Please note that Field Reports, Lab Notes, Gem News International, Micro-World, Colored Stones Unearthed, Diamond Reflections, Charts, and In the Spotlight are not peer-reviewed sections but do undergo technical and editorial review.

Gems & Gemology is published quarterly by the Gemological Institute of America, a nonprofit educational organization for the gem and jewelry industry.

Postmaster: Return undeliverable copies of *Gems & Gemology* to GIA, The Robert Mouawad Campus, 5345 Armada Drive, Carlsbad, CA 92008.

Our Canadian goods and service registration number is 126142892RT.

About the Cover

This issue spotlights "Garanatus: From Rough to Cut," a Spectrum Award–winning platinum necklace featuring 28 garnets totaling more than 77 carats. Designed and fabricated by Mary van der Aa using garnets collected and faceted by Todd Wacks, it contains 22 rhombic dodecahedrons encasing the precious stones; the garnet's type and locality are imprinted on each link. Photos by Robert Weldon; courtesy of Mary van der Aa Fine Jewels and Tucson Todd's Gems.

Printing is by L+L Printers, Carlsbad, CA.

FSC
www.fsc.org
MIX
Paper from responsible sources
FSC® C006300

GIA World Headquarters The Robert Mouawad Campus 5345 Armada Drive Carlsbad, CA 92008 USA

ISSN 0016-626X

Gems & Gemology Turns 90!

Welcome to the Spring 2024 issue of *Gems & Gemology*! With this new volume year, we reach a special milestone at *G&G*: our 90th anniversary. In this first issue of our 90th year, we present research studies on colored stones and treatments, recap the Tucson gem shows, highlight an extraordinary garnet necklace, and offer our annual *G&G* Challenge quiz.

> *"...we reach a special milestone at* G&G: *our 90th anniversary."*

Turquoise has been highly valued in China for thousands of years. Our lead article examines turquoise from the Tianhu East deposit in Xinjiang, China. Following a summary of the area's geology and the results of studied samples, Ling Liu and coauthors identify atacamite as a unique geographic origin indicator differentiating Tianhu East turquoise from other Chinese turquoise. The authors also propose a hypothesis for the origin of the deposit.

Next, a team led by Zhaoying Huang investigates a translucent variety of jadeite jade from Guatemala known as "ice jade" that has become prominent in the Chinese market, second to jadeite jade from Myanmar. The authors detail the structural characteristics, mineral compositions, and color origin of the pale green material from the Morales mine in the Izabal Department of Guatemala.

In our final feature article, Tsung-Jen Wu's research team analyzes colored gemstone coatings, using coated synthetic moissanite as a case study. Applying nanoscale analytical methods, the authors provide a basis for characterizing colored coatings on gemstones and identifying possible techniques used in the coating process.

Our regular features have much to offer as well. *Lab Notes* continues to deliver interesting reports from GIA's global laboratories, including a natural blue diamond colored by fine milky cloud inclusions, a resubmission of a CVD-grown diamond after HPHT treatment, and a study of pearls from windowpane oysters. *Micro-World* provides a glimpse at the inner beauty of gemstones, highlighting an intriguing inclusion in a Kashmir sapphire, stunning pink and red epidote crystals in quartz, colorful parallel rays of light in rainbow lattice sunstone, and more. The latest installment of *Diamond Reflections* explores how superdeep diamonds make their way to the earth's surface. Our *Gem News International* section begins with 30 pages covering the 2024 Tucson gem shows: trends, noteworthy designs, and interesting finds. The GNI regular features report on beryl with emerald rims from Newfoundland, phenomenal emeralds from Pakistan, Liberian ruby, and more. Also in this issue, we put a spectacular collaboration by Mary van der Aa and Todd Wacks *In the Spotlight*. The "Garanatus" necklace, featuring 28 garnets from all over the world, recently won two AGTA Spectrum Awards.

Finally, test your knowledge of our 2023 feature articles in the annual *G&G* Challenge, and find out which of those articles earned a Dr. Edward J. Gübelin Most Valuable Article Award.

Throughout our 90th anniversary year, we will renew the journal's longstanding commitment to the gem trade with a variety of special content features. We hope you enjoy this first issue!

Duncan Pay | Editor-in-Chief | dpay@gia.edu

MINERALOGY AND GEOCHEMISTRY OF TURQUOISE FROM TIANHU EAST, XINJIANG, CHINA

Ling Liu, Mingxing Yang, Qiaoqiao Li, Yi Tang, Huilin Wen, Ye Yuan, Yan Li, and Jia Liu

The Tianhu East turquoise deposit is located 180 km southeast of the city of Hami (also known as Kumul) in the Xinjiang Uyghur Autonomous Region of China. This deposit has been mined since as early as 1279–379 BCE. New mining activity took place around 2015, and some of the production emerged briefly on the Chinese market. Mining was subsequently prohibited because of the location's protected status as an archaeological site. The geology of Tianhu East turquoise as well as updated reports and field exploration are systematically summarized in this study. The turquoise usually occurs as blue and bluish green veins in the fissures and shear zones of quartzite in the Cambrian Pochengshan Formation. It is characterized by high lithium, vanadium, chromium, strontium, and gallium concentrations and low barium content. Multiple associated minerals (e.g., quartz, apatite, goethite, hematite, jarosite, bonattite, muscovite, atacamite, svanbergite, and gypsum) were identified using Raman spectroscopy and electron probe microanalysis. This study contains the first report of atacamite in Chinese turquoise. Petrography, mineralogy, and geochemistry of the bedrock as well as the crystallization sequences of the associated minerals are highlighted. Based on the results, the authors propose a supergene weathering origin and elemental derivation for Tianhu East turquoise. Black shale was likely the main original source of the aluminum, phosphorus, and copper necessary for formation, while quartzite provided enough space for precipitation.

Tianhu East turquoise is found in the Xinjiang Uyghur Autonomous Region (hereafter referred to as Xinjiang) of northwestern China (figure 1), the geographic hinterland of Eurasia bordering Mongolia, Russia, Kazakhstan, Kyrgyzstan, Tajikistan, Afghanistan, Pakistan, and India. Xinjiang was once a vital part of the historic Silk Road trade route. The term "Tianhu" is a geographic descriptor, with the specific turquoise deposit located to the east of Tianhu, hence the name "Tianhu East." The region boasts rich gem resources and is regarded as a significant source for high-quality nephrite (Y. Liu et al., 2011a,b, 2016; Gao et al., 2019).

Turquoise is a treasured gemstone with a 9,000-year history in China, capturing the attention and imagination of not only the ancient Chinese but also modern geologists, gemologists, and archaeologists (Pang, 2014; Qin, 2020; Zhang, 2022). Two important ancient deposits, located at Tianhu East and Heishanling in Xinjiang, were mined between 3,300 and 2,400 years ago (Y.X. Li et al., 2019). From 2016 to 2021, Chinese archaeologists conducted excavations of these two sites, which revealed clear evidence of stone tools used for mining, as well as turquoise fragments and other relics (Y.X. Li et al., 2019, 2020). In the 2010s, Tianhu East turquoise briefly emerged on the Chinese jewelry market for a few years (figure 2).

Geologically, the parent rocks of Chinese turquoise are mainly magmatic or sedimentary. The deposits can be classified into two distinct types: igneous-related and black shale–related. The igneous-related deposits are distributed mainly in Ma'anshan and Tongling City, in Anhui Province of east-central China, where turquoise is usually discovered in the oxidized, fractured zones of altered igneous rocks (Wei and Guan, 2003; Zhou et al., 2013; Shen and Zhao, 2019; Shen, 2020b).

However, most turquoise deposits in China are related to black shale, and these are widely distributed in the Hubei, Shaanxi, Henan, and Qinghai provinces, as well as Xinjiang (Tu, 1996, 1997a; Huang, 2003;

See end of article for About the Authors and Acknowledgments.
GEMS & GEMOLOGY, Vol. 60, No. 1, pp. 2–25,
http://dx.doi.org/10.5741/GEMS.60.1.2

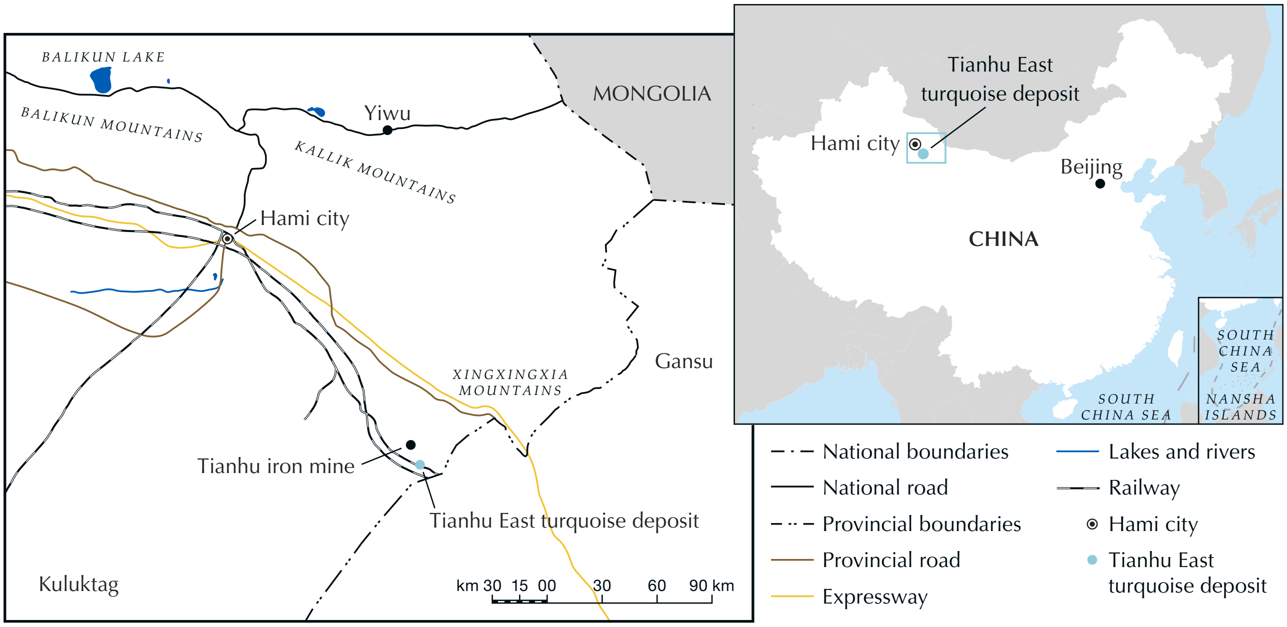

Figure 1. Location maps of the Tianhu East turquoise deposit, which lies about 180 km from the city of Hami in Xinjiang. Inset map courtesy of the Ministry of Natural Resources of China.

Zhou and Jiang, 2005) and the Inner Mongolia Autonomous Region (Cao et al., 2021). About 90% of this turquoise, especially the material with desirable color used for large, high-value ornaments and carvings in the Chinese jewelry market today, originates from black shale–related deposits. The mines in Zhushan County, China's most commercially significant locality, are one example. While the hypotheses of turquoise genesis (hydrothermal, contact metasomatic, and supergene origin) were proposed by Pogue (1915), the genesis of black shale–related deposits remains unsolved. Because of the complex geologic settings and local geography, few recent investigations have been conducted on these deposits to clearly demonstrate the formation process. Generally, black shale zones are not only the original source of the elements necessary for formation but also where the precipitation of turquoise occurs.

In Brief

- Chinese turquoise from the Tianhu East deposit in the Xinjiang region holds significant geological, gemological, and archaeological importance.
- Petrographic and geochemical characteristics shed light on the formation process of the deposit.
- Tianhu East serves as a representative case for deciphering the genesis of black shale–related turquoise deposits. In this deposit, the black shale source zones are clearly stratified with quartzite precipitation zones, differentiating them from China's other black shale–related deposits.
- Atacamite is a significant geographic origin indicator in separating Tianhu East turquoise from other Chinese turquoise. Tianhu East turquoise also has high lithium, vanadium, chromium, strontium, and gallium concentrations as well as low barium content.

Fortunately, the occurrence in Tianhu East offers a representative case to decipher the genesis of black shale–related deposits. Here the turquoise is hosted in quartzite, as the black shale source zones are located on quartzite precipitation zones. Thus, the distribution and relationship of black shale and quartzite in the Tianhu East deposit would help clarify the processes of leaching, migration, and deposition of the weathering solution, allowing us to determine the formation mechanism for black shale–related turquoise deposits.

Spectroscopic (Raman, infrared, and ultraviolet/visible), structural, and major/trace element characteristics of Tianhu East turquoise were reported by X.F. Liu et al. (2018). But detailed geological field reports were unpublished, and formation was not discussed. This study summarizes the earlier historical reports and presents the geology of this deposit based on the authors' field exploration. Mineral assemblages in Tianhu East turquoise have not been previ-

Figure 2. Turquoise with various colors from Tianhu East, mined during the 2010s. A: A ring set with turquoise (1.2 × 0.8 × 0.6 cm). B–F: Carved turquoise pendants measuring 4.5 × 2.5 × 1.2 cm (B), 7.0 × 5.0 × 3.5 cm (C), 4.0 × 1.9 × 0.6 (D), 5.5 × 2.4 × 0.5 cm (E), and 4.5 × 2.5 × 1.6 cm (F). Photos courtesy of Haitao Wang (A, C, D, E, and F) and Hanqing Dai (B).

ously studied, but they could provide useful information about the geologic formation process. Techniques such as Raman spectroscopy and electron probe microanalysis (EPMA) with energy-dispersive spectroscopy (EDS) were applied to investigate the associated minerals. The gemological, mineralogical, and geochemical features of Tianhu East turquoise are significant fingerprints pointing to its origin. This study also illuminates the essential petrographic and geochemical clues to its genetic origin and proposes a formation model for black shale–related turquoise.

LOCATION AND MINING

The Tianhu East deposit is located at 41°36′7″N and 94°36′3″E, 180 km southeast of the city of Hami in East Tianshan of Xinjiang, northwestern China (figure 1). This area is at an elevation of 1186–1444 m, lying in the denuded hills of the Gobi Desert in the Beishan Mountains. The region is characterized by extreme drought, and the bedrock is well exposed. In 2017, with the support of local miners, the authors conducted field exploration of the Tianhu East deposit. Turquoise had recently been mined on a small scale using open-pit mining, but no mining was being conducted during our fieldwork. Mining has been prohibited by the local government because of the site's cultural heritage significance.

GEOLOGY

Regional Geology. The Tianhu East turquoise deposit is located on the southern edge of the multi-period composite continental margin magmatic arc of the Middle Tianshan Mountains west of the Nalati and Hongliuhe suture zone, adjacent to the Early Paleozoic rift of the North Beishan belt. There are multi-stage tectonic-magmatic activities in this area where intrusive rocks are found and the strata are extensively deformed (Chen and Xu, 2001). The tectonic structures are in the middle of the Jianshanzi uplift, which belongs to the Kuluktag-Xingxingxia continental collision zone of the Tarim plate, extending in a NEE direction between the Jianshanzi fault and the Hongliuhe deep fault (Yang et al., 2008). The geologic structure is based on the monoclinal structure of the ore deposit and metamorphic rock strata (strike NE60°–75°) between the regional east-west Jianshanzi fault and the Hongliuhe fault, which are chronically active and control the local stratigraphic distribution as well as the tectonic and magmatic activities. The stratigraphic structure is dominated by longitudinal faults that mainly extend NE and NEE and are accompanied by multiple sets of secondary faults, reflecting multistage tectonic activities (Yang et al., 2008). The rocks in the zone are severely weathered and fragmented.

Related Stratigraphy. The stratigraphic units in the region belong to the Beishan stratigraphic division of the Tarim North Rim–Beishan stratigraphic area in the Tarim region (Wang, 1996). The exposed strata mainly consist of the Hutuo Tianhu Rock Group, the Cambrian Pochengshan Formation, the Lower Silurian Heijianshan Formation, the Jixian Pingtoushan Formation, the lower Permian Shuangbaotang Formation, the Upper Permian Hongyanjing Formation, middle-upper Pleistocene diluvium, and Pleistocene alluvial diluvium. The strata are generally distributed in an east-west direction. The Tianhu East deposit occurs in the upper section of the Cambrian Pochengshan Formation (figure 3).

The Cambrian Pochengshan Formation can be broadly divided into upper and lower lithological segments. The lower segment is primarily a set of rock assemblages consisting of siliceous rocks intercalated with carbonate rocks. The lithology is mainly light gray to gray schistoid siliceous rock and gray to dark gray siliceous rock intermixed with gray-white to light gray schistose crystalline limestone. The upper section is primarily a set of fine clastic rocks intercalated with carbonate rocks, siliceous slates, and siliceous rocks. Here the lithology is mainly gray schistose siltstone intercalated with gray thin silty shale, gray-brown calcareous siltstone, dark gray siliceous rock, and a small amount of light gray-yellow silicified crystalline limestone. The siliceous slate underwent both pyritization and limonization. The formation was subjected to two-stage compression and affected by later faults, resulting in significant formation extrusion and deformation (Xinjiang Uyghur Autonomous Region Bureau of Geology and Mineral Resources, 1993; Yang et al., 2008).

Regional Magmatic Rocks. These are mainly Variscan intermediate-acid magmatic rocks with numerous Carboniferous and Permian intrusions and a small number of Devonian intrusions. The predominant rock types are monzogranite and diorite, accompanied by minor granite and quartz veins. The magmatic rocks are generally distributed in a NWW to nearly EW direction. The formation sequence of magmatic rocks was Devonian diorite, Carboniferous monzogranite, Permian diorite, and then Permian monzogranite.

Metamorphism. The contact metamorphism in the area occurred mainly between magmatic rock and surrounding rock. This process caused crystallization and recrystallization of the surrounding rock. The lithology exposed in the mining area is primarily from regional low-temperature dynamic metamorphism.

Occurrence. Tianhu East turquoise is found in a previously excavated outcrop, where it is hosted by quartzite (figure 4A) with minor turquoise filling in the shear joints. The turquoise occurs mainly as

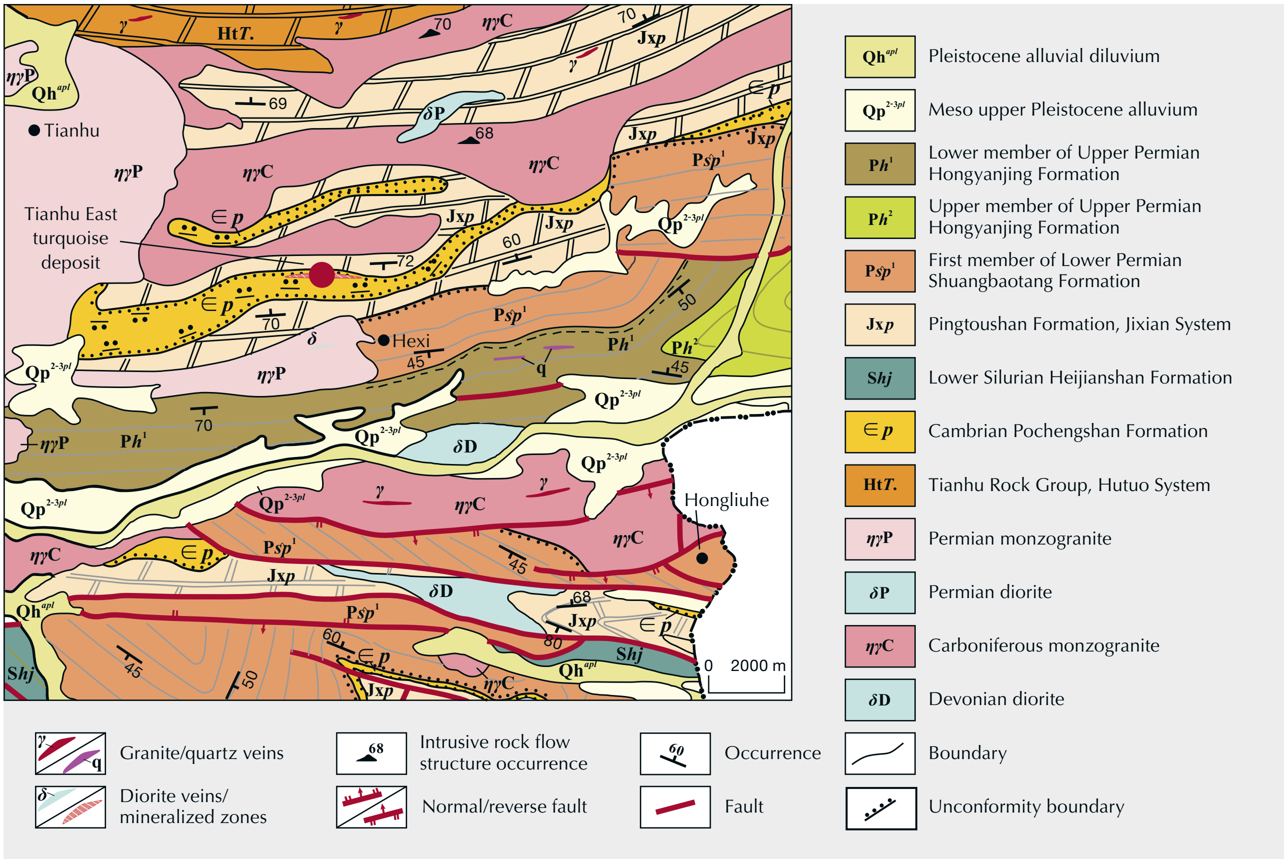

Figure 3. Simplified regional geologic map of the turquoise deposit in Tianhu East. Modified from Zhu et al. (n.d.).

veins (up to 8 mm thick; figure 4B) and nodules (approximately 3–5 cm in diameter; figure 4C) of high density and good color. Its color range includes blue, greenish blue, and light green. Few pale chalky materials are found in this deposit. The top and bottom parts of the rocky outcrop are covered by quartzite (figure 5), which usually displays rhythmic stratification (0.5–5.0 cm). The quartzite is mostly quartz (~90%) with minor muscovite and has undergone limonization. The middle portion of the outcrops is black shale, which contains carbon-rich minerals and stains easily. The black shale contains silicified car-

Figure 4. A: This turquoise vein is hosted within a quartzite matrix, illustrating the geological context of the mineral's formation. B: One of the collected samples showcasing a turquoise vein; field of view 8 cm. C: A high-quality blue turquoise nodule surrounded by matrix; field of view 5 cm. Photos by Ling Liu.

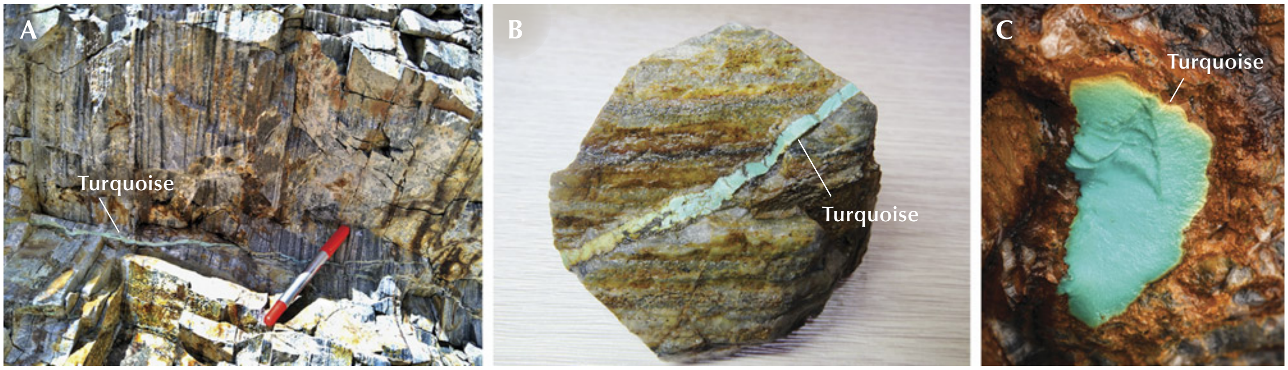

Figure 5. The outcrop profile of the bedrocks in the Tianhu East deposit, composed mainly of quartzite and black shale. Photo by Ling Liu.

bonaceous slate, siliceous slate, and schist, all strongly weathered. The clastic components of black shale are mainly argillaceous and clay minerals. In Tianhu East, turquoise is confined to the quartzite, and none is found in the black shale (figure 6). This distribution is distinct from the deposits in Hubei and Shaanxi, where turquoise is primarily hosted in black shale.

MATERIALS AND METHODS

Specimens. For this study, 42 pieces of rough turquoise were collected from Tianhu East during field exploration in 2017. They were named HM001 to HM042, indicating samples collected from Hami. All 42 pieces (some of which are shown in figure 7) were cut and polished into slabs measuring 0.5–0.8

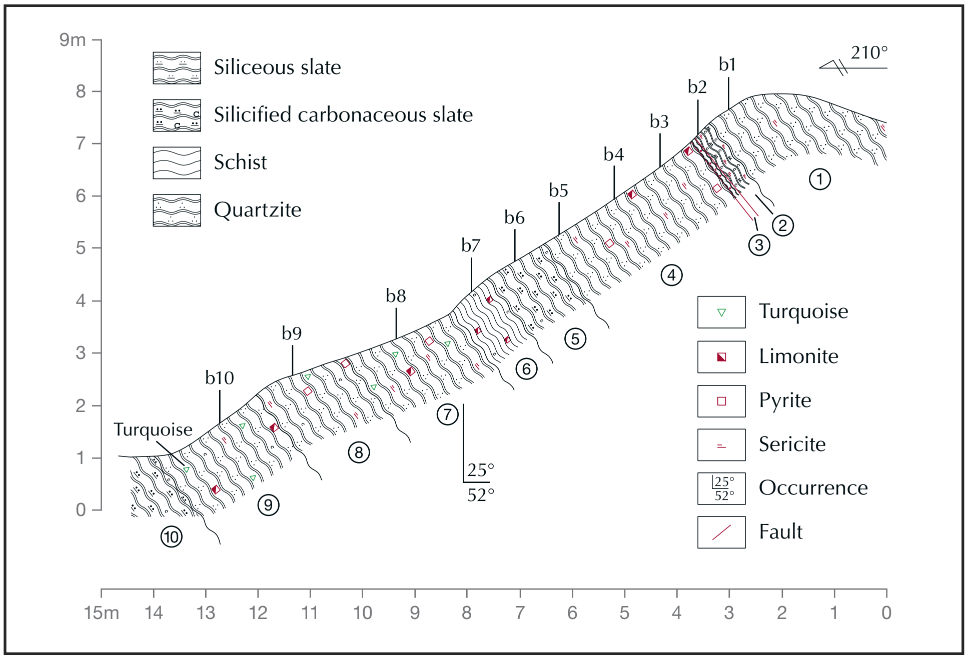

Figure 6. The measured outcrop profile at Tianhu East. Here, b1–b10 represent the sampling location and serial number, while the circled numerals 1–10 indicate rock units.

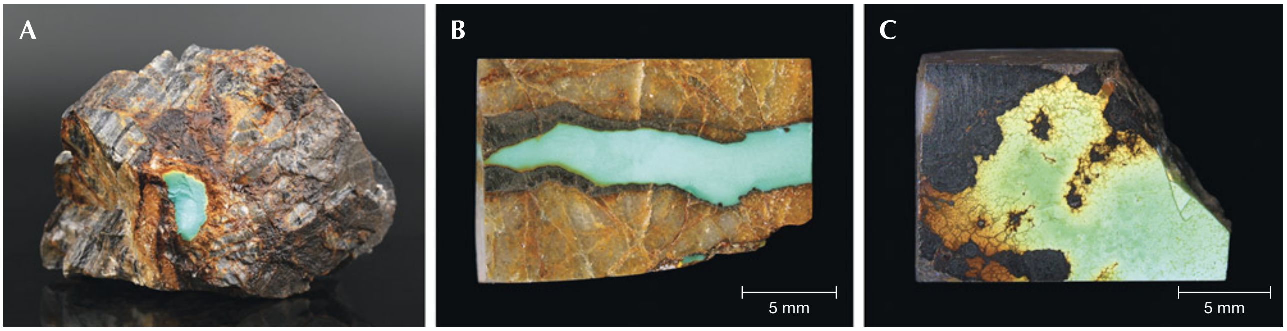

Figure 7. Turquoise collected from the Tianhu East mines. A: A blue turquoise-in-matrix hand specimen (1163.1 g total). B and C: Greenish blue (3.11 g) and yellowish green (4.65 g) turquoise samples investigated in this research. The matrix consists of quartzite with limonization. Photos by Ling Liu and Qiaoqiao Li.

mm thick and weighing 1.14–8.79 g for standard gemological testing, Raman spectroscopy, and laser ablation–inductively coupled plasma–mass spectrometry (LA-ICP-MS). From these, five samples were selected for field emission scanning electron microscopy (FESEM) and ten samples for EPMA.

Four samples of black shale and six samples of quartzite collected from the deposit were prepared as polished thin sections and bulk powders (200 mesh) for petrographic, quantitative mineral, and chemical analyses. Petrographic examinations were performed on the thin sections using a Leica DM2500P polarizing microscope. The bedrocks were prepared with fusion sampling, a technique used in analytical chemistry and materials science to melt and prepare solid samples into homogeneous powders for analysis by various analytical instruments. The major and trace elements of the bedrocks were analyzed with the whole rock analytical method using a Shimadzu XRF-1800 X-ray fluorescence spectrometer, a Thermo Scientific X2 inductively coupled plasma–mass spectrometer, a Thermo Scientific iCAP6300 inductively coupled plasma–optical emission spectrometer (ICP-OES), and a CCD-I powder solid injection arc emission spectrometer developed by the Hubei Geological Research Laboratory.

Standard Gemological Testing. Specific gravity of the 42 samples was determined hydrostatically with an electronic balance. Ultraviolet fluorescence reactions were observed under long-wave (365 nm) and short-wave (254 nm) UV from a mercury lamp. Microscopic features were observed and photographed with a Leica M205A microscope. Testing was performed at the Gemmological Institute, China University of Geosciences in Wuhan.

Micro-Raman Analysis. Micro-Raman spectroscopy was conducted on the 42 turquoise samples using a Bruker Optics Senterra R200L with a 532 nm laser. The laser power was 20 mW, and the spectral resolution was set at approximately 9–15 cm^{-1}. In all, 20 scans were performed with a 5 s integration time for each scan. The mineral phases were identified by comparison with reference spectra from the RRUFF database at http://rruff.info; see Lafuente et al. (2016).

FESEM. The microstructural morphologies of five samples with different color and texture were investigated using a Zeiss Gemini Sigma 300 high-resolution FESEM with a secondary electron detector. Samples were coated with platinum (7 nm thickness) to reduce charging. SEM images were collected at an accelerating voltage of 10 kV and high vacuum mode.

EPMA. Backscattered electron (BSE) imaging, EPMA, and element mapping were performed on 10 turquoise specimens of different color as well as 10 bedrocks using a JEOL JXA-8230 microprobe with four wavelength-dispersive spectrometers (WDS) at the Center for Global Tectonics, School of Earth Sciences, China University of Geosciences in Wuhan. The operating conditions for quantitative analysis were: 15 kV accelerating voltage, 20 nA probe current, and 1 μm beam diameter. Dwell times were 10 s on element peaks and half that on background locations adjacent to peaks. Raw X-ray intensities were corrected using a ZAF (atomic number, absorption, fluorescence) correction procedure. A series of natural and synthetic standards were utilized for calibration: jadeite for sodium, pyrope for magnesium and aluminum, orthoclase for silicon and potassium, apatite for phosphorus, diopside for calcium, magnetite for iron, chalcopyrite for cop-

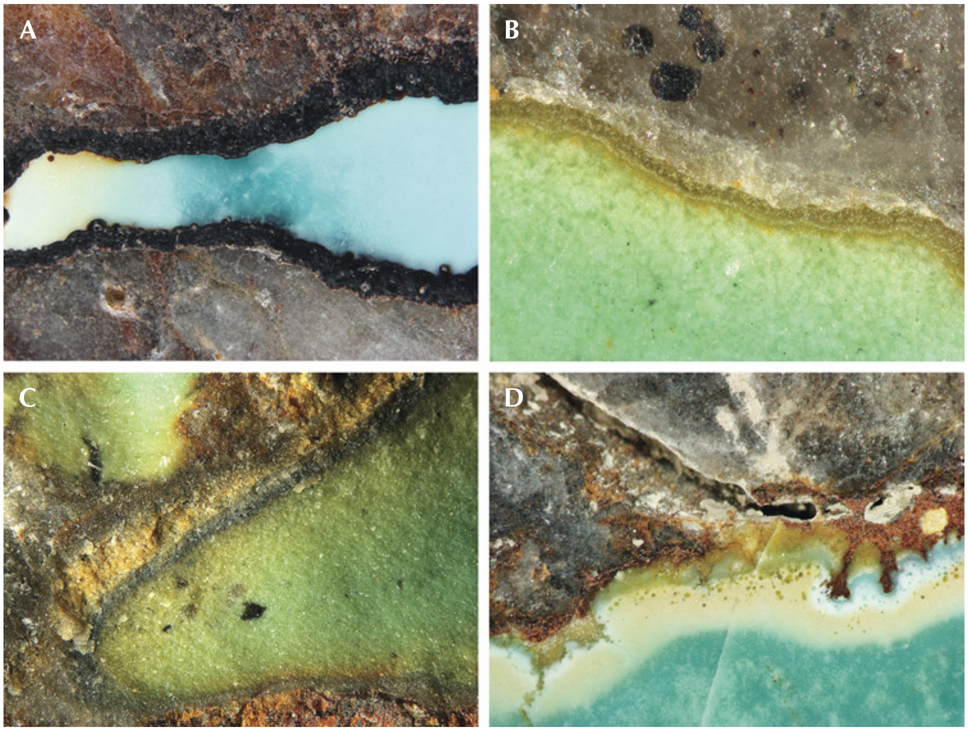

Figure 8. Turquoise samples shown in reflected light. A: Laminar turquoise (0.6–1.5 mm thick) occurred in the siliceous matrix. B–D: Yellowish green, black, and brownish yellow minerals were sandwiched between the turquoise and the siliceous matrix, exhibiting a banded or layered appearance. Photomicrographs by Ling Liu; fields of view 4.2 mm (A), 0.9 mm (B), 4.5 mm (C), and 5.8 mm (D).

per, and sphalerite for zinc. The compositional ranges and mean values of the tested samples were recorded. 15 kV accelerating voltage, 100 nA probe current, 1 × 1 μm^2 pixel size, and stage scan model were utilized during EPMA mapping. EPMA stage mapping was performed at a relatively high probe current to compensate for reduced pixel dwell time and to acquire a higher spatial resolution. All mapping time was spent at the WDS X-ray peak positions.

LA-ICP-MS. The trace elements of the 42 turquoise samples (two spots per sample) were analyzed by an Agilent 7700e ICP-MS combined with a GeoLasPro laser ablation system consisting of a COMPexPro 102 ArF excimer laser (wavelength of 193 nm and maximum energy of 200 mJ) and a MicroLas optical system. Analytical conditions consisted of a 44 μm diameter laser spot size, a laser frequency of 6 Hz, an 80 mJ laser energy, an energy density of 5.5 J/cm^2, and a dwell time of 6 microseconds. National Institute of Standards and Technology (NIST) Standard Reference Material (SRM) 610 glass and U.S. Geological Survey (USGS) glass standards BHVO-2G, BCR-2G, and BIR-1G were used as external standards. Due to the lack of a phosphate standard, the element homogeneity and stability of the specimens was evaluated, which was used as a measurement standard (not a calibration standard) to monitor the drift of the instrument and ensure the validity and accuracy of the data obtained.

RESULTS

Gemological Properties. The Tianhu East turquoise displayed various colors: blue, greenish blue, green, and yellowish green. All samples were opaque and inert to both long-wave and short-wave UV radiation. The specimens had waxy to glassy luster and a wide range of specific gravity (2.51–3.38), as most samples were composed of turquoise and matrix. These laminar specimens had thicknesses of 0.6–7.0 mm in the siliceous matrix (figure 8A). Goethite, apatite, and svanbergite occurred between the turquoise and the siliceous matrix, exhibiting a banded or layered structure (figure 8, A–D). The inner black or red-brown layers often consisted of iron minerals with oolitic shapes. Iron-bearing pigments scattered throughout the turquoise were responsible for its brownish color (figure 8D). Tiny round inclusions were clustered at the border between the matrix and turquoise (figure 8D).

Chemical Composition. The ideal chemical formula of turquoise is [A $B_6(PO_4)_4(OH)_8 \cdot 4H_2O$], with Cu^{2+} at the A position and Al^{3+} at the B position (Foord and Taggart, 1998). Tianhu East turquoise contained major amounts of Al_2O_3, P_2O_5, CuO, and FeO, with minor contents of SiO_2, ZnO, CaO, Na_2O, and K_2O (table 1). The compositions varied, with wide ranges of CuO (6.37–8.74 wt.%), Al_2O_3 (32.68–37.62 wt.%), P_2O_5 (30.74–36.54 wt.%), and FeO (0.76–5.67 wt.%).

TABLE 1. Chemical composition (in wt.%) of Tianhu East turquoise, analyzed by EPMA.

	P_2O_5	SiO_2	CuO	ZnO	CaO	Na_2O	K_2O	Al_2O_3	FeO[a]	H_2O[b]
Min	30.74	bdl[c]	6.37	bdl	0.05	0.07	bdl	32.68	0.76	15.55
Max	36.54	5.65	8.74	0.56	0.38	0.52	0.23	37.62	5.67	18.92
Average	35.00	0.66	7.70	0.19	0.13	0.17	0.06	36.65	2.30	17.14
Detection limit (wt.%)	0.044	0.031	0.049	0.061	0.018	0.020	0.013	0.021	0.037	—

[a] *All Fe was analyzed as FeO by EPMA.*
[b] *H_2O was calculated by the difference from 100%.*
[c] *bdl = below detection limit*

Higher FeO (4.06–5.67 wt.%) contents combined with lower Al_2O_3 (32.68–35.02 wt.%) and P_2O_5 (30.74–33.67 wt.%) contents were obtained from the yellowish green samples. The rest of the samples had narrow ranges of Al_2O_3 (36.10–37.62 wt.%), P_2O_5 (34.26–36.54 wt.%), and FeO (0.76–2.91 wt.%).

Cations per formula unit of turquoise were calculated based on 16 oxygen atoms (O) and 8 hydroxide groups (OH) (see table S-1 in the appendix at www.gia.edu/doc/spring-2024-turquoise-tianhu-east-appendix1.pdf). Tianhu East turquoise was characterized by 0.6547–0.8735 atoms per formula unit (apfu) of Cu^{2+}, 0.0064–0.0556 apfu of Zn^{2+}, 0–0.2671 apfu of Fe^{2+}, 0.0087–0.0552 apfu of Ca^{2+}, 0.0170–0.1368 apfu of Na^+, 0.0055–0.0391 apfu of K^+, 5.2059–5.9439 apfu of Al^{3+}, and 0–0.6411 apfu of Fe^{3+} at the B site. Also, the ranges of P^{5+} and Si^{4+} were 3.5176–4.0872 and 0.0041–0.7641 apfu, respectively. In this study, the A site was mostly filled with Cu^{2+}, with the rest occupied by Zn^{2+}, Fe^{2+}, Ca^{2+}, Na^+, and K^+. Al^{3+} and Fe^{3+} oc-

TABLE 2. Concentration (in ppm) of selected trace elements in Tianhu East turquoise, analyzed by LA-ICP-MS (range and average) and compared with other localities.

Locality	Hami, China[a]	Hubei, China		Shaanxi, China	
Reference	This study	Wang et al. (2007) (3 spots)	She et al. (2009) (6 spots)	Wang et al. (2007) (4 spots)	She et al. (2009) (2 spots)
Li	0.90–583 (237)	1.06–3.06 (2.37)	0.10–2.20 (1.65)	21.69–23.19 (22.48)	5.70–14.30 (10.00)
V	279–1407 (560)	na	na	na	na
Cr	625–5875 (2482)	na	na	na	na
Ga	4.97–1487 (269.75)	0.32–14.62 (5.37)	2.81–12.36 (7.06)	3.46–4.26 (3.73)	0.78–23.69 (12.24)
Sr	4.07–545 (101.12)	3.54–9.10 (6.25)	na	10.87–16.57 (13.95)	na
Ba	23.47–781 (260.62)	947–1599 (1279)	na	726–819 (771)	na

[a] *Detection limits = Li: 0.41; V: 0.16; Cr: 2.15; Ga: 0.22; Sr: 0.11; Ba: 0.48. bdl = below detection limit.*
[b] *V, Sr, and Ba were analyzed by EPMA; na = not analyzed.*

curred at the B site. Si^{4+} was assigned to the P site since phosphorus can be substituted by silicon in the turquoise structure (Abdu et al., 2011). Accordingly, the chemical formula of the analyzed turquoise (e.g., sample HM010) can be expressed as $(Cu_{0.8735}Zn_{0.0128}Fe_{0.0735}Ca_{0.0117}Na_{0.017}K_{0.0071})_{\Sigma=0.9956}(Al_{5.8783}Fe_{0.1041})_{\Sigma=5.9824}(P_{3.9977}Si_{0.0243})_{\Sigma=4.0220}O_{16}(OH)_8 \cdot 4H_2O$, indicating the samples analyzed by EPMA belong to the turquoise end-member.

Trace Element Chemistry. Trace elements were determined from 42 samples by LA-ICP-MS, with two analysis points (often in different color zones) per sample. This resulted in 82 total data points (two invalid data points were excluded). Trace elements of lithium, vanadium, chromium, gallium, strontium, and barium showed large variations in concentration (table 2).

Lithium concentrations (0.90–583 ppm, avg. 237 ppm) were slightly lower in Tianhu East turquoise than in French turquoise from Montebras Creuse (Rossi et al., 2017) but higher than those from China's Hubei, Shaanxi, and Anhui provinces (Wang et al., 2007; She et al., 2009) and from Santa Fe in New Mexico (Rossi et al., 2017). Tianhu East turquoise had high vanadium (avg. 560 ppm) and chromium (avg. 2482 ppm) contents, which were higher than those in Anhui (Shen, 2020a), the Sinai Peninsula, Santa Fe, Montebras Creuse, and Neyshabur (Rossi et al., 2017). The samples' gallium content (4.97–1487 ppm) overlapped with that of turquoise from other deposits except Neyshabur (Rossi et al., 2017), and the average gallium value (269.75 ppm) was higher than the others. Tianhu East turquoise had higher strontium content (4.07–545 ppm, avg. 269.75 ppm) compared to Tongling (J. Liu et al., 2019) but much lower than from Xichuan (X.T. Li et al., 2019), Sinai, and Santa Fe (Rossi et al., 2017). Barium content (23.47–781 ppm, avg. 260.62 ppm) overlapped with that of turquoise from most deposits but was lower compared to turquoise from Hubei and Shaanxi provinces (Wang et al., 2007) and Sinai (Rossi et al., 2017). Since most previous investigations of turquoise from other deposits were on a limited scale or only reported one data point, such as studies on turquoise from Sinai, Santa Fe, Montebras, and Neyshabur (Rossi et al., 2017), they were unable to determine the geographic origin based on trace element profiles and required additional research data.

TABLE 2 (continued). Concentration (in ppm) of selected trace elements in Tianhu East turquoise, analyzed by LA-ICP-MS (range and average) and compared with other localities.

Locality	**Anhui, China**			**Xichuan, China**	**Sinai, Egypt**	**Santa Fe, New Mexico**	**Montebras Creuse, France**	**Neyshabur, Iran**
Reference	Wang et al. (2007) (3 spots)	Shen (2020a) (3 spots)	Liu et al. (2019) (3 spots)	Li et al. (2019) (2 spots)	Rossi et al. (2017) (1 spot)	Rossi et al. (2017) (1 spot)	Rossi et al. (2017) (1 spot)	Rossi et al. (2017) (1 spot)
Li	0.17–1.90 (0.97)	—	—	—	103.08	2.08	690.9	336.96
V	na	132–149 (138)	5.72–21.20 (13.64)	bdl–784.24[b]	14.75	29.70	0.44	0.19
Cr	na	2.31–7.11 (4.32)	3.44–8.76 (6.85)	na	88.56	40.47	1.93	1.62
Ga	3.88–14.08 (10.21)	6.03–9.79 (7.94)	na	na	7.73	44.71	30.56	3.77
Sr	0.61–143.62 (88.61)	87.60–1279 (533.20)	0.05–0.30 (0.16)	3619–6266 (4943)[b]	8667.38[b]	3945.56[b]	94.23	90.17
Ba	9.05–562 (199.68)	297–672 (459)	277–1870 (858)	627–761 (694)[b]	7236.90[b]	801.50	195.71	951.22

[a] *Detection limits = Li: 0.41; V: 0.16; Cr: 2.15; Ga: 0.22; Sr: 0.11; Ba: 0.48. bdl = below detection limit.*

[b] *V, Sr, and Ba were analyzed by EPMA; na = not analyzed.*

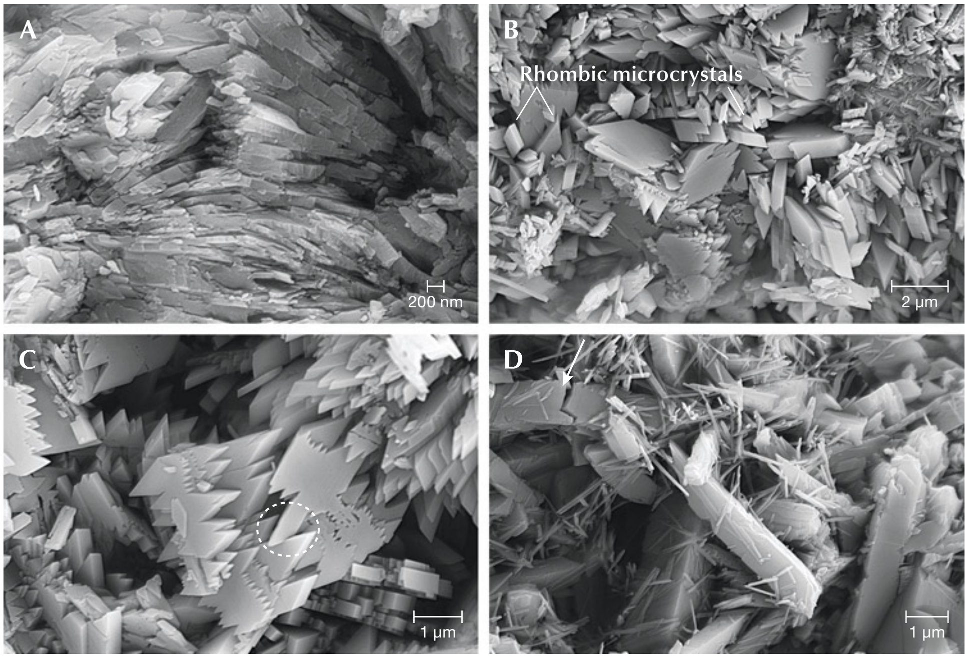

Figure 9. Various microstructures of Tianhu East turquoise observed using FESEM. A: Platy microcrystals arranged in parallel. B: Rhombic microcrystals with different sizes. C: A rhomboidal shape with jagged edges. D: Tiny columnar microcrystals attached to larger columnar ones.

Microstructure. Platy, long columnar, laminar, rhombic, and rhomboidal structures were observed in SEM images (figure 9). One blue specimen revealed a compact platy structure consisting of closely stacked plate-like crystals with few pores (see figure S-1A in the appendix). By comparison, turquoise specimens with light blue or light green color contained numerous pores among microcrystals (figure 9, B–D). Some long columnar microcrystals were distributed radially in one light blue specimen (see figure S-1B in the appendix).

One light green turquoise sample had platy and laminar structures, with some microcrystals arranged locally in parallel (figure 9A). Interestingly, two shapes of platy microcrystals were observed in this specimen: rhombic and rhomboidal (figure 9, B and C). The rhombic platy microcrystals ranged from approximately 0.42–2.40 μm in length but showed only a slight variation in thickness (average 0.38 μm) (figure 9B). Most of them were disordered and partially parallel. The rhomboidal platy microcrystals had jagged edges that varied in length (figure 9C). Occasionally, two rhomboidal platy microcrystals were intergrown (figure 9C). Both the rhombic and the rhomboidal platy microcrystals had particularly sharp edges and a clear outline.

Two structures coexisted in one light yellowish green specimen: large columnar microcrystals and tiny columnar microcrystals (figure 9D). The large columns varied from approximately 4–8 μm in length and 0.5–1.6 μm in width, and some were up to 13 μm long. Occasionally, these large columnar

Figure 10. Euhedral quartz crystals in turquoise. A: Quartz with a hexagonal prism cross section (perpendicular to the c-axis). B: Quartz with a pyramidal trigonal habit. C: Quartz showing transverse striations under differential interference contrast microscopy. Photomicrographs by Ling Liu; fields of view 0.9 mm (A), 0.5 mm (B), and 0.6 mm (C).

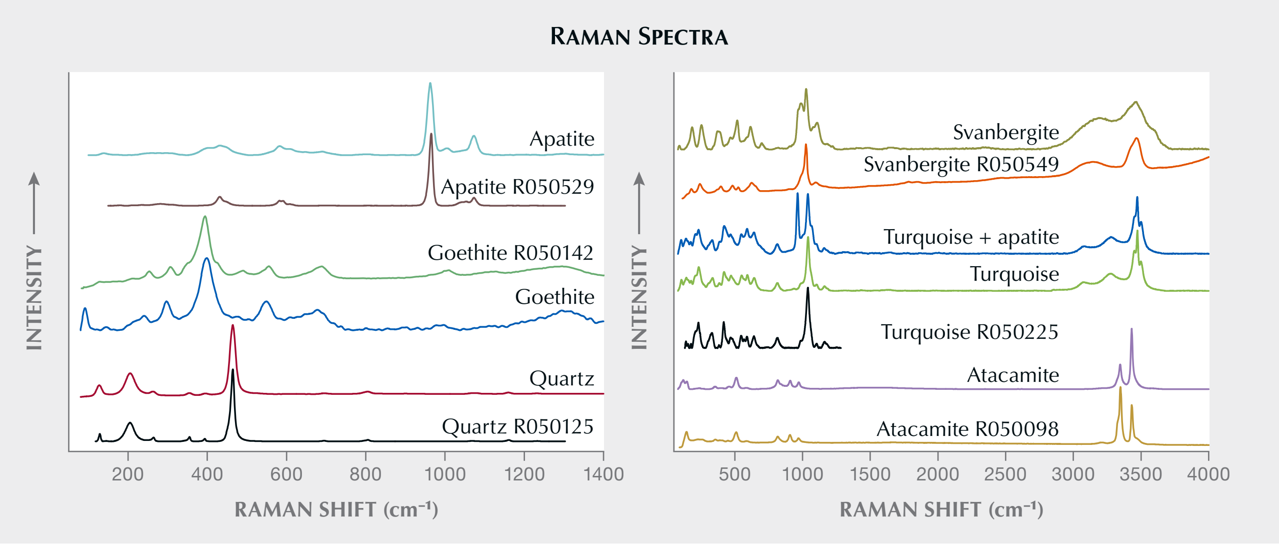

Figure 11. Raman spectra of different minerals in the samples (left: quartz, goethite, and apatite; right: atacamite, turquoise, mixtures of turquoise and apatite, and svanbergite), with standard RRUFF reference spectra included for comparison. Spectra are offset vertically for clarity.

microcrystals were distorted and broken (figure 9D). Under magnification, many of the tiny columnar microcrystals were sparsely scattered over the large columnar microcrystals (figure 9D), while some were clustered together. The tiny microcrystals generally had similar thickness (about 80 nm) and were less than 1.5 µm in length. Both the large and the tiny columnar microcrystals had a well-defined shape, sharp edges, and a clear outline. These structures were disorderly and loosely stacked together, with large pores clearly observed between them.

Mineral Associations. Tianhu East turquoise was associated with various minerals, such as quartz, apatite, goethite, hematite, jarosite, bonattite, muscovite, atacamite, svanbergite, and gypsum. These associated minerals were identified using Raman spectroscopy and EPMA-EDS.

Quartz. The most common mineral inclusion was transparent and colorless to gray quartz, up to 1.9 mm in length. Well-developed quartz crystals occurred as euhedral and pyramidal trigonal habits with transverse growth patterns (figure 10). The crystals were identified as quartz based on their Raman spectra, with bands at 127, 205, 263, 355, 395, 464, 695, and 805 cm^{-1} (figure 11, left).

Goethite [FeO(OH)]. Goethite, identified by Raman spectroscopy (again, see figure 11, left), typically covered the surface of the turquoise with a thickness of 0.232–1.383 mm (figure 12A). Its Raman spectrum showed main bands at 240, 297, 398, 549, 678, and 1295 cm^{-1}. Oolite-like goethite was characterized by oscillatory zoning, with some zones displaying concentric layers under EPMA-BSE imaging (figure 12, B–D).

Furthermore, EPMA element mapping analysis revealed that the goethite exhibited uneven distributions of elemental contents, manifested in distinct band patterns of iron, vanadium, copper, phosphorus, aluminum, silicon, sulfur, and zinc. The elemental variations and distributions resulted in a core/rim structure with varying gray values in BSE images, indicating different generations of goethite (figure 12, C and D). The high concentrations of iron, vanadium, copper, and phosphorus were in the outer part of the goethite crystal, which appeared bright gray in the BSE images owing to these elements' low mean atomic number. Conversely, the inner part of the goethite crystal (which appeared dark in the BSE images) had low concentrations of iron, vanadium, copper, and phosphorus but high concentrations of aluminum, silicon, and sulfur (figure 12E). Variations in zinc content were less obvious than those of iron, vanadium, copper, phosphorus, aluminum, silicon, and sulfur (for element maps of phosphorus, silicon, sulfur, and zinc, see figure S-2 in the appendix).

Atacamite [$Cu_2Cl(OH)_3$]. Atacamite usually occurred in the host rock, occasionally associated with turquoise or quartz (figure 13). This mineral, rarely found in turquoise, is transparent and bright green and can resemble emerald in color. The atacamite

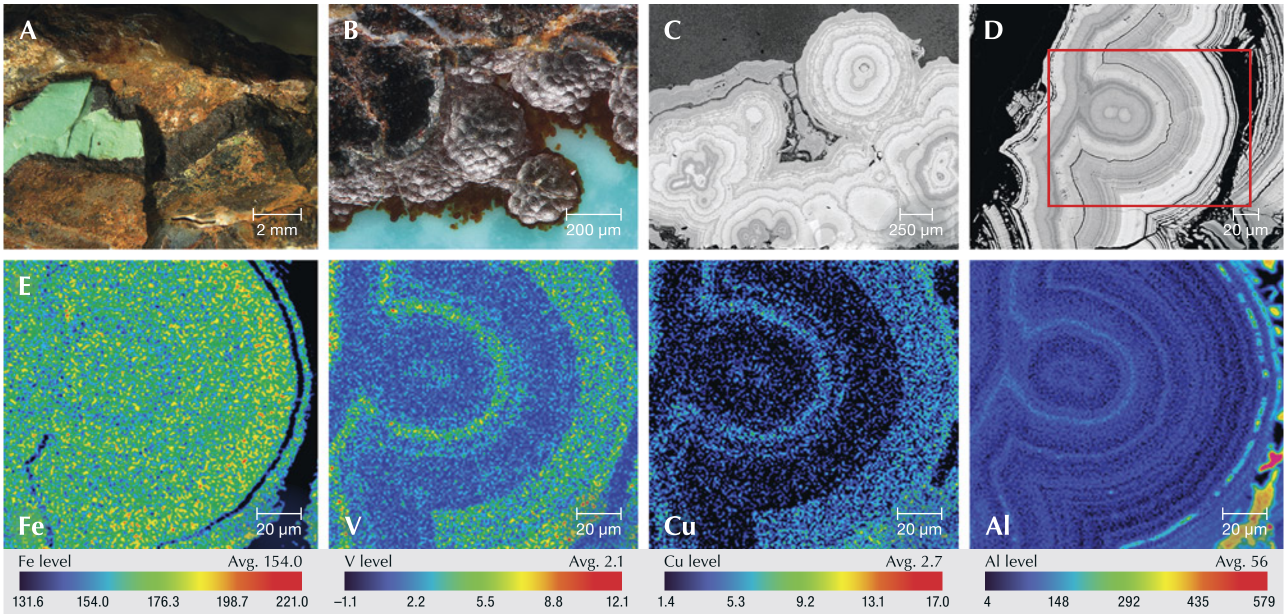

Figure 12. A: Goethite with 0.232–1.383 mm thickness. B: Oolite-like goethite. C: Goethite with concentric layers. D: Goethite showed distinct oscillatory zonings in BSE images. E: EPMA element mapping revealed variations in iron, vanadium, copper, and aluminum contents. Images by Ling Liu.

crystals often displayed elongate columnar or irregularly granular forms up to 3.134 mm. EPMA analysis identified major contents of CuO (70.68–71.59 wt.%) and Cl (12.84–12.99 wt.%) (see table S-2 in the appendix). Its Raman spectrum showed prominent bands at 119, 145, 354, 459, 511, 583, 818, 909, 972, 3211, 3346, and 3431 cm^{-1} (figure 11, right). The Raman and EPMA results were both consistent with the atacamite reference in the RRUFF database.

Apatite [$Ca_5(PO_4)_3F$]. Apatite was also identified by Raman spectroscopy. Its Raman spectrum matched that of fluorapatite, with prominent bands at 404, 432, 583, 607, 690, 963, 1005, and 1073 cm^{-1} (figure 11, left). The apatite had different forms with variable chemical compositions, some precipitating as sulfur-rich apatite and some containing iron and sodium (see table S-3 in the appendix). It often occurred as irregular particles, fine veins, and long prismatic crystals cementing the goethite fragments (figure 14D). Tabular and euhedral microcrystalline apatite, crystallized as perfect flaky hexagonal crystals stacked in the hollow core of goethite, were observed in one sample (figure 14A). Vermicular crystals of apatite

Figure 13. A: Bright green atacamite crystals associated with turquoise. B: Elongate columnar atacamite in matrix. C: Irregularly granular atacamite surrounded by quartz in matrix. Photomicrographs by Ling Liu; fields of view 1.1 mm (A) and 0.6 mm (B and C).

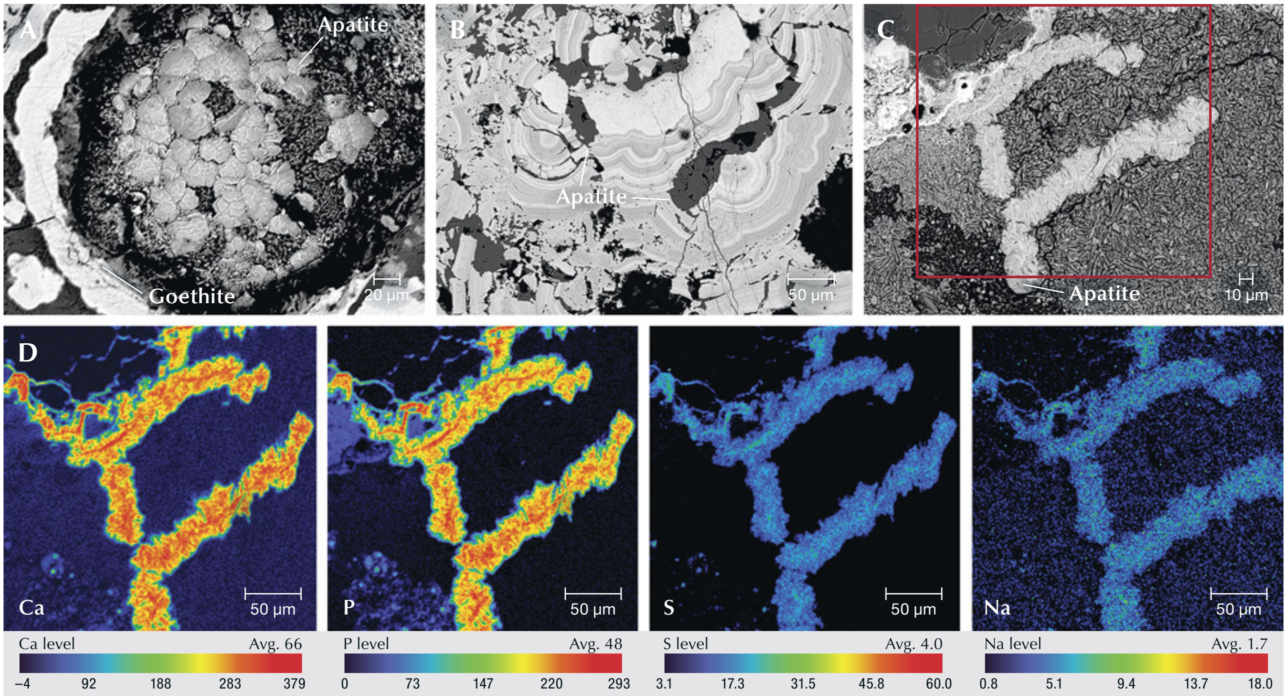

Figure 14. BSE images of euhedral apatite flakes precipitated in the cavities of goethite (A), irregular flakes and long-prismatic apatite (B), and vermicular crystals of apatite in matrix (C). D: EPMA element mapping of the calcium, phosphorus, sulfur, and sodium distributed in the apatite's vermicular form. Images by Ling Liu.

were also observed in the turquoise matrix using microscopy and BSE imaging (figure 14C). EPMA mapping showed that these vermicular apatite crystals contained abundant calcium and phosphorus, as well as minor sodium, sulfur, and antimony (figure 14). The high concentrations of calcium, phosphorus, sodium, sulfur, and antimony were the opposite of the low aluminum, silicon, and iron contents (see figure S-3 in the appendix). The distribution of element concentrations closely matched the apatite's vermicular form.

A mixture of apatite and turquoise was also identified in Tianhu East samples (figure 15). Round inclusions usually occurred in groups or clusters at the border between the turquoise and its matrix. They displayed a wide range of colors: blue, bluish green, and yellowish green. Ranging from 10 to 139 µm in diameter, they were not easily visible without magnification. When the samples were prepared as thin sections for electron probe measurements, the turquoise areas were opaque. Parts of the round inclusions (the mixture of turquoise and apatite) were transparent under

Figure 15. A: Bluish green round inclusions (a mixture of apatite and turquoise). B: The turquoise portion is opaque, while some mixture of apatite and turquoise is transparent under transmitted light in thin sections. C: Variations in brightness observed in an EPMA-BSE image of the round inclusions, with transparent parts appearing brighter than the opaque parts. Images by Ling Liu.

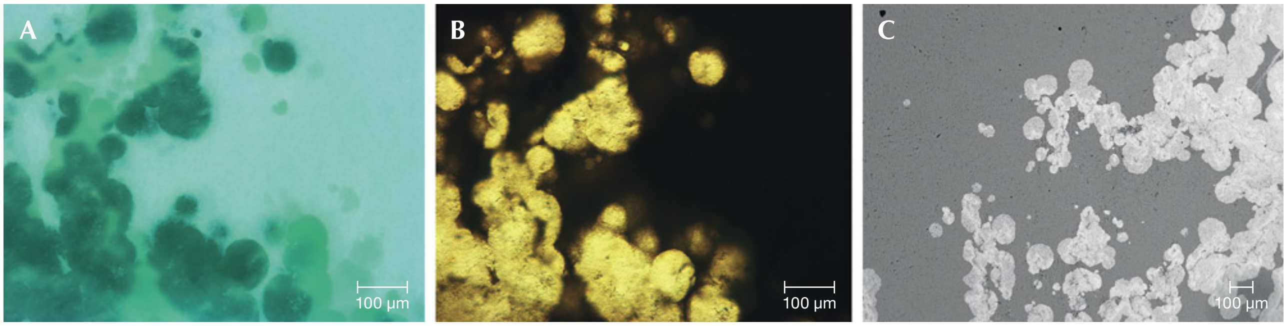

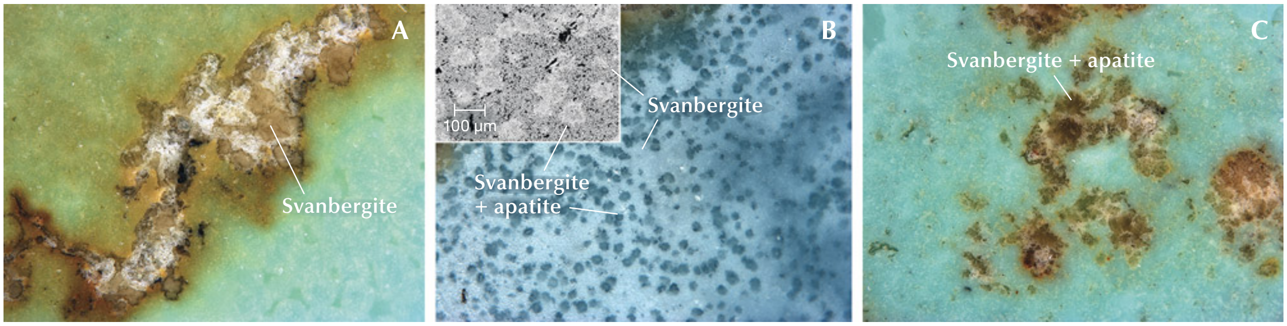

Figure 16. A: Beige svanbergite associated with quartz and turquoise. B: Deep blue spots (a mixture of svanbergite and apatite) unevenly distributed in svanbergite (BSE image inset). C: Irregular yellowish green fragments (also a mixture of svanbergite and apatite) surrounded by turquoise. Photomicrographs by Ling Liu; fields of view 2.8 mm (A and C) and 2.7 mm (B).

transmitted light, while the other parts were opaque (figure 15B). EPMA-BSE imaging revealed that these transparent parts were brighter than the opaque parts (figure 15C). Nevertheless, both the transparent and the opaque parts were identified as a mixture of fluorapatite and turquoise. Their spectra exhibit the Raman shifts typical of turquoise and a dominant band at 964 cm^{-1} (figure 11, right).

The EPMA and element mapping results clearly showed that in the round inclusions, the transparent portions had higher concentrations of CaO (8.09 wt.%) and fluorine (0.91 wt.%) than the opaque portions but lower Al_2O_3 (31.00 wt.%), CuO (6.73% wt.%), and P_2O_5 (34.21 wt.%) (see table S-2 in the appendix). This was caused by the large amount of apatite and small amount of turquoise in the transparent portions. The transparency of the round inclusions was associated with the ratio of apatite to turquoise. Element mapping highlighted the different element distributions between the turquoise parts and the round inclusions (see figure S-4 in the appendix). The round inclusions had higher calcium, phosphorus, and fluorine contents but lower aluminum, copper, and iron. The differences for calcium and phosphorus were the most pronounced. Element mapping also revealed that calcium and aluminum were unevenly distributed within the round inclusions.

Svanbergite [$SrAl_3(PO_4)(SO_4)(OH_6)$]. These opaque crystals were found in a wide range of colors (beige, brownish yellow, and bluish white) and occurred together with turquoise, goethite, or quartz (figure 16A). The Raman spectrum for svanbergite was inconclusive, with bands at 185, 254, 373, 468, 518, 616, 698, 988, 1026, 1108, 3189, and 3465 cm^{-1} (figure 11, right). The major compositions obtained by EPMA-EDS were Al_2O_3 (42.17 wt.%), P_2O_5 (26.23 wt.%), SO_3 (8.11 wt.%), CaO (10.95 wt.%), SrO (10.12 wt.%), and FeO (1.75 wt.%) (see table S-3 in the appendix). Svanbergite was often associated and mixed with apatite, occur-

Figure 17. A: Jarosite has the brightest gray value in this BSE image. B: Bonattite with a milky appearance filling in the fissures and wedge-shaped cavities of goethite. C: Muscovite with perfect cleavage, found in the matrix of rough samples. Photomicrographs by Ling Liu; fields of view 1.2 mm (A), 5.9 mm (B), and 1.1 mm (C).

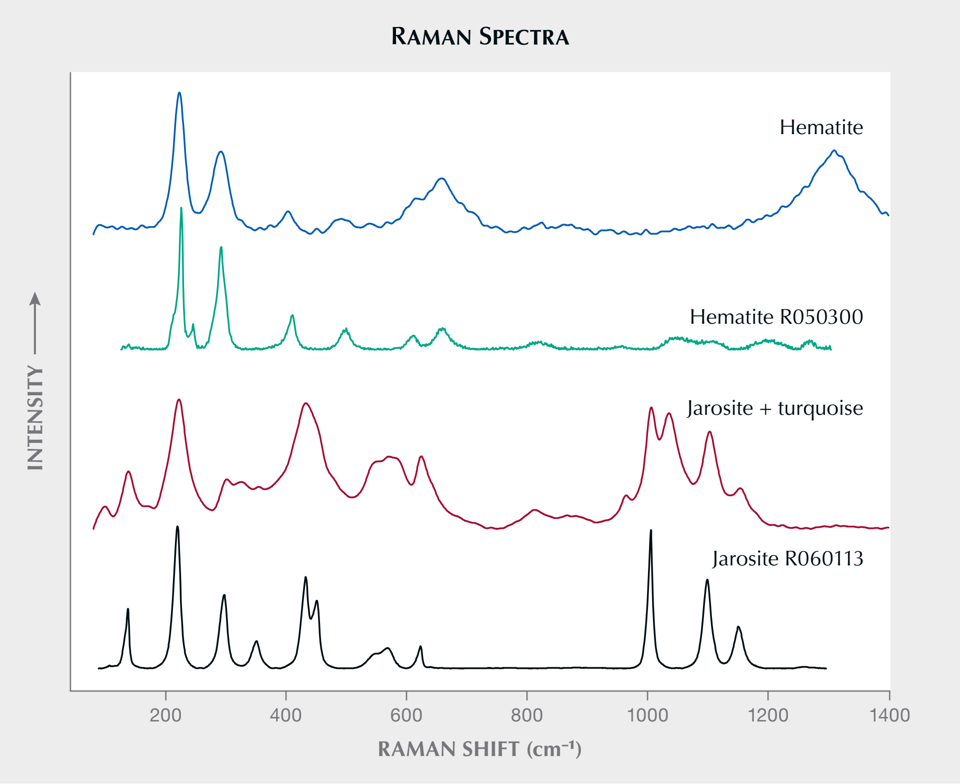

Figure 18. Raman spectra of jarosite and hematite in the turquoise samples, with standard RRUFF reference spectra included for comparison. Spectra are offset vertically for clarity.

ring as spots, veins, or irregular fragments embedded in turquoise, svanbergite, or goethite (figure 16, B and C). The mixture of svanbergite and apatite exhibited the combined Raman shifts and mixed compounds when analyzed by Raman spectroscopy and EPMA-EDS, respectively. Mixtures of turquoise and svanbergite and of turquoise, apatite, and svanbergite were also detected by Raman spectroscopy and EPMA-EDS.

Jarosite $[KFe^{3+}_3(SO_4)_2(OH)_6]$. Because of its lower mean atomic number, jarosite appeared brighter than turquoise in BSE images (figure 17A). The Raman results showed the combined characteristics of turquoise and jarosite, with peaks at 138, 222, 433, 571, 624, 1006, 1103, and 1154 cm^{-1} (figure 18). The chemical compositions were characterized by rich sulfur, potassium, and iron in addition to Al_2O_3, P_2O_5, and CuO. The concentrations obtained by EPMA-EDS were 14.06–15.95 wt.% for SO_3 and 3.65–4.49 wt.% for K_2O. FeO ranged from 22.69 to 24.93 wt.% (see table S-3 in the appendix).

Bonattite $[CuSO_4{\cdot}3H_2O]$. In the rough turquoise samples, a semitransparent milky mineral with a waxy luster appeared as fillers in the fissures or wedge-shaped cavities of goethite (figure 17B). This mineral occurred as irregular forms or veins, up to approximately 2 mm in length, and was identified by Raman spectrometry as bonattite.

Muscovite $[KAl_2(Si_3Al)O_{10}(OH)_2]$. The mineral muscovite was easily found in the matrix of rough samples. It was colorless and transparent, with perfect cleavage and glassy luster (figure 17C) and main Raman bands at 260, 400, and 703 cm^{-1}.

Generally, Tianhu East turquoise samples from the primary occurrence were accompanied by a variety of minerals. In addition to the minerals mentioned above, others such as hematite (Fe_2O_3) (figure 18) and gypsum $[Ca(SO_4){\cdot}2H_2O]$ were also identified by Raman analysis.

Evidence of Elemental Sources for Turquoise Formation. *Petrography and Mineralogy*. The quartzite samples were composed mainly of quartz (>87%) (figure 19A) and muscovite, as well as minor jarosite, gypsum, and goethite. The black shale consisted of quartz (13–75%), muscovite (6–74%) (figure 19B), jarosite, montmorillonite, goethite, and kaolinite. Apatite and pyrite were also detected in both quartzite and black shale by EPMA (see table S-4 in the appen-

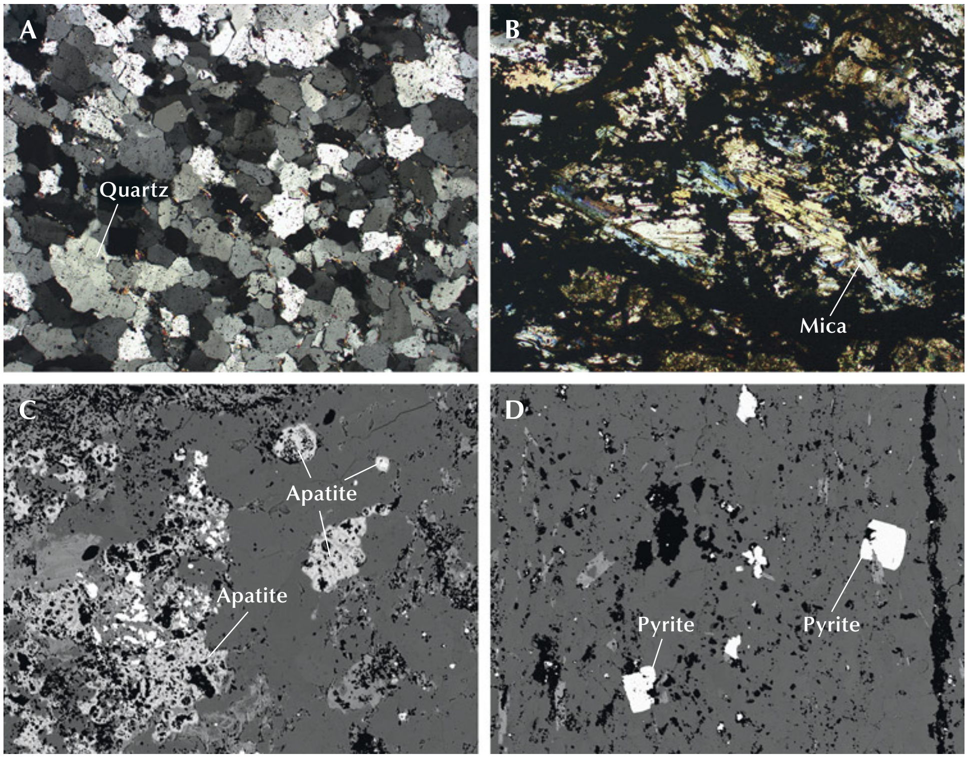

Figure 19. Minerals in the quartzite and black shale of Tianhu East. A: Quartz observed using a polarizing microscope with plane polarized light. B: Mica observed using a polarizing microscope with perpendicular polarized light. C and D: EPMA-BSE imaging reveals apatite (C) and cubic pyrite (D). Photomicrographs by Ling Liu; fields of view 2.1 mm (A), 1.0 mm (B and C), and 1.8 mm (D).

dix) and Raman analysis. The apatite was often irregular and toothed along the vermicular edge and occasionally found as fine granular crystals (figure 19C). The pyrite had typical cubic forms (figure 19D).

Geochemistry. In bedrocks from the Tianhu East deposit, black shale had higher concentrations of Al_2O_3 (avg. 4.74 wt.%), P_2O_5 (avg. 1.74 wt.%), Fe_2O_3 (avg. 12.62 wt.%), and Cu (avg. 164.2 ppm), but lower SiO_2 content (avg. 59.69 wt.%), than those of quartzite (see table S-4 in the appendix). The geochemical characteristics of phosphorus, copper, and iron in black shale were especially noteworthy, attributed to the enrichment of various minerals (e.g., apatite and pyrite) and polymetallic elements. According to the geochemical data of stream sediments surveyed by Xu (2005), the range of copper (20–30 ppm) and phosphorus (473–553 ppm) varied greatly in Tianhu East, but the chemical gradient of Al_2O_3 (10.2–11.6%) was relatively small. The data for stream sediments demonstrate that aluminum is widespread in this region, while copper and phosphorus are limited. The contents of copper and phosphorus in Tianhu black shale were higher than those in stream sediments (Xu, 2005), while the range of copper in quartzite (avg. 30.28 ppm) was similar. The high concentrations of phosphorus and copper in black shale were vital to the turquoise mineralization.

DISCUSSION

Mineral Assemblages. Table 3 lists the various minerals associated with turquoise from worldwide deposits, allowing a comparison of the mineralogical variability in determining geographic origin. Quartz is the most common mineral found (Jiang et al., 1983; Hull et al., 2008; Taghipour and Mackizadeh, 2014; Luo et al., 2017; Rossi et al., 2017; X.T. Li et al., 2019; J. Liu et al., 2019; Shen and Zhao, 2019). Mixtures of apatite and turquoise occur as inclusions in turquoise from both Tianhu East and Hubei (L. Liu et al., 2020). Apatite is also present in turquoise from Anhui (Yang et al., 2003), New Mexico (Hull et al., 2008), and Neyshabur (Rossi et al., 2017). The presence of goethite and hematite in the present study is consistent with iron oxides, as previously reported (Jiang et al., 1983; Tu, 1996; Hull et al., 2008; Taghipour and Mackizadeh, 2014; Luo et al., 2017; X.T. Li et al., 2019; Shen and Zhao, 2019). Jarosite has also been identified in turquoise from the Bijiashan mine in Anhui Province (Shen and Zhao, 2019), as well as Shaanxi and Hubei (Jiang et al., 1983; Tu, 1996, 1997a), and Damghan, Iran (Taghipour and Mackizadeh, 2014). Bonattite [$CuSO_4·3H_2O$] was found in the Tianhu East samples. The coexistence of svanbergite and turquoise is found in turquoise from both Tianhu East and Xichuan, Henan Province (X.T. Li et al., 2019). Nevertheless, the occurrence of other

TABLE 3. Summary of minerals found in turquoise deposits worldwide.

Locality		Minerals	References
Hami, China	Tianhu East	Quartz, fluorapatite, goethite, hematite, jarosite, bonattite, muscovite, atacamite, svanbergite, gypsum	This study
Anhui, China	Tongling	Quartz, anatase, barite, illite, albite, kaoline	J. Liu et al. (2019)
	Diananshan mine, Ma'anshan	Kaolinite	Zhou et al. (2013)
	Dahuangshan mine, Ma'anshan	Monazite	Shen (2020a)
	Bijiashan mine, Ma'anshan	Quartz, pyrite, kaolinite, pyrophyllite, limonite, jarosite, albite	Shen and Zhao (2019)
	Ma'anshan	Apatite	Yang et al. (2003)
Henan, China	Xichuan	Svanbergite, quartz, chalcedony, iron oxides (hematite and goethite)	X.T. Li et al. (2019)
Shaanxi, China	Luonan	Quartz, chalcedony, limonite, kaolinite, illite	Luo et al. (2017)
	Yuertain mine, Baihe	Woodhouseite	Shi and Cai (2008)
Adjacent districts of Shaanxi and Hubei, China		Quartz, sericite, pyrite, halloysite, metahalloysite, allophane, limonite, goethite, jarosite, variscite, woodhouseite, crandallite, barite, alunite, gypsum, kaolinite, chalcolite, autunite, malachite, azurite, covellite, chalcosiderite, tyuyamunite	Jiang et al. (1983); Tu (1996, 1997a, b)
Hubei, China	Zhushan	Hotsonite, woodhouseite, crandallite, chalcedony, viseite	Shi et al. (2008)
Arizona, United States	Canyon Creek mine	Metatorbernite	Hedquist et al. (2017)
New Mexico, United States	Castillian mine, Cerrillos Hills Mining District	Apatite, iron oxides, quartz, clay minerals	Hull et al. (2008)
	Santa Fe	Variscite, metavariscite, voltaite, adularia	Rossi et al. (2017)
	Iron Mask mine, Orogrande	Gypsum, sericite, kaolinite, jarosite, alunite, chalcosiderite, atacamite, malachite, apatite, xenotime	Crook and Lueth (2014)
Egypt	Sinai Peninsula	Faustite, crandallite, goyazite, quartz	Rossi et al. (2017)
France	Montebras Creuse	Planerite, variscite, wavellite	Rossi et al. (2017)
Khorasan, Iran	Neyshabur	Planerite, quartz, fluorapatite, crandallite	Rossi et al. (2017)
Damghan, Iran	Kuh-Zar	Tourmaline, alunite, sericite, quartz, chlorite, epidote, kaolinite, jarosite, iron oxides (hematite and goethite)	Taghipour and Mackizadeh (2014)

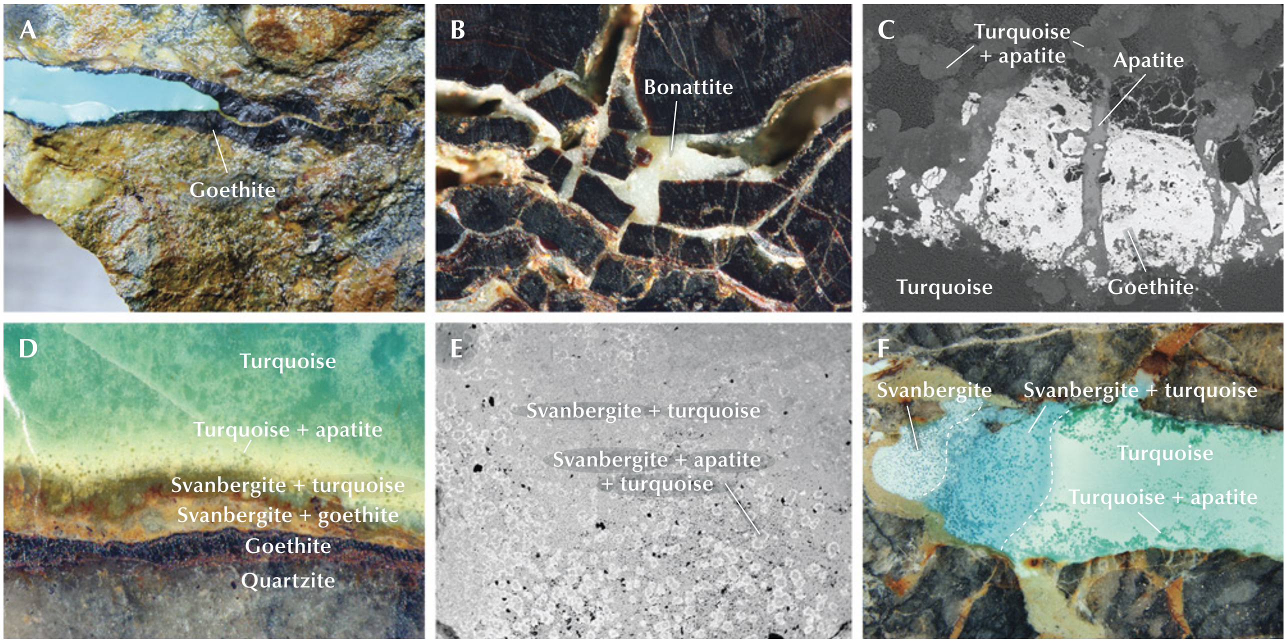

Figure 20. A: Turquoise filling in goethite showed later formation. B: Bonattite formed in a goethite fissure. C: Apatite grew along the fissures of goethite, revealed in EPMA-BSE images. D: The crystallization sequence of goethite, apatite, svanbergite, turquoise, and their mixtures hosted in quartzite. E: EPMA-BSE image showing mottled aggregates of the mixed svanbergite, apatite, and turquoise dispersed in the mixture of svanbergite and turquoise. F: Coexisting svanbergite, apatite, turquoise, and their mottled aggregates in a sample with a mineralogical transition zone. Photomicrographs by Ling Liu; fields of view 1.8 mm (B), 1.1 mm (C), 4.0 mm (D), 3.3 mm (E), and 18 mm (F).

aluminum phosphate-sulfate minerals (e.g., woodhouseite, crandallite, alunite, and goyazite) has been documented at turquoise deposits in Shaanxi and Hubei (Jiang et al., 1983; Shi and Cai, 2008; Shi et al., 2008), the Sinai Peninsula, and Khorasan, Iran (Rossi et al., 2017), but was not identified in our samples from this study.

Notably, the presence of atacamite separates Tianhu East turquoise from other Chinese turquoise. This is because it has never been reported previously from other Chinese deposits, but only from the Iron Mask mine in Orogrande, New Mexico (Crook and Lueth, 2014). Atacamite is a supergene product of the oxidation of copper deposits (Arcuri and Brimhall, 2003; Cameron et al., 2007) under arid and saline conditions. The Tianhu East deposit lies in the Gobi Desert region, which is characterized by a lack of moisture, high temperatures, and extreme temperature swings. It seems logical that atacamite is only found in Hami and not in China's other turquoise deposits.

Mineralogical variability also indicated the physical and chemical conditions of turquoise formation. The presence of jarosite and goethite suggests that Tianhu East turquoise formed in an acidic oxidizing environment (Jiang et al., 1983; Crook and Lueth, 2014). The paragenetic assemblage of svanbergite, jarosite, gypsum, and bonattite in turquoise from Tianhu East suggests high sulfur fugacity in the deposit.

Mineral Crystallization Sequence. Quartz, muscovite, and pyrite were the rock-forming minerals at Tianhu East. Apatite was formed in black shale during early diagenesis. The fractures of quartzite were initially filled by goethite and later by turquoise (figure 20A). It should be noted that bonattite precipitated in the cavities and fissures of goethite (figures 17B and 20B), indicating that it formed after goethite. The formation of bonattite demonstrates the availability of copper in the weathering solutions (Chavez, 2000).

Magnification revealed that goethite, secondary apatite, svanbergite, turquoise, and their mixtures (identified by Raman spectroscopy) precipitated successively in quartzite to form a layered structure (figure 20D). Apatite crystals formed in the fissures and cavities of goethite (figure 14, A and B). BSE images show apatite veinlets interspersed across goethite with reaction edges (figure 20C). Svanbergite mixed with goethite appeared as a yellow layer 0.38 mm

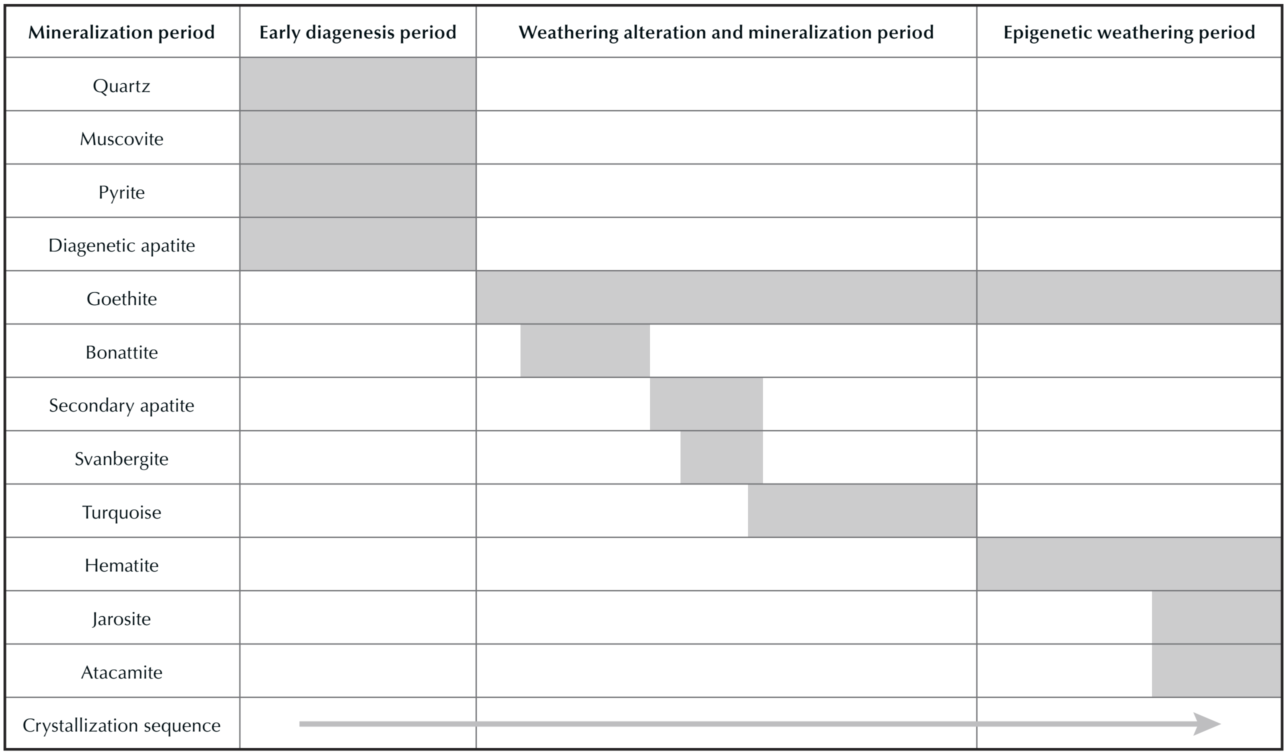

Mineralization period	Early diagenesis period	Weathering alteration and mineralization period	Epigenetic weathering period
Quartz	▨		
Muscovite	▨		
Pyrite	▨		
Diagenetic apatite	▨		
Goethite		▨	▨
Bonattite		▨	
Secondary apatite		▨	
Svanbergite		▨	
Turquoise		▨	
Hematite			▨
Jarosite			▨
Atacamite			▨
Crystallization sequence	→	→	→

Figure 21. Mineral crystallization sequence in the Tianhu East deposit.

thick (figure 20D). The svanbergite and turquoise mixture appeared in the middle of the green layers, followed by small grains of the turquoise and apatite mixture. Thus, the paragenetic sequences suggest that precipitation of svanbergite and apatite occurred after goethite but preceded turquoise.

Svanbergite was intimately intergrown with apatite. This mixture occurred as small blue inclusions dispersed within the svanbergite (figure 16B), indicating that the formation of svanbergite and apatite was nearly simultaneous. Additionally, turquoise coprecipitated with svanbergite and apatite (figure 20, D–F), creating mottled aggregates that are difficult to separate from each other. The paragenetic relationship reveals that the precipitation of svanbergite and apatite briefly overlapped with turquoise, with both minerals forming slightly earlier than turquoise during the preliminary period.

The apatite would have dissolved within an acidic weathering solution (Guidry and Mackenzie, 2003; Salama, 2014). The initial weathering solutions were acidic but would have become slightly alkaline after reacting with the diagenetic apatite (Salama, 2014). Under alkaline conditions, secondary apatite reprecipitated as filling phases in goethite when the weathering solutions were leached out. Svanbergite is more stable than apatite under acidic conditions (Salama, 2014; Vircava et al., 2015) and would have precipitated with decreasing pH of the weathering solution (Vircava et al., 2015). The formation of turquoise was possible when the weathering solutions became more acidic (pH = 4.45) (Spier et al., 2020) and had a high enough concentration of Cu^{2+}. The textural relationships and crystallization sequence of apatite, svanbergite, and turquoise also suggest that the turquoise precipitated from a more acidic solution than those of apatite and svanbergite.

The final period was the formation of minor minerals (hematite, jarosite, and atacamite). During the epigenetic weathering process, hematite and jarosite were typically dispersed in turquoise. Atacamite is usually recognized as a cavity-filling phase in turquoise or quartzite (figure 13), indicating a postgenetic relationship. After the formation of turquoise, the excess copper of the weathering solutions eventually transformed into atacamite. The presence of bonattite and atacamite confirmed significant enrichment of copper in the weathering solutions (Chavez, 2000; Crook and Lueth, 2014).

Accordingly, the minerals formed in three periods, according to mineral assemblages, as shown in figure 21.

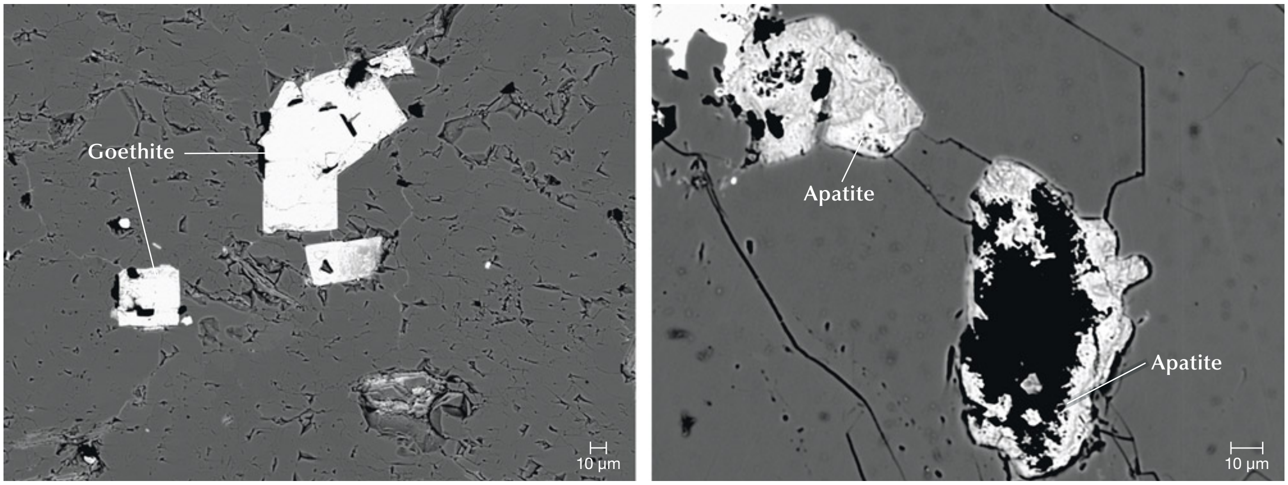

Figure 22. The occurrence of goethite and diagenetic apatite in the Tianhu East rocks, revealed in EPMA-BSE images. A: Goethite with pseudomorphic cubic forms produced by the oxidation of pyrite. B: The remaining dissolved apatite exhibits incomplete shapes with numerous cavities.

Genesis and Elemental Derivation for Formation. Mineralogical and geochemical characteristics confirmed the supergene origin of Tianhu East turquoise. The formation process can be proposed as four stages:

Stage I: Early Diagenesis. During regional dynamic metamorphism, metal sulfide (e.g., pyrite) was formed, and other minerals containing iron, copper, aluminum, and phosphorus accumulated in the strata.

Stage II: Weathering. Rock-forming minerals were subjected to weathering alteration when exposed to the supergene environment. During the weathering process, water and oxygen promoted the oxidation of metallic sulfides (e.g., pyrite), generating abundant sulfuric acid and creating an acidic environment (Crook and Lueth, 2014) that was beneficial to dissolving the essential elements of aluminum, phosphorus, and copper. Small, bright goethite crystals with pseudomorphic cubic forms in black shales were the oxidative product of pyrite (figure 22A). The acidic solutions facilitated the dissolution of apatite, releasing calcium and phosphorous (Guidry and Mackenzie, 2003). BSE images show that most diagenetic apatite in black shales has an incomplete shape with toothed edges and numerous cavities (figure 22B), indicating partial dissolution (Crook and Lueth, 2014).

Stage III: Leaching and Migration. Due to multiphase tectonic activities, fractures were well developed, especially in quartzite. Aluminum, phosphorus, and copper were subsequently leached from the rocks and concentrated in the weathering solutions, leaching downward and migrating along structural fractures of the quartzite. These fractures provided space for the precipitation of the solutions, enabling the crystallization and mineralization of turquoise.

Stage IV: Precipitation and Turquoise Formation. Finally, turquoise precipitated and formed as veins and nodules within the structural fractures of quartzite (figure 23).

Several studies have reported that connate waters, descending meteoric water, and surface waters were favorable to the formation of turquoise (Pogue, 1915; Tu, 1997a,b; Hull et al., 2008; Taghipour and Mackizadeh, 2014). We propose that descending meteoric water was mainly responsible for the formation of Tianhu East turquoise, since the deposit lies in a region with a dry climate. There is little perennial surface-streaming water in the area (Chen, 2016; Zhang, 2020), and aluminum is abundant. Sufficient alumina for turquoise formation was released from muscovite or sericite during the weathering process of the rocks. Phosphorus was derived mainly from diagenetic apatite hosted in the black shale. Copper-bearing minerals dispersed within the black shale were probably the source of copper (Pogue, 1915; Spier et al., 2020), as evidenced by the excess copper content in the black shales and the formation of bonattite and atacamite.

CONCLUSIONS

Tianhu East turquoise has significant geological and gemological value. The samples in this study had

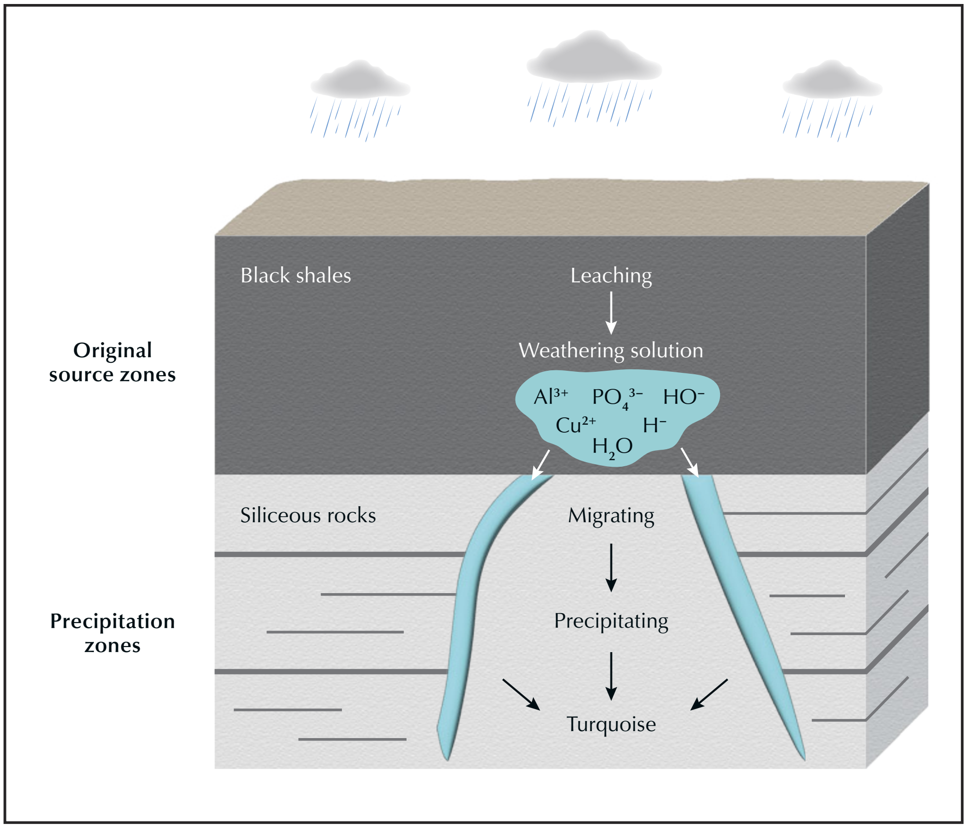

Figure 23. The genetic model for the formation of Tianhu East turquoise.

platy, long columnar, laminar, rhombic, and rhomboidal microstructures and were characterized by high lithium, vanadium, chromium, strontium, and gallium contents along with relatively low barium. Turquoise veins at the deposit are hosted by quartzite and accompanied by abundant minerals, including quartz, apatite, goethite, hematite, jarosite, bonattite, muscovite, atacamite, svanbergite, and gypsum. Atacamite is a unique geographic indicator for the origin of turquoise at Tianhu East, separating it from other Chinese deposits. Textural relationships among the associated minerals also indicated the crystallization sequence that is essential to understanding turquoise formation. Mineralogical and geochemical characteristics confirmed that the elemental sources of turquoise were derived mainly from black shale due to the presence of the mineral suite (apatite, pyrite, and muscovite) within the rocky outcrop. This study proposes a hypothesis of supergene weathering origin for the Tianhu East deposit.

ABOUT THE AUTHORS

Dr. Ling Liu (lingliu0928@163.com) is a postdoctoral researcher at China University of Geosciences (CUG) in Wuhan and also a manager at Hubei Turquoise Testing Technology Co., Ltd. Professor Mingxing Yang (yangc@cug.edu.cn, corresponding author), Dr. Ye Yuan (yyrequiem@vip.qq.com, corresponding author), and Professor Yan Li are with the Gemmological Institute, CUG. Qiaoqiao Li is a distinguished gemologist at Guild Laboratories in Shenzhen. Yi Tang is with the Xinjiang Geological Survey Institute. Jia Liu is a lab manager at the Gemmological Institute, CUG. Huilin Wen holds a master's degree in gemology from the Gemmological Institute, CUG.

ACKNOWLEDGMENTS

This research was financially supported by grant no. GZB20230683 from the Postdoctoral Fellowship Program of CPSF and grant no. 20BKG030 from the National Social Science Fund of China. This work was also partially supported by the Gemmological Institute, CUG. The authors sincerely thank Xiaoming Zhang, Haitao Wang, and Hanqing Dai for their kind assistance. The thoughtful and constructive comments by the peer reviewers and editors are gratefully acknowledged.

REFERENCES

Abdu Y.A., Hull S.K., Fayek M., Hawthorne F.C. (2011) The turquoise-chalcosiderite $Cu(Al,Fe^{3+})_6(PO_4)_4(OH)_8\cdot 4H_2O$ solid-solution series: a Mössbauer spectroscopy, XRD, EMPA, and FTIR study. *American Mineralogist*, Vol. 96, No. 10, pp. 1433–1442, http://dx.doi.org/10.2138/am.2011.3658

Arcuri T., Brimhall G. (2003) The chloride source for atacamite mineralization at the Radomiro Tomic porphyry copper deposit, northern Chile. *Economic Geology*, Vol. 98, No. 8, pp. 1667–1681, http://dx.doi.org/10.2113/gsecongeo.98.8.1667

Cameron E.M., Leybourne M.I., Palacios C. (2007) Atacamite in the oxide zone of copper deposits in northern Chile: Involvement of deep formation waters? *Mineralium Deposita*, Vol. 42, No. 3, pp. 205–218, http://dx.doi.org/10.1007/s00126-006-0108-0

Cao J.E., Sun J.S., Wang Y.C., Ma J. (2021) Investigation of ancient turquoise mining site in Haobeiru, Alxa Right Banner, Inner Mongolia. *Archaeology and Cultural Relics*, No. 3, pp. 23–32.

Chavez W.X. (2000) Supergene oxidation of copper deposits: Zoning and distribution of copper oxide minerals. *Society of Economic Geologists Newsletter*, Vol. 41, pp. 9–21, http://dx.doi.org/10.5382/SEGnews.2000-41.fea

Chen J.P. (2016) Analysis of hydrogeological conditions and engineering geological conditions in Tianhu East iron mine of Hami City, Xinjiang. *Xinjiang Youse Jinshu*, Vol. 39, No. 2, pp. 14–16 [in Chinese].

Chen S.D., Xu X. (2001) On compiling of map of tectonics of Xinjiang and neighbouring areas. *Xinjiang Geology*, Vol. 19, No. 1, p. 5 [in Chinese].

Crook J.C., Lueth V.W. (2014) A geological and geochemical study of a sedimentary-hosted turquoise deposit at the Iron Mask mine, Orogrande, New Mexico. *65th Fall Field Conference New Mexico Geological Society*, pp. 227–233.

Foord E., Taggart J. (1998) A reexamination of the turquoise group: The mineral aheylite, planerite (redefined), turquoise and coeruleolactite. *Mineralogical Magazine*, Vol. 62, No. 1 pp. 93–111, http://dx.doi.org/10.1180/002646198547495

Gao K., Shi G.H., Wang M.L., Xie G., Wang J., Zhang X.C., Fang T., Lei W.Y., Liu Y. (2019) The Tashisayi nephrite deposit from South Altyn Tagh, Xinjiang, northwest China. *Geoscience Frontiers*, Vol. 10, No. 4, pp. 1597–1612, http://dx.doi.org/10.1016/j.gsf.2018.10.008

Guidry M.W., Mackenzie F.T. (2003) Experimental study of igneous and sedimentary apatite dissolution: Control of pH, distance from equilibrium, and temperature on dissolution rates. *Geochimica et Cosmochimica Acta*, Vol. 67, No. 16, pp. 2949–2963, http://dx.doi.org/10.1016/s0016-7037(03)00265-5

Hedquist S.L., Thibodeau A.M., Welch J.R., Killick D.J. (2017) Canyon Creek revisited: New investigations of a late prehispanic turquoise mine, Arizona, USA. *Journal of Archaeological Science*, Vol. 87, pp. 44–58, http://dx.doi.org/10.1016/j.jas.2017.09.004

Hull S., Fayek M., Mathien F.J., Shelley P., Durand K.R. (2008) A new approach to determining the geological provenance of turquoise artifacts using hydrogen and copper stable isotopes. *Journal of Archaeological Science*, Vol. 35, No. 5, pp. 1355–1369, http://dx.doi.org/10.1016/j.jas.2007.10.001

Jiang Z.C., Chen D.M., Wang F.Y., Li W.Y., Cao X.Q., Wu Q.X. (1983) Thermal properties of turquoise and its intergrowing minerals in a certain district of China. *Acta Mineralogica Sinica*, No. 3, pp. 198–206, 247 [in Chinese].

Lafuente B., Downs R.T., Yang H., Stone N. (2016) The power of databases: The RRUFF project. In T. Armbruster and R.M. Danisi, Eds., *Highlights in Mineralogical Crystallography*. W. de Gruyter GmbH, Berlin, pp. 1–29.

Li X.T., Xian Y.H., Fan J.Y., Zhang L.F., Guo J.W., Gao Z.Y., Wen R. (2019) Application of XRD-SEM-XRD-EMPA to study the mineralogical characteristics of turquoise from Xichuan, Henan province. *Rock and Mineral Analysis*, Vol. 38, No. 4, pp. 373–381, http://dx.doi.org/10.15898/j.cnki.11-2131/td.201809090102 [in Chinese].

Li Y.X., Tan Y.C., Jia Q., Zhang D.Y., Yu J.J., Duan C.W., Xian Y.H. (2019) Preliminary investigation on two ancient turquoise mining sites in Kumul, Xinjiang. *Archaeology and Cultural Relics*, No. 6, pp. 22–27 [in Chinese].

Li Y.X., Yu J.J., Xian Y.H., Tan Y.C., Zhu Z.Z., Cao K., Yu C., Li X.T., Fan J.Y., Duan C.W., Jin P., Wen R., Ren M. (2020) A survey of the ancient turquoise mining site at Heishanling in Ruoqiang, Xinjiang. *Cultural Relics*, No. 8, pp. 4–13, http://dx.doi.org/10.13619/j.cnki.cn11-1532/k.2020.08.001 [in Chinese].

Liu J., Wang Y.M., Liu F.L., He C., Liu F. (2019) Gemmological and mineralogical characteristics of turquoise from Tongling, Anhui province. *Journal of Gems and Gemmology*, Vol. 21, No. 6, pp. 58–65 [in Chinese].

Liu L., Yang M.X., Li Y. (2020) Unique raindrop pattern of turquoise from Hubei, China. *G&G*, Vol. 56, No. 3, pp. 380–400, http://dx.doi.org/10.5741/GEMS.56.3.380

Liu X.F., Lin C.L., Li D.D., Zhu L., Song S., Liu Y., Shen C.H. (2018) Study on mineralogy and spectroscopy of turquoises from Hami, Xinjiang. *Spectroscopy and Spectral Analysis*, Vol. 38, No. 4, pp. 1231–1239 [in Chinese].

Liu Y., Deng J., Shi G., Sun X., Yang L. (2011a) Geochemistry and petrogenesis of placer nephrite from Hetian, Xinjiang, northwest China. *Ore Geology Reviews*, Vol. 41, No. 1, pp. 122–132, http://dx.doi.org/10.1016/j.oregeorev.2011.07.004

Liu Y., Deng J., Shi G., Yui T.-F., Zhang G., Abuduwayiti M., Yang L., Sun X. (2011b) Geochemistry and petrology of nephrite from Alamas, Xinjiang, NW China. *Journal of Asian Earth Sciences*, Vol. 42, No. 3, pp. 440–451, http://dx.doi.org/10.1016/j.jseaes.2011.05.012

Liu Y., Zhang R.Q., Abuduwayiti M., Wang C., Zhang S.P., Shen C.H., Zhang Z.Y., He M.Y., Zhang Y., Yang X.D. (2016) SHRIMP U-Pb zircon ages, mineral compositions and geochemistry of placer nephrite in the Yurungkash and Karakash River deposits, West Kunlun, Xinjiang, northwest China: Implication for a magnesium skarn. *Ore Geology Reviews*, Vol. 72, pp. 699–727, http://dx.doi.org/10.1016/j.oregeorev.2015.08.023

Luo Y.F., Yu X.Y., Zhou Y.G., Yang X.G. (2017) A study of texture and structure of turquoise from Luonan, Shaanxi Province. *Acta Petrologica et Mineralogica*, Vol. 36, No. 1, pp. 115–123, http://dx.doi.org/10.3969/j.issn.1000-6524.2017.01.012 [in Chinese].

Pang X.X. (2014) The researches on the turquoise objects of the neolithic age unearthed in China. *Acta Archaeologlca Sinica*, No. 2, pp. 139–168 [in Chinese].

Pogue J.E. (1915) *The Turquoise: A Study of Its History, Mineralogy, Geology, Ethnology, Archaeology, Mythology, Folklore, and Technology.* Third Memoir, Vol. XII, National Academy of Sciences, Washington DC.

Qin X.L. (2020) The research of turquoise and inlaid ritual ornaments from a cross-cultural perspective. *The Central Plains Culture Research*, Vol. 8, No. 6, pp. 12–19 [in Chinese].

Rossi M., Rizzi R., Vergara A., Capitelli F., Altomare A., Bellatreccia F., Saviano M., Ghiara R.M. (2017) Compositional variation of turquoise-group minerals from the historical collection of the Real Museo Mineralogico of the University of Naples. *Mineralogical Magazine*, Vol. 81, No. 6, pp. 1405–1429, http://dx.doi.org/10.1180/minmag.2017.081.055

Salama W. (2014) Paleoenvironmental significance of aluminum phosphate-sulfate minerals in the upper Cretaceous ooidal ironstones, E-NE Aswan area, southern Egypt. *International Journal of Earth Sciences*, Vol. 103, No. 6, pp. 1621–1639, http://dx.doi.org/10.1007/s00531-014-1027-4

She L.Z., Qin Y., Luo W.G., Huang F.C., Li T.Y. (2009) Provenance-tracing of turquoise in northwest Hubei using rare earth elements. *Chinese Rare Earths*, Vol. 30, No. 5, pp. 59–

62 [in Chinese].

Shen C.H. (2020a) Mineralogical features and genesis of the pseudomorphic turquoise in the Dahuangshan area, Anhui province, China. *Acta Mineralogica Sinica*, Vol. 40, No. 3, pp. 313–322 [in Chinese].

——— (2020b) Study on the genesis of typical deposits in Maanshan turquoise metallogenic belt of Ningwu basin. PhD thesis, China University of Geosciences (Beijing).

Shen C.H., Zhao E.Q. (2019) Mineralogical characteristics and genetic mechanism of turquoise deposit in Bijiashan area. *Journal of Jilin University (Earth Science Edition)*, Vol. 49, No. 6, pp. 1591–1606 [in Chinese].

Shi Z.R., Cai K.Q. (2008) A study of turquoise and secondary woodhouseite from Yuertan, Baihe County, Shaanxi Province. *Acta Petrologica et Mineralogica*, Vol. 27, No. 2, pp. 164–170, http://dx.doi.org/10.3969/j.issn.1000-6524.2008.02.009 [in Chinese].

Shi Z.R., Cai K.Q., Gong M.Q. (2008) The characteristics and significance of woodhouseite and crandallite series minerals in Cambrian carbon-silicon-slate, Zhushan, Hubei province. *Northwestern Geology*, Vol. 41, No. 2, pp. 56–62 [in Chinese].

Spier C., Kumar A., Nunes A. (2020) Mineralogy and genesis of rare Al-phosphate minerals in weathered itabirite and iron ore from the Quadrilátero Ferrífero, Minas Gerais, Brazil. *Ore Geology Reviews*, Vol. 118, pp. 1–19, http://dx.doi.org/10.1016/j.oregeorev.2020.103359

Taghipour B., Mackizadeh M.A. (2014) The origin of the tourmaline-turquoise association hosted in hydrothermally altered rocks of the Kuh-Zar Cu-Au-turquoise deposit, Damghan, Iran. *Neues Jahrbuch für Geologie und Paläontologie - Abhandlungen*, Vol. 272, Vol. 1, pp. 61–77, http://dx.doi.org/10.1127/0077-7749/2014/0397

Tu H.K. (1996) Geological characteristics of turquoise ore in the areas adjacent to Shaanxi and Hubei Province. *Geology of Shaanxi*, Vol. 14, No. 2, pp. 59–64 [in Chinese].

——— (1997a) Metallogenic characteristics of turquoise in the eastern Qinling mountains. *Nonmetallic Geology*, No. 3, pp. 24–25 [in Chinese].

——— (1997b) Study on prospecting targets of turquoise and uranium mineralization. *Acta Geological Gansu*, Vol. 6, No. 1, pp. 74–79 [in Chinese].

Vircava I., Somelar P., Liivamägi S., Kirs J., Kirsimäe K. (2015) Origin and paleoenvironmental interpretation of aluminum phosphate–sulfate minerals in a Neoproterozoic Baltic paleosol. *Sedimentary Geology*, Vol. 319, pp. 114–123, http://dx.doi.org/10.1016/j.sedgeo.2015.02.003

Wang R., Wang C.S., Feng M., Pan W.B. (2007) Exploring the origin of turquoise with trace elements. *Cultural Relics of Central China*, No. 2, pp. 101–106 [in Chinese].

Wang X.F. (1996) *Stratigraphical Lexicon of China*. Geology Press, Beijing.

Wei D.G., Guan R.H. (2003) Distribution, genesis and marks of turquoise deposits in Ma'anshan area. *Express Information of Mining Industry*, No. 10, pp. 19–20 [in Chinese].

Xin Jiang Uygur Autonomous Region Bureau of Geology and Mineral Resources (1993) *Regional Geology of Xin Jiang Uygur Autonomous Region*. Geology Press, Beijing.

Xu Y.M. (2005) Gaz coalfield range J-45-17 Eursupuarek range J-45-18 Yalulak range J-45-23 1/200 000 Description of geochemical map: stream sediment survey: Geological Survey Institute of Xinjiang Uygur Autonomous Region.

Yang H.Q., Li Y., Li W.M., Yang J.G., Zhao G.B., Sun N.Y., Wang X.H., Tan W.J. (2008) General discussion on metallogenitic tectonic setting of Beishan Mountain, northwestern China. *Northwestern Geology*, Vol. 41, No. 1, pp. 22–28.

Yang X.Y., Zheng Y.F., Yang X.M., Liu X.H., Wang K.R. (2003) Mineralogical and geochemical studies on the different types of turquoise from Maanshan area, East China. *Neues Jahrbuch für Mineralogie - Monatshefte*, Vol. 2003, No. 3, pp. 97–112, http://dx.doi.org/10.1127/0028-3649/2003/2002-0097

Zhang C.P. (2022) An overview of the development of turquoise objects and their ritual significance in ancient China. *Jianghan Archaeology*, Vol. 4, No. 181, pp. 35–44 [in Chinese].

Zhang H.T. (2020) Characteristics of fluid inclusion and the formation cause of Heishan gold deposit in Hami, Xinjiang. Master's thesis, Chan'an University.

Zhou Y., Qi L.J., Dai H., Yang L.Y., Zhang Q., Jiang X.P. (2013) Study on gemmological characteristics of turquoise from Dian'anshan, Anhui province. *Journal of Gems and Gemmology*, Vol. 15, No. 4, pp. 37–45 [in Chinese].

Zhu Z.X., Zhao T.Y., Chen M.Y., Li P., et al. (n.d.) *Geology of China·Xinjiang* [unpublished book, in Chinese].

Zhou S.Q., Jiang F.J. (2005) Research on the turquoise in Xichuan of Henan. *Journal of Nanyang Teachers' College*, Vol. 4, No. 3, pp. 63–65, http://dx.doi.org/10.3969/j.issn.1671-6132.2005.03.019 [in Chinese].

“ICE JADE” FROM GUATEMALA

Zhaoying Huang, Tao Chen, Jinyu Zheng, and Zebin Xu

“Ice jade” is a translucent variety of jadeite jade (also known as *fei cui*) that is generally of high value. Reportedly from the Morales mine in the Izabal Department of Guatemala, it has recently appeared in the Chinese jewelry market. In this study, the structural characteristics, mineral compositions, and color genesis of Guatemalan “ice jade” were studied using scanning electron microscopy, cathodoluminescence, X-ray diffraction, electron probe microanalysis, Raman spectroscopy, and ultraviolet/visible/near-infrared spectroscopy. “Ice jade” is composed almost exclusively of jadeite, with accessory minerals that include omphacite and albite. The chemical composition of the samples studied here was nearly pure sodium pyroxene. A small amount of fine-grained omphacite imparted a pale green color to this material. This “ice jade” exhibited fine-grained texture, occasionally with some microgranular texture. Guatemalan “ice jade” has a unique characteristic appearance, microstructure, accessory minerals, and chemical compositions, but further study is needed to distinguish it from the other origins.

Jadeite jade, also called *fei cui* in China, is the most popular jade variety and one of the best-selling gems in China. Color and transparency are the primary quality factors that determine value. Jadeite jade is a polycrystalline aggregate, primarily consisting of jadeite ($NaAlSi_2O_6$) and including accessory minerals such as omphacite, albite, amphibole, and chromite (Harlow and Sorensen, 2005; Yuan, 2009). Gem-quality material is only found in a few countries, namely Myanmar, Guatemala, Russia, Kazakhstan, and Japan (Tsujimori and Harlow, 2012; Coccato et al., 2014; Abduriyim et al., 2017). Myanmar is the traditional and most important producer of gem-quality jadeite jade, while Guatemala has become the second-largest producer (Zhang and Shi, 2022).

From the thirteenth century to the early twenty-first century, the jadeite jade sold in China came exclusively from Myanmar (Hughes et al., 2000; Zhang, 2003). The use of jadeite jade in Central America can be traced back to 1500 BCE, but the specific source was not identified until more recently. In 1952, Robert Leslie, a researcher at the Smithsonian Institution, first found detrital nodules of jadeite in Guatemala (Foshag and Leslie, 1955). Over the next 50 years, geologists and locals discovered more jadeite mines there. After 2000, small amounts of Guatemalan material began to enter the Chinese market (Zhang, 2003). The mineral composition of different varieties of Guatemalan jadeite varies greatly. According to its main composition, it can be divided into three categories: jadeite jade, omphacite jade, and jadeite-omphacite jade. The major mineral of these three categories is jadeite, omphacite, and mixed-phase jadeite-omphacite, respectively (McClure, 2012; Lin et al., 2020). The color range of Guatemalan jadeite jade includes light to medium green, white, purple, and blue (Hargett, 1990; Abduriyim et al., 2017; Ouyang et al., 2017; Spring 2024 Gem News International, pp. 97–99 of this issue). The Guatemalan jadeite jade initially sold in the Chinese market was coarsely grained and not transparent enough to be considered gem quality. Consequently, Guatemala was thought to produce low-quality material. But that has changed recently, as vivid green semitransparent as well as pale green translucent

In Brief

- “Ice jade" from the Morales mine in Guatemala has recently appeared in the Chinese jewelry market. It is transparent to semitransparent and near-colorless to pale green.
- The main mineral component is jadeite, with small amounts of accessory minerals omphacite and albite.
- The relatively pure jadeite chemical composition and the fine-grained texture make “ice jade” appear transparent to semitransparent and nearly colorless. The fine-grained omphacite dispersed in the jadeite matrix can produce a pale green color.

See end of article for About the Authors and Acknowledgments.

GEMS & GEMOLOGY, Vol. 60, No. 1, pp. 26–41,
http://dx.doi.org/10.5741/GEMS.60.1.26

Figure 1. Guatemalan "ice jade" carvings of Bodhisattva (4.6 × 3.1 cm) and a deer (2.3 cm diameter). Courtesy of T. Chen.

jadeite jade from Guatemala has entered the Chinese market (Wang et al., 2022).

In the Chinese market, nearly colorless jadeite with fine texture and high transparency is called "ice jade." A Guatemalan variety with a near-transparent appearance (figure 1) is called "white water jade" by Chinese sellers. This material is usually near-colorless with pale gray-green or pale gray-blue colors and often contains some white snowflake-shaped impurities. It has a fine texture, and the highest-value specimens are transparent. This article studies the gemological properties, textural characteristics, and mineral compositions of fine-quality "ice jade" from the Morales mine in Guatemala and aims to provide evidence that distinguishes it from similar Burmese material.

GEOLOGIC BACKGROUND

Guatemala is located in the northwest of Central America, bordering Mexico, Belize, Honduras, and El Salvador, and the Pacific Ocean to the south (figure 2). Jadeite jade occurs in tectonic serpentinites of the

Figure 2. Left: Map of Guatemala and the location of the Morales mine (adapted from Harlow et al., 2011; Xing et al., 2021). Right: The jadeite ore at the Morales mine is hosted in the laterite layer. Photo by X.Q. Yuan.

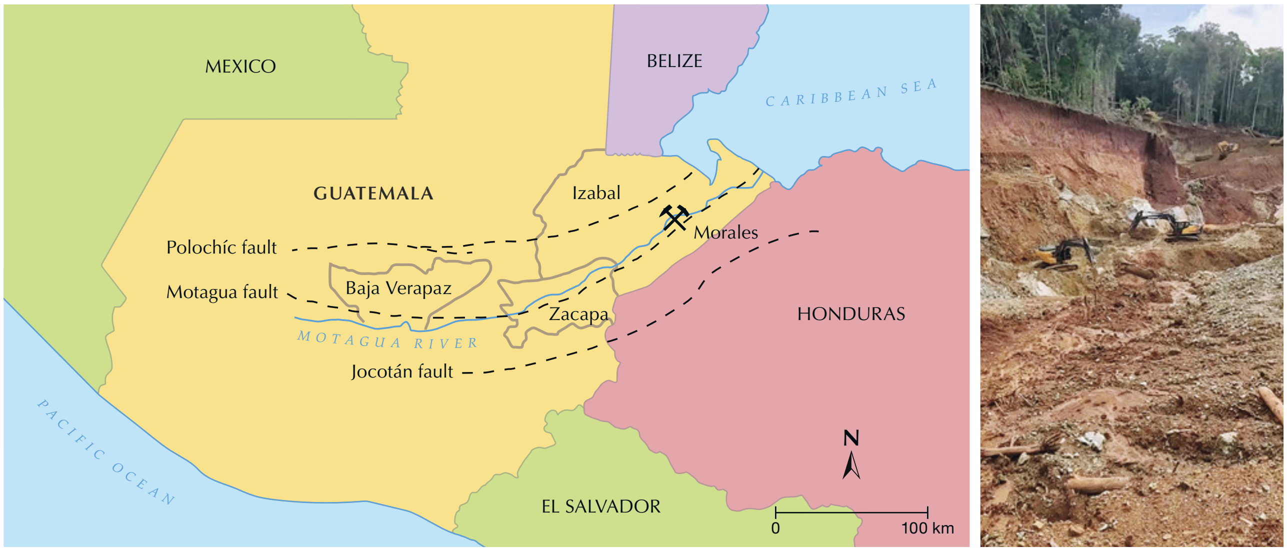

Figure 3. Guatemalan "ice jade" samples (0.086–0.770 g). The top row left to right is GB-1 to GB-5, and the bottom row left to right is GB-6 to GB-10. Photo by Z. Huang.

Motagua fault zone in Guatemala (Harlow et al., 2006). The Motagua fault zone is located in the collision zone of the North American–Caribbean plate and runs nearly parallel to the Polochíc fault zone in the north and the Jocotán fault zone in the south. The three faults form the Guatemala suture zone, which is considered a dividing line between the North American plate and the Caribbean plate (Brueckner et al., 2009; Yui et al., 2010). Jadeite jade is the product of fluid-mediated crystallization and/or metasomatism, and the formation of deposits is related to plate tectonic subduction zones (Sorensen et al., 2006; Tsujimori and Harlow, 2012; Flores et al., 2013).

Guatemalan jadeite jade was first discovered north of the Motagua River Valley (Hargett, 1990; Gendron et al., 2002), mined from primary deposits or from scattered boulders in the rivers. The primary deposits occur in serpentinite mélanges as vein or tectonic inclusions, showing a jadeite-albite-serpentinite transition zonation (Harlow, 1994). The distribution range of Guatemalan jadeitite extends from the Baja Verapaz Department to the Zacapa Department, spanning 110 km on the north side of the Motagua River Valley (Harlow et al., 2011).

The occurrence extends east to the Izabal Department, which is located in the northeastern part of the Motagua fault zone and is a newer jadeite mining location (Harlow et al., 2011). The studied "ice jade" comes from the Morales mine in Izabal (figure 2). Morales lies in the strike-slip basin in the eastern Motagua River Valley. Nearby ophiolite outcrops recrystallized under the influence of low-grade metamorphism, and mantle serpentinite was strongly deformed by shearing action. Ophiolite outcrops record sinistral slip of the Motagua fault (Giunta et al., 2002; Marshall, 2007; Bartole et al., 2019). The jadeite jade ore occurs in the laterite layer, which was weathered from serpentinite (again, see figure 2).

MATERIALS AND METHODS

The Guatemalan "ice jade" samples were collected by author ZX through the long-term cooperation of a jade merchant, who reported that the raw material was produced from the Morales mine. The merchant obtains the rough from the original source and then processes and sells it in the jewelry market in the city of Jieyang in China's Guangdong Province. The Jieyang market is one of four major trading centers for fine-quality jadeite in Guangdong. Guatemalan "ice jade" has good quality but usually sells for one-quarter to one-third the market price of its Burmese counterpart.

The samples shown in figure 3 were selected for spectroscopic, textural, and chemical composition analyses. The 10 samples, GB-1 to GB-10, weighed 0.086–0.770 g. The polished surface of each sample had a vitreous luster. A small number of white inclusions appeared to float on the surface like snowflakes. The mineral grains or texture were hard to detect without magnification, and all the samples had good transparency.

Analyses were done at the China University of Geosciences (CUG) in Wuhan. Standard gemological testing and photomicrography were performed at the Gemmological Institute, CUG. Refractive index was measured using a gemological refractometer, and specific gravity was determined using the hydrostatic method. Ultraviolet fluorescence was observed with UV lamps under long-wave (365 nm) and short-wave (254 nm). All samples and microscopic features were photographed and observed using a Leica M205A microscope camera. Diffuse reflectance ultraviolet/visible/near-infrared (UV-Vis-NIR) spectra were collected by a Skyray Instrument Gem UV-100 spectrometer, using an integrating sphere with a range of 200–1000 nm and an integration time of 100 ms, and eight cycles were collected for each spectrum.

X-ray diffraction (XRD) patterns were collected by a Bruker AXS D8 Advance X-ray powder diffractometer at the Faculty of Materials Science and Chemistry. The system was equipped with a copper target X-ray tube set to 40 kV and 40 mA. The scanning speed was 10°/min in the 2θ range of 3–70°, and fragments of the samples were pulverized into 200-mesh powder for the experiment.

Raman spectra of main minerals and inclusions were recorded using a Horiba-LabRAM HR Evolution Raman spectrometer and a Jasco NRS-7500 Raman spectrometer with a 532 nm solid state laser, an acquisition time of 15 s, and an accumulation of 3 scans in the range of 100–1500 cm^{-1}. Chemical composition was analyzed using a JEOL JXA-8230 electron probe microanalysis (EPMA) system with a tungsten filament gun equipped with an X-ray wavelength-dispersive spectrometer. The voltage was set to 15 kV and the current to 20 nA, with a beam spot diameter of 1 μm. Measurement times were set at 10 s for the peak counts of each element. The system reported oxide test results after automatic ZAF (atomic number, absorption, fluorescence) correction. Jadeite (Na, Si), hematite (Fe), olivine (Mg), diopside (Ca), corundum (Al), chromite (Cr), rhodonite (Mn), potassium feldspar (K), and rutile (Ti) were used to calibrate the EPMA data. Backscattered electron (BSE) images of mineral structural characteristics were collected using a Thermo Fisher Helios G4 double-beam electron microscope at an accelerating voltage of 20 kV. The microscope was equipped with energy-dispersive X-ray spectroscopy (EDS) for simultaneous chemical analysis at a working voltage of 20 kV.

The experiments were completed at the State Key Laboratory of Geological Processes and Mineral Resources. Half of the samples (GB-1, GB-4, GB-5, GB-9, and GB-10) were randomly selected and fabricated into thin slices for chemical composition analysis and BSE images. The thin sections were sputtered with carbon film on the surface to enhance electrical conductivity before the EDS and EPMA experiments.

Color cathodoluminescence (CL) was observed at the School of Earth Sciences using a CITL CL8200 MK5-2 optical cathodoluminescence stage equipped with a Leica DM2700P polarizing microscope for imaging. The operating current was 250 μA, and the voltage was 12 kV.

RESULTS

Gemological Properties. Most Guatemalan "ice jade" sold in the market is nearly colorless or pale green, though some pale green samples have a light blue tone. The samples in this study were nearly colorless with very light greenish color, except for sample GB-9, which was bluish. White inclusions are common, and the presence of numerous white inclusions leads to a decrease in transparency. Compared with Guatemalan "ice jade," Burmese material is colorless or nearly white (Tang, 2020).

TABLE 1. Gemological properties of Guatemalan "ice jade" samples.

Sample no.	Color	Transparency	Weight (g)	Thickness (mm)	SG	RI	Fluorescence reaction
GB-1	Pale green	Transparent	0.375	1.8	3.32	1.66	Inert to long-wave and short-wave
GB-2	Pale green	Transparent	0.149	1.7	3.24	1.66	Inert to long-wave and short-wave
GB-3	Pale green	Transparent	0.086	0.8	3.31	1.66	Inert to long-wave and short-wave
GB-4	Pale green	Transparent	0.202	2.3	3.31	1.66	Inert to long-wave and short-wave
GB-5	Pale green	Transparent	0.343	1.4	3.30	1.66	Inert to long-wave and short-wave
GB-6	Pale green	Transparent	0.552	2.5	3.35	1.66	Inert to long-wave and short-wave
GB-7	Pale green	Semitransparent	0.770	3.2	3.33	1.66	Inert to long-wave and short-wave
GB-8	Pale green	Transparent	0.388	1.9	3.34	1.66	Inert to long-wave and short-wave
GB-9	Pale blue-green	Semitransparent	0.544	3.3	3.30	1.66	Inert to long-wave and short-wave
GB-10	Pale green	Transparent	0.353	1.4	3.33	1.66	Inert to long-wave and short-wave

The gemological properties of the 10 samples are summarized in table 1. They were transparent to semitransparent, with a refractive index of 1.66 and a specific gravity of 3.24–3.35. All the samples were inert under both long-wave and short-wave UV light.

Microscopic Observation. Mineral grains were usually difficult to observe even by microscopy, indicating the fine texture of the samples. White inclusions were randomly distributed and occurred in two different sizes. The large ones were clustered like snowflakes, which could be observed without magnification (figures 1 and 3). They showed no crystallized shape under magnification. Some were exposed on the polished surface (figure 4A), displaying a cloudy appearance. This indicated that the large inclusions were composed of micro-crystals rather than formed by a single crystal. On the other hand, numerous microscopic colorless mineral grains were distributed throughout the matrix (figure 4, A and B). Other impurities such as grossular garnet and rutile were not found in the "ice" samples, although these characteristic inclusions have been reported in green and blue jadeite from Guatemala (Abduriyim et al., 2017).

Jadeite has two sets of cleavage, and the reflection of the cleavage plane can often be observed on the surface of the jadeite jade with a coarse or relatively coarse-grained texture, either visually or by microscopy. In the "ice jade" samples, the cleavage planes were difficult to observe on the polished surface, even with microscopy. Some tiny cleavage planes were observed on the unpolished surfaces. Relatively large cleavage planes were distributed sporadically on the surface; these were not complete cleavage planes but occurred as step-like breakages (figure 4D). This indicated that the jadeite crystals of

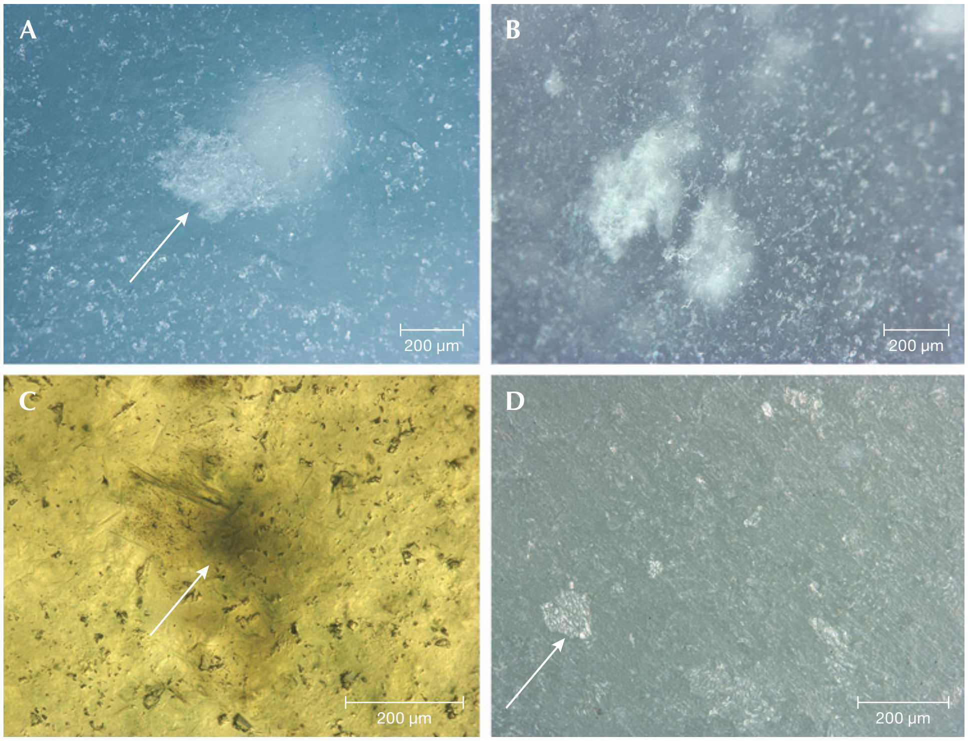

Figure 4. Guatemalan "ice jade" samples showing fine texture. A: Large white inclusion partially exposed to the surface (indicated by arrow) and multiple small white inclusions distributed throughout the sample. B: Two large and numerous small white inclusions. C: Green spotted inclusion composed of green fibrous crystals (indicated by arrow). D: Cleavage planes (indicated by arrow). Photomicrographs by Z. Huang.

large grain size were not intact crystals, but rather fragments broken along cleavage planes.

UV-Vis-NIR Spectroscopy. The diffuse reflectance UV-Vis-NIR spectra of the samples are shown in figure 5.

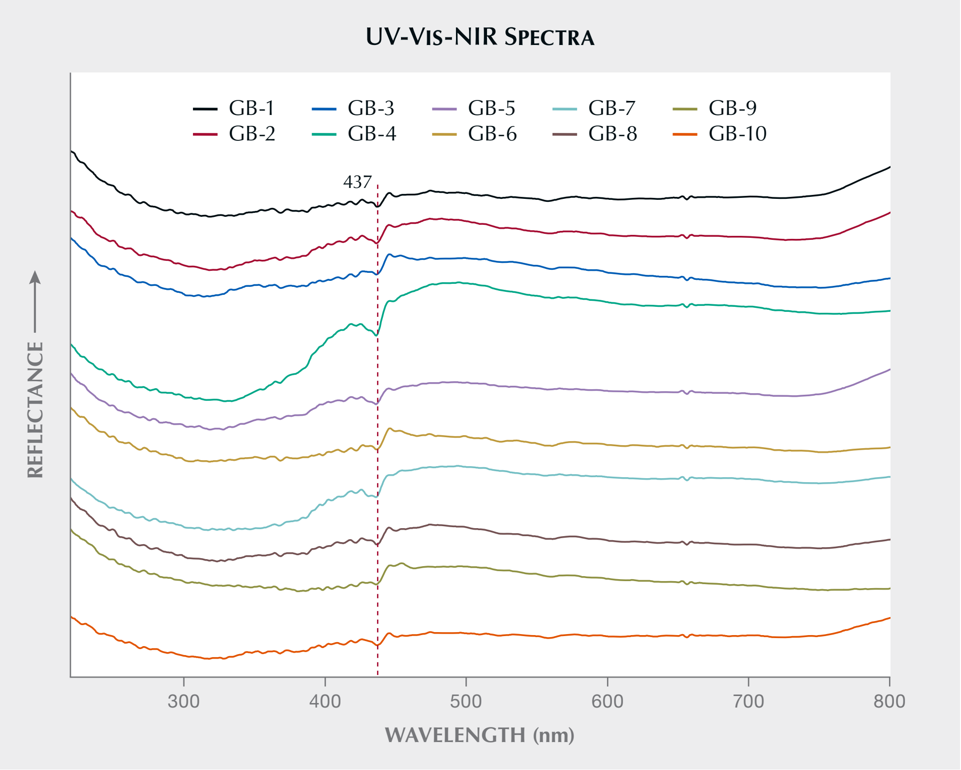

Figure 5. UV-Vis-NIR spectra of Guatemalan "ice jade" samples. All the samples showed a significant absorption peak at 437 nm, which is related to trivalent iron ions. Spectra are offset vertically for clarity.

All the samples had an absorption peak at 437 nm, which was the only absorption peak in the range of visible light (400–700 nm). The 437 nm absorption peak is related to trivalent iron ions (Fe^{3+}) (Yuan et al., 2003; Lu, 2012).

X-ray Diffraction. XRD diffraction was used to obtain the overall mineral composition of the "ice jade" samples. Their XRD patterns are shown in figure 6, and the data is listed in table 2. Almost all the diffraction peaks belonged to jadeite, and their intensity was consistent with the jadeite standard diffraction pattern provided by the International Centre for Diffraction Data Powder Diffraction File 71-1504 (ICDD PDF, Gates-Rector and Blanton, 2019) (figure 6A). The diffraction peaks were sharp, indicating high crystallinity. In the range of $2\theta = 26–33°$ (figure 6B), there was a weak diffraction peak at $d_{-221} = 2.952$Å ($2\theta = 30.34°$), which is the strongest diffraction peak of omphacite (ICDD PDF 71-1068; Gates-Rector and Blanton, 2019), indicating a very small amount of omphacite in the samples. No other mineral diffraction peak was found in the samples. Therefore, the main mineral of the Guatemalan "ice jade" was jadeite.

Raman Spectroscopy. Raman spectra were used to study the phase of inclusions. Transparent jadeite

Figure 6. Powder XRD patterns of Guatemalan "ice jade" samples. The patterns are stacked for clarity. A: Almost all the diffraction peaks fit with jadeite standard diffraction peaks (ICDD PDF 71-1504). B: Matching with ICDD PDF 71-1068 reveals that a weak peak at $d_{-221} = 2.952$Å ($2\theta = 30.34°$) belongs to omphacite (Omp).

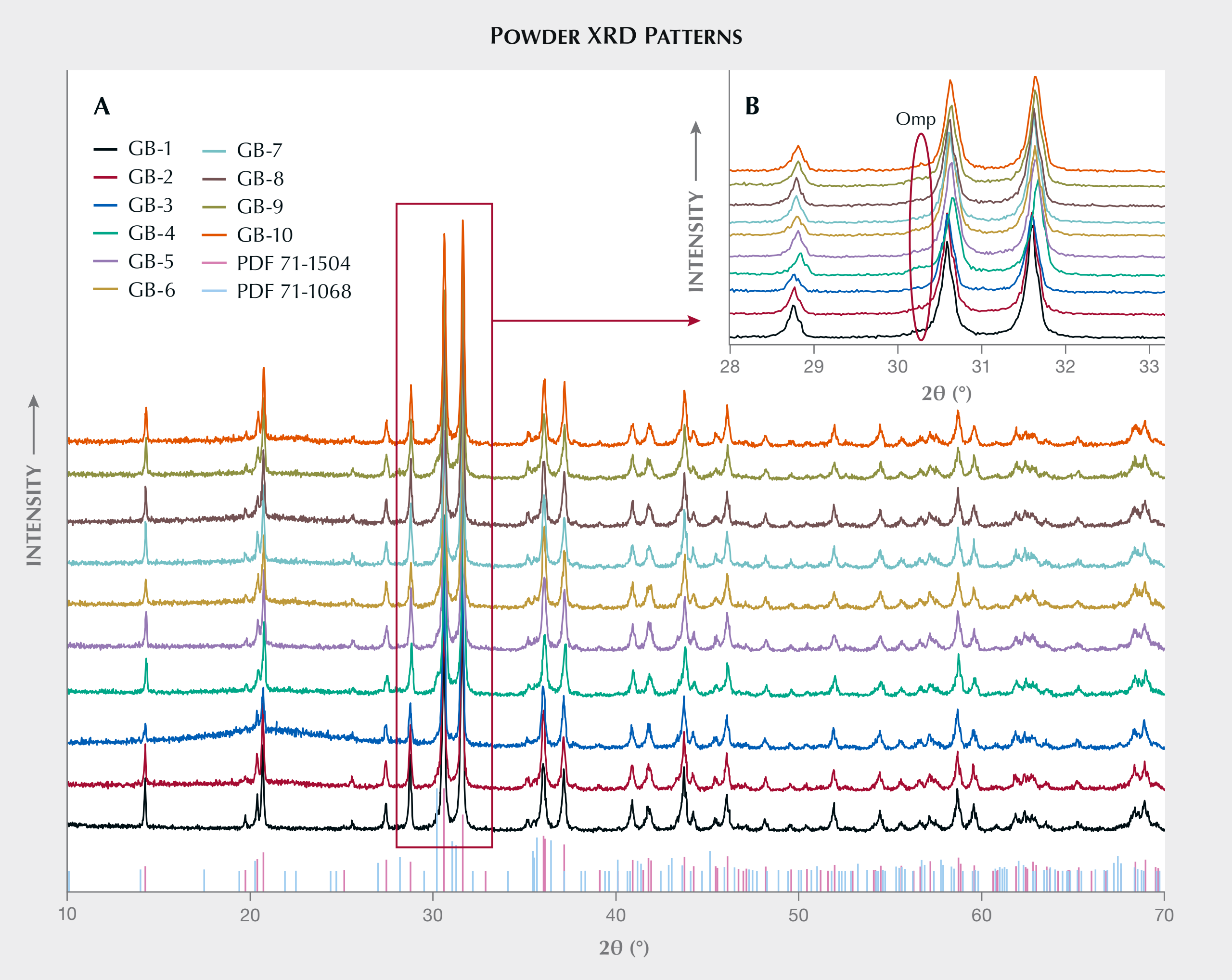

POWDER XRD PATTERNS

TABLE 2. Powder XRD results of mineral phases in Guatemalan "ice jade" samples.

Phase	2θ (°)	d-spacing (Å)	(hkl)
Jadeite	14.31	6.189	(110)
Jadeite	20.75	4.279	(020)
Jadeite	28.81	3.099	(220)
Omphacite	30.34	2.952	(–221)
Jadeite	30.63	2.918	(–221)
Jadeite	31.64	2.827	(310)
Jadeite	36.09	2.488	(–131)
Jadeite	37.20	2.416	(221)
Jadeite	43.77	2.068	(330)
Jadeite	46.10	1.968	(041)
Jadeite	58.72	1.572	(–531)

matrix was tested first to separate the superimposed peaks from those of inclusions. The Raman spectra of transparent jadeite matrix and inclusions are shown in figure 7. (For Raman spectra of all 10 samples, see appendix 1 at www.gia.edu/doc/spring-2024-ice-jade-appendix1.pdf.) The Raman shift peaks of jadeite were mainly concentrated in the range of 100–1200 cm^{-1}. The Raman shift peaks at the 1034 and 981 cm^{-1} bands belong to Si-O stretching vibrations, the peaks at the band 695 cm^{-1} are caused by Si-O-Si stretching vibrations, the peak at the 522 cm^{-1} band is related to O-Si-O bending vibrations, and the 490–200 cm^{-1} band can be assigned to M-O vibrations (Lin et al., 2020). The green spot in the jadeite matrix had Raman shift peaks at 1028, 681, and 190 cm^{-1}, consistent with the characteristic peaks of omphacite (Gendron et al., 2002; Coccato et al., 2014). The obvious Raman shift peaks of the white inclusions at 1097, 814, 760, 504, 476, 288, 183, and 146 cm^{-1} correspond to the standard Raman peaks of albite (Xue et al., 2020).

BSE Images and Element Mapping. The contrast of BSE images is related to atomic number; elements with higher atomic number are brighter. This method is very suitable for identifying changes in chemical composition in a solid-solution series of minerals. Figures 8 and 9 present the BSE and element mapping images of the Guatemalan "ice jade" samples, which were used to show the chemical changes in jadeite and the distribution of omphacite.

Figure 8 shows jadeite crystals with zoning in sample GB-9. Some of the crystals showed a contrasting dark core (figure 8A), which corresponded to the lowest calcium content (figure 8B). According to the EPMA results, the average calcium oxide content of the darkest area was less than 1.00 wt.%. The brightness of zones increased directly with calcium content. Some of the brightest areas were at the boundaries of the jadeite grains with the highest calcium content shown in the mapping area, which had become the omphacite phase. The chemical compositions of the omphacite phase were further analyzed by EPMA. Figure 9 shows an omphacite vein distributed through the fine-grained jadeite (about 50–100 μm) matrix in sample GB-10. In addition, some microscopic jadeite crystals (about 1–50 μm) with higher calcium content can be seen randomly scattered among the fine-grained jadeite matrix in figure 9A.

Figure 10 presents more structural characteristics coupled with chemical composition data from BSE images. Figure 10A shows fragmented jadeite crystals of sample GB-9. These crystals had a common core with the same dark contrast and similar zoning, indicating an initially large jadeite grain that cracked into fragments. Figure 10B reveals several intact jadeite grains with darker zones in sample GB-1, indicating the pure sodium and aluminum composition of these grains. Samples GB-5 and GB-4 displayed typical microparticles in the fine texture of "ice jade" (figure 10, C and D). The omphacite and albite grains and the small omphacite veins were occasionally observed scattered in the jadeite matrix.

Chemical Compositions. The compositions of sodium pyroxene and sodium-calcium pyroxene can be classified on a Quad-Jd-Ae diagram, in which "Quad" represents quadrilateral for the calcium-magnesium-iron pyroxene. Jadeite (Jd) and aegirine (Ae) are the most common components of sodium pyroxene. They can form extensive solid solutions with calcium-magnesium-iron pyroxene, leading to sodium-calcium pyroxene (Morimoto, 1989). All of the tested EPMA data are classified on the Quad-Jd-Ae ternary diagram in figure 11. The test points located in the darkest gray area of the jadeite grains on

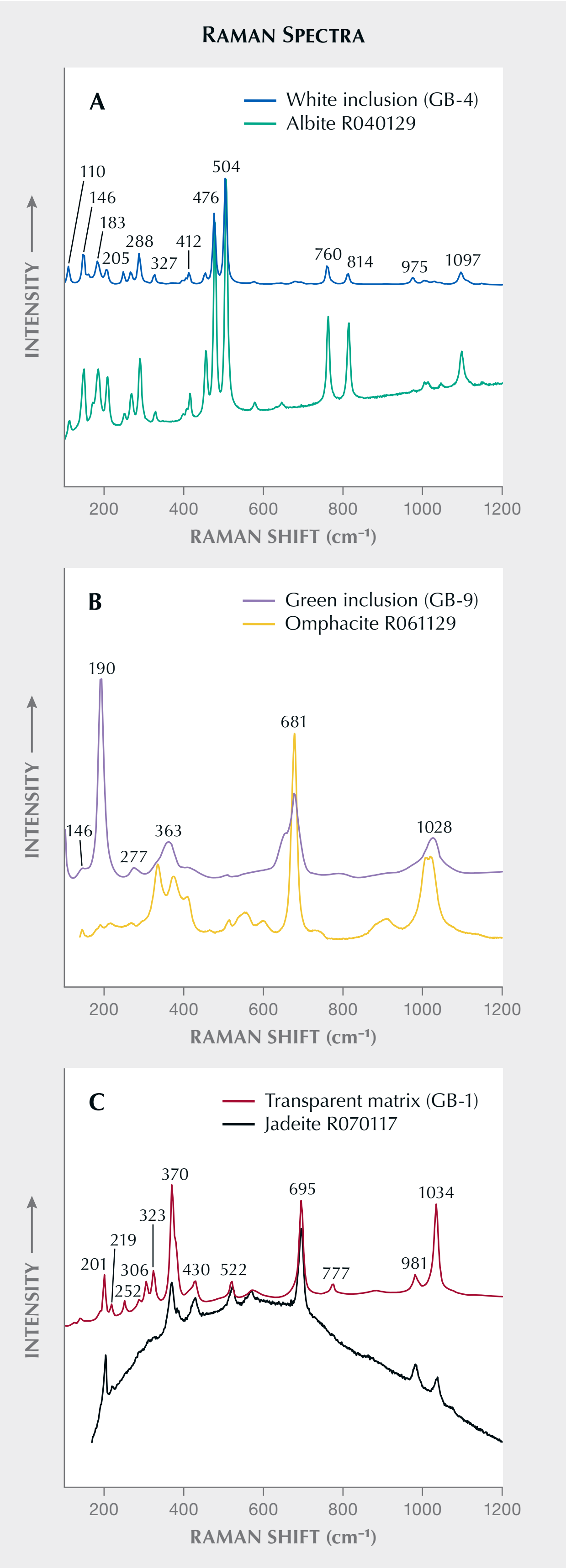

Figure 7. Raman spectra of Guatemalan "ice jade" (the Raman spectra of all 10 samples can be found in the appendix). A: The white inclusion in sample GB-4 matches with the albite spectrum from the RRUFF database. B: The green inclusion in sample GB-9 matches with the omphacite spectrum from the RRUFF database. C: The Raman spectrum of sample GB-1's transparent matrix matches with the jadeite spectrum from the RRUFF database.

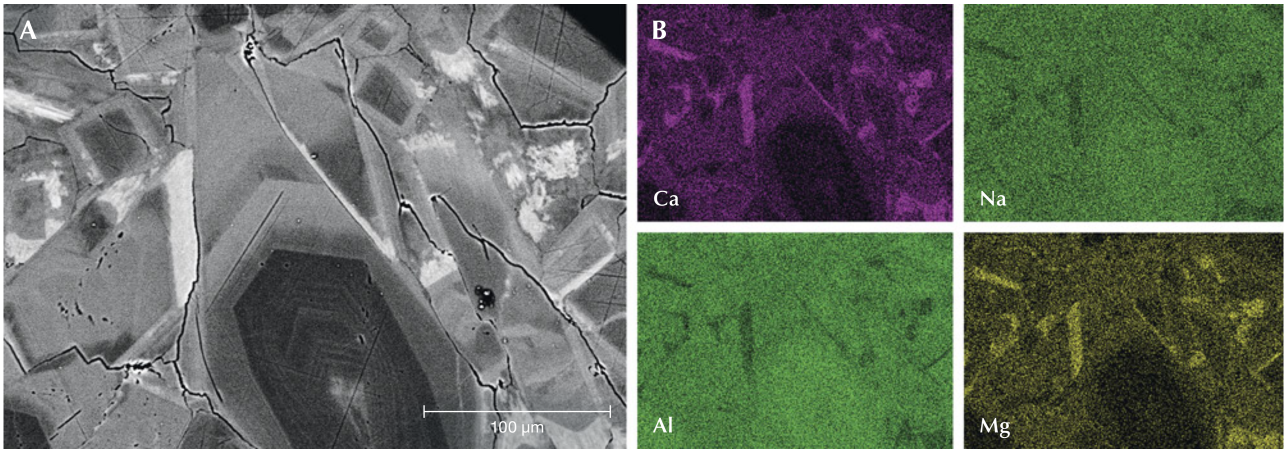

Figure 8. Element mapping of sample GB-9 using EDS. A: The BSE image shows jadeite crystals with zoning and omphacite forming on the boundary of jadeite. B: Element mapping of the sample for calcium, sodium, aluminum, and magnesium.

the BSE images are concentrated in the ternary diagram apex of Jd. The test points located in the light gray area of the jadeite grains are plotted on the edge of the jadeite region. A few test points concentrated in the omphacite region were collected from the brightest omphacite grains or veins on BSE images.

The pyroxene grains with different contrast in BSE images are shown in figures 8–10. The chemical composition results are listed in table 3. According to Quad-Jd-Ae diagram classifications suggested by the Commission on New Minerals and Mineral Names (CNMMN) of the International Mineralogical Association (IMA), jadeite belongs to sodium pyroxene, commonly containing more than 80% $NaAlSi_2O_6$ (Morimoto, 1989). EPMA results show that the darkest gray areas in the BSE images were nearly "pure" jadeite. The nearly pure jadeite had high contents of aluminum oxide (>21.967 wt.%) and sodium oxide (>13.526 wt.%), and low contents of calcium oxide (<2.583 wt.%) and magnesium oxide (<1.735 wt.%). Calculations revealed that in the sodium-calcium pyroxene series, the jadeite content was more than 90 mol.%, indicating that the first crystallized cores and grains were nearly pure jadeite. In the light gray area of jadeite grains, the contents of sodium oxide (19.635–21.636 wt.%) and aluminum oxide (12.239–13.632 wt.%) were often lower than those of the darkest gray area, while the contents of calcium oxide

Figure 9. Element mapping of sample GB-10 using EDS. A: The BSE image of an omphacite vein distributed in the jadeite matrix. B: Element mapping of the sample for calcium, sodium, aluminum, and magnesium.

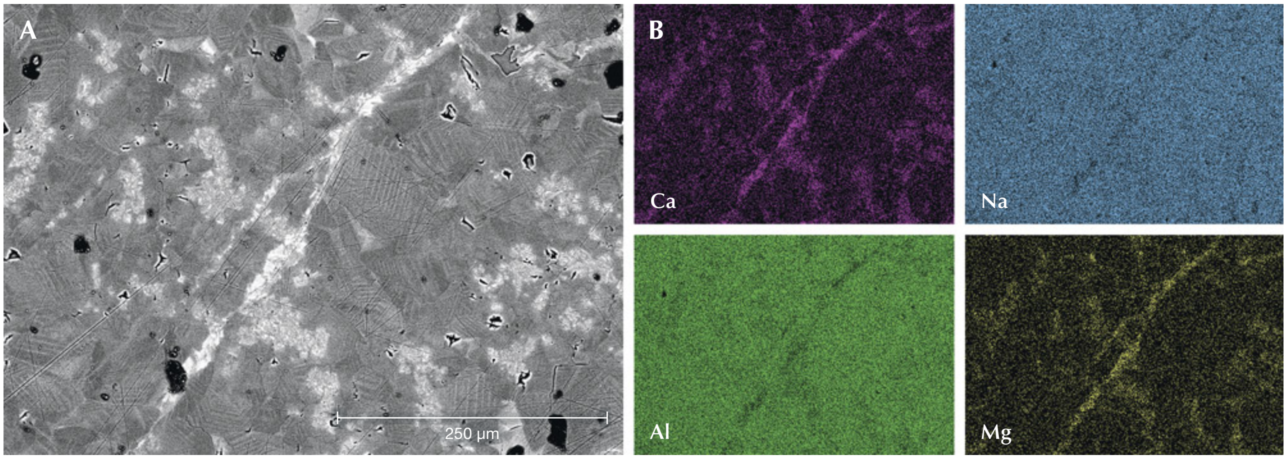

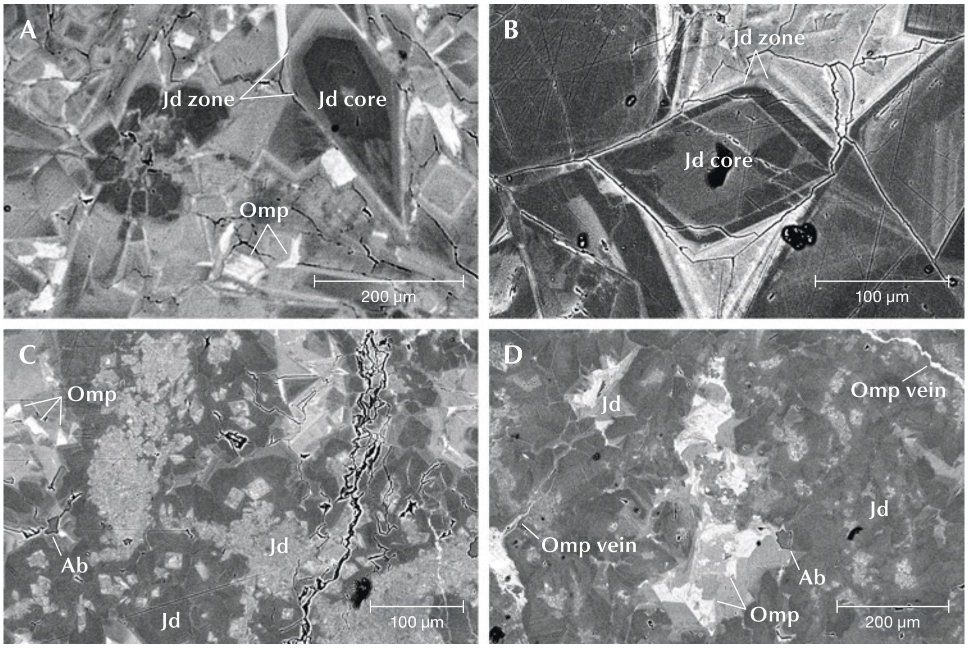

Figure 10. BSE images of Guatemalan "ice jade" samples. A: Fragmented jadeite crystals with zoning. The bright grains are omphacite (sample GB-9). B: Chemical zoning of jadeite crystals. Several different gray contrast zones surrounded the dark core (sample GB-1). C: Fine grains (50–100 μm) of jadeite with different contrast. The bright grains are omphacite. A small albite grain is surrounded by jadeite (sample GB-5). D: Omphacite veins and grains filled in jadeite matrix (sample GB-4). Jd-jadeite; Omp-omphacite; Ab-albite.

(4.562–3.052 wt.%) and magnesium oxide (2.056–3.371 wt.%) increased. The content of jadeite is in the range of 80 mol.% to 90 mol.%. Omphacite belongs to sodium-calcium pyroxene. According to the

Figure 11. A ternary diagram of jadeite (Jd)-aegirine (Ae)-Quad plotted using EPMA data, with divisions defined at 20% and 80% of Quad. Test points of jadeite grains with different contrast (light gray and darkest gray) are plotted in the jadeite region, and test points plotted in the omphacite region come from the brightest omphacite vein or grains. From Morimoto (1989).

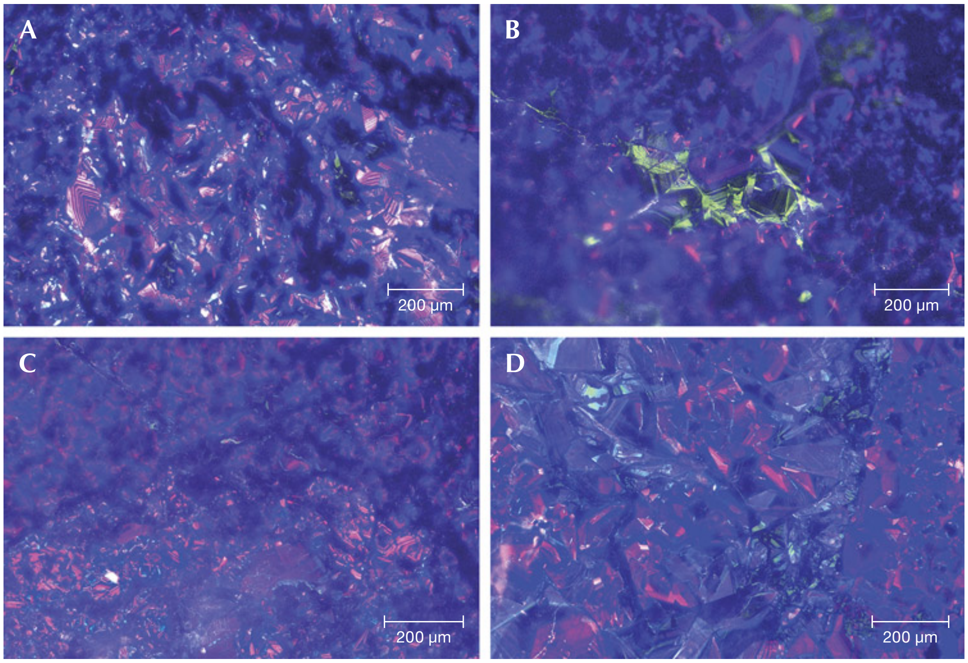

Figure 12. Color cathodoluminescence images of Guatemalan "ice jade" samples mainly showed blue-violet and violet-red fluorescence. A: Rhythmic zoning of coarser jadeite grains. B: Green fluorescence grains. C and D: Some broken jadeite grains and fragments.

nomenclature of pyroxenes (Morimoto, 1989), the tested spots with no more than 80% jadeite or diopside can be considered omphacite, which were coupled with a very low content of aegirine (<4.2 wt.%). The total impurity cations (Fe^{3+} + Cr + Fe^{2+} + Mn + Ti) in the octahedral site were very low. They were in the range of 0.033–2.359 wt.%. The calcium oxide content was higher in the omphacite vein than in the individual omphacite grain.

The chemical compositions of albite were pure. The tested albite contained silicon dioxide (68.55 wt.%, detection limit of 0.86 wt.%), sodium oxide (11.28 wt.%, detection limit of 0.38 wt.%), and aluminum oxide (20.17 wt.%, detection limit of 0.51 wt.%). The other components were not detected by EDS.

Cathodoluminescence. The color CL images in figure 12 illustrate luminescence color and zoning associated with lattice defects or impurity chemical composition. The samples mainly showed blue-violet and violet-red fluorescence, though a small number of individual grains or parts of grains fluoresced green. The blue-violet and violet-red fluorescence was often more intense than the green fluorescence. The cathodoluminescence color is related to the chemical composition. The colorless and transparent jadeite jade with pure sodium, aluminum, and silicon composition will show blue-violet and violet-red fluorescence. When the jadeite jade contains a certain amount of iron, it will produce green fluorescence (Yuan et al., 2005; Takahashi et al., 2017). The color of our samples' CL images matched well with the chemical composition study.

The CL images also revealed the growth structure of the "ice jade." Some coarse jadeite grains (about 100–200 µm) showed prismatic shapes with clear and straight boundaries and had rhythmic zoning (figure 12A), suggesting a regular crystallization cycle of jadeite (Sorensen et al., 2006). The fine-grained jadeite (about 50–100 µm) had irregular shapes and blurred boundaries (figure 12, B and C). Some grains were fragmented (figure 12, C and D), indicating that the jadeites were overstressed or recrystallized (Zhou, 2002).

DISCUSSION

In this study, the "ice jade" from Guatemala was mainly composed of jadeite and included the accessory minerals omphacite and albite. Compared with the previously reported gray-green and blue-green Guatemalan jadeite jade, the Guatemalan "ice jade" is a purer variety. The main mineral component of the gray-green and blue-green Guatemalan jadeite jade is also jadeite, but dark green spotted omphacite and white agglomerated albite are common in their jadeite matrix (Lin et al., 2020; Xue et al., 2020; Zhang and Shi, 2022). In the Guatemalan "ice jade" samples, the omphacite grains were difficult to observe directly with the unaided eye. The albites were

TABLE 3. Chemical compositions (wt.%) of jadeite and omphacite obtained by EPMA.

Sample no.	GB-1							GB-4					GB-5		
Tested point	D[a]-1	D-2	O[b]-1	D-3	D-4	D-5	L[c]-1	D-1	L-1	D-2	O-1	D-3	D-1	O-1	D-2
Oxide content															
SiO_2	58.811	58.405	57.131	59.095	58.585	58.939	58.244	58.948	58.643	59.115	57.092	59.322	59.742	56.733	58.895
TiO_2	bdl	0.177	0.257	bdl	0.420	0.062	0.200	0.039	0.122	0.066	0.213	0.014	0.014	0.281	0.006
Al_2O_3	25.130	22.439	13.831	25.081	21.967	24.638	19.635	24.778	21.313	24.369	9.772	24.668	25.507	12.296	25.328
Fe_2O_3	—	—	—	—	—	—	—	—	—	—	—	—	—	—	—
Cr_2O_3	0.010	bdl	bdl	0.002	0.036	0.016	bdl	bdl	bdl	bdl	0.023	bdl	0.001	0.007	bdl
FeO	0.152	0.797	1.762	0.095	1.049	0.239	1.296	0.105	1.249	0.681	1.830	0.486	0.018	1.741	0.032
MnO	bdl	0.013	0.036	bdl	0.018	0.012	0.018	bdl	bdl	bdl	0.072	bdl	bdl	0.047	0.020
MgO	0.039	1.529	7.225	0.014	1.735	0.317	3.371	bdl	2.224	0.197	10.233	0.249	bdl	8.267	0.026
CaO	0.270	2.177	10.191	0.367	2.583	0.413	4.562	0.478	3.053	0.407	14.514	0.395	0.057	11.648	0.064
Na_2O	15.257	13.729	9.060	15.300	13.526	14.975	12.668	15.120	13.511	15.035	6.686	14.918	15.716	7.821	14.979
K_2O	0.006	bdl	0.007	0.007	bdl	0.001	bdl	0.012	bdl	bdl	0.006	bdl	0.007	bdl	bdl
Total	99.675	99.266	99.500	99.961	99.919	99.612	99.994	99.480	100.115	99.870	100.441	100.052	101.062	98.841	99.350
Tetrahedral cations (IV)															
Si	1.99	2.00	2.00	1.99	2.00	1.99	1.99	2.00	1.99	2.00	2.00	2.00	1.99	2.01	2.00
Al	0.01	—	—	0.01	—	0.01	0.01	—	0.01	—	—	—	0.01	—	—
Octahedral cations (VI)															
Al	0.98	0.90	0.57	0.98	0.88	0.98	0.78	0.99	0.85	0.97	0.40	0.98	0.98	0.51	1.01
Fe^{3+} + Cr + Fe^{2+} + Mn + Ti	—	0.03	0.06	—	0.04	0.01	0.04	—	0.04	0.02	0.06	0.01	0.00	0.06	—
Mg	0.02	0.07	0.37	—	0.08	0.01	0.17	—	0.11	0.01	0.53	—	—	0.42	—
Cubic cations (VIII)															
Mg	—	0.01	—	—	0.01	—	—	—	—	—	—	0.01	—	0.02	—
Ca	0.01	0.08	0.38	0.01	0.09	0.01	0.17	0.02	0.11	0.01	0.54	0.01	—	0.44	—
Na	1.00	0.91	0.61	1.00	0.89	0.98	0.84	0.99	0.89	0.99	0.45	0.98	1.01	0.54	0.98
End members of sodium and calcium pyroxene (mol.%)															
Aegirine	0.43	—	3.58	0.26	—	0.68	3.68	0.29	3.54	1.47	3.81	—	0.05	—	—
Jadeite	98.61	91.94	58.09	98.43	90.45	97.82	79.72	97.99	85.35	97.05	41.65	98.56	99.75	54.85	99.76
Diopside	0.97	8.06	38.33	1.31	9.55	1.50	16.60	1.72	11.10	1.47	54.54	1.44	0.20	45.15	0.24

Note: Detection limits of single elements were 0.01 wt.% for Na, Si, Al, Mg, Fe, Mn; 0.02 wt.% for Cr, Ti; and 0.005 wt.% for K, Ca. bdl = below detection limits.
[a]Jadeite grains in dark gray area of BSE images. [b]Omphacite grains in brightest area of BSE images. [c]Jadeite grains in light gray area of BSE images.

TABLE 3 (continued). Chemical compositions (wt.%) of jadeite and omphacite obtained by EPMA.

Sample no.	**GB-5 (continued)**			**GB-9**						**GB-10**					
Tested point	O-2	L-1	L-2	O-1	D-1	L-1	L-2	D-2	O-2	L-1	D-1	O-1	D-2	O-2	L-2
Oxide content															
SiO_2	56.920	58.403	58.217	56.607	58.961	58.507	58.502	58.873	56.725	58.473	59.056	57.006	58.625	57.381	58.742
TiO_2	0.312	0.050	0.019	0.177	0.146	0.035	0.115	0.167	0.158	0.076	0.195	0.156	0.132	0.066	0.014
Al_2O_3	12.323	20.223	20.462	9.336	24.627	21.636	19.725	25.128	9.282	21.113	24.644	12.312	24.743	14.349	21.157
Fe_2O_3	—	—	—	—	—	—	—	—	—	—	—	—	—	—	—
Cr_2O_3	bdl	0.021	0.007	0.013	bdl	bdl	0.008	bdl	0.002	bdl	bdl	0.047	0.029	0.007	bdl
FeO	1.835	1.588	1.588	1.896	0.462	1.343	1.473	0.159	2.099	1.594	0.577	1.484	0.476	1.244	1.485
MnO	0.067	0.022	bdl	0.064	bdl	0.024	0.001	0.008	0.100	0.004	0.001	0.075	0.018	0.070	0.005
MgO	8.286	2.905	2.565	10.339	0.069	2.056	2.879	0.018	10.266	2.161	0.038	8.571	0.026	7.278	2.224
CaO	11.795	4.048	3.771	14.690	0.510	3.063	4.038	0.272	14.357	3.052	0.418	12.216	0.345	10.303	2.996
Na_2O	7.945	12.239	12.889	6.404	14.853	13.172	12.835	15.179	6.366	13.519	15.252	7.783	14.955	8.891	13.632
K_2O	0.007	bdl	bdl	bdl	bdl	0.002	0.003	0.011	0.006	bdl	bdl	bdl	bdl	0.009	0.001
Total	99.490	99.499	99.518	99.526	99.628	99.838	99.579	99.815	99.361	99.992	100.181	99.650	99.349	99.598	100.256
Tetrahedral cations (IV)															
Si	2.00	2.01	2.00	2.00	2.00	2.00	2.01	1.99	2.01	1.99	1.99	2.00	1.99	2.00	1.99
Al	—	—	—	—	—	—	—	0.01	—	0.01	0.01	—	0.01	—	0.01
Octahedral cations (VI)															
Al	0.51	0.82	0.83	0.39	0.98	0.87	0.80	0.99	0.39	0.84	0.97	0.51	0.98	0.59	0.84
Fe^{3+} + Cr + Fe^{2+} + Mn + Ti	0.06	0.05	0.05	0.06	0.02	0.04	0.05	0.01	0.07	0.05	0.02	0.05	0.02	0.04	0.04
Mg	0.42	0.12	0.13	0.54	—	0.09	0.15	—	0.53	0.11	—	0.44	—	0.37	0.11
Cubic cations (VIII)															
Mg	0.01	0.03	—	—	—	0.02	—	—	0.02	—	—	0.01	—	0.01	—
Ca	0.44	0.15	0.14	0.56	0.02	0.11	0.15	0.01	0.55	0.11	0.02	0.46	0.01	0.39	0.11
Na	0.54	0.82	0.86	0.44	0.98	0.87	0.85	0.99	0.44	0.89	1.00	0.53	0.99	0.60	0.90
End members of sodium and calcium pyroxene (mol.%)															
Aegirine	0.90	—	3.24	3.14	—	0.14	3.56	0.45	1.39	4.52	1.61	0.81	0.30	0.20	4.19
Jadeite	54.03	84.55	82.84	40.95	98.14	88.48	81.63	98.57	43.13	84.39	96.90	52.74	98.44	60.76	84.98
Diopside	45.07	15.45	13.92	55.90	1.86	11.39	14.81	0.98	55.48	11.09	1.49	46.45	1.26	39.04	10.83

Note: Detection limits of single elements were 0.01 wt.% for Na, Si, Al, Mg, Fe, Mn; 0.02 wt.% for Cr, Ti; and 0.005 wt.% for K, Ca. bdl = below detection limits.
[a]Jadeite grains in dark gray area of BSE images. [b]Omphacite grains in brightest area of BSE images. [c]Jadeite grains in light gray area of BSE images.

clustered as white snowflake-like inclusions or dispersed in the jadeite matrix. Unlike Burmese "ice jade," Guatemalan material rarely contains fibrous and agglomerate albite (Hu et al., 2003; Liang, 2018).

Compared with the other varieties of Guatemalan jadeite jade, the "ice jade" has lower calcium and magnesium content and higher sodium and aluminum content, and it has a very low omphacite content (Xing et al., 2021). A very small amount of iron and titanium cations was detected in both jadeite and omphacite (FeO = 0.018–2.099 wt.%, TiO_2 = 0–0.42 wt.%). Although the amounts of iron and titanium were often higher in omphacite than those in jadeite in the studied samples, they were much lower than those in omphacite in the reported gray-green and blue-green Guatemalan jadeite jade (Xue et al., 2020; Zhang and Shi, 2022). Because of its dispersive fine omphacite and low iron content, the "ice jade" takes on a much lighter green color than the other Guatemalan jadeite jade.

In terms of structural characteristics, Guatemalan "ice jade" showed fine texture and small jadeite grains. The originally larger grains were usually broken into small grains, as shown by microscopy and BSE studies (figures 4D and 10A). The relict intact jadeite grains showed a rhythmic zoning of chemical composition, which was reflected in the cathodoluminescence image. Meanwhile, the small grains often displayed relatively uniform BSE and CL images and higher calcium and magnesium contents in the core. On the other hand, the metasomatism edge and vein composed of omphacite were common in the jadeite matrix. The structural characteristics indicated that the "ice jade" had undergone complex geological processes, not limited to dynamic metamorphism and metasomatic metamorphism (Tsujimori et al., 2005; Sorensen et al., 2006; Brueckner et al., 2009; Shi et al., 2009).

CONCLUSIONS

"Ice jade" from the Morales mine in Guatemala is composed of almost pure jadeite, containing very small amounts of accessory minerals, including omphacite and albite. The omphacite grains were often nearly colorless and not easily observed, while the albite grains were clustered as white snowflake-like inclusions or dispersed as small specks. The "ice jade" exhibited a fine-grained texture, occasionally coexisting with a micro-granular texture. The relatively pure chemical composition of sodium pyroxene accompanied with a fine texture produced a transparent to semitransparent and near-colorless appearance. A small amount of dispersed fine-grained omphacite is considered the cause of the pale green color in Guatemalan "ice jade."

ABOUT THE AUTHORS

Zhaoying Huang (HZYgemology@cug.edu.cn) is a postgraduate student, and Dr. Tao Chen (chentao@cug.edu.cn, co-first author and corresponding author) is a professor and the dean of the gemology department, at the Gemmological Institute, China University of Geosciences in Wuhan. Jinyu Zheng (gemfisher@cug.edu.cn) is a PhD student at the School of Earth Sciences, China University of Geosciences in Wuhan. Zebin Xu is the director of the Guangdong Provincial Gem & Precious Metal Testing Centre in Jieyang.

ACKNOWLEDGMENTS

The authors are grateful for the constructive comments and suggestions of Dr. Edward Liu and two anonymous peer reviewers. Professor Xinqiang Yuan is thanked for providing the photo of the Morales mine.

REFERENCES

Abduriyim A., Saruwatari K., Katsurada Y. (2017) Japanese jadeite: History, characteristics, and comparison with other sources. *G&G*, Vol. 53, No. 1, pp. 48–67, http://dx.doi.org/10.5741/GEMS.53.1.48

Bartole R., Lodolo E., Obrist-Farner J., Morelli D. (2019) Sedimentary architecture, structural setting, and Late Cenozoic depocentre migration of an asymmetric transtensional basin: Lake Izabal, eastern Guatemala. *Tectonophysics*, Vol. 750, pp. 419–433, http://dx.doi.org/10.1016/j.tecto.2018.12.004

Brueckner H.K., Lallemant H.G.A., Sisson V.B., Harlow G.E., Hemming S.R., Martens U., Tsujimori T., Sorensen S.S. (2009) Metamorphic reworking of a high pressure-low temperature mélange along the Motagua fault, Guatemala: A record of Neocomian and Maastrichtian transpressional tectonics. *Earth and Planetary Science Letters*, Vol. 284, No. 1-2, pp. 228–235, http://dx.doi.org/10.1016/j.epsl.2009.04.032

Coccato A., Karampelas S., Wörle M., van Willigend S., Pétrequin P. (2014) Gem quality and archeological green 'jadeite jade' versus 'omphacite jade'. *Journal of Raman Spectroscopy*, Vol. 45, No. 11-12, pp. 1260–1265, http://dx.doi.org/10.1002/jrs.4512

Flores K.E., Martens U.C., Harlow G.E., Brueckner H.K., Pearson N.J. (2013) Jadeite formed during subduction: *In situ* zircon geochronology constraints from two different tectonic events within the Guatemala Suture Zone. *Earth and Planetary Science Letters*, Vol. 371-372, pp. 67–81, http://dx.doi.org/10.1016/j.epsl.2013.04.015

Foshag W.F., Leslie R. (1955) Jadeite from Manzanal, Guatemala. *American Antiquity*, Vol. 21, No. 1, pp. 81–83, http://dx.doi.org/10.2307/276111

Gates-Rector S., Blanton T. (2019) The powder diffraction file: A quality materials characterization database. *Powder Diffraction*. Vol. 34, No. 4, pp. 352–360, http://dx.doi.org/10.1017/S0885715619000812

Gendron F., Smith D.C., Gendron-Badou A. (2002) Discovery of jadeite-jade in Guatemala confirmed by non-destructive Raman microscopy. *Journal of Archaeological Science*, Vol. 29, No. 8, pp. 837–851, http://dx.doi.org/10.1006/jasc.2001.0723

Giunta G., Beccaluva L., Coltorti M., Cutrupia D., Dengo C., Harlow G.E., Mota B., Padoa E., Rosenfeld J., Siena F. (2002) The Motagua Suture Zone in Guatemala: Field-trip guidebook of the IGCP-433 Workshop and 2nd Italian-Latin American Geological Meeting "In memory of Gabriel Dengo" January 2002. *Ofioliti*, Vol. 27, No. 1, pp. 47–72.

Hargett D. (1990) Jadeite of Guatemala: A contemporary view. *G&G*, Vol. 26, No. 2, pp. 134–141, http://dx.doi.org/10.5741/GEMS.26.2.134

Harlow G.E. (1994) Jadeitites, albitites and related rocks from the Motagua Fault Zone, Guatemala. *Journal of Metamorphic Geology*, Vol. 12, No. 1, pp. 49–68, http://dx.doi.org/10.1111/j.1525-1314.1994.tb00003.x

Harlow G.E., Sorensen S.S. (2005) Jade (nephrite and jadeitite) and serpentinite: Metasomatic connections. *International Geology Review*, Vol. 47, No. 2, pp. 113–146, http://dx.doi.org/10.2747/0020-6814.47.2.113

Harlow G.E., Sorensen S.S., Sisson V.B., Cleary J. (2006) Jadeite jade from Guatemala: Distinctions among multiple deposits. *G&G*, Vol. 42, No. 3, pp. 146–147.

Harlow G.E., Sisson V.B., Sorensen S.S. (2011) Jadeitite from Guatemala: New observations and distinctions among multiple occurrences. *Geologica Acta*, Vol. 9, No. 3-4, pp. 363–387, http://dx.doi.org/10.1344/105.000001694

Hughes R.W., Galibert O., Bosshart G., Ward F., Oo T., Smith M., Sun T.T., Harlow G.E. (2000) Burmese jade: The inscrutable gem. *G&G*, Vol. 36, No. 1, pp. 2–26, http://dx.doi.org/10.5741/GEMS.36.1.2

Hu C.Y., Li H. Q., Xu L. (2003) Flocculation in jadeite and its relationship with transparency. *China Gems*, Vol. 12, No. 2, pp. 140–142.

Liang T. (2018) Mineralogical characteristics of jadeite and their effect on its quality. *Geology of Anhui*, Vol. 28, No. 1, pp. 77–80, http://dx.doi.org/10.3969/j.issn.1005-6157.2018.01.020

Lin C.L., He X.M., Lu Z.Y., Yao Y.W. (2020) Phase composition and genesis of pyroxenic jadeite from Guatemala: Insights from cathodoluminescence. *RSC Advances*, Vol. 10, No. 27, pp. 15937–15946, http://dx.doi.org/10.1039/D0RA01772H

Lu R. (2012) Color origin of lavender jadeite: An alternative approach. *G&G*, Vol. 48, No. 4, pp. 273–283, http://dx.doi.org/10.5741/GEMS.48.4.273

Marshall J.S. (2007) The geomorphology and physiographic provinces of Central America. In J. Bundschun and G.E. Alvarado, Eds., *Central America: Geology, Resources and Hazards*. CRC Press, Taylor & Francis Group, Boca Raton, Florida, pp. 75–121.

McClure S.F. (2012) The jadeite/omphacite nomenclature question. *GIA News from Research*, www.gia.edu/ongoing-research/the-jadeite-omphacite-nomenclature-question. Apr. 10.

Morimoto N. (1989) Nomenclature of pyroxenes. *Mineralogical Journal*, Vol. 14, No. 5, pp. 198–221, http://dx.doi.org/10.2465/minerj.14.198

Ouyang C.M., Shi G.H., Zhang W., Man K.Y., Yen K. (2017) The chemical composition & gemmological characteristics of fei cui from Guatemala. *Journal of the Gemmological Association of Hong Kong*, Vol. 38, pp. 84–89.

Shi G.H., Wang X., Chu B.B., Cui W.Y. (2009) Jadeite jade from Myanmar: Its texture and gemmological implications. *Journal of Gemmology*, Vol. 31, No. 5-8, pp. 185–195.

Sorensen S., Harlow G.E., Rumble III D. (2006) The origin of jadeitite-forming subduction-zone fluids: CL-guided SIMS oxygen-isotope and trace-element evidence. *American Mineralogist*, Vol. 91, No. 7, pp. 979–996, http://dx.doi.org/10.2138/am.2006.1949

Takahashi N., Tsujimori T., Kayama M., Nishido H. (2017) Cathodoluminescence petrography of P–type jadeitites from the New Idria serpentinite body, California. *Journal of Mineralogical and Petrological Sciences*, Vol. 112, No. 5, pp. 291–299, http://dx.doi.org/10.2465/jmps.170403

Tang H.Y. (2020) Variety and transparency of jadeite. *Quality and Standardization*, Vol. 12, pp. 30–33.

Tsujimori T., Liou J.G., Coleman R.G. (2005) Coexisting retrograde jadeite and omphacite in a jadeite-bearing lawsonite eclogite from the Motagua Fault Zone, Guatemala. *American Mineralogist*, Vol. 90, No. 5-6, pp. 836–842, http://dx.doi.org/10.2138/am.2005.1699

Tsujimori T., Harlow G.E. (2012) Petrogenetic relationships between jadeitite and associated high-pressure and low-temperature metamorphic rocks in worldwide jadeitite localities: A review. *European Journal of Mineralogy*, Vol. 24, No. 2, pp. 371–390, http://dx.doi.org/10.1127/0935-1221/2012/0024-2193

Wang L.S., Zhang H.H., Liu J.Y., Wang L.S., Ouyang Q.M., Liu D.M., Liu W. (2022) Mineral component and genesis of high-grade green jadeite jade from Guatemala. *Journal of Gems & Gemmology*, Vol. 24, No. 5, pp. 11–30, http://dx.doi.org/10.15964/j.cnki.027jgg.2022.05.002

Xing B.Q., Shi G.H., Zhang J.H., Long C., Zhang Y., He L.Y., Hu R.J. (2021) Characteristics of the Guatemalan Feicui and its comparison to the Myanmar Feicui. *Geoscience*, Vol. 35, No. 6, pp. 1769–1788, http://dx.doi.org/10.19657/j.geoscience.1000-8527.2021.23

Xue H.Y., Chen T., Li Z.G. (2020) Mineralogical comparison between omphacite-bearing jadeite from Guatemala and that from Myanmar. *Acta Petrologica et Mineralogica*, Vol. 39, No. 4, pp. 481–494.

Yuan X.Q. (2009) *Applied Jadeite Gemology*. China University of Geosciences Press, Wuhan.

Yuan X.Q., Qi L.J., Du G.P., Chen X.Y. (2003) UV-Vis-NIR spectrum of jadeite jade from Burma. *Journal of Gems & Gemmology*, Vol. 5, No. 4, pp. 11–16, http://dx.doi.org/10.15964/j.cnki.027jgg.2003.04.003

Yuan X.Q., Qi L.J., Zhang S. (2005) Characteristic of cathodoluminescence spectra of jadeite jades from Burma. *Journal of Gems & Gemmology*, Vol. 7, No. 2, pp. 9–13+51.

Yui T.F., Maki K., Usuki T., Lan C.Y., Martens U., Wu C.M., Wu T.W., Liou J.G. (2010) Genesis of Guatemala jadeitite and related fluid characteristics: Insight from zircon. *Chemical Geology*, Vol. 270, No. 1-4, pp. 45–55, http://dx.doi.org/10.1016/j.chemgeo.2009.11.004

Zhang Q.L. (2003) Jadeite jade deposits in the other state. *China Gems & Jades*, No. 3, pp. 38–39.

Zhang Y., Shi G.H. (2022) Origin of blue-water jadeite jades from Myanmar and Guatemala: Differentiation by non-destructive spectroscopic techniques. *Crystals*, Vol. 12, No. 10, article no. 1448, http://dx.doi.org/10.3390/cryst12101448

Zhou Y. (2002) Cathode-luminescence texture of jadeite jade and its gemmological significance. *Journal of Gems & Gemmology*, Vol. 4, No. 3, pp. 31–35, http://dx.doi.org/10.15964/j.cnki.027jgg.2002.03.009

NANOSCALE TECHNIQUES FOR CHARACTERIZING GEMSTONE COATINGS: A CASE STUDY ON SYNTHETIC MOISSANITE

Tsung-Jen Wu, Sheng-Rong Song, Wen-Shan Chen, Wen Lin, and Chien-Tai Cheng

This study investigated the application of colored coatings on synthetic moissanite, a process aimed at simulating the appearance of rare blue and pink diamonds. The analysis focused on characterizing colored coatings on commercial synthetic moissanite and uncovering the possible techniques used. By employing a range of nanoscale analytical methods (including Auger electron spectroscopy combined with argon ion beam sputtering, spherical aberration–corrected transmission electron microscopy with electron energy loss spectroscopy, and electron probe microanalysis), the compositions and thicknesses of the coatings were determined, revealing their nanoscale thin-film properties. These films varied in composition, leading to the distinct blue and pink hues observed for the synthetic moissanite samples. The suite of analytical techniques presented in this study offers a robust basis for characterizing colored coatings on a variety of polished gemstones, providing compelling evidence of the fabrication principles and mechanisms behind these coatings.

People have always loved the rich colors of natural gemstones. Owing to the development of advanced technologies, there are now a variety of processing techniques to enhance and alter these colors, such as heat treatment, radiation treatment, and lattice diffusion (McClure and Smith, 2000). Coating technologies are also used to change the appearance and color of gemstones, and these have evolved significantly over time. Ancient civilizations such as the Egyptians and Romans used natural dyes and oils to enhance gemstones. During the Middle Ages and beyond, from the Renaissance period to the eighteenth century, the application of metal oxides and foil backing techniques emerged. The introduction of electroplating technology in the nineteenth century revolutionized coating, enabling the deposition of thin metal layers on gemstones. The development of chemical vapor deposition (CVD) and physical vapor deposition (PVD) in the latter half of the twentieth century truly transformed the scope of gemstone coating, achieving precise and durable enhancements (Nassau, 1984; McClure and Smith, 2000; Breeding et al., 2010). Continual technological advancements have enabled coatings to be applied to a wide range of gemstones, including diamonds (Shen et al., 2007), topaz (Schmetzer, 2008), tanzanite (Cooper and Renfro, 2014), jadeite jade (Zhang et al., 2013), and synthetic cubic zirconia (Shigley et al., 2012).

In Brief

- An innovative application of nanoscale analytical techniques can be used to characterize the coatings on gem materials, such as the ones studied here on synthetic moissanite.
- The coatings on the light greenish blue samples were identified as silicon dioxide films doped with vanadium, cobalt, and manganese.
- The pink samples featured gold-containing layers, with a unique surface plasmon resonance effect responsible for the color.

Synthetic silicon carbide (SiC, known as synthetic moissanite) entered the gemstone market around a quarter of a century ago (Nassau et al., 1997). It gained a large market as a diamond imitation because some of its physical properties, such as refractive index, hardness, and specific gravity, are similar to those of natural diamond. Unlike diamond, synthetic

---

See end of article for About the Authors and Acknowledgments.

GEMS & GEMOLOGY, Vol. 60, No. 1, pp. 42–54,
http://dx.doi.org/10.5741/GEMS.60.1.42

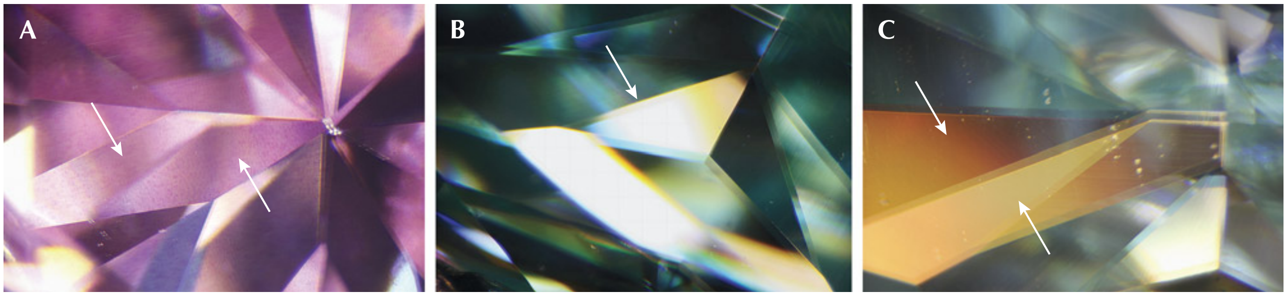

Figure 1. Microscopic images of pink sample PM01 (A) and blue sample BM01 (B and C). A: The white arrows indicate regions where the color is unevenly distributed on the surface of a facet. B and C: The white arrows indicate regions with differences in luster between the upper and lower portion of the pavilion facets and a bronze-colored appearance. Photomicrographs by Tsung-Jen Wu; field of view 4 mm.

moissanite is not cubic. Therefore, the simplest means of distinguishing it is the doubling of facets. Synthetic moissanite has many applications, including abrasives and the fabrication of semiconductors (Elasser and Chow, 2002; Friedrichs et al., 2011; Liu et al., 2015). The structure of large single-crystal SiC used as gem material is mainly 4H-SiC and 6H-SiC (α-SiC, polytype, hexagonal) (Li and Bradt, 1986; Nassau et al., 1997; Chen et al., 2008; He and Shen, 2020).

Rare blue and pink diamonds have always been expensive, so these two colors are often seen in imitation diamonds. To date, colored synthetic moissanite has been produced by modifying the crystal structures or doping with trace elements during the production process. For example, the 3C-SiC structure (β-SiC, polytype, cubic) is yellow, while n-type α-SiC doped with nitrogen and p-type α-SiC doped with aluminum give colors such as light brown, green, and deep blue (Chen et al., 2008; He and Shen, 2020). However, doping methods have not yet achieved synthetic moissanite with light blue and pink colors similar to those encountered in colored diamonds. Although such colors can be produced by a coating process, coated gems are not widely accepted in the market.

This study applied characterization techniques common within the materials science community to analyze the type of coating found on the colored synthetic moissanites as well as the possible processing technology used to produce the coating.

BACKGROUND

As a diamond substitute, synthetic moissanite has acquired a certain market share because it is affordably priced. With the increase in production capacity, the market price of colorless material has fallen drastically in recent years. However, when pink and light blue coated synthetic moissanite initially entered the market, their prices were several times higher. When gem laboratories receive samples of colored synthetic moissanite, most producers and sellers claim they are not coated. On one occasion, the Tai-Da Gem Research Laboratory in Taiwan received a pink synthetic moissanite, and the seller insisted that the color was not from a coating. However, microscopic observation revealed an uneven distribution of color on the surface of the gem (figure 1A), similar to the phenomenon described by Delaunay (2018). Unlike the samples in the present study, the images provided in that study showed additional golden spots described as "metallic flakes on the surface," and it was concluded that the pink gem was color-coated synthetic moissanite. Later, the laboratory received a light blue synthetic moissanite that did not show these characteristics under microscopic observation. A difference in luster between the upper and lower portion of the pavilion facets was observed, along with a bronze-colored hue under reflected light (figure 1, B and C) similar to that of coated tanzanite described by Cooper and Renfro (2014) and coated diamond described by Shen et al. (2007).

Furthermore, GIA's Carlsbad laboratory reported a light greenish blue synthetic moissanite in which the color originated from the bulk crystal itself (Tsang, 2017). A pink color-coated synthetic moissanite was analyzed and reported by the Laboratoire Français de Gemmologie (LFG) in Delaunay (2018). However, these two reports described characteristics that were different from the light blue and pink samples mentioned above. In addition, there was an instance of black synthetic moissanite used to imitate black diamond (Moe et al., 2013).

To avoid damage during examination, nondestructive testing methods are typically used. Some methods commonly used in gem laboratories are Raman spectroscopy, Fourier-transform infrared (FTIR) spectroscopy, ultraviolet/visible/near-infrared

BOX A: AUGER ELECTRON SPECTROSCOPY (AES)

Electrons orbiting the nucleus in an atom are allocated to different "shells" based on their energy states, designated as K, L (L_1, L_2, L_3), etc., in order from closest to farthest from the nucleus. This arrangement corresponds to the increasing energy of the electrons. AES uses a high-energy incident electron beam with an energy E_Δ to excite and dissociate electrons from the orbitals of atoms. For example, dissociating an electron from the K shell generates an electron hole in the shell, making the atom unstable and excited. When an electron from the outer L shell fills the created hole, an amount of energy is released that is equal to the energy gap between the K shell and L_1 shell (E_K–E_{L1}). The energy released is transferred to another electron in the L_2 or L_3 shell in the same atom, causing the electron to be excited and dissociated. The dissociated electron is called the Auger electron, and its kinetic energy E_A (Ewart, 2019) (figure A-1) is calculated using $E_A = E_K – E_{L1} – E_{L2,\ L3}$. The E_A of the Auger electron depends only on the energy gap between the electron shells in the atom and not on E_Δ. Therefore, the magnitude of E_A is characteristic of the various elements comprising the surface materials.

AES can identify elements and perform qualitative and semi-quantitative analyses on elements with atomic numbers as low as 3 (down to lithium) (Chung and Jenkins, 1970; Ertl and Küppers, 1985; Wolstenholme, 2015). When an atom is exposed to incident light or an electron beam, it produces Auger electrons and may also release energy in the form of electromagnetic radiation (e.g., X-rays). The probability of generating Auger electrons and X-rays is related to the atomic number of the element. When the atomic number exceeds 20, this probability changes drastically and the material tends to produce X-rays preferentially (Wolstenholme, 2015). The Auger effect is a phenomenon in which the filling of an inner-shell vacancy within an atom is accompanied by the emission of an electron from that same atom. Hence, it involves the rearrangement of electrons within an atom accompanied by the emission of electrons. Elements with large atomic numbers have many electrons, and many interactions between electrons occur, making it difficult for electron rearrangement to happen. Therefore, the probability of producing Auger electrons is also low, and fluorescence is more likely to be produced (Walters and Bhalla, 1971). Gold, with an atomic number of 79, is an example of such an element with low Auger activity.

AES and X-ray photoelectron spectroscopy (XPS) are often discussed together in surface analysis, as both techniques offer similar analytical capabilities. The critical distinctions between AES and XPS lie in their excitation sources, resolution, and applicability. AES typically features scanning electron microscopy (SEM) imaging functionality, capturing secondary electrons with significant depth of field, allowing for spatial observation at the nanoscale. Conversely, XPS employs optical microscopy, utilizing visible light to contrast the sample surface, resulting in less pronounced surface morphology and lower resolution than SEM. The excitation source for AES is an electron beam, which can be focused down to a beam diameter of 12 nm, while XPS uses X-rays with a larger beam diameter (minimum of 15 μm), giving AES an advantage in microanalysis. AES achieves a surface analysis depth of approximately 5 nm, with a detection limit of 0.1–1 at.%. XPS offers an analysis depth of approximately 7.5 nm, with a detection limit of 0.01–0.5 at.%. Additionally, XPS induces Auger electron generation during photoelectric reactions, resulting in the appearance of Auger electron signals in XPS spectra. This can complicate elemental identification in surfaces with multiple and complex elements due to interference from different orbital energies and Auger electron signals, leading to difficulties in distinguishing certain elemental peaks (Shen, 2014; Watts and Wolstenholme, 2019). In summary, XPS has advantages for analyzing

(UV-Vis-NIR) spectroscopy, energy-dispersive X-ray fluorescence (EDXRF) spectroscopy, and laser ablation–inductively coupled plasma–mass spectrometry (LA-ICP-MS) (Breeding et al., 2010). However, these conventional testing methods are usually not sufficient to conclusively identify the most recent coatings and other treatments that have come from the materials engineering sector, such as the advanced coating used extensively to produce topaz of various colors. Identifying and characterizing these types of coatings poses a challenge for gemological laboratories. The previously observed results mentioned earlier highlight the limitations of standard gemological equipment. Gabasch et al. (2008) performed experiments using X-ray photoelectron spectroscopy (XPS) to analyze the thickness and composition of the coating on color-coated pink topaz. The study revealed that the coating comprised silicon dioxide as a surface layer and gold as an interfacial layer, with a total coating thickness of approximately 400 nm. Relying on a single analytical technique may not be sufficient to reveal the properties of gemstone coatings, because each method has strengths and limitations. Multiple methods may be necessary to achieve a more comprehensive and accurate evaluation.

Owing to the advancements made in the semiconductor industry and nanomaterial technology, the sensitivity and accuracy of available analytical in-

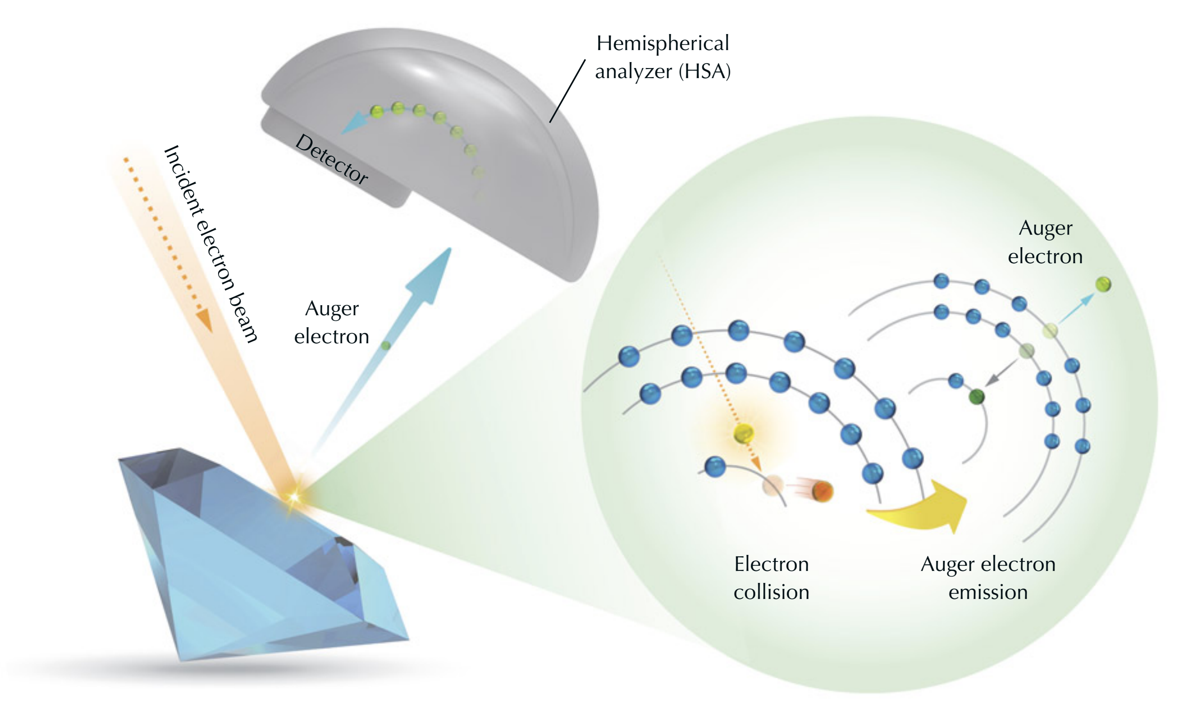

Figure A-1. Diagram of the Auger effect and the processes occurring during testing. The impact of high-energy electron beams excites an inner electron and generates a hole. The outer electron combines with the hole and transfers energy to the outer electron to generate the Auger electron.

non-conductive materials and providing information about the chemical state, while AES provides high-resolution imaging and precise elemental microanalysis that is preferable for certain materials.

Because AES is extremely sensitive to the surface conditions of the sample, it must be performed under a high-vacuum environment, with a maximum pressure of 1 × 10^{-6} Pa. Moreover, the shape and cleanliness of the surface are essential for achieving accurate analysis results. Contaminants such as chlorine, carbon, sodium, and oxygen can be detected if the sample surface is touched by a finger.

struments have improved significantly. The National Science Council in Taiwan has even established a Valuable Instrument Center to coordinate these instrument resources and make them available to the public. In addition to faculty and students from educational institutions, external organizations can access the instruments after completing the required training. The equipment used in the present study was made available to us through this process.

We mainly used Auger electron spectroscopy (AES) to analyze the coatings of pink and light greenish blue synthetic moissanite. This method is suitable for the nanoscale analysis of elemental components and sufficiently sensitive for surface analysis (box A). AES is generally used to analyze components such as coatings, thin films, and oxide layers in machines such as generators and motors, as well as materials used in electronics, semiconductors, and materials science. To the best of our knowledge, this study presents the first application of AES in gemology. Other detection methods used in this study included spherical aberration–corrected transmission electron microscopy (AC-TEM) with electron energy loss spectroscopy (EELS) and electron probe microanalysis (EPMA). These methods were used to obtain micro-longitudinal profiles and images of element distribution, for the qualitative and quantitative analysis of the elements in the surface coating.

TABLE 1. Colored synthetic moissanite samples used in the study.

				
Sample	BM01	BM02	PM01	PM02
Weight (ct)	0.94	0.99	0.97	0.97
Size (mm)	6.99 × 4.96 × 3.54	7.01 × 5.03 × 3.57	5.57 × 5.53 × 3.92	5.56 × 5.54 × 3.95

MATERIALS AND METHODS

Materials. For this study, two pink, two light greenish blue, and one colorless synthetic moissanite sample typical of those encountered in the lab were purchased in 2020 from the same supplier (Tian Shi Zhi Yue company), which sourced the material from a growth facility in Guangxi Province, China. The four colored samples are shown in table 1.

Methods. The light greenish blue and pink samples were cut along the girdle using a conventional gem saw to separate the crown from the pavilion.

In many surface analysis methods, the user must select possible elements in advance, especially trace elements. EDXRF analysis was performed with a Rigaku EDXL-300 using the standardless fundamental parameter detection method. This method is advantageous in that it quickly analyzes and filters the major and trace elements in a sample. Although EDXRF has a large analytical margin of error for trace elements, it is useful for the preliminary screening of experimental samples. The light greenish blue, pink, and colorless synthetic moissanite samples were tested by EDXRF and the differences in the chemical compositions were analyzed.

In this study, a JEOL JAMP-9510F AES instrument was used with a hemispherical analyzer (HSA) system. HSA is widely used with AES, XPS, and ultraviolet photoelectron spectroscopy methods to obtain electronic energy spectra. Furthermore, HSA combined with argon ion beam sputtering (AIS) is used to ablate the surface of the sample to conduct depth-profile analyses. We used an incident electron beam energy of 10 keV, current of 10.4 nA, and sample tilt angle of 30°. The sputtering energy of the argon ion beam of 2 keV and scan rate of 22.2 nm/min (3 s/cycle) were set based on a standard sample of silicon dioxide. The spatial resolution of AES with AIS was 1 nm. The vacuum pressure of the sample chamber was below 1×10^{-6} Pa.

Furthermore, high-resolution TEM imaging and elemental analysis of a micro-sectional profile (JEOL JEM-ARM300F Grand Arm AC-TEM with EELS) and elemental analysis and surface-plane mapping (Shimadzu EPMA-8050G high-resolution field-emission EPMA) were performed. A significant feature of AC-TEM is the use of spherical aberration correction to obtain a higher image resolution (Tanaka, 2008). Before TEM experiments, the samples were coated with carbon and platinum as conductive and protective layers, which were identified as the outermost layers in the TEM images. Focused ion beam (FIB) milling was used to prepare lamellae (thickness <100 nm) for TEM analysis. The TEM sample was transferred onto a copper bracket. The operating voltage of the TEM was 300 kV, and the resolution in the high-resolution configuration was 0.063 nm. EELS spectra were obtained in TEM imaging mode, with an energy resolution of 0.8–1.5 eV. The spectral sampling rate was 8000 spectra/s. The vacuum pressure in the sample chamber was maintained below 1×10^{-8} Pa.

In this study, the EPMA surface images were obtained in backscattered electron (BSE) mode. Throughout the experiment, the electron-beam accelerating voltage and current were set at 15 keV and 10 nA, respectively. A mapping resolution of 50 nm was achieved, with a compositional resolution of 0.1 at.%. The vacuum pressure in the sample chamber was kept below 6×10^{-4} Pa.

We employed several techniques used in the materials science field, including AES, FIB sample preparation for TEM, AC-TEM with EELS analyses, and

EPMA. All these methods require high-vacuum conditions, with the evacuation process requiring approximately 10–15 min. The total analysis time includes the time taken for sample positioning, actual analysis, and removal of the sample from the instrument. The entire process, from initiation to sample retrieval, required approximately 3 h for AES/AIS. For TEM analysis, the process of positioning, carbon and platinum coating, FIB preparation of the TEM lamellae, and sample analysis took approximately 4 h. The duration for EPMA analysis varies depending on the scanning area; for example, evaluating three elements over a 500 × 500 μm area takes about 1.5 h.

It should be noted that some sample preparation methods permanently damage the gemstone. For example, TEM analysis requires coating the samples with carbon and platinum, which remain on the surface. Additionally, AES/AIS and FIB preparation of TEM lamellae result in permanent pore features on the sample surfaces.

These methods analyze a microscopic region of a sample and are only suitable for the detailed examination of individual gemstones to provide critical information about the material characteristics. AES allows for point analysis and can be combined with AIS for depth profiling; TEM analyzes microscopic cross sections of samples; and EPMA provides point, line, and planar mapping analyses.

RESULTS

After the light greenish blue and pink samples were cut along the girdle and examined without magnification, we observed that the color was concentrated on the outer edge and the samples were colorless in the middle (figure 2). The coating was applied to all facet surfaces. Furthermore, the EDXRF results (overall averages of the entire colored samples) were compared with those of a colorless sample (CL01). Compared to CL01, the light greenish blue samples had higher concentrations of vanadium, cobalt, and manganese, while the pink samples had a higher concentration of gold. None of these elements were detected in CL01 (table 2). Vanadium, cobalt, and manganese were assumed to be present as coloring agents on the light greenish blue synthetic moissanite, while gold is very common in pink and red coated examples (Yu et al., 2005; Shen et al., 2007; Gabasch et al., 2008).

AES was performed as a function of depth from the surface during AIS. These results showed that the oxygen and vanadium contents on the light greenish blue samples (BM01 and BM02) decreased rapidly at depths of 38 and 54 nm, respectively, while the concentration of carbon and silicon increased rapidly at similar

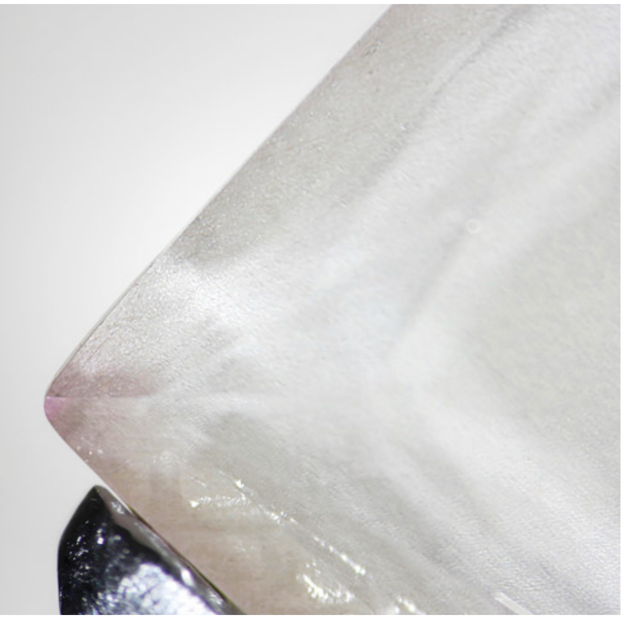

Figure 2. After the crown was separated from the pavilion of sample PM01, the observed color was concentrated on the outer edge, and the middle area was colorless. Photo by Tsung-Jen Wu.

TABLE 2. EDXRF results (in ppm) of pink, blue, and colorless coated synthetic moissanite samples.

Element	PM01	PM02	BM01	BM02	CL01
Au	85.8 ± 1.0	106.0 ± 3.6	bdl[a]	bdl	bdl
V	bdl	bdl	26.1 ± 1.5	35.0 ± 1.2	bdl
Mn	bdl	bdl	92.0 ± 3.5	64.0 ± 2.6	bdl
Co	bdl	bdl	46.0 ± 1.8	23.0 ± 0.8	bdl

[a] bdl = below detection limit (detection limits for Au, V, Mn, and Co are 0.1 ppm).

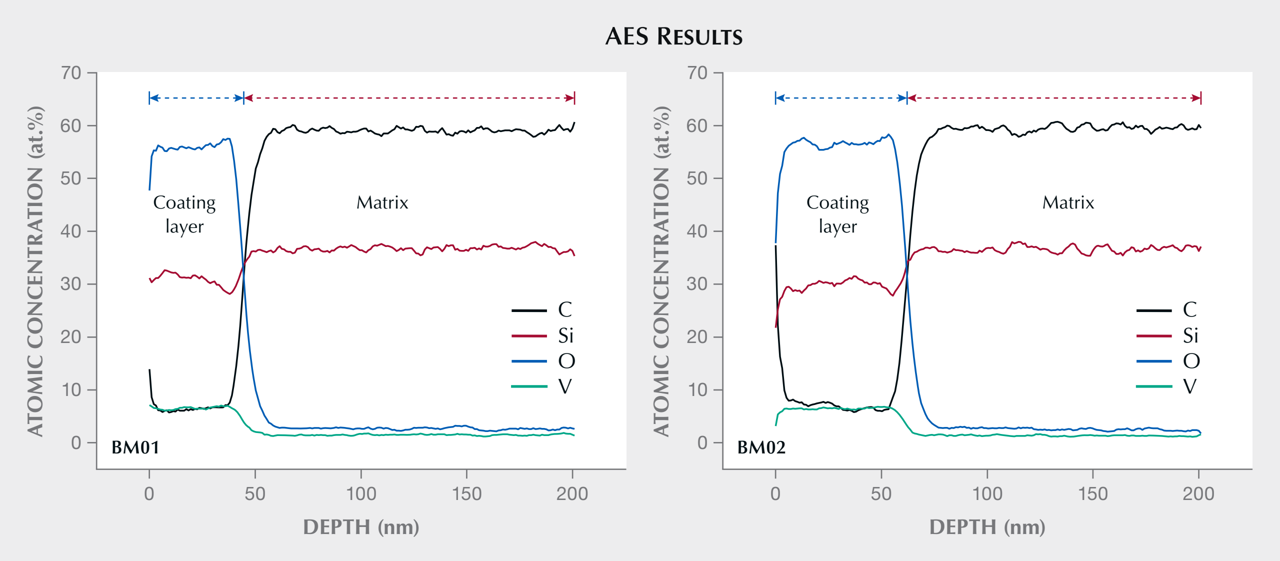

Figure 3. AES results obtained during AIS analysis of samples BM01 (left) and BM02 (right). The main elements are carbon, silicon, and oxygen. The trace element is vanadium. Both show noticeable concentration changes with increasing AIS ablation depth. The location where the oxygen and carbon concentration curves intersect was defined as the thickness of the coating.

depths. Comparing the surface and bulk regions, the concentrations of oxygen and carbon changed by a factor of ten (in opposite directions), silicon increased by ~12%, and vanadium decreased from a maximum value of 7.15% (BM01) and 6.41% (BM02) to below detection limits in the bulk region (figure 3). Cobalt and manganese were not detected by AES analysis because it was difficult to separate the weak signals from background noise. We concluded that the coatings on samples BM01 and BM02 were silicon dioxide films doped with vanadium, cobalt, and manganese with thicknesses of approximately 45 and 62 nm, respectively, defined by the crossover points where the concentrations of carbon and oxygen were identical (31.27% and 31.52%, respectively).

The images of sample BM01 analyzed by AC-TEM with EELS confirmed the AES experimental results. An amorphous silicon dioxide layer with a thickness of approximately 45 nm was observed on top of the SiC matrix. In addition, a damaged SiC layer was observed between the substrate and coating layer (figures 4 and 5). The EPMA map of BM01 confirmed an uneven distribution of small amounts of vanadium, cobalt, and manganese in the coating (figure 6).

For the pink samples, PM01 did not show the expected AES result and is not presented in the results but discussed later. For sample PM02, it was observed that the thickness of the gold-containing layer was less than 20 nm. In addition, the concentration of gold decreased rapidly from the surface to a depth of ~15 nm, and the concentration in the 15–20 nm depth range was very close to that of the background.

Figure 4. TEM image of sample BM01. Pt/C is the conductive platinum/carbon coating applied before imaging, while the yellow dashed lines mark the amorphous silicon dioxide coating and SiC is the matrix.

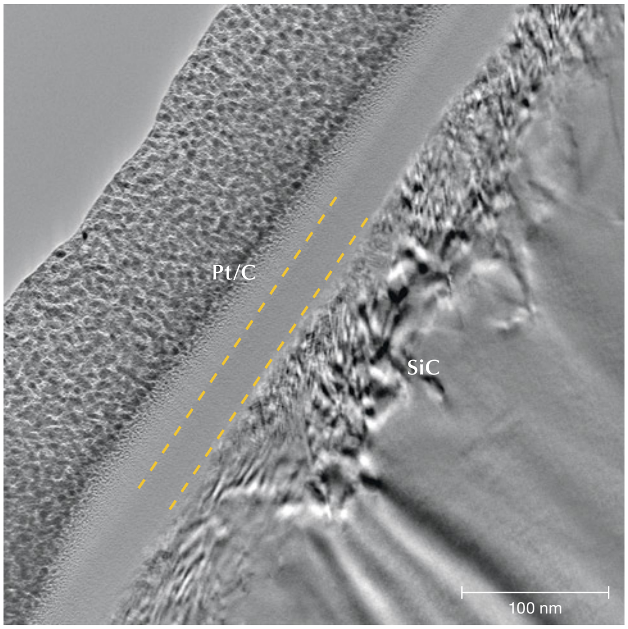

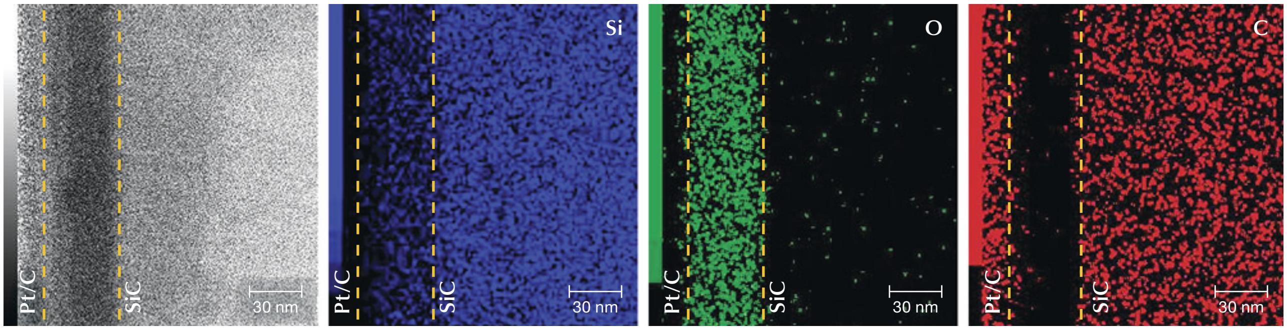

Figure 5. TEM and corresponding EELS images of sample BM01. These images corroborate the AES experimental results and clearly show the film thickness and composition.

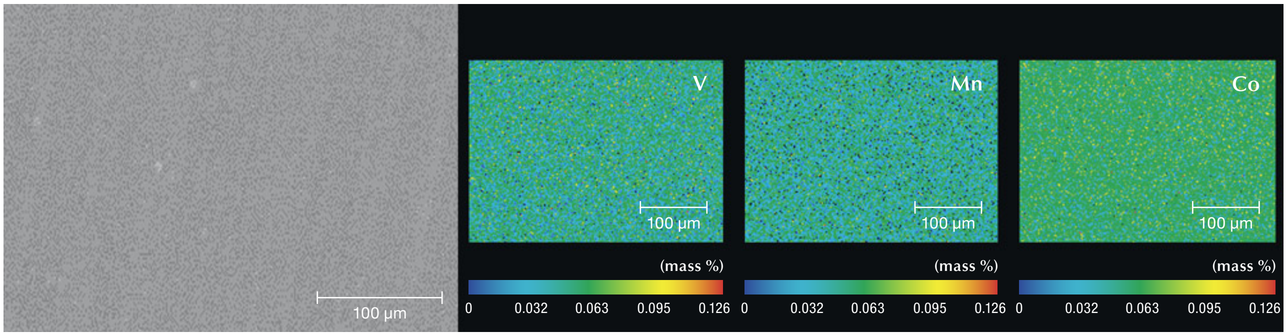

Figure 6. BSE image and corresponding EPMA maps of the coated surface of sample BM01, showing that it contained uneven distributions of vanadium, manganese, and cobalt. All three elements were examined in the same area.

The atomic concentration of gold was very low, and it was distinguished by comparing it against the concentrations of the main elements with lower atomic concentration (i.e., silicon) (figure 7). In AES analysis

Figure 7. AES results obtained for PM02 during AIS for main elements (left) and comparison of gold and silicon (right). The gold content decreases rapidly with increasing depth. In the range of ~15–20 nm, the signal becomes very close to the background value.

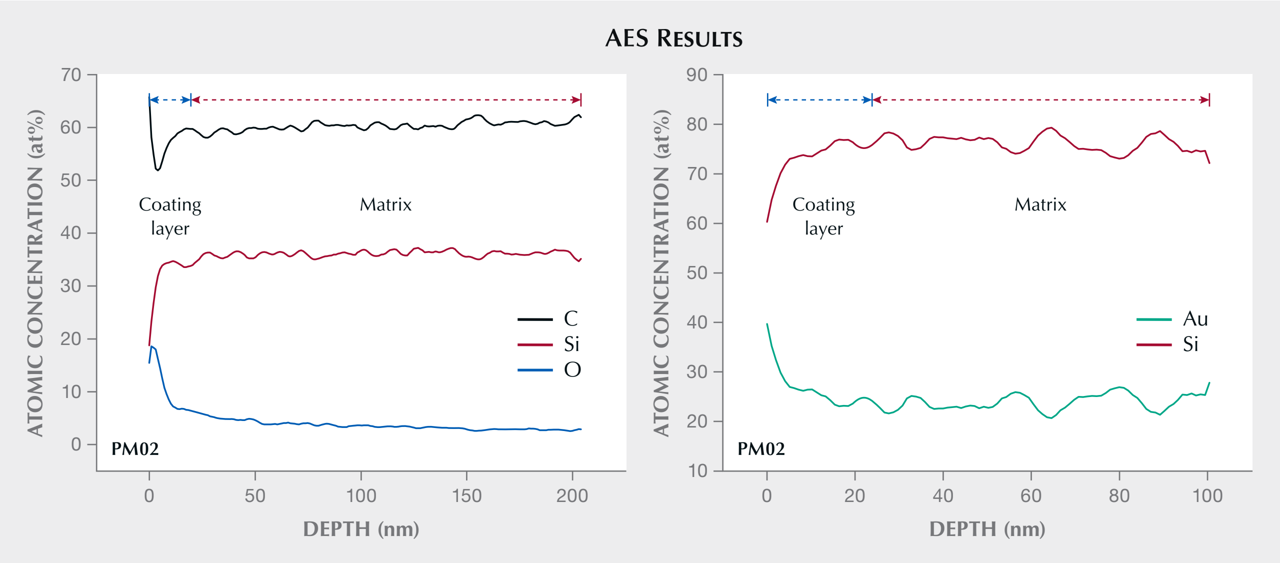

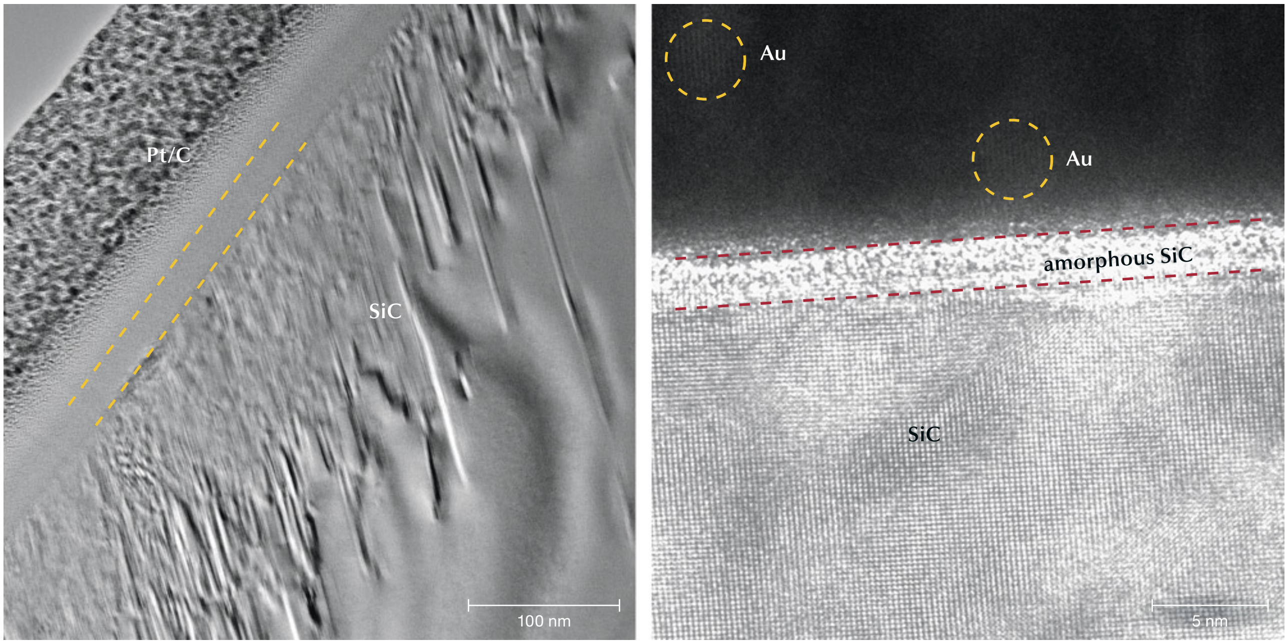

Figure 8. TEM images of PM02. Left: Pt/C is the conductive platinum/carbon coating applied before imaging, and the yellow lines indicate the coating layer. Right: The red lines separate the amorphous SiC film (inner layer) and gold-containing film (outer layer); SiC is the matrix. The yellow circles indicate the indistinct lattice fringes of gold.

or similar surface analytical techniques, atomic percentages (at.%) refer to the relative content of each element within a designated area compared to the total concentration of all analyzed elements—i.e., the sum of the atomic percentages of all analyzed elements equals 100%. Only the curves for the major element silicon and the trace element gold are plotted in figure 7 (right), to enable easier analysis of the distribution of gold (with low concentration) without interference from other curves. Despite the low concentration of gold, this comparative analysis allowed us to effectively highlight the presence and variations of gold. The AC-TEM images of PM02 also showed an amorphous SiC film on the SiC substrate with a thickness of approximately 3–5 nm (figure 8, left and right), which is consistent with the AES results. However, EELS analysis of the area did not identify the presence of gold (figure 9). The EPMA map of PM02 confirmed that the coating was uneven and contained gold (figure 10).

Figure 9. TEM image and the corresponding EELS images of sample PM02, which corroborate the AES experimental results and verify the film thickness and composition.

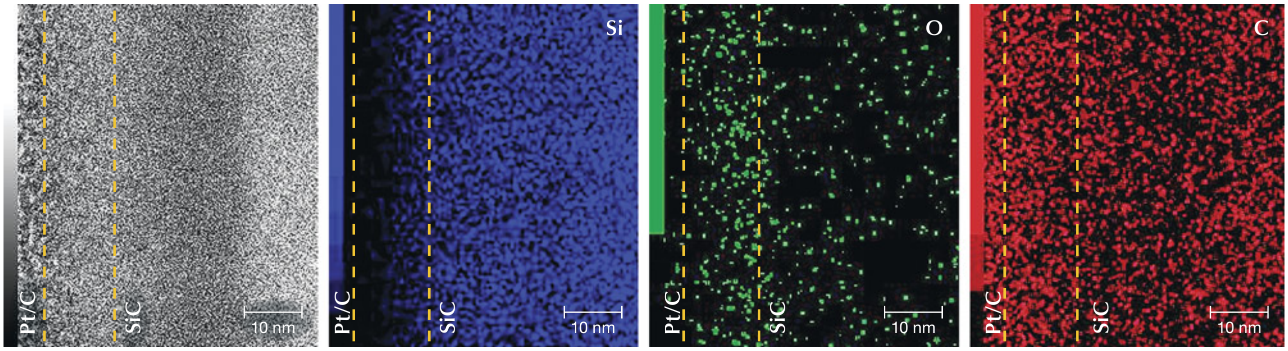

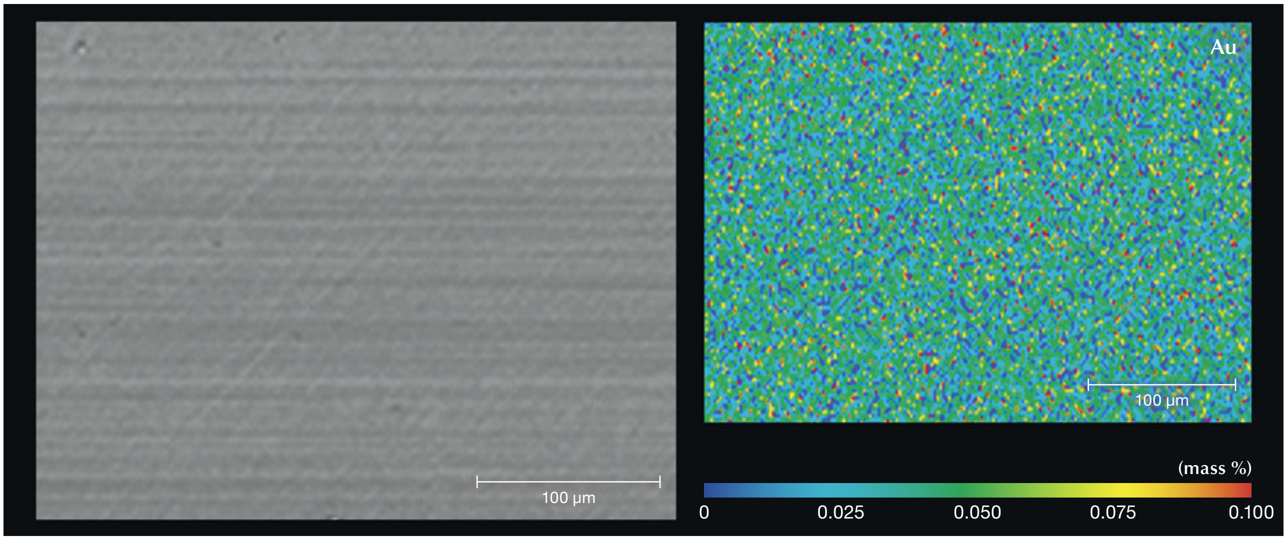

Figure 10. The BSE image and corresponding EPMA map of the coated surface of PM02 show that it contained gold with an uneven distribution.

DISCUSSION

Detection of Trace Elements. AES analysis detected gold for PM02 but not PM01. Because the thin gold-containing coating had a low concentration and uneven distribution of gold, the gold content at the test point of sample PM01 was lower than the detection limit of the AES method (0.1 wt.% for most elements). Because the gold concentration was higher at the test point of sample PM02 than in PM01, trace amounts of gold were detected. The atomic numbers of vanadium, manganese, and cobalt are 23, 25, and 27, respectively; therefore, at the same concentration, vanadium has a slightly higher probability of generating Auger electrons than manganese and cobalt. However, the EPMA mapping results of BM01 showed that these elements had a similar concentration. With a low concentration and large atomic number, it is difficult to detect manganese and cobalt in the synthetic moissanite coating using AES.

The EELS method is similar to AES but has a better resolution for lighter elements. Theoretically, EELS can analyze the elements from carbon to 3d orbital transition metals. Due to the lower resolution for elements with larger atomic numbers, a higher concentration is required to detect these elements (Ahn, 2006). Therefore, the EELS method is suitable for obtaining analysis images of the main elements in the coating, such as silicon, oxygen, and carbon. But because the trace elements (vanadium, manganese, and cobalt) in the coating of BM01 have large atomic numbers and low concentrations, the obtained data is extremely difficult to analyze.

The same problem was encountered for PM02 because gold is a heavy element and not easy to identify using EELS at low concentration. In this case, the EPMA mapping results provide strong evidence that the coating on sample BM01 contained vanadium, manganese, and cobalt, and that the coating on sample PM02 contained gold. The uneven distribution of vanadium, manganese, and cobalt in the film on BM01 was presumably due to the ion implantation technique used to dope these trace elements into the colorless silicon dioxide coating to add color.

Colorization of Coated Synthetic Moissanite. *Light Greenish Blue*. The thin-film technology used to fabricate SiC and SiO_2 coatings is very mature, and there have been many related studies (e.g., Afanasev et al., 1997; Kim et al., 2016; Li et al., 2017; Liu et al., 2019; Kobayashi et al., 2020; Liu et al., 2020). According to our analysis results, the coatings on the SiC of the blue moissanite sample substrates were uniformly distributed amorphous SiO_2 films. Common methods for thin-film growth include PVD and CVD. However, the film thickness produced by PVD is not as uniform as that produced by CVD (Jin, 2004). Hence, CVD is considered the best method for applying such coatings. Based on the analysis of the blue moissanite, referencing Isenberg et al. (2003), we believe multiple fabrication steps were used, as discussed below. There are three main benefits of combining fabrication technologies:

1. The SiO_2 film, presumably deposited by the CVD method, is robust and cannot be easily delaminated from the SiC matrix.
2. SiO_2 has good chemical stability and can resist strong acids and alkalis.
3. Doping the coating with trace elements by ion implantation can easily adjust the color as desired. Hence, it is speculated that the blue color arises from doping the silicon dioxide film with vanadium, manganese, and cobalt ions.

Pink. In the pink synthetic moissanite samples, there was a thin film of amorphous SiC on the SiC substrate. The outer layer of this film contained gold nanoparticles (AuNPs) and SiO_2 as a dielectric (insulator) with a thickness below 20 nm, such as those indicated by the yellow circles in figure 8 (right). In these samples, the size of the AuNPs was 5–10 nm. When there is no contact between such particles or they are also separated by a dielectric material, upon exposure to light, the groups of conducting electrons in the outer shell of the AuNPs undergo collective oscillations due to the oscillating incident electric field. As a result of the oscillating electric field, a portion of the electron cloud of the AuNPs escapes the influence of the nuclei. The coulomb force between the electrons and the nuclei causes the nuclei to oscillate together, forming a surface plasmon resonance (LSPR) effect (Kelly et al., 2003). Moreover, the LSPR of AuNPs results in anomalous absorption in the range of 520–580 nm (green and yellow light), causing the appearance of complementary colors: red, pink, and purple (Abadeer and Murphy, 2016). The surfaces of both the 6H-SiC and 4H-SiC structures are suitable for nucleation and growth of dome-shaped AuNPs and gold nanocubes (Li et al., 2015; Li et al., 2016; Shtepliuk et al., 2021) but less suitable for the adhesion of the color-generating AuNP-containing surface coating. The high-resolution AC-TEM image in figure 8 (right) only shows indistinct local lattice fringes, which support this hypothesis. In contrast, amorphous SiC is more suitable for the adhesion of AuNPs. Therefore, it is necessary to coat the crystalline SiC substrate with an amorphous SiC film, presumably by the CVD method, to facilitate AuNP adhesion.

According to the distribution characteristics and considering the high cost of gold, the AuNP films are believed to have been deposited on the SiC film directly by electron beam evaporation (Zhang et al., 2006) or sputtering (Anderson, 2005; Shtepliuk et al., 2021), both of which are PVD methods. Combining two different processing methods (such as first depositing the inner amorphous thin film by CVD method, followed by the deposition of an outer film of AuNP-doped SiO_2 by PVD) seems to be necessary to achieve pink synthetic moissanite. The observation that gold was not detected in PM01 during AES analysis is likely due to the uneven distribution of AuNPs within the outer layer. Thus, the selected test location on PM01 might be a region between AuNPs or a region with a concentration of gold below the detection limit of AES. Owing to limited access to the testing instruments, the experiments were not repeated to investigate the presence of gold. The EPMA mapping results support this perspective. Moreover, the very large difference between the lattice constants of the coating layer and the matrix results in lattice mismatches that produce dislocation and defects (Devynck, 2008). Such defects were not directly observed in this study, however. In addition, the coating material may also agglomerate due to the high surface energy. These mechanisms explain the source of the color and the phenomenon of uneven distribution at the atomic scale but consistent color at the macroscale.

CONCLUSIONS

The colored coatings on the light greenish blue synthetic moissanite samples were amorphous SiO_2 layers with a thickness of approximately 45–62 nm. The coating was doped with small amounts of vanadium, manganese, and cobalt, which were present as coloring agents. The coating layer appeared to have high chemical stability and was not likely to peel off, while trace element contents could be adjusted to produce the required color. The colored coatings of the examined pink synthetic moissanite samples were AuNP-containing layers with a thickness of approximately 15 nm, which was unevenly distributed on an amorphous SiC film with a thickness of approximately 3–5 nm. Based on the existing knowledge of AuNP-based films, varying the particle size of AuNPs could produce other colors in addition to pink. However, AuNP coatings can delaminate under mechanical or thermal stress and are susceptible to corrosion under certain conditions.

The results of this study show that making coatings for gemstones requires careful attention to the compatibility between the gem substrate and the coating materials to avoid dislocations and defects in the film. Excessive dislocations and defects can promote delamination, resulting in an uneven coating that is easily detected. Given the characteristics of the coatings, they are expected to be durable under normal circumstances. Complete removal of the colored coatings would require polishing the entire gemstone.

As mature technologies from materials science are increasingly being used to treat gem materials, the identification and study of gems becomes significantly more challenging. In addition to traditional gem-related fields such as mineralogy, research will need to include aspects of materials science. Further, addressing the challenges of gem treatment in the future may require the use of instruments and equipment traditionally reserved for materials science.

ABOUT THE AUTHORS

Tsung-Jen Wu is a PhD candidate at the Department and Institute of Geosciences, National Taiwan University and a researcher at the Tai-Da Gem Research Laboratory, Taiwan. Dr. Sheng-Rong Song (corresponding author) and Dr. Wen-Shan Chen are professors at the Department and Institute of Geosciences, National Taiwan University. Dr. Wen Lin is a professor at the Department of Materials and Mineral Resources Engineering, National Taipei University of Technology. Chien-Tai Cheng, who assisted in completing sample pre-processing and AES experiment, is a postgraduate student at the Department of Materials Science and Engineering, National Taiwan University.

ACKNOWLEDGMENTS

The authors would like to thank Ming-Chang Chou, head of Chou Gem Lapidary, for his assistance in cutting the samples, and Hui-Jun Ji, technician at the Instrumental Analyzing & Research Center of Shanghai Yanku, for his assistance in completing the AC-TEM and EPMA experiments.

REFERENCES

Abadeer N.S., Murphy C.J. (2016) Recent progress in cancer thermal therapy using gold nanoparticles. *The Journal of Physical Chemistry C*, Vol. 120, No. 9, pp. 4691–4716, http://dx.doi.org/10.1021/acs.jpcc.5b11232

Afanasev V.V., Bassler M., Pensl G., Schulz M. (1997) Intrinsic SiC/SiO_2 interface states. *Physica Status Solidi (a)*, Vol. 162, No. 1, pp. 321–337, http://dx.doi.org/10.1002/1521-396X(199707)162:1%3C321::AID-PSSA321%3E3.0.CO;2-F

Ahn C.C., Ed. (2006) *Transmission Electron Energy Loss Spectrometry in Materials Science and the EELS Atlas*. John Wiley & Sons, New York.

Anderson M.S. (2005) Surface enhanced infrared absorption by coupling phonon and plasma resonance. *Applied Physics Letters*, Vol. 87, No. 14, article no. 144102, http://dx.doi.org/10.1063/1.2077838

Breeding C.M., Shen A.H., Eaton-Magaña S., Rossman G.R., Shigley J.E., Gilbertson A. (2010) Developments in gemstone analysis techniques and instrumentation during the 2000s. *G&G*, Vol. 46, No. 3, pp. 241–257, http://dx.doi.org/10.5741/GEMS.46.3.241

Chen X.F., Xu X.G., Tian G.L., Jiang M.H. (2008) Synthetic silicon carbide gemstone. In B.K. Chen, Ed., *Chinese Artificial Gemstones*. Geological Publishing House, pp. 54–56 [in Chinese].

Chung M.F., Jenkins L.H. (1970) Auger electron energies of the outer shell electrons. *Surface Science*, Vol. 22, No. 2, pp. 479–485, http://dx.doi.org/10.1016/0039-6028(70)90099-3

Cooper A., Renfro N. (2014) Lab Notes: Titanium-coated tanzanite. *G&G*, Vol. 50, No. 1, p. 71.

Delaunay A. (2018) Gem News International: Coated pink synthetic moissanite. *G&G*, Vol. 54, No. 4, pp. 459–460.

Devynck F. (2008) First-principles study of defects at the SiC/SiO_2 interface through hybrid functionals. PhD thesis, Swiss Federal Institute of Technology Lausanne.

Elasser A., Chow T.P. (2002) Silicon carbide benefits and advantages for power electronics circuits and systems. *Proceedings of the IEEE*, Vol. 90, No. 6, pp. 969–986, http://dx.doi.org/10.1109/JPROC.2002.1021562

Ertl G., Küppers J. (1985) *Low Energy Electrons and Surface Chemistry*. Verlag Chemie, Weinheim, West Germany.

Ewart P. (2019) *Atomic Physics*. Morgan & Claypool Publishers, San Rafael, California.

Friedrichs P., Kimoto T., Ley L., Pensl G., Eds. (2011) *Silicon Carbide: Volume 1: Growth, Defects, and Novel Applications*. John Wiley & Sons, New York.

Gabasch H., Klauser F., Bertel E., Rauch T. (2008) Coloring of topaz by coating and diffusion processes: An X-ray photoemission study of what happens beneath the surface. *G&G*, Vol. 45, No. 4, pp. 148–155, http://dx.doi.org/10.5741/GEMS.44.2.148

He X.M., Shen C.Q. (2020) *Artificial Synthesis Technology of Gemstones*, 3rd ed. Chemical Industry Press, pp. 175–183 [in Chinese].

Isenberg J., Reber S., Warta W. (2003) Diffusion properties of ion-implanted vanadium in PECVD SiO_2 and PECVD SiN_x. *Journal of The Electrochemical Society*, Vol. 150, No. 7, pp. G365–G370, http://dx.doi.org/10.1149/1.1575741

Jin H.P. (2004) *New Technology and New Standard of Modern Surface Treatment*. Contemporary China Audiovisual Publishing House, pp. 435–475 [in Chinese].

Kelly K.L., Coronado E., Zhao L.L., Schatz G.C. (2003) The optical properties of metal nanoparticles: The influence of size, shape, and dielectric environment. *The Journal of Physical Chemistry B*, Vol. 107, No. 3, pp. 668–677, http://dx.doi.org/10.1021/jp026731y

Kim D.K., Jeong K.S., Kang Y.S., Kang H.K., Cho S.W., Kim S.O., Suh D., Kim S., Cho M.H. (2016) Controlling the defects and transition layer in SiO_2 films grown on 4H-SiC via direct plasma-assisted oxidation. *Scientific Reports*, Vol. 6, No. 1, article no. 34945, http://dx.doi.org/10.1038/srep34945

Kobayashi T., Okuda T., Tachiki K., Ito K., Matsushita Y.I., Kimoto T. (2020) Design and formation of SiC (0001)/SiO_2 interfaces via Si deposition followed by low-temperature oxidation and high-temperature nitridation. *Applied Physics Express*, Vol. 13, No. 9, article no. 091003, http://dx.doi.org/10.35848/1882-0786/ababed

Li M.Y., Zhang Q., Pandey P., Sui M., Kim E.S., Lee J. (2015) From the Au nano-clusters to the nanoparticles on 4H-SiC (0001). *Scientific Reports*, Vol. 5, No. 1, article no. 13954, http://dx.doi.org/10.1038/srep13954

Li M.Y., Sui M., Pandey P., Zhang Q.Z., Kunwar S., Salamo G.J., Lee J. (2016) Precise control of configuration, size, and density of self-assembled Au nanostructures on 4H-SiC (0001) by systematic variation of deposition amount, annealing temperature and duration. *Crystal Engineering Communications*, Vol. 18, No. 19, pp. 3347–3357, http://dx.doi.org/10.1039/C5CE02439K

Li X., Ermakov A., Amarasinghe V., Garfunkel E., Gustafsson T., Feldman L.C. (2017) Oxidation induced stress in SiO_2/SiC structures. *Applied Physics Letters*, Vol. 110, No. 14, article no. 141604, http://dx.doi.org/10.1063/1.4979544

Li Z., Bradt R.C. (1986) Thermal expansion of the hexagonal (4*H*) polytype of SiC. *Journal of Applied Physics*, Vol. 60, No. 2, pp. 612–614, http://dx.doi.org/10.1063/1.337456

Liu G., Tuttle B.R., Dhar S. (2015) Silicon carbide: A unique platform for metal-oxide-semiconductor physics. *Applied Physics Reviews*, Vol. 2, No. 2, article no. 021307, http://dx.doi.org/10.1063/1.4922748

Liu X., Hao J., You N., Bai Y., Wang S. (2019) High-pressure microwave plasma oxidation of 4H-SiC with low interface trap density. *AIP Advances*, Vol. 9, No. 12, article no. 125150, http://dx.doi.org/10.1063/1.5115538

Liu X.Y., Hao J.L., You N.N., Bai Y., Tang Y.D., Yang C.Y., Wang S.K. (2020) High-mobility SiC MOSFET with low density of interface traps using high pressure microwave plasma oxidation. *Chinese Physics B*, Vol. 29, No. 3, article no. 037301, http://dx.doi.org/10.1088/1674-1056/ab68c0

McClure S.F., Smith C.P. (2000) Gemstone enhancement and detection in the 1990s. *G&G*, Vol. 36, No. 4, pp. 336–359, http://dx.doi.org/10.5741/GEMS.36.4.336

Moe K.S., Johnson P., Lu R. (2013) Lab Notes: Large synthetic moissanite with silicon carbide polytypes. *G&G*, Vol. 49, No. 4, pp. 255–256.

Nassau K. (1984) The early history of gemstone treatments. *G&G*, Vol. 20, No. 1, pp. 22–33, http://dx.doi.org/10.5741/GEMS.20.1.22

Nassau K., McClure S.F., Elen S., Shigley J.E. (1997) Synthetic moissanite: A new diamond substitute. *G&G*, Vol. 33, No. 4, pp. 260–275, http://dx.doi.org/10.5741/GEMS.33.4.260

Schmetzer K. (2008) Surface treatment of gemstones, especially topaz—An update of recent patent literature. *Journal of Gemmology*, Vol. 31, No. 1/2, pp. 7–13.

Shen A.H., Wang W., Hall M.S., Novak S., McClure S.F., Shigley J.E., Moses T.M. (2007) Serenity coated colored diamonds: Detection and durability. *G&G*, Vol. 43, No. 1, pp. 16–33, http://dx.doi.org/10.5741/GEMS.43.1.16

Shen Y.L. (2014) Surface analysis characterizations of Auger electron spectroscopy and X-ray photoelectron spectroscopy. *Journal of the Vacuum Society of the R.O.C*, Vol. 27, No. 2, pp. 51–58 [in Chinese].

Shigley J.E., Gilbertson A., Eaton-Magaña S. (2012) Characterization of colorless coated cubic zirconia (Diamantine). *G&G*, Vol. 48, No. 1, pp. 18–30, http://dx.doi.org/10.5741/GEMS.48.1.18

Shtepliuk I., Ivanov I.G., Pliatsikas N., Iakimov T., Lara-Avila S., Kim K.H., Ben Sedrine N., Kubatkin S., Yakimova R. (2021) Clustering and morphology evolution of gold on nanostructured surfaces of silicon carbide: Implications for catalysis and sensing. *ACS Applied Nano Materials*., Vol. 4, No. 2, pp. 1282–1293, http://dx.doi.org/10.1021/acsanm.0c02867

Tanaka N. (2008) Present status and future prospects of spherical aberration corrected TEM/STEM for study of nanomaterials. *Science and Technology of Advanced Materials*, Vol. 9, No. 1, article no. 014111, http://dx.doi.org/10.1088/1468-6996/9/1/014111

Tsang R. (2017) Lab Notes: Synthetic moissanite imitating rough diamond. *G&G*, Vol. 53, No. 4, pp. 462–463.

Walters D.L., Bhalla C.P. (1971) Nonrelativistic Auger rates, X-ray rates, and fluorescence yields for the 2*p* shell. *Physical Review A*, Vol. 4, No. 6, pp. 2164–2170, http://dx.doi.org/10.1103/PhysRevA.4.2164

Watts J.F., Wolstenholme J. (2019) *An Introduction to Surface Analysis by XPS and AES*, 2nd ed. John Wiley & Sons, New York.

Wolstenholme J. (2015) *Auger Electron Spectroscopy: Practical Application to Materials Analysis and Characterization of Surfaces, Interfaces, and Thin Films*. Momentum Press, New York.

Yu G.Q., Tay B.K., Zhao Z.W., Sun X.W., Fu Y.Q. (2005) Ion beam co-sputtering deposition of Au/SiO_2 nanocomposites. *Physica E: Low-Dimensional Systems and Nanostructures*, Vol. 27, No. 3, pp. 362–368, http://dx.doi.org/10.1016/j.physe.2004.12.011

Zhang J., Lu T., Chen H. (2013) Characteristics of coated jadeite jade. *G&G*, Vol. 49, No. 4, pp. 246–251, http://dx.doi.org/10.5741/GEMS.49.4.246

Zhang S., Pereira L., Hu Z., Ranieiro L., Fortonato E., Ferreira I., Martins R. (2006) Characterization of nanocrystalline silicon carbide films. *Journal of Non-Crystalline Solids*, Vol. 352, No. 9-20, pp. 1410–1415, http://dx.doi.org/10.1016/j.jnoncrysol.2006.02.027

The
Dr. Edward J. Gübelin
Most Valuable Article
AWARD

Most Valuable Article

First Place

Yellow Sapphire: Natural, Heat-Treated, Beryllium-Diffused, and Synthetic

Fall 2023

John L. Emmett, Ungkhana Atikarnsakul, Jennifer Stone-Sundberg, and Supharart Sangsawong

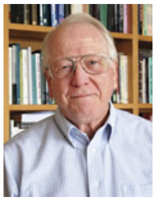

John Emmett

Ungkhana Atikarnsakul

Jennifer Stone-Sundberg

John L. Emmett received a PhD in physics from Stanford University. For the majority of his career, Dr. Emmett was an associate director of the Lawrence Livermore Laboratory, responsible for all laser research and development. He is currently a technical consultant to GIA. **Ungkhana Atikarnsakul** is a staff gemologist of colored stone identification at GIA in Bangkok. She holds a master's degree in analytical chemistry science from Chulalongkorn University in Thailand. **Jennifer Stone-Sundberg** received a PhD in inorganic chemistry from Oregon State University. She has worked in the synthetic oxide crystal growth industry for 20 years, specializing in growing and characterizing materials such as sapphire, spinel, and garnet. She is a technical advisor for GIA and senior technical editor for *Gems & Gemology*. **Supharart Sangsawong** (not pictured) is a research scientist and gemologist at GSTV Corporation in Tokyo.

Second Place

Gemological Characterization of Montana Sapphire from the Secondary Deposits at Rock Creek, Missouri River, and Dry Cottonwood Creek

Spring 2023

Aaron C. Palke, Nathan D. Renfro, Jeffrey R. Hapeman, and Richard B. Berg

Aaron Palke

Nathan Renfro

Jeffrey Hapeman

Aaron Palke is senior manager of research at GIA in Carlsbad, California. He holds a PhD in geology from Stanford University. **Nathan Renfro** is senior manager of colored stone identification at GIA in Carlsbad. He earned a bachelor's degree in geology from Appalachian State University in North Carolina. A scientist by education, **Jeffrey Hapeman** is the founder of Earth's Treasury, which specializes in precision-cut gemstones and fine jewelry, with a focus on Montana sapphires. **Richard Berg** (not pictured) is research geologist emeritus at Montana Bureau of Mines and Geology at Montana Tech in Butte. For approximately the last 30 years, Dr. Berg's research has been mainly on Montana sapphires.

Third Place (tie)

Color Modification of Spinel by Nickel Diffusion: A New Treatment

Summer 2023

Michael Jollands, Abadie Ludlam, Aaron C. Palke, Wim Vertriest, Shiyun Jin, Pamela Cevallos, Sarah Arden, Elina Myagkaya, Ulrika D'Haenens-Johannson, Vararut Weeramongkhonlert, and Ziyin Sun

Michael Jollands

Michael Jollands is a research scientist with a background in geology, working at GIA in New York. Dr. Jollands studies defects in crystals, with a focus on how they relate to diffusion.

Special Colors and Optical Effects of Oregon Sunstone: Absorption, Scattering, Pleochroism, and Color Zoning

Fall 2023

Shiyun Jin, Aaron C. Palke, Nathan D. Renfro, and Ziyin Sun

Shiyun Jin

Shiyun Jin is a research scientist of colored stones at GIA in Carlsbad. Dr. Jin's research focuses on the crystal chemistry, crystallography, and optical effects of gem minerals.

Many thanks to the members of G&G*'s Editorial Review Board for voting this year.*

The following 25 questions are from the four 2023 issues of *G&G*. Please refer to the articles in those issues to find the single best answer to each question.

Visit gia.edu/gems-gemology to take the Challenge online. Entries must be received no later than **September 1, 2024**. All entries will be acknowledged with an email.

Score 75% or better, and you will receive a certificate of completion (PDF file). Earn a perfect score, and your name also will be listed in the Fall 2024 issue of *Gems & Gemology*.

1. Until the late 1920s, most secondary Montana sapphire mined was
   A. more popular than Yogo sapphire.
   B. used in industrial applications.
   C. sold to Tiffany & Co.
   D. cornflower blue.

2. Nickel-diffused spinel
   A. is widely available commercially.
   B. fluoresces red under UV light.
   C. can range from bluish green to blue.
   D. is limited to shades of green.

3. Which chromophore will *not* produce yellow in sapphire?
   A. $h^{\bullet}\text{-Fe}^{3+}$
   B. $h^{\bullet}\text{-Cr}^{3+}$
   C. Fe^{3+}
   D. Ni^{3+}

4. The collecting of Texas topaz began in
   A. the World War II era.
   B. the early 2000s.
   C. the late 1800s.
   D. 1977.

5. The formation of conical Colombian emerald *vasos* or cups results from
   A. overgrowth of the basal faces.
   B. mechanical carving.
   C. presence of pyrite.
   D. skeletal growth.

6. Green augite from Vietnam
   A. has a higher specific gravity than brown augite.
   B. fluoresces strongly under long-wave UV light.
   C. has a higher refractive index than brown augite.
   D. is easily confused with chrysoberyl.

7. Green color in Oregon sunstone results from
   A. light scattering and absorption from copper nanoparticles.
   B. light scattering by macroscopic copper flakes.
   C. light absorption by gold

nanoparticles.
D. fluorescence of copper nanoparticles.

8. Decorative Bohemian garnet use has been documented since as early as the
A. eighteenth century.
B. sixteenth century.
C. fifth century.
D. first century.

9. Montana sapphire from the three secondary deposits
A. cannot be classified as typical magmatic or metamorphic.
B. typically has multiple twinned sectors.
C. is unusually high in gallium.
D. is generally not heat treated.

10. The brown color in fossilized ivory results from the presence of
A. high levels of phosphorous compared to unfossilized ivory.
B. high levels of collagen compared to unfossilized ivory.
C. iron and manganese compounds.
D. vivianite.

11. The Volyn pegmatites in Ukraine do *not* produce
A. emerald.
B. heliodor.
C. quartz.
D. topaz.

12. Iolite from the Blue Arrow and Blue Bear claims in British Columbia, Canada, is
A. only suitable for cabochons.
B. alluvial material.
C. all chatoyant.
D. gem quality.

13. Opal from Slovakia was once known as
A. Hungarian opal.
B. German opal.
C. Russian opal.
D. French opal.

14. The tree fern genus that was petrified in northeast China grew during the
A. modern era.
B. Cenozoic era.
C. Jurassic period.
D. Cretaceous period.

15. Schiller in Oregon sunstone results from
A. light scattering and absorption by copper nanoparticles.
B. light scattering by macroscopic copper flakes.
C. light scattering by gold nanoparticles.
D. fluorescence of copper nanoparticles.

16. Nickel diffuses into spinel
A. more uniformly than cobalt.
B. more readily than cobalt.
C. about the same as cobalt.
D. less readily than cobalt.

17. Which is required to form trapped holes in yellow sapphire?
A. Heating in a hydrogen-rich environment
B. [donors] > [acceptors]
C. [acceptors] > [donors]
D. An excess of silicon

18. A deeply saturated blue color is found in what percentage of Texas topaz?
A. 0%
B. 50%
C. >50%
D. <10%

19. The garnets adhered to glass objects from the 1600s were held in place using
A. molten lead.
B. lead glass.
C. prongs.
D. wax.

20. Additional emerald overgrowth of the features within a conical Colombian emerald cup produces a
A. *gota de aceite* inclusion pattern.
B. deepening of the cup.
C. trapiche emerald.
D. stepped surface.

21. Compared to beryl from other locales, the F-type etch pits on Volyn beryl are generally
A. not as large as the C- and P-type etch pits.
B. larger and can exhibit overlapping.
C. strongly curved in outline.
D. irregular in shape.

22. Glassy Slovak opal is referred to as
A. Slovak Ice Opal.
B. precious opal.
C. jelly opal.
D. fire opal.

23. Compared to elephant ivory, fossilized mammoth ivory has
A. a lower amount of iron compounds present.
B. smaller Schreger line intersection angles.
C. a thinner cementum layer.
D. more collagen present.

24. Which of the following is diagnostic for iolite from Thor-Odin, Canada?
A. Inclusions of primary muscovite
B. Unusually low specific gravity
C. Inclusions of primary biotite
D. Chatoyancy

25. Which feature distinguishes tiger's-eye from petrified tree fern?
A. Refractive index
B. Specific gravity
C. Chatoyancy
D. Color

To take the Challenge online, please scan the QR code.

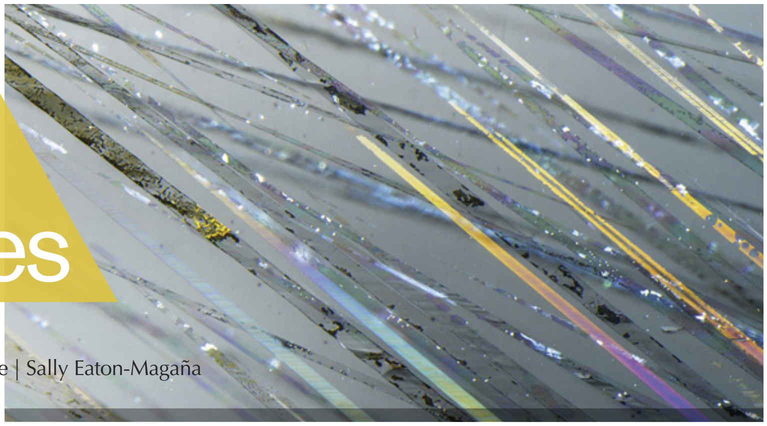

Lab Notes

Editors
Thomas M. Moses | Shane F. McClure | Sally Eaton-Magaña

DIAMONDS

Cloud Inclusions Causing Fancy Light Blue Color in Diamond

The most common cause of blue color in diamond is the incorporation of boron into the diamond crystal lattice (type IIb), such as the recently auctioned Cullinan Blue (Summer 2022 Lab Notes, pp. 216–217). Other causes of blue color in diamond are hydrogen-related absorption (C.H. van der Bogert et al., "Gray-to-blue-to-violet hydrogen-rich diamonds from the Argyle mine, Australia," Spring 2009 *G&G*, pp. 20–37) and irradiation, either natural or artificial. Artificial irradiation using an electron beam is a common diamond treatment (Winter 2020 Lab Notes, pp. 517–518).

Recently submitted to the New York laboratory for colored diamond grading service was a 2.20 ct Fancy Light grayish blue diamond (figure 1). Compared to the Cullinan Blue, which was graded as Fancy Vivid blue on GIA's color grading scale, this diamond was type IIa (i.e., no boron) (figure 2). In addition to the absence of boron-related impurities, this diamond lacked any hydrogen-related impurities (observed in the ultraviolet/visible/near-infrared spectrum in figure 3) (van der Bogert et al., 2009) or any GR1-related color centers, thus ruling out these major causes of blue color in diamond. Instead, the UV absorption for the 2.20 ct diamond was similar to what would be expected for a yellow type Ib (isolated nitrogen) diamond (figure 3).

The diamond was heavily included with fine cloud-like inclusions, giving it a milky appearance (figure 4). Clouds, sometimes hydrogen-related, often cause gray, brown, black, or even white color in natural diamonds (S. Eaton-Magaña et al., "Natural-color fancy white and fancy black diamonds: Where color and clarity converge," Fall 2019 *G&G*, pp. 320–337). In this case, the cloud micro-inclusions caused Rayleigh light scattering, creating a desirable blue color and not the expected yellow color resulting from a slight rise in absorption from lower to higher energy.

Figure 1. The 2.20 ct Fancy Light grayish blue diamond.

Figure 2. The mid-infrared spectrum of type IIb diamond compared to the 2.20 ct grayish blue diamond, which was type IIa with no boron or hydrogen-related features. Spectra are offset vertically for clarity.

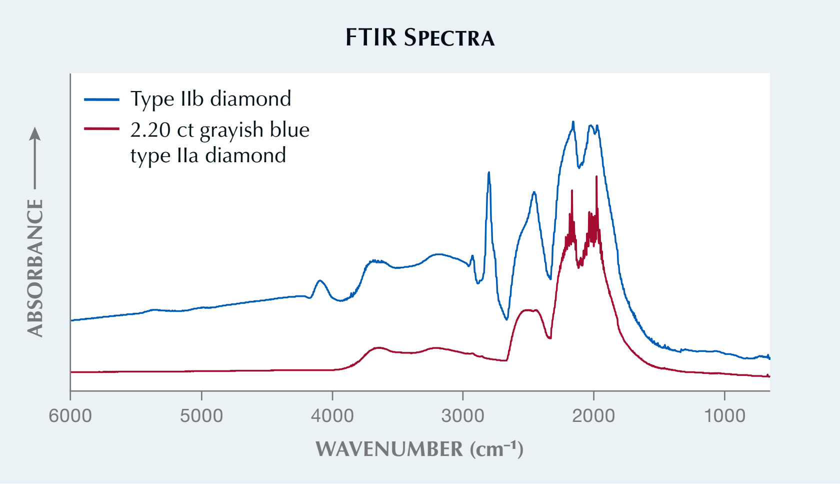

Based on these cloud inclusions, the diamond was given a final color

Editors' note: All items were written by staff members of GIA laboratories.

GEMS & GEMOLOGY, Vol. 60, No. 1, pp. 58–72.

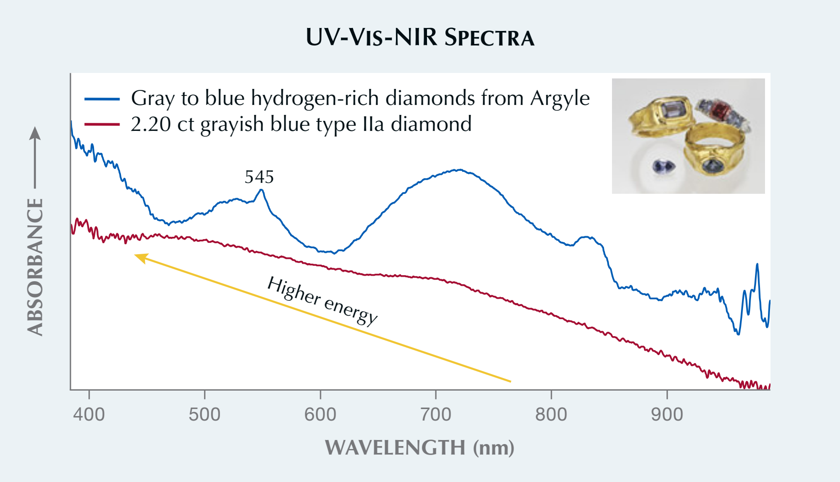

Figure 3. The UV-Vis-NIR spectrum of the 2.20 ct grayish blue diamond compared to a UV-Vis-NIR spectrum with typical hydrogen absorbance (notably at ~545 nm) and broad bands at ~700–800 nm, causing the desirable violet to blue colors. The inset shows typical colors associated with this absorbance spectrum. The red trace is also inconsistent with type IIb absorption. With a slight rise to higher energy, a yellow color is expected. Spectra are offset vertically for clarity.

Figure 4. Fine milky cloud inclusions are responsible for the natural blue color of the type IIa diamond, shown in darkfield illumination.

grade of Fancy Light grayish blue, a natural origin of color, and an I_3 clarity grade.

Paul Johnson

Natural Orange Diamond with Unusual Absorption Features

Orange is a very desirable color for diamond in the gem trade. GIA's New York laboratory received two type Ia (nitrogen-bearing) orange diamonds for colored diamond grading service, one 0.16 ct Fancy Vivid orange and the other 0.23 ct Fancy Intense orange (figure 5). Both diamonds showed orange fluorescence to long-wave and short-wave UV, along with few inclusions (clarity grades of VS_2 and VVS_1, respectively) and strong color zoning related to crystal growth (figure 6).

This diamond hue is often caused by a broad-band absorption at 480 nm. While the 480 nm band was observed in both diamonds, it was supplemented by the presence of a 525 nm peak and the 550 nm band along with a series of absorption features from ~700 to 780 nm with pronounced peaks at 735, 753, and 769 nm (figure 7). The 830 nm photoluminescence (PL) spectra showed very strong nickel peaks at 883/884 nm, in addition to numerous other PL features (A.M. Zaitsev, *Optical Properties of Diamond: A Data Handbook*, Springer-Verlag, Berlin, 2001). Thus, the 480 nm band was not the exclusive cause of color. The 550 nm band is the most common cause of color in natural pink diamond but, when present with other color centers, can contribute to many different bodycolors.

The optical defects in these orange diamonds differed from those in diamonds exclusively colored by the 480 nm band (M.Y. Lai et al., "Spectroscopic characterization of diamonds colored by the 480 nm absorption band," *Diamond and Related Materials*, Vol.

Figure 5. A 0.16 ct Fancy Vivid orange pear (left) and 0.23 ct Fancy Intense orange pear (right).

Figure 6. Fancy Vivid orange color distribution with strong zoning related to crystal growth.

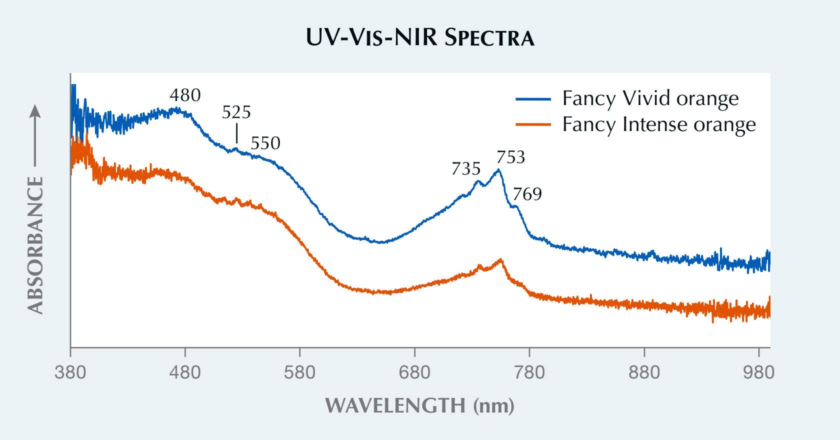

Figure 7. Ultraviolet/visible/near-infrared spectra of the Fancy Vivid orange and Fancy Intense orange diamonds are shown with several peaks and bands that combine to create these very rare colors. Spectra are offset vertically for clarity.

142, 2024, p. 110825). The combination of an unusual absorption band in the near infrared with the 480 and 550 nm absorption bands creates a transmission window that produces the rich, warm orange hue, devoid of any secondary modifying color. This appears to be a newly identified cause of orange color in diamonds.

A'Dhi Lall, Sally Ruan, and Paul Johnson

Dual-Color Double Chatoyancy in EMERALD

GIA's Tokyo laboratory recently received for origin service a ring with an emerald displaying dual-color double chatoyancy (figure 8). One band showed white chatoyancy, while the other exhibited greenish chatoyancy similar to the bodycolor. The emerald had an oval double-cabochon shape with a polished crown and pavilion and contained parallel tubes slightly oblique to the polished pavilion, resulting in semitransparency. The dual-color double chatoyancy was caused by the same mechanism identified in dual-color star corundum and quartz by Schmetzer et al. ("Dual-color double stars in ruby, sapphire, and quartz: Cause and historical account," Summer 2015 *G&G*, pp. 112–143). The white chatoyancy was caused by the linear reflection of the parallel tube inclusions from the upper cabochon surface. The greenish chatoyancy was caused by the linear reflection of the polished curved base through the interior of the stone to the surface (figure 9). Double chatoyancy is occasionally observed, but it is rare to find a very clear example of dual-color double chatoyancy.

Kazuko Saruwatari

Figure 8. The emerald in this ring displays dual-color light green and white double chatoyancy. The stone measures 8.39 × 5.71 × 4.22 mm.

Figure 9. Side view of the emerald ring. Parallel tube inclusions are oblique to the pavilion. The white reflection on the right is caused by the inclusions near the surface of the curved cabochon, while the greenish reflection on the left is caused by the reflection off of the bottom face of the cabochon.

Electroformed GOLD Bracelet

GIA has provided a service for validating mounted gemstones in jewelry for decades. Recently, these services have been expanded to include precious metal items (rings, necklaces, and bracelets) to ensure their authenticity and ensure the metal is as stated. The service is intended to protect both buyer and seller.

As part of this service, a gold bracelet measuring 8 inches in circumference and 1.25 inches wide and weighing 41 g was recently examined in the Carlsbad laboratory (figure 10). It was submitted as 14K solid gold, but initial observations raised suspicion. The bracelet felt too light and almost hollow, and there was a significant contrast in textures: a matte finish on the inside surface of the bracelet compared with the wavy, shiny exterior

Figure 10. The electroformed gold bracelet submitted as 14K solid gold.

Figure 11. The hallmark is not actually stamped onto the metal but is on a separate disk adhered to the inside of the bracelet.

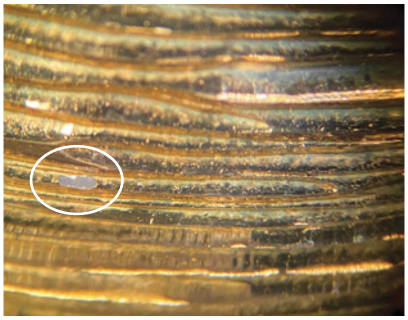

Figure 12. An area where the gold plating has flaked off from the bracelet is shown in the circled region.

surface. The bracelet had a 14K hallmark, which appeared to be stamped or engraved onto a different metal piece that was glued or otherwise adhered to the bracelet (figure 11).

X-ray fluorescence (XRF) analysis of the shiny exterior surface gave a result of 17.99K gold, and no subsurface material was detected that would indicate plating. Additional testing of another smooth surface yielded a result of 22.47K. Further analysis under brighter lighting conditions revealed areas where gold plating had flaked off from the piece (figure 12). We believe this wavy texture of the gold was used intentionally to hide the poor quality of the finish and the flaking gold plating, as shadows can often mask imperfections on initial sight.

A wax or resin material was observed under the plating, and we concluded that the bracelet had been created using electrodeposition to electroform the piece. Electroforming is a method of adding a thick gold plating, sometimes as thick as 200 microns, to a wax, resin, ceramic, or organic material base. Thick plating and electroforming may not be detected by XRF methods alone, and additional testing may be necessary to detect the application of these processes. We believe this wax- or resin-filled electroformed bracelet was being sold as solid 14K gold with the intention to deceive the buyer. This example demonstrates the importance of testing and verification services such as GIA's jewelry verification service.

Carlos Bautista and Paul Johnson

LABORATORY-GROWN DIAMONDS

CVD with "Ancient Text" Clouds

The Surat lab received a 1.67 ct D-color pear shape submitted for laboratory-grown diamond service. Spectroscopy and fluorescence imaging confirmed this was a diamond grown by chemical vapor deposition (CVD) that had undergone post-growth high-pressure, high-temperature (HPHT) annealing. This CVD diamond with SI_1 clarity displayed an interesting cloud feature that resembled lines of text in an ancient manuscript (figure 13).

The "lines" of clouds—a feature never before seen by the authors—were oriented approximately 45° to the growth interface seen with DiamondView imaging (figure 14). Examination of the fluorescence images (including those collected with selective-wavelength filters) revealed that the cloud features did not coincide with dislocation bundles, and striations were not observed. Photoluminescence mapping with 532 nm excitation showed high concentrations of the silicon vacancy (SiV^-) defect at 737 nm but did not indicate any spatial features corresponding to the clouds. Infrared absorption spectroscopy indicated a type IIb diamond with very low concentrations of uncompensated boron.

This diamond was noteworthy for its unusual and visually appealing clarity characteristic. Additionally, the dichotomy of a thoroughly modern diamond with a cloud feature that evoked an ancient text provided an interesting submission.

Sally Eaton-Magaña, Manisha Bhoir, and Girish Dodiya

Figure 13. The pavilion of this 1.67 ct pear-shaped CVD-grown diamond displayed an interesting feature with numerous cloud features resembling lines of text. Field of view ~2 mm.

Figure 14. A DiamondView image of the pavilion shows the region containing the cloud characteristic. While this image reveals the growth interfaces and the coloration confirms HPHT annealing, it does not show features corresponding to the cloud.

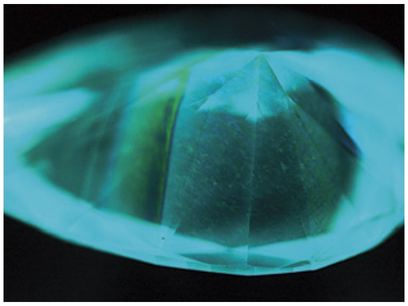

Figure 15. This 15.73 ct G-color CVD-grown diamond showed indications of HPHT treatment.

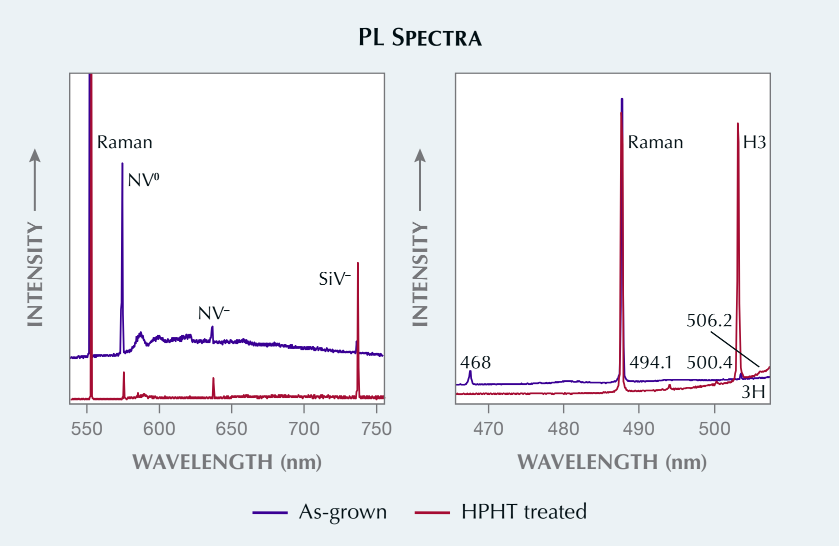

Figure 17. PL spectra collected on the CVD-grown diamond in January 2022 and recently with 514 nm (left) and 457 nm (right) excitation. Diamond Raman lines are scaled as equal, and spectra are offset vertically for clarity.

Large CVD-Grown Diamond Resubmitted after HPHT Treatment

In January 2022, the record holder for largest diamond grown by chemical vapor deposition (CVD) was a 16.41 ct square modified brilliant with G color and VVS$_2$ clarity that showed no indications of post-growth treatment (Spring 2022 Lab Notes, pp. 54–56). Recently, this diamond was resubmitted to the Carlsbad laboratory with a weight of 15.73 ct (figure 15). Standard data collection indicated that since the original submission, the stone had undergone high-pressure, high-temperature (HPHT) treatment. Consequently, this provided a case study showing the spectral and fluorescence differences between the as-grown and HPHT-treated versions. The color and clarity grades remained unchanged.

Although HPHT processing of CVD-grown diamonds is often performed to improve the color grade by reducing brown coloration (S. Eaton-Magaña and J.E. Shigley, "Observations on CVD-grown synthetic diamonds: A review," Fall 2016 *G&G*, pp. 222–245), the diamond displayed no observable color improvement. It is also likely that the HPHT treatment created frosting of the facets that required repolishing, which could partially account for the 0.68 ct weight loss.

Figure 16. DiamondView fluorescence images collected on the originally submitted CVD-grown diamond (left, from Spring 2022 Lab Notes) exhibited no evidence of post-growth treatment, while the recent submission (right) showed signs of HPHT treatment.

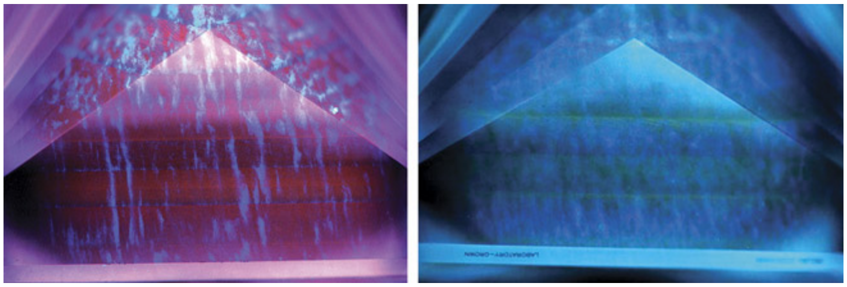

DiamondView fluorescence imaging showed pronounced differences between the as-grown and treated stages (figure 16). This color change in fluorescence imaging is often seen in HPHT-treated CVD-grown diamonds due to the reduction of nitrogen vacancy (NV) centers (NV^0 with zero-phonon line [ZPL] at 575 nm and NV^- at 637 nm) and an increase in H3 (NVN^0; ZPL at 503.2 nm). The changes in the defect concentrations leading to the differences in the fluorescence colors were also evident in photoluminescence (PL) spectroscopy collected at liquid nitrogen temperature. Figure 17 shows the PL results with 514 and 457 nm excitation for the 16.41 and 15.73 ct stages of the diamond.

With HPHT treatment, there was a decrease in the NV centers and an increase in the silicon vacancy (SiV^-) center at 737 nm in the 514 nm PL spectrum. In the 457 nm PL spectrum, the 468 nm peak and 3H peak (ZPL at 503.5 nm) were no longer detected, while features developed at 494.1, 500.4, and 506.2 nm along with the H3 peak at 503.2 nm.

As expected with a treated CVD-grown diamond, there were no major changes in many of the growth features. The cathodoluminescence images in figure 18 show no observable

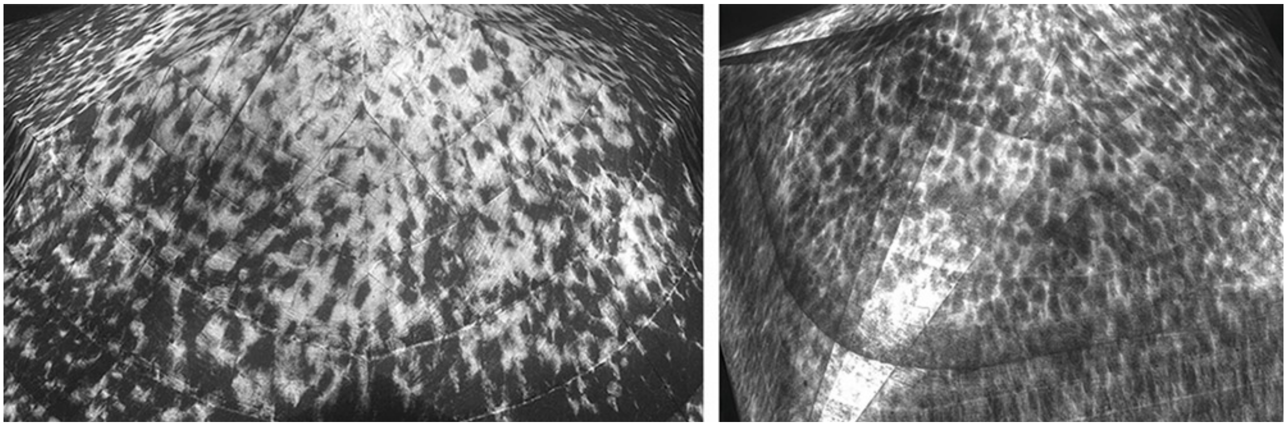

Figure 18. Comparison of the cathodoluminescence images from before HPHT treatment (left, from Spring 2022 Lab Notes) and afterward (right) showed no observable differences.

differences; the black dots are associated with lattice dislocations. The seven growth interfaces seen in figures 16 and 18 appear unmodified.

This stone allowed for an interesting comparison of a CVD-grown diamond before and after commercial HPHT treatment.

Sally Eaton-Magaña and
Elina Myagkaya

PEARLS

Large Freshwater Cultured Pearls with Atypical Bead Nuclei

Freshwater cultured pearls are known for their wide range of attractive colors, including different combinations of white, orange, pink, and purple hues. In the past decade, round or near-round freshwater bead cultured pearls of large size, commonly called "Edison" pearls in the trade, have gained popularity (Summer 2015 Lab Notes, pp. 179–181; C. Zhou et al., "Detection of color treatment and optical brightening in Chinese freshwater 'Edison' pearls," Summer 2021 *G&G*, pp. 124–134). Recently, two necklaces consisting of large pearls of mostly orangy pink to purplish pink colors (figure 19), ranging in size from 15.40 to 17.42 × 16.70 mm and from 18.00 to 19.96 × 19.06 mm, were submitted to GIA's New York laboratory. The strands caught our attention for their size and intense colors, as well as the growth features found inside these pearls.

Real-time X-ray microradiography (RTX) revealed that all the pearls were bead cultured—but not with the shell bead nuclei typically used for cultured pearls. Instead, a more X-ray transparent material with a distinct outline and near-round shape was found inside them (figure 20). The material appeared porous and nonuniform and did not resemble the "mud-like" material found in "soufflé" freshwater cultured pearls previously studied (Spring 2010 Gem News International, pp. 61–63). However, the exact nature of this material could not be determined.

Figure 19. These two necklaces consisting of large freshwater cultured pearls displayed strong hues with orient. Courtesy of Yvel.

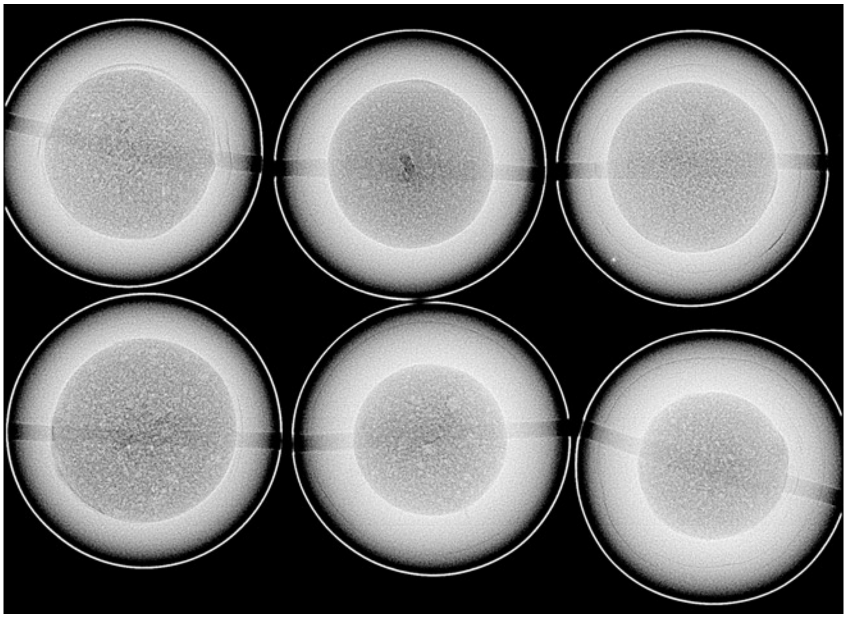

Figure 20. RTX analysis revealed the near-round atypical bead nucleus used to culture each of the pearls.

Energy-dispersive X-ray fluorescence analysis of their trace elemental concentrations (such as manganese and strontium) confirmed that the pearls were grown in a freshwater environment. Furthermore, Raman spectroscopy using 514 nm laser excitation indicated that their colors were natural, with two strong peaks around 1125 and 1510 cm^{-1} associated with natural polyenic pigment.

Cultured freshwater pearls with large size, near-round shape, and intense coloration are highly sought after and more valuable than traditional freshwater cultured pearls. These large freshwater cultured pearls are especially noteworthy because of the unique bead nuclei used during the culturing process, which suggests that culturing techniques are continuously evolving, resulting in higher-quality products.

Chunhui Zhou, Emiko Yazawa, and Madelyn Dragone

Figure 21. This 8.03 ct brown oval imitation pearl resembled a pen pearl at first glance.

Iridescent Imitation Pearl

An unusual brown oval specimen weighing 8.03 ct was recently submitted to GIA's Bangkok laboratory for pearl identification. At first sight, the material resembled a pen pearl due to its dark color and non-nacreous appearance (figure 21). Upon closer inspection, however, it lacked the cellular structure characteristic of such pearls (N. Sturman et al., "Observations on pearls reportedly from the Pinnidae family (pen pearls)," Fall 2014 *G&G*, pp. 202–215). It instead displayed a wispy, fibrous-like pattern and mosaic patches of iridescence, resembling a lava cave sheathed in spiderwebs (figure 22, left). Under fiber-optic illumination, the iridescence phenomenon was visible within the body and varied

Figure 22. Left: The material exhibited iridescent patches in its wispy, fibrous-like structure, resembling a lava cave covered in spiderwebs. Right: The iridescence phenomenon changed as the angle of view shifted under fiber-optic illumination. Fields of view 3.60 mm (left) and 1.88 mm (right).

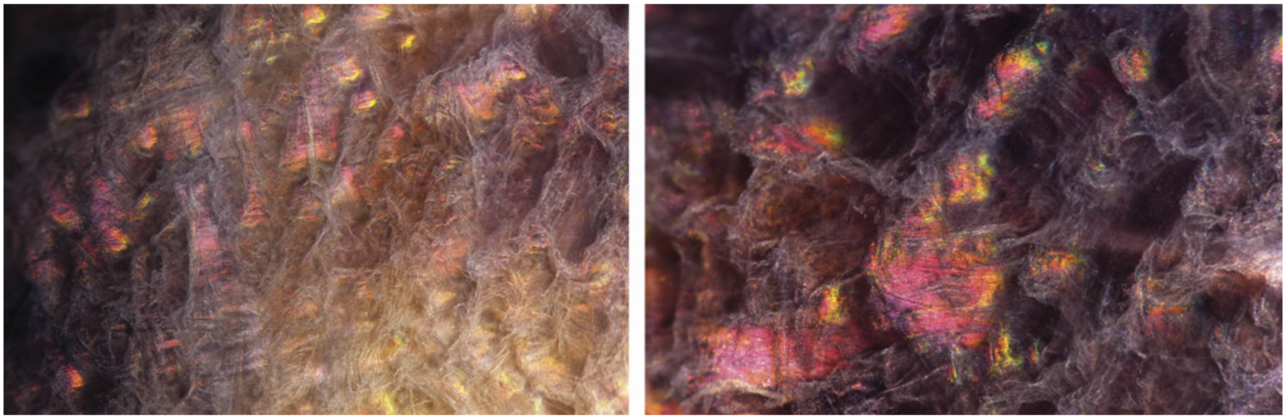

as the item was moved and turned in the light (figure 22, right).

Observed externally were both a banding feature (commonly found in shell-related materials) and numerous lines across the base indicating it had been worked and altered from its original form. Real-time X-ray microradiography also revealed a distinct banded internal growth structure and parasite tubes. Raman spectroscopy identified this imitation pearl as calcite, and its bodycolor was likely treated. All this evidence, combined with energy-dispersive X-ray fluorescence analysis, indicated that the material was not a whole pearl but likely fashioned from the shell of a marine organism.

Although GIA has encountered a variety of imitation materials, this is the most fascinating specimen seen by the author.

Ravenya Atchalak

Irradiated and Dyed Akoya Pearls

Since the 1960s, irradiation has been a known treatment for modifying the color of freshwater cultured pearls (Developments and Highlights at the Gem Trade Lab in Los Angeles, Spring 1967 *G&G*, pp. 153–154). It was found that freshwater shells and pearls contained higher amounts of manganese, which could be oxidized by irradiation to produce a darkened color (T. Tsujii, "The change of pearl colors by the irradiation with γ-ray or neutron ray," *Journal of Radiation Research*, Vol. 4, No. 2-4, 1963, pp. 120–125). While saltwater pearls contain much less manganese than freshwater pearls, cultured saltwater akoya pearls could also be treated with irradiation. During treatment, the freshwater shell bead nuclei inside these cultured pearls would turn darker and cause the surface color, luster, and overtone to change (Winter 1988 Gem Trade Lab Notes, p. 244).

Recently, GIA's New York laboratory obtained two groups of reportedly irradiated akoya pearls from two different vendors. These samples were either drilled or partially drilled, ranging from 3.82 mm to 8.15 mm in diameter and from 0.29 to 3.58 ct in weight (figure 23). They exhibited a variety of light to dark-toned gray with bluish and greenish bodycolors, with variously colored overtones.

Figure 23. The two groups of reportedly irradiated akoya pearls used in this study.

Real-time X-ray microradiography and energy-dispersive X-ray fluorescence confirmed that these were bead cultured pearls grown in a saltwater environment. No silver content was detected on any of the surfaces, suggesting that the colors of these pearls had not been modified by silver nitrate treatment. Upon microscopic examination, however, some of the samples displayed obvious color concentrations at their drill holes or unnatural patchy surface color distributions, while also revealing a darkened bead nucleus inside. On the other hand, some light-colored pearls did not possess color concentrations at the drill hole and only contained a darkened bead nucleus (figure 24).

To further investigate the color origin, we cut several samples as well as a typical white akoya cultured pearl to compare their internal appearances (figure 25). The results confirmed that the reportedly irradiated pearls contained darkened bead nuclei showing brownish stripes rather than the usual white bead nucleus found in a white akoya pearl, indicative of irradiation treatment (Winter 1988 Gem Trade Lab Notes, p. 244). In addition, some samples exhibited a distinctly different color appearance at the nacre and drill-hole areas, indicating dye treatment.

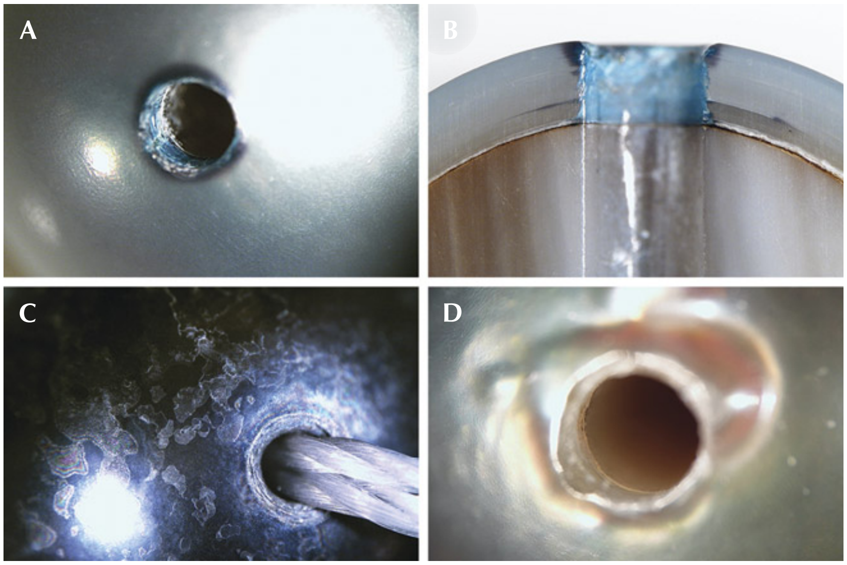

Figure 24. Images showing obvious color concentrations at the drill holes of some samples with darkened bead nuclei (A and B), an unnatural dark patchy surface (C), and a darkened bead nucleus without color concentration (D). Fields of view 4.79 mm (A and C) and 3.57 mm (B and D).

Short-wave UV fluorescence spectroscopy confirmed that the akoya pearls may have been treated by any number of processes (C. Zhou et al., "Detection of color treatment and optical brightening in Chinese freshwater 'Edison' pearls," Summer 2021 *G&G*, pp. 124–134), based on low fluorescence counts at around 320–360 nm. Raman spectroscopic analyses using 514 nm laser excitation revealed aragonite as the main component. Some treated pearls exhibited a series of unusual Raman shift peaks between 560 and 3200 cm^{-1} on the nacre (probably due to dye materials) but not on the darkened shell bead nucleus, suggesting two forms of treatment: dyeing and irradiation (figure 26).

Figure 25. Left to right: Cross sections of an irradiated akoya pearl, a white akoya pearl, and an irradiated and dyed akoya pearl. Field of view 14.52 mm.

Figure 26. Raman spectra of one sample's surface nacre, nacre on the cross section, and bead nucleus, along with the surface nacre of a white akoya pearl for comparison. Unusual peaks were found in both nacre areas but not on the bead nucleus. Also shown are typical aragonite features at 702, 704, and 1086 cm^{-1}.

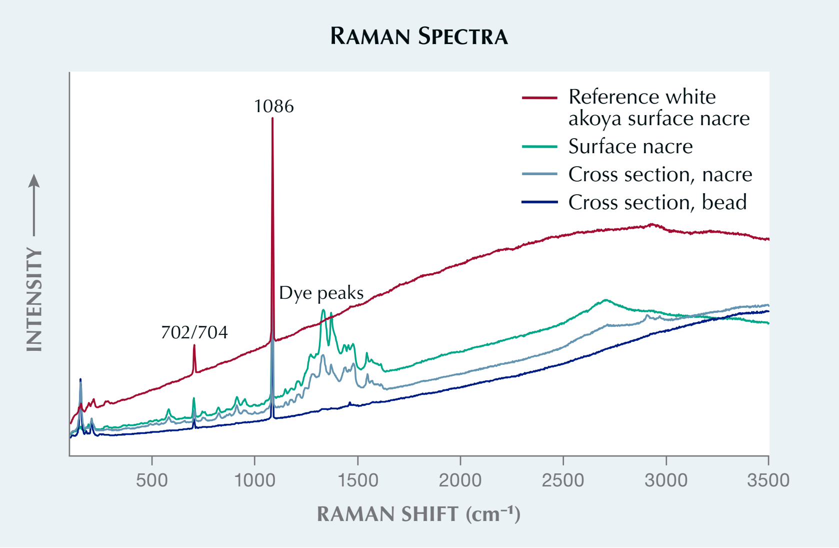

Naturally colored gray pearls are usually light in color and tend to show uneven color distribution, making them difficult to match. Some grayish akoya pearls on the market have been treated to imitate these natural colors, since they command higher prices. While dye treatments are more easily detected by unnatural bodycolors, obvious color concentrations, and advanced testing, irradiation treatment is harder to detect since the nacre is not affected and the difference in bodycolor is subtle. Careful visual observation is necessary. The combination of irradiation and dye treatments in some of these treated pearls is not commonly encountered in our laboratory.

Emiko Yazawa and Chunhui Zhou

"Lily Pad" Structure in an Orangy Yellow Pearl

GIA's Mumbai laboratory recently received for identification an orangy yellow semi-baroque pearl weighing 4.14 ct and measuring 9.51 × 8.43 × 7.51 mm (figure 27). Externally, the pearl had a distinct indentation on its

Figure 27. The orangy yellow pearl weighing 4.14 ct and measuring 9.51 × 8.43 × 7.51 mm.

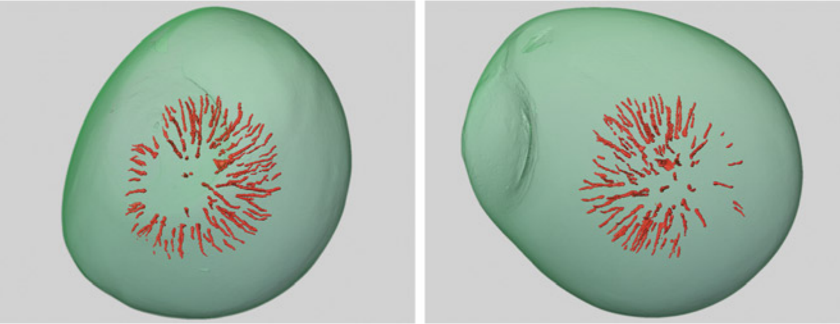

Figure 29. The 3D models generated using μ-CT scans show the acicular feature in red resembling a lily pad with a small core at the center, while the green area represents the pearl's growth structure.

top portion and possessed a medium surface luster. Observation of the surface under 40× magnification showed typical fine overlapping platelets of aragonite.

Energy-dispersive X-ray fluorescence revealed a manganese level below detection limits and a strontium level of 1226 ppm. When exposed to X-ray fluorescence, the pearl showed an inert reaction. Both results confirmed the pearl's saltwater origin. Under long-wave ultraviolet light, it exhibited a yellowish green reaction. Raman analysis using a 514 nm laser excitation revealed a doublet at 701 and 704 cm^{-1} and a peak at 1085 cm^{-1}, indicating the presence of aragonite. Photoluminescence spectra revealed two strong broad peaks at 620 and 650 nm as well as one weak peak at 680 nm, confirming the pearl's natural color origin.

Upon further testing using real-time X-ray microradiography (RTX), the pearl displayed an unusual acicular feature resembling the shape of a lily pad, with tiny flame-like structures radiating from the center. This feature was intersected by several growth arcs (figure 28A). X-ray computed microtomography (μ-CT) provided a more detailed view, revealing a distinct small void at the center. Surprisingly, the acicular "lily pad" feature observed in the RTX images appeared as numerous elongated, spiky structures with very fine lines cutting through the shape (figure 28, B and C).

To further study this feature, three-dimensional models were created using specialized software to render the μ-CT scan images (C. Zhou et al., "New 3-D software expands GIA's pearl identification capabilities," *GIA Research News*, May 13, 2016). In both the μ-CT scan images and the 3D models shown in figure 29, it was evident that this unique feature was confined to the central part of the pearl and did not extend to the outer nacre layers. Notably, the lily pad feature had elongated spikes that were thicker at one end and gradually tapered as they radiated outward from the center.

Gemological laboratories do encounter pearls with internal structures that are very difficult to positively identify. Due to the lack of conclusive evidence proving it was a cultured pearl combined with the presence of a rare and distinctive nat-

Figure 28. A: RTX image revealing a unique acicular "lily pad" feature with tiny flame-like structures. B: μ-CT scan displaying a small central core with elongated spiky features. C: A magnified μ-CT scan showing the spiky features surrounded by prominent growth arcs.

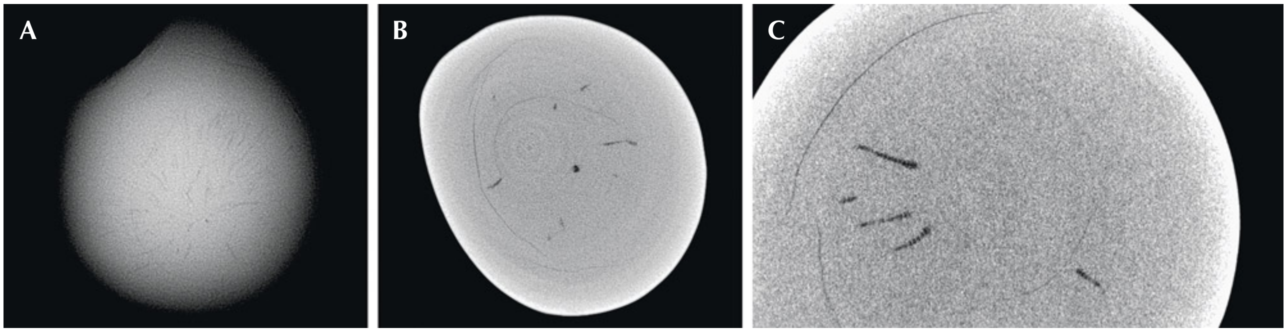

ural structure, this pearl was considered noteworthy. Such intriguing natural growth structures can be influenced by several factors, including environmental conditions, the health of the mollusk during formation, and other external causes impacting the pearl formation process. The precise mechanism of natural pearl formation continues to be widely debated, and encountering such pearl samples causes us to further contemplate the creation of these exquisite gems.

Anukul Belanke, Roxane Bhot Jain, Emiko Yazawa, and Abeer Al-Alawi

Figure 30. A freshwater shell blister weighing 40.91 ct and measuring 22.79 × 20.59 × 13.21 mm.

Vaterite in Freshwater Natural Shell Blister

A cream-colored baroque-shaped shell blister with a light orange base, weighing 40.91 ct and measuring 22.79 × 20.59 × 13.21 mm, was recently submitted to GIA's Mumbai laboratory for identification (figure 30). Externally, the large shell blister had a botryoidal arrangement with deep grooves. Viewed under 40× magnification, its high-luster surface displayed a typical nacreous structure of overlapping aragonite platelets. The base of the shell blister was sawn and polished, revealing concentric arcs and numerous polishing lines. Real-time X-ray microradiography (RTX) and X-ray computed microtomography (μ-CT) showed a distinct pattern of concentric growth arcs that terminated at the base. This was accompanied by an array of fine lines opposite the direction of the growth arcs forming grooves within the pearl (figure 31, A and B).

X-ray fluorescence (XRF) revealed a strong yellowish green reaction, indicative of its freshwater origin, with a small patch of reddish orange fluorescence observed at one end (figure 31C). Reddish orange fluorescence has been associated with vaterite in freshwater pearls (U. Wehrmeister et al., "Vaterite in freshwater cultured pearls from China and Japan," *Journal of Gemmology*, Vol. 30, No. 7/8, 2007, pp. 399–412). Further chemical analysis using energy-dispersive X-ray fluorescence spectrometry was conducted on multiple spots. The yellowish green area yielded manganese levels ranging from 261 to 504 ppm and a strontium level of 413 to 452 ppm, while the reddish orange spot had a manganese level of 323 ppm and a strontium level of 415 ppm. Raman spectroscopy using 514 nm laser excitation on multiple surface spots revealed a combination of two calcium carbonate ($CaCO_3$) polymorphs: aragonite and vaterite. The spot with reddish orange fluorescence had vaterite peaks at 752, 1075, and 1090 cm^{-1}; the areas with a yellowish green fluorescence showed peaks at 701, 704, and

Figure 31. A: RTX image showing banded structures. B: μ-CT image revealing arcs. C: X-ray fluorescence shows yellowish green fluorescence along with the reddish orange spot, indicating the presence of vaterite.

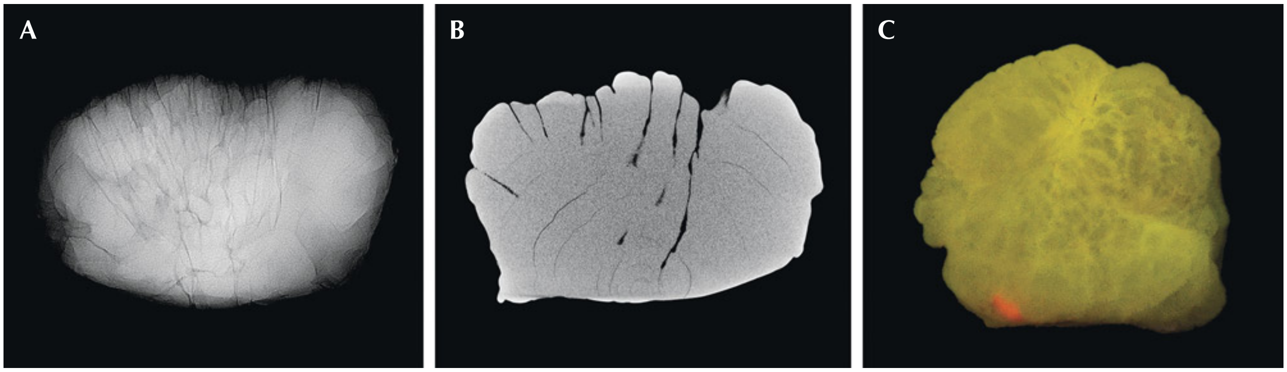

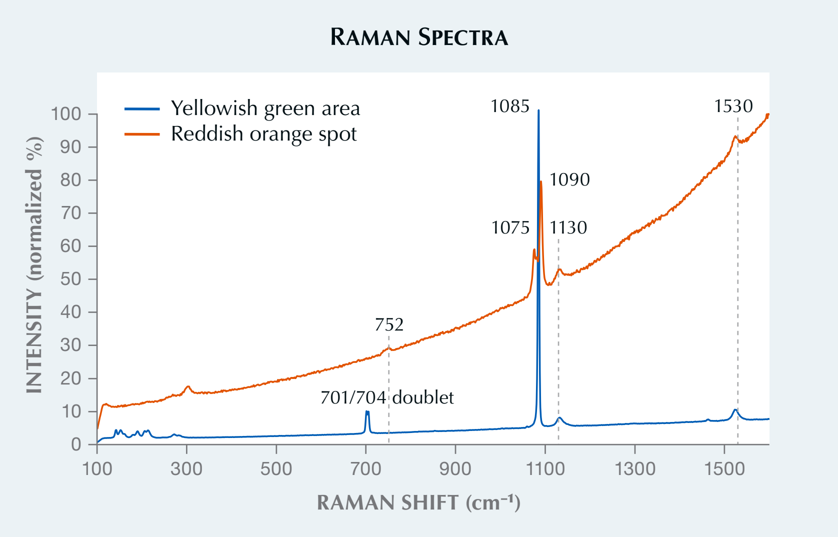

Figure 32. Raman analysis of shell blister spots fluorescing yellowish green and reddish orange under XRF revealed the presence of aragonite and vaterite peaks, respectively.

1085 cm^{-1}, indicative of aragonite, along with polyenic pigment peaks at 1130 and 1530 cm^{-1} (figure 32). The photoluminescence spectra were consistent with the Raman and displayed strong fluorescence.

The presence of vaterite in association with aragonite in freshwater pearls has been extensively researched and recorded both in natural and cultured pearls. These minerals have also been occasionally documented in mollusk shells. It is therefore interesting to see such dual mineral phases in shell blisters as well. While it has often been speculated that vaterite serves as a precursor to aragonite during biomineralization, the presence of this mineral on the periphery suggests simultaneous formation within the shell blister (A.L. Soldati et al., "Structural characterization and chemical composition of aragonite and vaterite in freshwater cultured pearls," *Mineralogical Magazine*, Vol. 72, No. 2, 2008, pp. 579–592). In certain cases, the presence of vaterite can be very difficult to detect through XRF analysis, especially when located within or around the core of the pearl. However, vaterite is more visible when the pearl is cut (Summer 2021 Gem News International, pp. 171–174).

Distinguishing between a natural blister pearl and a natural shell blister can be very challenging for laboratories due to the subtle variations in the definitions of these terms. Although such identifications are always debatable, the examined item was identified as a natural freshwater shell blister based mainly on its structural composition, external appearance, and distinct worked base, in addition to its notably large size.

Pfokreni Nipuni, Abeer Al-Alawi, and Nishka Vaz

Pearls from the Placunidae Family (Windowpane Oysters)

Nacreous pearls are commonly constructed from layers of stacked aragonite platelets. In recent years, however, GIA laboratories in Bangkok, Hong Kong, Mumbai, and New York have reported unusual pearls with a "nacreous-looking" surface caused by the presence of calcite instead of aragonite (figure 33) (Winter 2022 Lab Notes, pp. 477–478). These findings piqued curiosity and prompted a more comprehensive study involving research samples and

Figure 33. Two loose pearls from windowpane oysters submitted to the Bangkok laboratory and a mixed strand containing mostly windowpane and Pteria *species pearls submitted to the New York laboratory.*

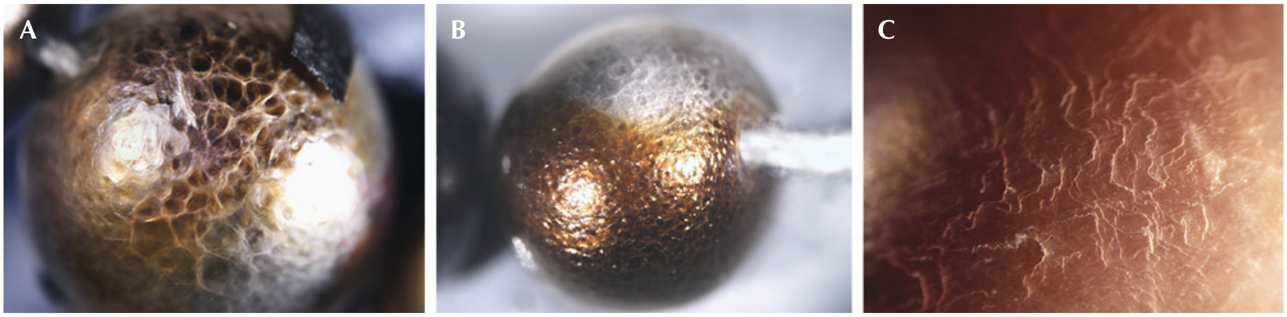

Figure 34. Characteristic surface features of mosaic pattern (A) and botryoidal structure (B) were observed on a pearl from the necklace in figure 33, compared to the typical nacreous-looking surface of fingerprint-like platy structure (C) on a loose pearl. Fields of view 7.19 mm, 9.61 mm, and 2.90 mm, respectively.

mollusk shells. The study indicated that these calcite "nacreous-looking" pearls were likely produced by mollusks belonging to the *Placuna* genus in the Placunidae family.

These marine bivalve mollusks, commonly known as "windowpane oysters," are found along the coasts of India, Malaysia, China, and the Philippines (C.M. Yonge, "Form and evolution in the Anomiacea (Mollusca: Bivalvia)-*Pododesmus*, *Anomia*, *Patro*, *Enigmonia* (Anomiidae): *Placunanomia*, *Placuna* (Placunidae, fam. Nov.)," *Philosophical Transactions of the Royal Society of London*, Vol. 276, No. 950, 1977, pp. 502–503). *Placuna* mollusks are widely valued for their thin, durable mica-like translucent flat shells, called *capiz* or *kapis* shells, which were once a popular alternative to glass and often used as windowpanes and decorations. Although the mollusks were also known to produce small pearls, these were not commercially available until recent decades (C.T. Achuthankutty et al., "Pearls of the windowpane oysters, *Placuna placenta*," *Mahasagar*, Vol. 12, No. 3, 1979, pp. 187–189).

The studied pearls were variously shaped, measuring 3 to 8 mm and weighing 1 to 3 ct. Their bodycolors ranged from silver to brown or gray, with varying degrees of tone and saturation. Viewed under 40× magnification, they exhibited diagnostic surface features of distinctive mosaic or cellular patterns, and some appeared similar to a botryoidal structure. While these features are unique and have not been observed in typical nacreous pearls, a few of the samples also showed overlapping platelets typically found in nacreous pearls (figure 34).

Under long-wave ultraviolet radiation, the pearls displayed a striking reddish fluorescence, particularly from the darker areas, which is comparable to the reactions observed on the windowpane oyster shells (figure 35). Similar reddish fluorescence has been observed in dark pearls from the *Pteria* species (L. Kiefert et al., "Cultured pearls from the Gulf of California, Mexico," Spring 2004 *G&G*, pp. 26–38; Winter 2014 Lab Notes, pp.

Figure 35. Three variously colored windowpane shells and a brown windowpane pearl, shown in daylight (left) and long-wave UV light (right). Shells courtesy of Robin Willis.

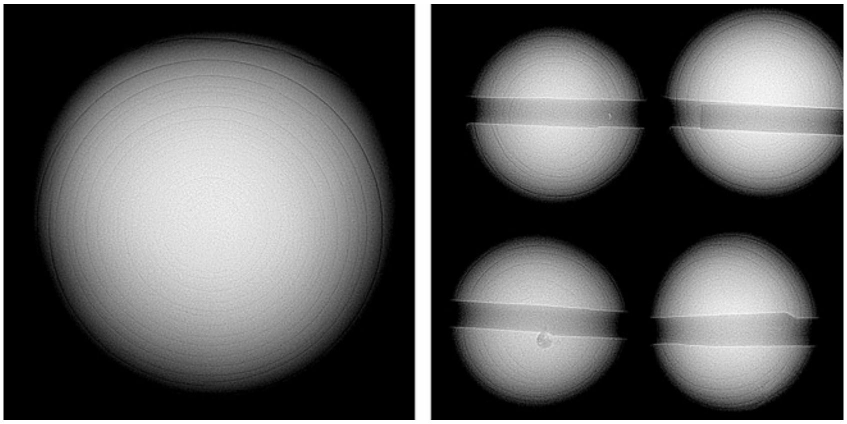

Figure 36. RTX images revealed concentric growth rings typical of the internal structure commonly observed in windowpane oyster pearls.

295–296). However, it is important to note that the composition of calcite in windowpane pearls and aragonite in *Pteria* species can be distinguished using Raman spectroscopy.

Ultraviolet/visible (UV-Vis) reflectance and photoluminescence (PL) spectra from a laser excitation at 514 nm collected on the darker areas unveiled features similar to those typically observed in natural dark nacre of *Pteria* species, as well as *Pinctada margaritifera* and *Pinctada maxima*. The UV-Vis spectra exhibited absorption features at 405 and 495 nm. The 405 nm feature is related to uroporphyrin, a type of pigment responsible for gray to black tones in some pearl oyster species (Y. Iwahashi and S. Akamatsu, "Porphyrin pigment in black-lip pearls and its application to pearl identification," *Fisheries Science*, Vol. 60, No. 1, 1994, pp. 69–71). All the samples showed bands at approximately 620, 650, and 680 nm in their PL spectra. These three PL bands have been commonly recorded in darker-colored pearls from the species mentioned above.

The saltwater origin was confirmed by energy-dispersive X-ray fluorescence spectrometry, which revealed very low or below detection limit manganese content and high levels of strontium ranging from 1000 to 1500 ppm.

Intriguingly, real-time X-ray microradiography (RTX) uncovered a distinct, evenly spaced fine concentric ring structure throughout most of the inner area of the pearls (figure 36). This structure was identified in most of the submitted pearls as well as the research samples studied. With these combined unique characteristic features, we were able to confidently conclude that the mollusks producing these pearls were from the Placunidae family. The first GIA Pearl Identification report for a pearl from this mollusk was issued in May 2023.

While most shelled mollusks have the potential to produce pearls, identifying the exact species remains a challenge, particularly with less commonly encountered species. Conducting continuous research studies with known samples from reliable sources is crucial and greatly assists in identification. As a continuation of this lab note, a comprehensive article featuring detailed studies will be prepared.

Joyce Wing Yan Ho,
Kwanreun Lawanwong, and
Artitaya Homkrajae

Exceptionally Rare TITANOHOLTITE

A first-time submission of a rare dumortierite supergroup member was recently examined at the Carlsbad laboratory. A 0.85 ct titanoholtite (figure 37) was identified after extensive testing. The stone was submitted as dumortierite, but its physical properties and chemistry did not support this. The dark orangy brown stone had a hydrostatic specific gravity of 3.65 and a refractive index of 1.720–1.740 (birefringence of 0.020). These properties stand in contrast to dumortierite, which usually forms as an inclusion rather than a single crystal and typically has a blue to violet color, a specific gravity of 3.21 to 3.41, and a refractive index of 1.659

Figure 37. A 0.85 ct oval modified brilliant titanoholtite. Although its bodycolor was dark orangy brown, a bluish haze was visible from certain angles due to light scattering off polish lines as well as internal colorless graining.

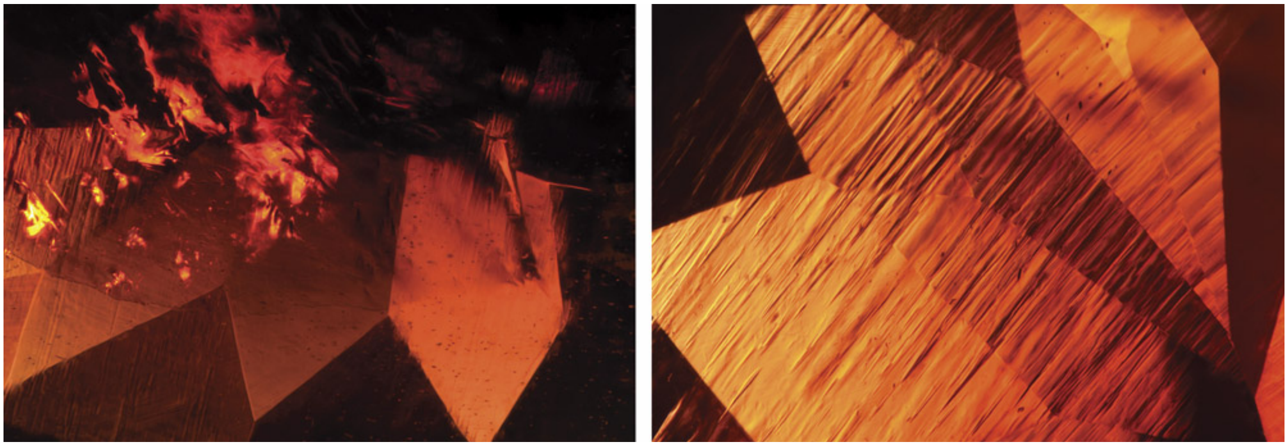

Figure 38. *Left: A clean and reflective surface-reaching fracture was seen under the table; field of view 3.57 mm. Right: Abundant transparent graining, scattered particles, and thin films were seen throughout the stone; field of view 2.34 mm.*

to 1.692 with a birefringence of 0.027.

A look into the stone offered a vibrant scene composed of a reflective surface-reaching fracture breaking the crown (figure 38, left) and an abundance of transparent graining throughout with small flecks of reflective thin films and unidentified particles (figure 38, right). Microscopic observation revealed a strong resemblance to garnet, but the material's doubly refractive nature was inconsistent with garnet. Raman spectroscopy results did not match any existing minerals within GIA's reference databases, but they did show some general similarities with dumortierite. Finally, laser ablation–inductively coupled plasma–mass spectrometry was performed on the stone for a full quantitative chemical analysis. Given the general similarities with dumortierite, the chemical data was fit to a dumortierite supergroup formula of $(Al_{0.35}Ti_{0.41\square0.24}Fe_{0.02})Al_6B(Si_{2.60}Sb_{0.32}Al_{0.07})O_{17.67}$. The dominant component in this formula is titanoholtite, $(Ti_{0.75\square0.25})Al_6BSi_3O_{18}$, with minor dumortierite, $Al_7BSi_3O_{18}$, and incorporation of significant antimony.

Titanoholtite is a recently discovered mineral within the holtite group and a member of the dumortierite supergroup. It was first published in 2013, when microscopic crystals were found in a Polish pegmatite (A. Pieczka et al., "The dumortierite supergroup. II. Three new minerals from the Szklary pegmatite, SW Poland: Nioboholtite, $(Nb_{0.6\square0.4})Al_6BSi_3O_{18}$, titanoholtite, $(Ti_{0.75}\square_{0.25})Al_6BSi_3O_{18}$, and szklaryite, $\square Al_6BAs^{3+}{}_3O_{15}$," *Mineralogical Magazine*, Vol. 77, No. 6, 2013, pp. 2841–2856). This stone submitted to GIA appears to be the first macroscopic titanoholtite specimen ever reported in the literature.

Britni LeCroy and Aaron Palke

PHOTO CREDITS
Jian Xin (Jae) Liao—1, 15, 33; 5; Robert Weldon—3 (inset); Paul Johnson—4; A'Dhi Lall—6; Momo Matsumura—8; Shunsuke Nagai—9; Rambod Bahadory—10–12; Raju Jain—13; Suvarna Gaikwad—14; Stephanie Persaud—16 (left); Elina Myagkaya—18; Sood Oil (Judy) Chia—19, 23; Ravenya Atchalak—21, 22; Emiko Yazawa—24, 25; Gaurav Bera—27, 30; Pfokreni Nipuni—31 (right); Joyce Wing Yan Ho—34 (A and B), 35 (top); Artitaya Homkrajae—34C; Kwanreun Lawanwong—35 (bottom); Adriana Robinson—37; Britni LeCroy—38

G&G

Micro-World

Editor: Nathan Renfro

Contributing Editors: John I. Koivula and Tyler Smith

Shrinkage Cracks in Fire Agate

Over the last few years, the author has encountered numerous examples of fire agate (a variety of quartz chalcedony) displaying a random weblike pattern, including a parcel of cabochons from Mexico purchased at the 2023 Tucson gem shows. Fire agates typically show a botryoidal structure reminiscent of a cluster of grapes, so this unusual pattern was quite noteworthy.

Microscopic examination of the cabochons revealed that the pattern was most likely the result of shrinkage cracks caused by desiccation. This drying out created a volume reduction that pulled apart the silica material during formation of the fire agate, producing a pattern of irregular separations that were later infilled by a secondary generation of chalcedony, which then preserved the pattern (figure 1). These shrinkage cracks stand out in high contrast to the host chalcedony as interruptions in the iridescent phenomenon that result from broken layers of goethite where shrinkage occurred. While not particularly common, shrinkage cracks in fire agate create a unique pattern in this colorful gem material.

Nathan Renfro
GIA, Carlsbad

About the banner: This goldstone glass contains numerous copper crystals that are responsible for the aventurescent phenomenon seen in this manufactured material. Photomicrograph by Nathan Renfro; field of view 2.18 mm.

Gems & Gemology, Vol. 60, No. 1, pp. 74–82.

Hairlike Inclusions in Benitoite

The authors recently examined a 3.55 ct benitoite that featured whitish hairlike inclusions throughout the stone (figure 2). The inclusions were too thin to be identified by Raman spectroscopy.

Gem-quality benitoite has been extracted from a single mine in California and is reported to occur with natrolite gangue in altered blueschist within serpentinite. Minerals found within benitoite include actinolite-tremolite, aegirine-augite, diopside, serandite pseudomorphs, neptunite, joaquinite, albite, apatite, and djurleite (B.M. Laurs et al.,

Figure 1. This fire agate from Mexico displays an interesting weblike network of shrinkage cracks that were likely the result of desiccation during formation. Photomicrograph by Nathan Renfro; field of view 4.11 mm.

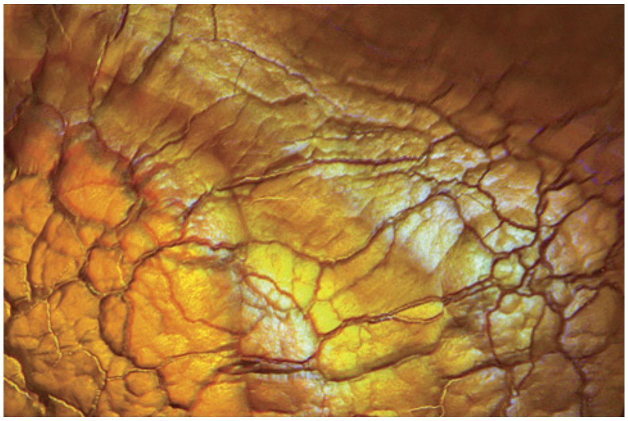

Figure 2. Whitish hairlike inclusions in a 3.55 ct faceted benitoite. Photomicrograph by Taku Okada; field of view 2.37 mm.

"Benitoite from the New Idria District, San Benito County, California," Fall 1997 *G&G*, pp. 166–187). Therefore, the hairlike inclusions in this stone could be natrolite, chrysotile (white asbestos), or tremolite, which have whitish colors and acicular or fibrous crystal habits.

Taku Okada and Yusuke Katsurada
GIA, Tokyo

Stellate Cloud in Diamond

Impurity clouds in diamonds occur in a variety of forms such as scattered, planar, or patchy clouds. The author recently observed one such cloud with an unusual morphology in a 1.51 ct natural diamond with E color and SI_2 clarity (figure 3). This remarkable cluster of pinpoints took the form of a four-point star. This celestial inclusion is sure to be seen as a lucky charm.

Figure 3. This patchy cloud with an uneven distribution of pinpoints observed in a natural diamond appears to depict a celestial star. The image was captured in monochrome. Photomicrograph by Tejas Jhaveri; field of view 2.9 mm.

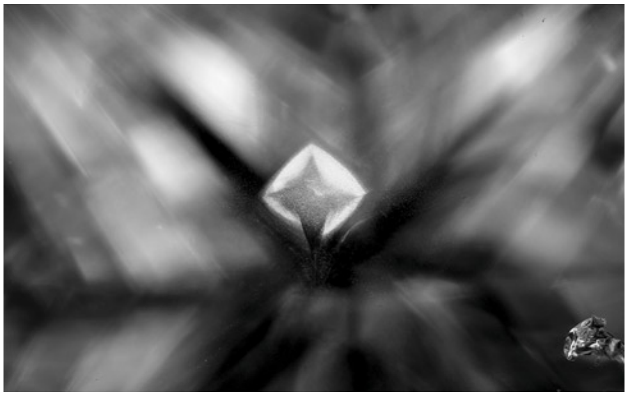

Tejas Jhaveri
GIA, Mumbai

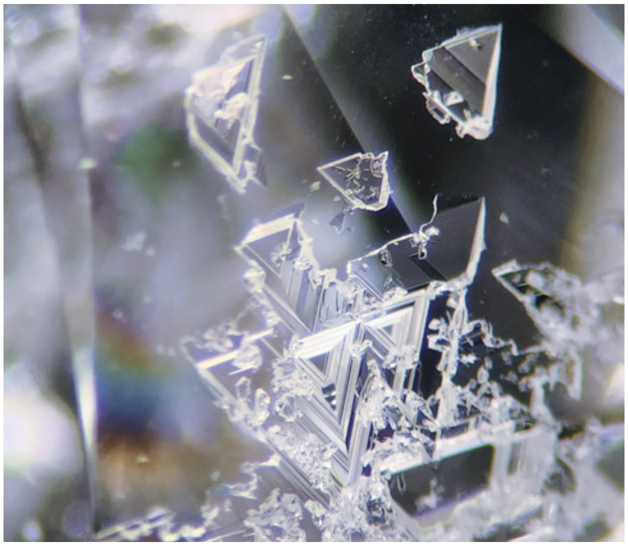

Figure 4. A collection of trigons on the pavilion surface of a round brilliant-cut diamond. Photomicrograph by Isabelle Corvin; field of view approximately 2.0 mm.

Trigon Party on a Diamond

Triangular-shaped markings known as trigons are common in natural diamond. These "birthmarks" formed during growth are signs of a diamond's ancient origin deep within the earth. The trigons in figure 4 form a striking cluster on the faceted girdle and extend into two of the lower girdle facets of a 1.01 ct natural diamond. Even through the cutting and polishing process, these trigons remained on the surface.

Although trigons are not exceedingly rare, the assortment of this many trigons grouped together provides a remarkable portrait created by Mother Nature. The perfection of a diamond is on full display in the angles, luster, and alignment of each trigon.

Isabelle Corvin
Olympia, Washington

Iridescent Healed Fissures in Epidote

The author recently examined a 4.18 ct yellowish brown cushion-cut epidote. Under fiber-optic illumination, the stone revealed iridescent healed fissures (figure 5). Healed fissures are not uncommon in various gemstones. They are believed to result from a secondary fluid that facilitated the

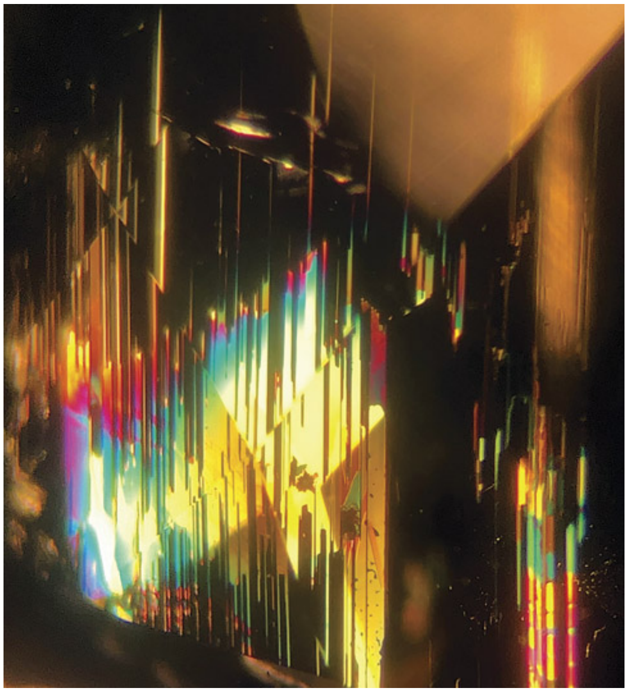

Figure 5. Iridescent healed fissures observed in a 4.18 ct faceted epidote. Photomicrograph by Tinh Xuan Nguyen; field of view 2.5 mm.

healing process of previously surface-reaching fractures. In the case of this epidote, the healed fissures resulted in a striking feature revealed when illuminated under the microscope.

Tinh Xuan Nguyen
PNJ Laboratory Company Limited
Ho Chi Minh City, Vietnam

Pink and Red Epidote in Quartz

We recently discovered very photogenic clusters of hot pink to red crystals as "firework" sprays (figure 6) in two transparent cabochons of rock crystal quartz. The cabochons weighed 5.47 ct and 11.18 ct and measured 15.85 × 9.87 × 5.92 mm and 16.06 × 11.49 × 7.83 mm, respectively (figure 7). These cabochons, which came from Sara Crystal in Shanghai, are thought to be from Chenzhou in China's Hunan Province.

After performing gemological testing and optical microscopy, we thought the inclusions might be piemontite based on their behavior in polarized light and the monoclinic morphology of the individual terminated crystals. Because some of the pink crystals reached the surface of their polished hosts, we decided to analyze them using Raman microanalysis. The result was a close match for epidote, which was surprising since epidote is normally thought of as a dark brownish green mineral.

The results of chemical analysis using laser ablation–inductively coupled plasma–mass spectrometry were consistent with epidote, but with one additional element present: manganese, which caused the pink to red color in these microcrystals. We concluded that the inclusions were indeed epidote instead of piemontite, but pink to red epidote was something completely new to us.

Searching the literature for piemontite and epidote uncovered the following statement from Mindat.org, which seemed to explain the existence of these pink to red epidotes:

> "Piemontite" has two different uses: Piemontite (sensu stricto) is the mineral species described here, but more commonly "piemontite" refers incorrectly to deep red colored, Mn^{3+}-bearing epidotes that are really varieties of the species epidote, and not strictly speaking piemontite. "Piemontites"

Figure 6. Bright pink to red epidote crystals as "firework" sprays were a surprising discovery in rock crystal quartz. Photomicrograph by Nathan Renfro; field of view 2.16 mm.

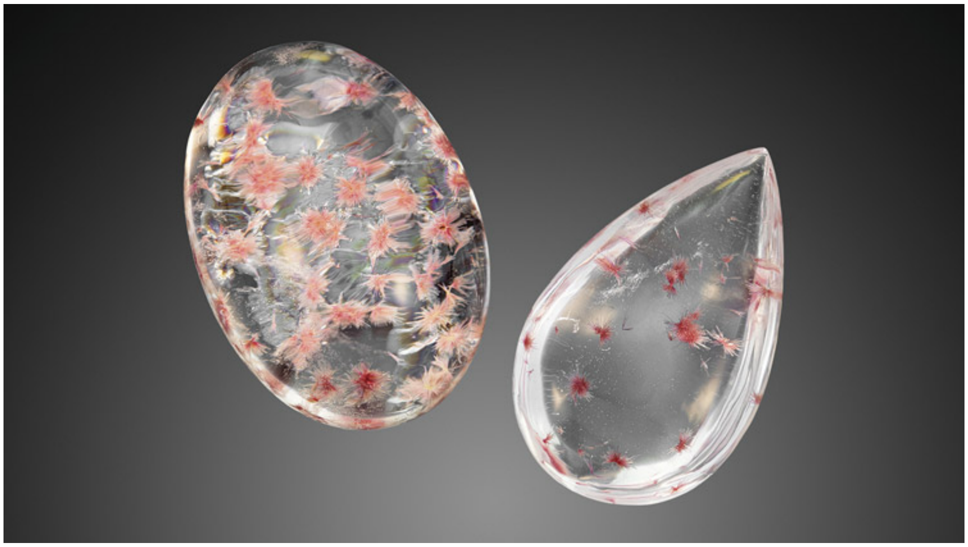

Figure 7. Weighing 11.18 ct (left) and 5.47 ct (right), these two rock crystal quartz cabochons play host to very unusual pink crystal sprays. Photo by Adriana Robinson.

> rarely contain more than 40% of the piemontite molecule, so many "piemontites" in collections (and pictured here in Mindat) are really Mn-rich red varieties of epidote.

To our knowledge, this pink to red epidote-quartz inclusion-host association has not previously been reported.

John I. Koivula, Nathan Renfro, and Maxwell Hain
GIA, Carlsbad

Fluorite in Brazilian Alexandrite

The author recently examined a 1.25 ct transparent oval modified brilliant alexandrite. The stone possessed a single crystal inclusion in the shape of a perfect octahedron (figure 8). Raman analysis identified the crystal as fluorite (CaF_2), which supported the alexandrite host's origin determination of Brazil.

Fluorite crystals are occasionally found in Brazilian alexandrite (Z. Sun et al., "Geographic origin determination of alexandrite," Winter 2019 *G&G*, pp. 660–681). However, they are often rounded in shape and rarely perfectly octahedral like the observed crystal here.

Figure 8. An octahedral fluorite crystal in a 1.25 ct Brazilian alexandrite. Photomicrograph by Hikaru Sato; field of view 2.37 mm.

Hikaru Sato
GIA, Tokyo

Radial Limonite in Sapphire

Limonite, a composite of hydrated iron oxide minerals, is an inclusion commonly seen in corundum, usually as a thin yellow veil of epigenetic deposits within surface-reaching fractures. A unique example of this material is shown in figure 9, where limonite precipitated into a small fracture and formed in a radial fashion. When viewed under diffused reflected light, the inclusion displayed bright interference colors. The inclusion stands in sharp

Figure 9. Radial limonite within a surface-reaching fracture of a violet sapphire shows bright interference colors when viewed under diffused reflected light. Photomicrograph by Nathan Renfro; field of view 1.44 mm.

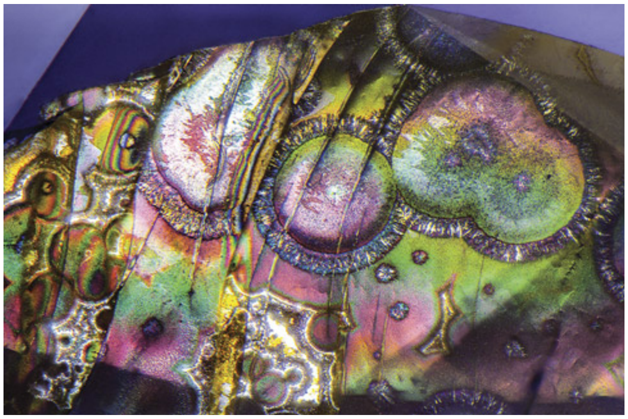

Figure 10. A parasite channel with a surface opening and finer branch-like etch channels in a natural saltwater pearl. Photomicrograph by Emiko Yazawa; field of view 4.79 mm.

contrast to the violet sapphire host. As a composite of hydrated iron oxide minerals, the limonite's yellow color is a strong indication that the stone has not been heat treated, as this would cause the yellow limonite to alter into red hematite (J.I. Koivula, "Useful visual clue indicating corundum heat treatment," Fall 2013 *G&G*, pp. 160–161). This example demonstrates that even the most common of inclusions can occasionally materialize as something remarkable.

Britni LeCroy and Nathan Renfro
GIA, Carlsbad

Parasite Channels in a Saltwater Natural Pearl

Shell-boring parasitic worms are commonly found inside the shells of various pearl-producing mollusk species. Consequently, mollusk shells may exhibit elongated channels indicating the presence of such organisms. Recently, the author observed interesting parasite channel features inside an 8.25 mm natural saltwater pearl (figure 10) set in a brooch with other pearls and near-colorless stones.

Microscopic examination revealed a Y-shaped channel with numerous finer branches that likely formed as the parasite searched for a way out of the pearl. The channel opening was observed at the surface of the nacre, while the tunnel was located slightly beneath the nacre. This interesting feature matched the pearl's internal structure, with a similarly Y-shaped structure visible in the X-ray image. Although such channels are often found in shells, they are rarer in pearls, and this channel's unique shape and morphology are noteworthy.

Emiko Yazawa
GIA, New York

Rose Channels in Ruby

The author recently examined a 0.5 ct pear-shaped ruby measuring 6 × 4 mm that contained twinning planes and hollow channels known as Rose channels (figure 11). Because the Rose channels were hollow and empty, they had a refractive index of 1 (the RI of air), while the RI of the surrounding host ruby was 1.76–1.77. The contrasting refractive indices resulted in high optical relief, making the Rose channels easily visible. These linear inclusions are common in natural corundum and were once thought to be boehmite needles (F. Notari et al., "'Boehmite needles' in corundum are Rose channels," Fall 2018 *G&G*, p. 257).

Aamir Sayed
Al Zain Jewellery, Bahrain

Figure 11. Rose channels in a 0.5 ct ruby. Photomicrograph by Aamir Sayed; field of view 0.75 mm.

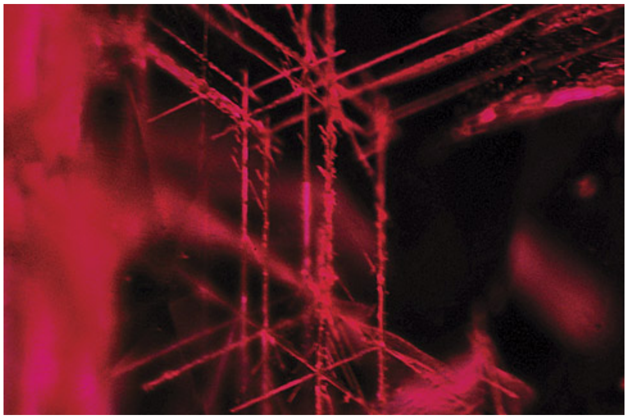

"Cyber" Butterfly

The author recently examined a 2.56 ct purple octagonal step-cut sapphire. This sapphire contained a negative crystal with a sharp rectilinear zigzag-patterned fingerprint, providing strong evidence that no heat treatment took place. Under fiber-optic illumination, the fingerprint displayed vibrant colors due to thin-film interference. The combination of the fingerprint and negative crystal created an image reminiscent of a digital butterfly (figure 12). Both the negative crystal and the unique fingerprint were caused by the natural healing of a surface-reaching fracture in the sapphire host. The healed areas parallel to the *c*-axis displayed rectangular outlines, resulting in the "cyber" appearance of the wings.

Yuxiao Li
GIA, Tokyo

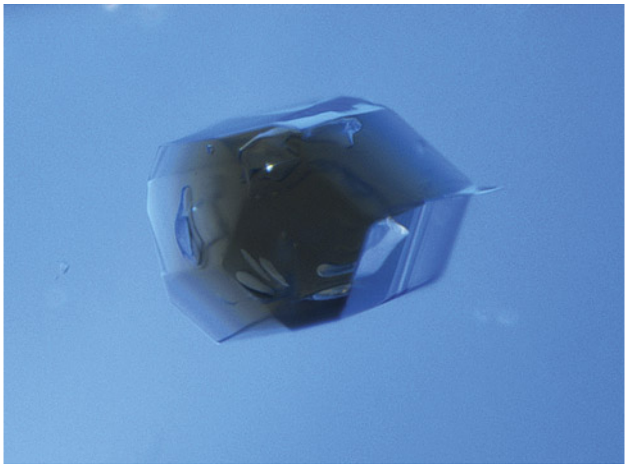

Figure 13. This tourmaline inclusion in a 1.81 ct Kashmir sapphire contains a few unusual "daughter" crystals with rounded edges. Photomicrograph by Yusuke Katsurada; field of view 0.73 mm.

Tourmaline Inclusion with Included Crystals in Kashmir Sapphire

The authors recently examined a 1.81 ct blue cushion mixed cut identified as sapphire. Microscopic examination showed sharp-banded milky clouds, particle stringers, and a well-formed euhedral greenish crystal. The crystal displayed a triangular prismatic habit with sharp basal pinacoids. This is typical of tourmaline, and the inclusion's identity was later confirmed by Raman spectroscopy.

Tourmaline inclusions in sapphire are diagnostic of a Kashmir origin (see R. Schwieger, "Diagnostic features and heat treatment of Kashmir sapphires," Winter 1990 *G&G*, pp. 267–280). Trace element analysis with laser ablation–inductively coupled plasma–mass spectrometry supported the microscopic observations, revealing a chemistry consistent with classic Kashmir samples from GIA's colored stone reference collection.

Interestingly, the tourmaline possessed uneven rounded inclusions of its own (figure 13). These crystals were presumably a different material, given their lighter

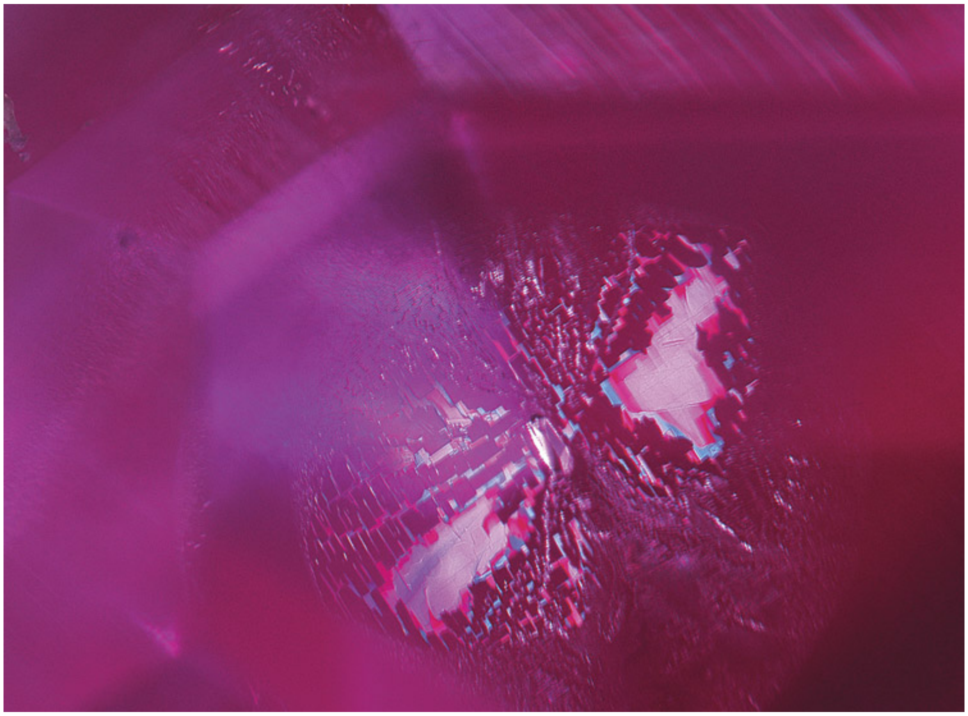

Figure 12. The rectilinear zigzag-patterned fingerprint and the negative crystal in the center are reminiscent of a beautiful "cyber" butterfly trapped in this 2.56 ct purple sapphire. Photomicrograph by Yuxiao Li; field of view 2.60 mm.

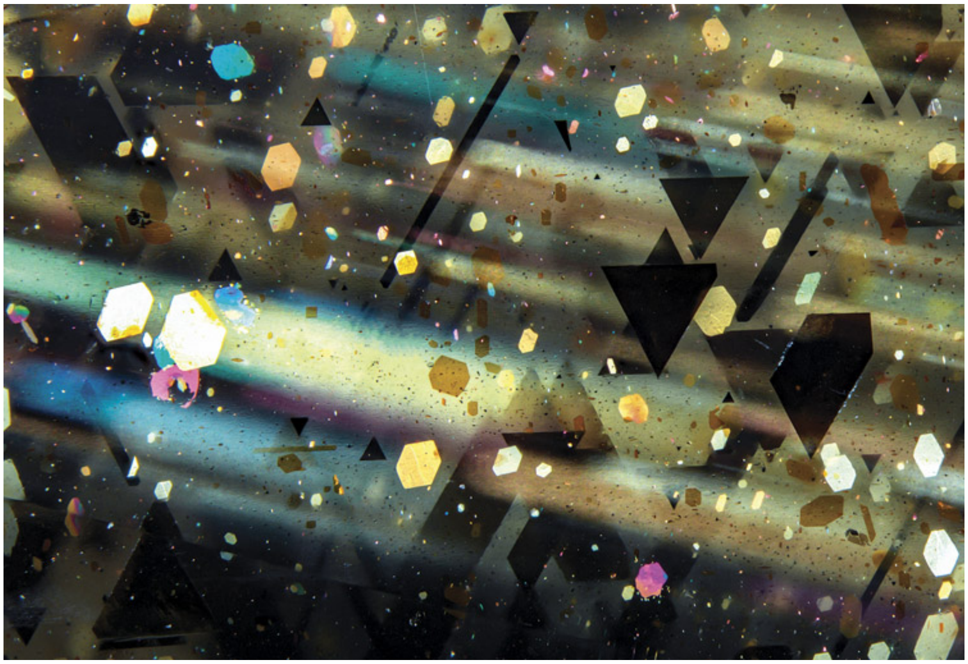

Figure 14. Parallel rays of golden, pink, and blue light were observed in this sample of rainbow lattice sunstone. Photomicrograph by Rosie Young; field of view 5.33 mm.

tone and sharp boundaries, which contrasted with the tourmaline host. Unfortunately, they could not be identified with Raman spectroscopy, leaving us to speculate about their true nature.

Yusuke Katsurada
GIA, Tokyo

Tyler Smith
GIA, New York

Rainbow Rays in Rainbow Lattice Sunstone

While examining a polished sample of Australian rainbow lattice sunstone, the author noticed a series of parallel "rays" illuminated with fiber-optic lighting (figure 14). These rays were initially considered some kind of internal structure within the feldspar. However, the orientation of the rays changed direction when the stone was tilted (figure 15). This indicated an optical effect whereby the fiber-optic light reflected off hematite inclusions and produced a ray of light corresponding to the color of the hematite platelet. This can be observed most easily in the upper right corner of figure 14. Extremely small particles within the sunstone likely allow the path of light to be visible, much like headlights shining through fog.

Rosie Young
Gemmological Certification Services, London

Figure 15. The changing direction of the rays is visible here when the stone is viewed through the same polished face but tilted to a slightly different orientation. Photomicrographs by Rosie Young; field of view 19.27 mm.

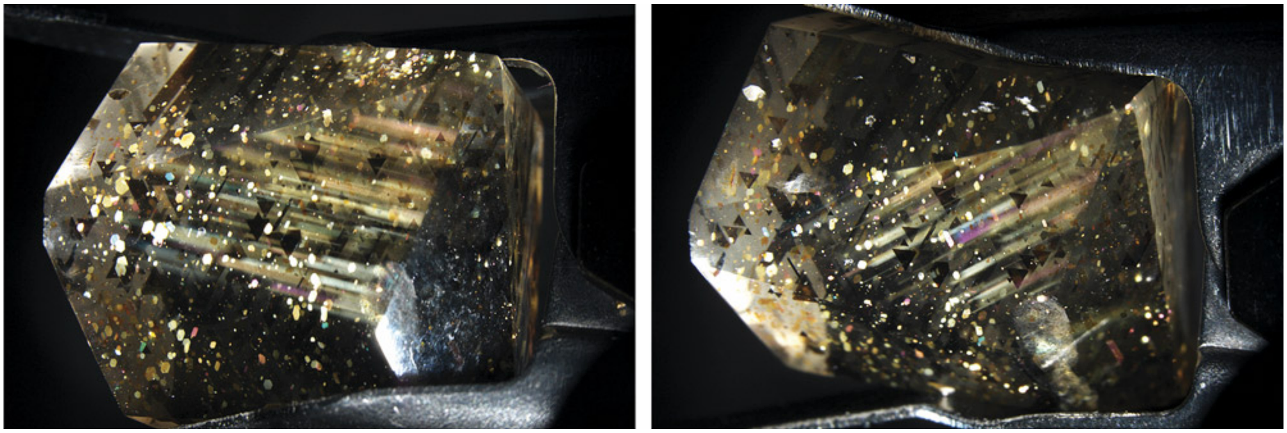

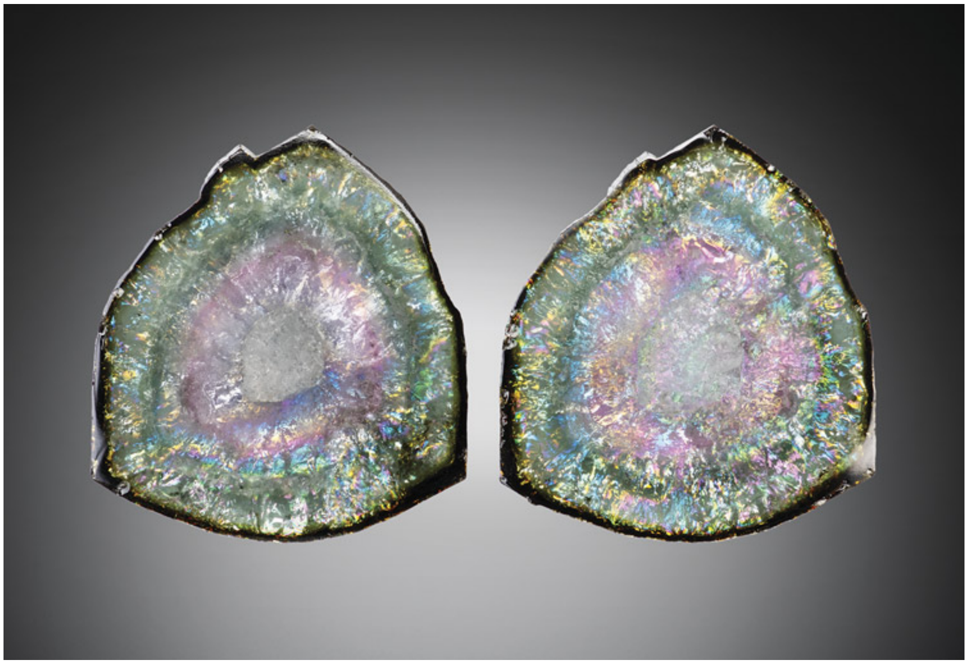

Figure 16. These 18 × 18 × 4 mm watermelon tourmaline slices (17.82 ct on the left and 17.17 ct on the right) display an exceptional iris effect. Photo by Jeffrey Scovil.

Brazilian Watermelon Tourmaline with Iris Effect

The watermelon tourmaline slices shown in figure 16 are remarkable for their mesmerizing iris effect. Unearthed from the famed Cruzeiro mine in the Brazilian state of Minas Gerais more than seven years ago, they were precisely cut to unveil their rainbow spectrum. Each slice, measuring 18 × 18 × 4 mm, radiates an alluring interplay of colors attributed to the iris effect, a phenomenon created by subtle internal fractures within the gemstone. This rare flawlessly matched pair weighed 34.99 carats total, conjuring the enchantment of fiery Australian opals.

Russ Behnke
Meriden, Connecticut

Quarterly Crystal: Diamond in Diamond

Mineral inclusions in diamonds are always very interesting to gemologists and other geoscientists, and the colorful minerals such as bright green chromium diopside and orange almandine-pyrope usually attract the most attention. This Quarterly Crystal is slightly different, in that the inclusion is both transparent and colorless, with relatively low relief compared to the diamond crystal host. The parent diamond, a transparent colorless, gem-quality glassy octahedron, weighed 0.71 ct and measured 5.88 × 3.99 × 3.01 mm (figure 17). Reportedly from South Africa, the diamond was purchased at the Tucson shows from David New.

When inclusion-host pairs are composed of the same mineral, it causes a low-relief situation bordering on in-

Figure 17. With a weight of 0.71 ct and measuring 5.88 mm in longest dimension, this glassy colorless diamond octahedron contains an eye-visible diamond inclusion. Photo by Diego Sanchez.

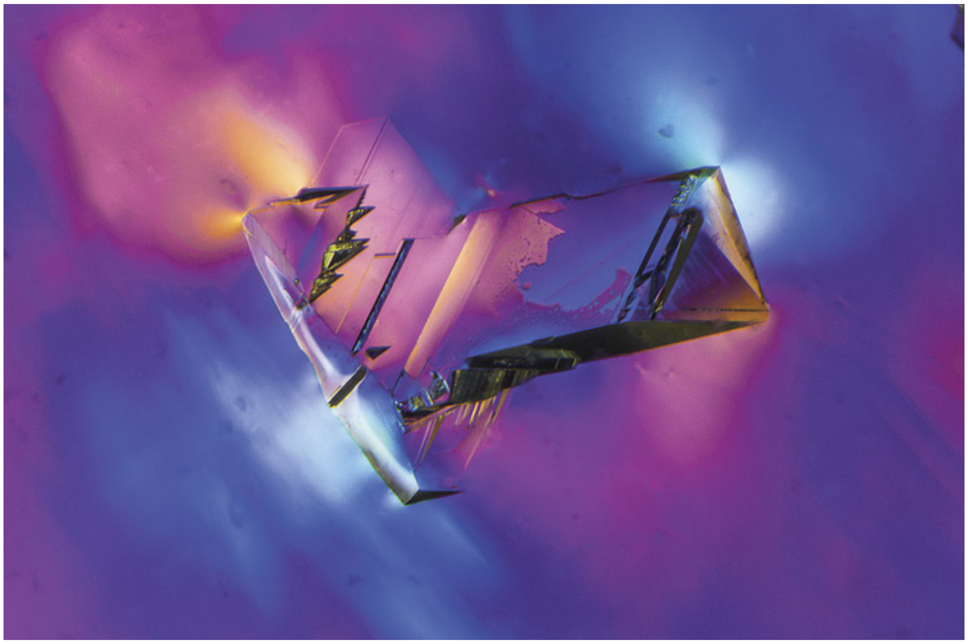

Figure 18. Polarized light shows an elongated modified diamond octahedron displaying various degrees of interfacing with the host diamond crystal. Photomicrograph by Nathan Renfro; field of view 2.18 mm.

visibility. Such inclusions become visible when the orientation of the inclusion is different or when there is an interface or partial interface between the host and the inclusion. In the case of diamond in diamond, if the inclusion is visible, then the interface can consist of various fluids and gases, other minerals (most commonly graphite formed through graphitization), combinations of all of these, or nothing at all.

Examining the outline of the diamond inclusion in figure 18, there are areas at the interface where the inclusion and host diamond appear to blend perfectly and the interface seems to completely disappear. These are areas of perfect contact where the diamond inclusion and the diamond host merge, without any form of interfacial separation.

John I. Koivula and Nathan Renfro
GIA, Carlsbad

Editor: Evan M. Smith

The Lengthy Vertical Journey of Superdeep Diamonds

Aside from their dazzling gem appeal, one thing that makes diamonds so interesting is the great depths below the earth's surface at which they form. The majority of diamonds mined as gemstones were formed in the base of ancient thick regions of continents, at a depth of about 150–200 km. This is already an incredible depth compared to virtually all the other rocks and minerals around us at the earth's surface. Even more extreme, however, are superdeep or sublithospheric diamonds, which originate from a depth of approximately 300–800 km (Shirey et al., 2024). With these superdeep origins in mind, how is it that they can be found at the earth's surface?

Exactly how superdeep diamonds make their way up to the surface has long remained a curiosity. It has been considered that kimberlites and related mantle-source volcanic eruptions might simply originate from comparable depths as superdeep diamonds, providing a single mechanism to carry superdeep diamonds all the way to the surface (Giuliani and Pearson, 2019). The depth of kimberlite formation is still unclear, however, and a shallower kimberlite origin from just below the continental lithosphere, no deeper than 300 km in the asthenosphere, appears more likely (Giuliani et al., 2023).

Such a shallow origin is supported by a recent model that links the timing and placement of kimberlites with convective instabilities or eddy currents associated with continental rifting (Gernon et al., 2023). As illustrated in figure 1, this model places the origin of kimberlites far closer to the surface than superdeep diamonds. An intermediate transport mechanism likely brings them up closer to the base of the lithosphere to be sampled by kimberlites alongside shallower lithospheric diamonds.

Several potential intermediate transport mechanisms have been proposed. These include mantle convection (Davies et al., 2004; Harte, 2010), localized buoyancy of the mantle rocks associated with diamond formation (Smith et al., 2018), upward-percolating melts (Walter et al., 2022), and—perhaps the most widely accepted—mantle plumes, which are hot columns of rock rising through the mantle due to their lower relative density (Stachel et al., 2000; Tappert et al., 2005; Bulanova et al., 2010; Walter et al., 2011; Harte and Richardson, 2012). The timing of this journey with respect to diamond formation and later kimberlite eruption has also been unclear. There may be an intermediate period of storage in the upper mantle (Stachel et al., 2000). A recent study by Timmerman et al. (2023) reporting superdeep diamond ages has shed new light on their lengthy vertical journey.

A Primer on Superdeep Diamonds

There are multiple ways in which diamonds can form in the mantle. Diamond growth can occur in different geologic settings and involve different types of host rocks and carbon-bearing fluids (Shirey and Shigley, 2013). Diamonds in the mantle can be broken down into two principal geologic settings or places where they grow: the lithospheric mantle and the sublithospheric mantle (figure 1). Further subdivisions are possible, but for simplicity we will only consider these two overarching groups. Note that here we are strictly speaking about mantle-derived diamonds found in kimberlites and related rocks or their eroded components. These are the kinds of diamonds mined as gemstones, which excludes diamonds from sources such as ultra-high-pressure metamorphic terranes, meteorites, impact sites, and ophiolites.

Diamonds from the lithospheric mantle crystallize in the base of old and thick regions of continental lithosphere (figure 1). These are the most common kinds of diamonds.

Editor's note: Questions or topics of interest should be directed to Evan Smith (evan.smith@gia.edu).

Gems & Gemology, Vol. 60, No. 1, pp. 84–89.

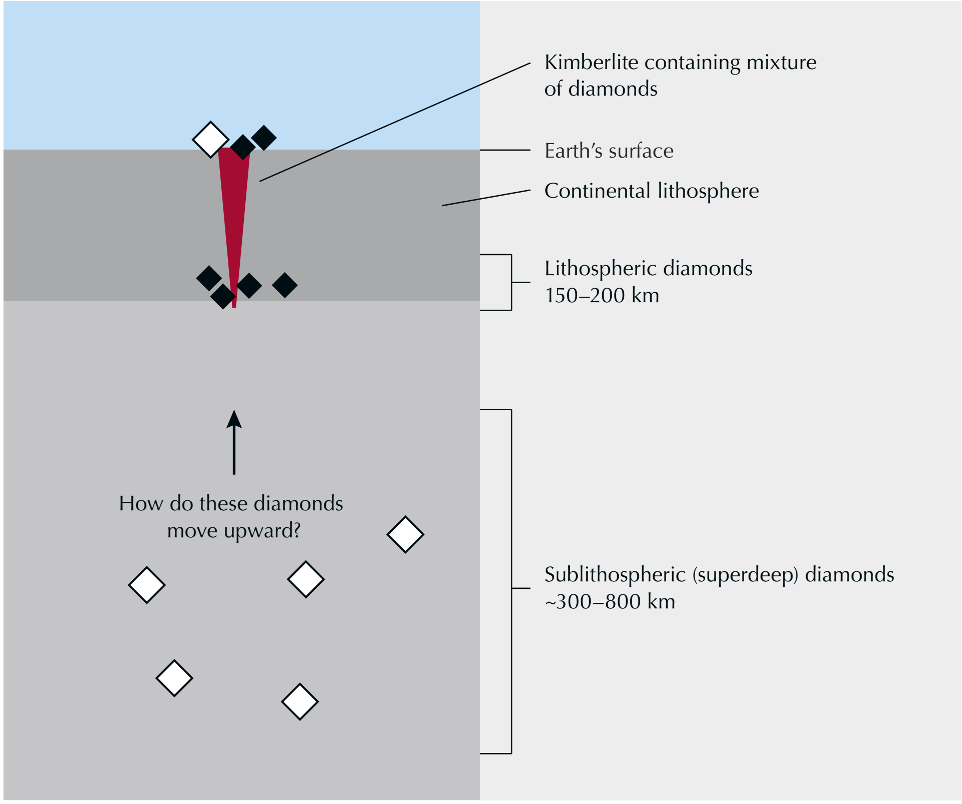

Figure 1. Simplified cross section of the earth showing diamonds in the mantle. How do the sublithospheric diamonds get into the kimberlite? The small black diamond symbols represent lithospheric diamonds, and the larger white symbols represent sublithospheric diamonds. A kimberlite, shown in red, erupts to the surface and contains both lithospheric and sublithospheric diamonds. Not to scale.

The second major geologic setting is the sublithospheric mantle, below the rigid lithospheric plates that make up the earth's surface. Diamonds formed here are termed *sublithospheric* or *superdeep* diamonds. Superdeep diamonds make up an estimated 2% of diamonds mined globally, although the exact proportions are not well constrained and can vary greatly by deposit (Stachel et al., 2022).

When we encounter diamonds at the surface, they have been swept up into kimberlites or related mantle-derived igneous rocks. Lithospheric and superdeep diamond populations often mix together, as depicted in figure 1. Mineral inclusions provide a method for identifying these different kinds of diamonds because the mineralogy of mantle rocks changes with depth. When diamonds contain one or more inclusions that could only have been trapped within the sublithospheric mantle, this is conclusive evidence that the host diamond is superdeep. Good examples are ringwoodite (Pearson et al., 2014) or coexisting inclusion pairs of ferropericlase and bridgmanite (found as enstatite) (Stachel et al., 2005).

Superdeep diamonds have been studied with fervor since their discovery unfolded in the mid-1980s (Moore and Gurney, 1985; Scott Smith et al., 1984). A brief history of superdeep diamond research is recounted by Shirey et al. (2024). These crystals obtained from the deep have captivated scientists because they provide the only well-preserved samples of the sublithospheric mantle, making them uniquely suited to study the composition, dynamics, and evolution of the earth's interior.

More recently, the breadth of superdeep diamonds has increased substantially as two varieties of high-quality gem diamonds were found to be sublithospheric. These are the nitrogen-poor, large, high-clarity diamonds subsequently named CLIPPIR diamonds and type IIb diamonds, which can have beautiful blue colors resulting from their boron content (Smith et al., 2016, 2017, 2018). Both of these newly recognized superdeep varieties, as well as many previously documented diamonds from the Juína region of Brazil and other global localities, have an association with subducted slabs of oceanic lithosphere (Walter et al., 2011; Smith et al., 2021; Regier et al., 2023). Subduction is a major geological process capable of recycling material such as carbon and water from the surface down into the mantle. The fact that superdeep diamonds offer insight into subduction processes makes them all the more valuable for learning about the geological evolution of our planet. For further background on superdeep diamonds, see reviews by Harte (2010), Harte and Hudson (2013), Kaminsky (2012), Shirey et al. (2024), Smith and Nestola (2021), Stachel et al. (2005), and Walter et al. (2022).

Ages of Superdeep Diamonds

Rock and mineral ages help unravel sequences of geologic events. For diamonds, however, measuring an age of crystallization is often difficult and sometimes impossible because it relies on radiometric dating of inclusions. In order to obtain a reliable age, it is essential to obtain a diamond with the right kinds of inclusions to be analyzed for radiogenic isotopes. Radioactive isotopes decay at a prescribed rate and can be used as a sort of internal clock to date inclusions. Generally, the age of an inclusion is assumed to correspond to the age of its entrapment in the diamond host, and therefore the age of diamond growth. Overviews of diamond dating were contributed by Smit and Shirey (2019) and Smit et al. (2022).

Finding superdeep diamonds with the right kinds of inclusions has been challenging, in part because of their rarity and the often small sizes of the inclusions (Shirey et al., 2024). There are fewer diamonds and fewer inclusions to choose from. Another challenge stems from the fact that isotopic measurements need to be representative of the entire inclusion. This is not a problem if an inclusion is homogeneous, but if it is unmixed or separated into multiple phases, the entire inclusion needs to be sampled in a bulk analysis. The latter is typical for superdeep diamonds because their inclusions tend to be retrograded or unmixed in texturally complex mineral assemblages and surrounded by large fractures into which parts of the inclusion may spread. In some cases the large fractures extend to the diamond's exterior, which effectively opens the inclusion system to leakage or contamination and compromises the inclusion entirely. Some limited preliminary dating work suggested generally young ages compared to lithospheric diamonds (Bulanova et al., 2010; Harte and Richardson, 2012).

Despite these difficulties, a recent study by Timmerman et al. (2023) has found coherent ages from four isotope systems (Rb-Sr, Sm-Nd, U-Pb, and Re-Os) applied to a suite of 11 diamonds from the Juína area of Brazil and two from Kankan, Guinea. Both localities are well-known occurrences for superdeep diamonds. The analyzed inclusions were calcium silicates, interpreted as former calcium silicate perovskite, as well as one example of iron sulfide. Taking all the data together gives overlapping ages of approximately 450 to 650 million years old (Timmerman et al., 2023). Although this range may seem imprecise, it is a remarkable result given the agreement across multiple isotope systems. Establishing this two-locality superdeep diamond age is a big piece of the puzzle of how the diamonds reached the surface.

Putting the Pieces Together

Ages help put the diamonds into a broader geological context. First, we can compare the 450–650 Ma (million years ago) ages of Juína and Kankan superdeep diamonds with the Cretaceous ages of their host kimberlite eruptions (the Cretaceous period spanned 145–66 Ma). Some of the Juína diamonds were from the Juína-5 and Collier-4 kimberlites, but the remaining Juína and Kankan diamonds studied by Timmerman et al. were from alluvial deposits, eroded from nearby kimberlites. Therefore, the kimberlite eruption age for all the samples was conservatively bracketed as Cretaceous (Timmerman et al., 2023).

The fact that these diamonds formed 450–650 Ma and later arrived at the surface in kimberlites around 145–66 Ma means the diamonds must have spent more than 300 million years in storage somewhere in the mantle. One scenario could be that the diamonds were formed and stored deep in the sublithospheric mantle, perhaps drifting with mantle convection currents. Later, in the Cretaceous, random packages of diamonds of coincidentally similar ages were carried upward by unidentified mechanisms and sampled by kimberlites at Juína and Kankan. However, this scenario of deep and mobile storage does not fit well with the spatial context of these two localities, considering past tectonic plate movements.

At the time of diamond formation, Juína and Kankan, now separated by the Atlantic Ocean, were actually close neighbors in the supercontinent Gondwana. Given that these localities were adjacent, Timmerman et al. suggest that the similar age of the diamonds is not merely a coincidence but an indication that they formed in broadly the same sublithospheric setting. Subducting oceanic lithosphere around Gondwana's edges (figure 2, step 1) would have made the sublithospheric mantle beneath Gondwana an ideal place for superdeep diamond growth. It is plausible that the studied diamonds formed in the sublithospheric mantle directly beneath the ancient neighboring Juína and Kankan sources (figure 2, step 2).

Since 450 Ma, the Juína and Kankan locations migrated about 6,500 km as the tectonic plates drifted. At the beginning of the Cretaceous, Juína and Kankan separated as the Atlantic Ocean spread open (Timmerman et al., 2023). The notion that subsequent kimberlite eruptions contained those ancient sub-Gondwanan superdeep diamonds suggests that the diamonds were somehow pinned to the overlying continental blocks and were able to migrate with them. Timmerman et al. argue that the diamonds ascended in packages of buoyant, low-density rock shortly following their growth and that these diamond-studded rocks adhered to the underside of the continental lithosphere (figure 2, step 3). Melt-depleted metaperidotitic rock in the subducting slab could heat up near the top of the lower mantle (660 km), becoming less dense than the surrounding mantle and tearing apart to shed buoyant blobs of rock.

It is not an obvious answer that emerges, but with the above lines of reasoning from Timmerman et al. we arrive at the multistage model shown in figure 2. Knowing the diamond ages and being able to put them into the context of subduction and plate movements suggests steps 1 through 4 are successive and related. Subduction beneath Gondwana (step 1) creates a favorable setting for diamond growth (step 2). Portions of the subducted slab heat up and become buoyant, ascending through the mantle (step 3) and adhering to the bottom of the overlying continental lithosphere (step 4). These steps likely occurred within 450–650 Ma, after which the diamonds spent more than 300 million years in storage at the base of the continental lithosphere as the plates drifted across the earth's surface. At the start of the Cretaceous,

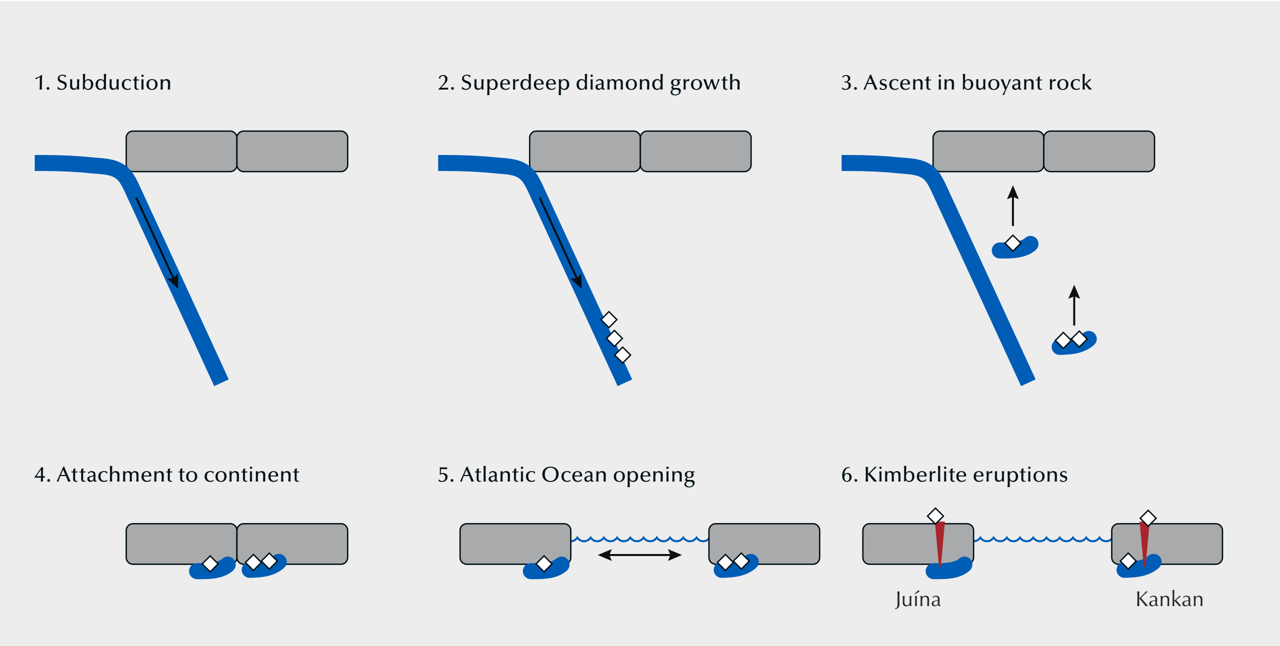

Figure 2. Multistage model for Juína and Kankan superdeep diamond formation and ascent. 1: Subduction (blue slab) beneath the Gondwana supercontinent, simplified here as two lithospheric blocks (gray) that represent the Amazonian and West African portions that will contain the future Juína and Kankan deposits, respectively. 2: Superdeep diamond growth occurs at a depth of 300–800 km in association with the subducting oceanic plate. 3: As the oceanic plate warms, portions of rock decrease in density and serve as buoyant rafts for diamonds, carrying them upward. 4: Ascending superdeep diamond-bearing rocks adhere to the base of the continental lithosphere, where they are proposed to reside for about 300 million years. 5: Continental rifting at the start of the Cretaceous divides the Amazonian and West African cratons and their attached superdeep diamonds. 6: Multiple kimberlite eruptions in the Juína area and Kankan sweep superdeep diamonds up to the surface. Not to scale. Based on Timmerman et al. (2023).

continental rifting separates the continental blocks as the Atlantic Ocean opens up (step 5). Mantle instabilities caused by rifting lead to kimberlite eruptions within tens of millions of years (Gernon et al., 2023) and the dormant superdeep diamonds are finally swept up to the surface (step 6).

The model outlined in figure 2, with consecutive processes of diamond formation and ascent that are both linked to the subducted slab, could apply to other superdeep diamonds, not just those at Juína and Kankan. An intermediate period of storage in the upper mantle has been proposed previously based on the textures of unmixed or retrograded mineral inclusions (Stachel et al., 2000). For example, some superdeep diamonds contain two-phase inclusions of breyite ($CaSiO_3$) and perovskite ($CaTiO_3$), which are interpreted as unmixed from an original single-phase $Ca(Si,Ti)O_3$-perovskite (figure 3). Unmixing of these two phases would have occurred at a depth shallower than about 300 km, consistent with a period of shallow mantle storage prior to kimberlite eruption (e.g., following step 4 in figure 2). These and other types of inclusions, such as majoritic garnets, show consistent evidence of re-equilibration that could occur during storage in the upper mantle (Timmerman et al., 2023).

Even beyond mineral inclusions, CLIPPIR and type IIb superdeep diamonds have textural evidence consistent with a period of storage in the mantle. These diamonds contain ubiquitous dislocation networks, seen in cathodoluminescence and deep-UV (<230 nm) imaging (figure 4) (Smith et al., 2017, 2018; Regier et al., 2023). Plastic deformation generates the dislocations, but their movement and reorganization into network patterns requires a period of recovery at high temperatures (Hanley et al., 1977). If these kinds of superdeep diamonds also ascend with buoyant slab-derived rocks and adhere to the continental base, this period of quiescent storage could provide the right conditions for dislocation network formation.

Importance for Diamond Mining and Exploration

Superdeep diamonds have long been thought of as small and generally not of gem quality, and thus they were deemed irrelevant in assessing the value of a potential diamond deposit. But the recognition that some of the highest-quality and most valuable type IIa and type IIb diamonds are superdeep is changing this perception (Smith et al., 2016, 2017, 2018). Now we can recognize that some diamond mines, such as Letšeng (Lesotho),

Figure 3. An inclusion-bearing pink superdeep diamond. The largest inclusion is a two-phase mixture dominated by colorless breyite ($CaSiO_3$) and small spots of brown perovskite ($CaTiO_3$), the latter circled in image C. The inclusion is surrounded by graphitized fractures that appear black. The original rough weight was 1.37 ct, before windows were polished to examine the inclusions. Photomicrographs by Evan M. Smith; fields of view 14.52 mm (A), 1.42 mm (B), and 0.50 mm (C).

Cullinan (South Africa), and Karowe (Botswana), derive a major portion of their revenue from superdeep diamonds.

The development of tools for exploration and mining that can specifically target superdeep diamonds would be advantageous. Currently, lithospheric mantle indicator minerals such as eclogitic and chromium-pyrope garnets are used as a proxy for diamond potential, but this tool is blind to superdeep diamonds. Developing a better understanding of how superdeep diamonds reach the surface does not necessarily reveal a simple solution for their exploration, but it might help geologists look in the right direction. It appears likely that superdeep diamonds ascend in packages of buoyant rock and are stored in the upper mantle, which could be an important clue. Host rocks in this intermediate setting might shed distinct indicator minerals or geochemical signatures into erupting kimberlites that are more widespread and easier to detect than the superdeep diamonds themselves.

Figure 4. Blue type IIb diamond with dislocation networks. Left: Face-up image of a 0.08 ct Fancy Light blue diamond (2.76 × 2.42 mm). Photo by Jian Xin (Jae) Liao. Right: Cathodoluminescence image revealing dislocation networks. Image by Elina Myagkaya; field of view 2.18 mm.

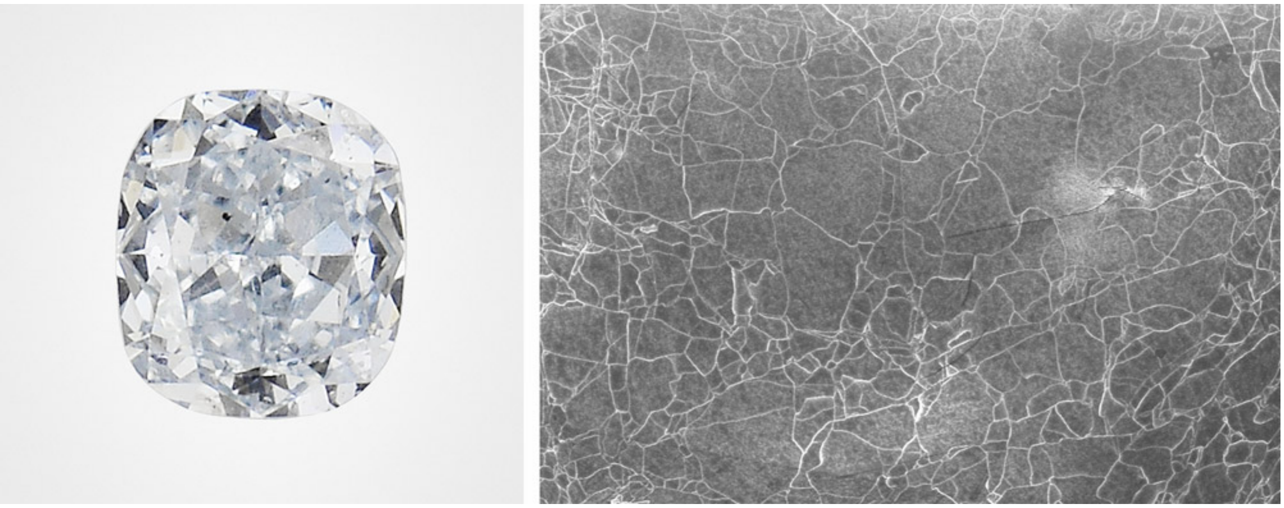

ACKNOWLEDGMENT

Many thanks to Dr. Suzette Timmerman (University of Bern, Switzerland) for suggestions that improved this column.

REFERENCES

Bulanova G.P., Walter M.J., Smith C.B., Kohn S.C., Armstrong L.S., Blundy J., Gobbo L. (2010) Mineral inclusions in sublithospheric diamonds from Collier 4 kimberlite pipe, Juína, Brazil: Subducted protoliths, carbonated melts and primary kimberlite magmatism. *Contributions to Mineralogy and Petrology*, Vol. 160, No. 4, pp. 489–510, http://dx.doi.org/10.1007/s00410-010-0490-6

Davies R.M., Griffin W.L., O'Reilly S.Y., McCandless T.E. (2004) Inclusions in diamonds from the K14 and K10 kimberlites, Buffalo Hills, Alberta, Canada: Diamond growth in a plume? *Lithos*, Vol. 77, No. 1-4, pp. 99–111, http://dx.doi.org/10.1016/j.lithos.2004.04.008

Gernon T.M., Jones S.M., Brune S., Hincks T.K., Palmer M.R., Schumacher J.C., Primiceri R.M., Field M., Griffin W.L., O'Reilly S.Y., Keir D., Spencer C.J., Merdith A.S., Glerum A. (2023) Rift-induced disruption of cratonic keels drives kimberlite volcanism. *Nature*, Vol. 620, No. 7973, pp. 344–350, http://dx.doi.org/10.1038/s41586-023-06193-3

Giuliani A., Pearson D.G. (2019) Kimberlites: From deep earth to diamond mines. *Elements*, Vol. 15, No. 6, pp. 377–380, http://dx.doi.org/10.2138/gselements.15.6.377

Giuliani A., Schmidt M.W., Torsvik T.H., Fedortchouk Y. (2023) Genesis and evolution of kimberlites. *Nature Reviews Earth & Environment*, Vol. 4, No. 11, pp. 738–753, http://dx.doi.org/10.1038/s43017-023-00481-2

Hanley P.L., Kiflawi I., Lang A.R. (1977) On topographically identifiable sources of cathodoluminescence in natural diamonds. *Philosophical Transactions of the Royal Society of London. Series A, Mathematical and Physical Sciences*, Vol. 284, No. 1324, pp. 329–368, http://dx.doi.org/10.1098/rsta.1977.0012

Harte B. (2010) Diamond formation in the deep mantle: The record of mineral inclusions and their distribution in relation to mantle dehydration zones. *Mineralogical Magazine*, Vol. 74, No. 2, pp. 189–215, http://dx.doi.org/10.1180/minmag.2010.074.2.189

Harte B., Richardson S. (2012) Mineral inclusions in diamonds track the evolution of a Mesozoic subducted slab beneath West Gondwanaland. *Gondwana Research*, Vol. 21, No. 1, pp. 236–245, http://dx.doi.org/10.1016/j.gr.2011.07.001

Harte B., Hudson N.F.C. (2013) Mineral associations in diamonds from the lowermost upper mantle and uppermost lower mantle. In D.G. Pearson et al., Eds., *Proceedings of 10th International Kimberlite Conference: Volume 1*, pp. 235–253, http://dx.doi.org/10.1007/978-81-322-1170-9_15

Kaminsky F. (2012) Mineralogy of the lower mantle: A review of 'super-deep' mineral inclusions in diamond. *Earth-Science Reviews*, Vol. 110, No. 1-4, pp. 127–147, http://dx.doi.org/10.1016/j.earscirev.2011.10.005

Moore R.O., Gurney J.J. (1985) Pyroxene solid solution in garnets included in diamond. *Nature*, Vol. 318, pp. 553–555, http://dx.doi.org/10.1038/318553a0

Pearson D.G., Brenker F.E., Nestola F., McNeill J., Nasdala L., Hutchison M.T., Matveev S., Mather K., Silversmit G., Schmitz S., Vekemans B., Vincze L. (2014) Hydrous mantle transition zone indicated by ringwoodite included within diamond. *Nature*, Vol. 507, No. 7491, pp. 221–224, http://dx.doi.org/10.1038/nature13080

Regier M.E., Smit K.V., Chalk T.B., Stachel T., Stern R.A., Smith E.M., Foster G.L., Bussweiler Y., DeBuhr C., Burnham A.D., Harris J.W., Pearson D.G. (2023) Boron isotopes in blue diamond record seawater-derived fluids in the lower mantle. *Earth and Planetary Science Letters*, Vol. 602, article no. 117923, http://dx.doi.org/10.1016/j.epsl.2022.117923

Scott Smith B.H., Danchin R.V., Harris J.W., Stracke K.J. (1984) Kimberlites near Orroroo, South Australia. In J. Kornprobst, Ed., *Kimberlites I: Kimberlites and Related Rocks*. Elsevier, Amsterdam, pp. 121–142.

Shirey S.B., Shigley J.E. (2013) Recent advances in understanding the geology of diamonds. *G&G*, Vol. 49, No. 4, pp. 188–222, http://dx.doi.org/10.5741/gems.49.4.188

Shirey S.B., Pearson D.G., Stachel T., Walter M.J. (2024) Sublithospheric diamonds: Plate tectonics from Earth's deepest mantle samples. *Annual Review of Earth and Planetary Sciences*, Vol. 52, No. 1, http://dx.doi.org/10.1146/annurev-earth-032320-105438

Smit K.V., Shirey S.B. (2019) Diamonds from the Deep: How old are diamonds? Are they forever? *G&G*, Vol. 55, No. 1, pp. 102–109.

Smit K.V., Timmerman S., Aulbach S., Shirey S.B., Richardson S.H., Phillips D., Pearson D.G. (2022) Geochronology of diamonds. *Reviews in Mineralogy and Geochemistry*, Vol. 88, No. 1, pp. 567–636, http://dx.doi.org/10.2138/rmg.2022.88.11

Smith E.M., Nestola F. (2021) Super-deep diamonds: Emerging deep mantle insights from the past decade. In H. Marquardt et al., Eds., *Mantle Convection and Surface Expressions*. American Geophysical Union, pp. 179–192.

Smith E.M., Shirey S.B., Nestola F., Bullock E.S., Wang J., Richardson S.H., Wang W. (2016) Large gem diamonds from metallic liquid in Earth's deep mantle. *Science*, Vol. 354, No. 6318, pp. 1403–1405, http://dx.doi.org/10.1126/science.aal1303

Smith E.M., Shirey S.B., Wang W. (2017) The very deep origin of the world's biggest diamonds. *G&G*, Vol. 53, No. 4, pp. 388–403, http://dx.doi.org/10.5741/gems.53.4.388

Smith E.M., Shirey S.B., Richardson S.H., Nestola F., Bullock E.S., Wang J., Wang W. (2018) Blue boron-bearing diamonds from Earth's lower mantle. *Nature*, Vol. 560, No. 7716, pp. 84–87, http://dx.doi.org/10.1038/s41586-018-0334-5

Smith E.M., Ni P., Shirey S.B., Richardson S.H., Wang W., Shahar A. (2021) Heavy iron in large gem diamonds traces deep subduction of serpentinized ocean floor. *Science Advances*, Vol. 7, No. 14, article no. eabe9773, http://dx.doi.org/10.1126/sciadv.abe9773

Stachel T., Harris J.W., Brey G.P., Joswig W. (2000) Kankan diamonds (Guinea) II: Lower mantle inclusion parageneses. *Contributions to Mineralogy and Petrology*, Vol. 140, No. 1, pp. 16–27, http://dx.doi.org/10.1007/s004100000174

Stachel T., Brey G.P., Harris J.W. (2005) Inclusions in sublithospheric diamonds: Glimpses of deep Earth. *Elements*, Vol. 1, No. 2, pp. 73–78, http://dx.doi.org/10.2113/gselements.1.2.73

Stachel T., Aulbach S., Harris J.W. (2022) Mineral inclusions in lithospheric diamonds. *Reviews in Mineralogy and Geochemistry*, Vol. 88, No. 1, pp. 307–391, http://dx.doi.org/10.2138/rmg.2022.88.06

Tappert R., Stachel T., Harris J.W., Muehlenbachs K., Ludwig T., Brey G.P. (2005) Diamonds from Jagersfontein (South Africa): Messengers from the sublithospheric mantle. *Contributions to Mineralogy and Petrology*, Vol. 150, No. 5, pp. 505–522, http://dx.doi.org/10.1007/s00410-005-0035-6

Timmerman S., Stachel T., Koornneef J.M., Smit K.V., Harlou R., Nowell G.M., Thomson A.R., Kohn S.C., Davies J.H.F.L., Davies G.R., Krebs M.Y., Zhang Q., Milne S.E.M., Harris J.W., Kaminsky F., Zedgenizov D., Bulanova G., Smith C.B., Cabral Neto I., Silveira F.V., Burnham A.D., Nestola F., Shirey S.B., Walter M.J., Steele A., Pearson D.G. (2023) Sublithospheric diamond ages and the supercontinent cycle. *Nature*, Vol. 623, No. 7988, pp. 752–756, http://dx.doi.org/10.1038/s41586-023-06662-9

Walter M.J., Kohn S.C., Araujo D., Bulanova G.P., Smith C.B., Gaillou E., Wang J., Steele A., Shirey S.B. (2011) Deep mantle cycling of oceanic crust: Evidence from diamonds and their mineral inclusions. *Science*, Vol. 334, No. 6052, pp. 54–57, http://dx.doi.org/10.1126/science.1209300

Walter M.J., Thomson A.R., Smith E.M. (2022) Geochemistry of silicate and oxide inclusions in sublithospheric diamonds. *Reviews in Mineralogy and Geochemistry*, Vol. 88, No. 1, pp. 393–450, http://dx.doi.org/10.2138/rmg.2022.88.07

GEM NEWS INTERNATIONAL

Contributing Editors
Gagan Choudhary, *IIGJ-Research & Laboratories Centre, Jaipur, India* (gagan.choudhary@iigjrlc.org)
Christopher M. Breeding, *GIA, Carlsbad* (christopher.breeding@gia.edu)
Guanghai Shi, *School of Gemmology, China University of Geosciences, Beijing* (shigh@cugb.edu.cn)

TUCSON 2024

Overall, 2024 was a good year at the various Tucson shows. Foot traffic throughout the venues was noticeably slow at times, but less window-shopping and more serious buying of particularly higher-end items made up for the lack of bustling crowds. Most vendors interviewed reported strong sales and many returning buyers, noting that sales have continued to grow post-pandemic.

The American Gem Trade Association reported a small uptick in buyer attendance (+1%) and a 3% growth in vendors at the AGTA GemFair. In fact, they only had one empty booth in both the designer showroom and the gem hall. Vendors in both venues indicated that the show floor felt slower but that visitors were there to buy, often with shopping lists. AGTA's added security measures that included ID checks were well received by both buyers and exhibitors.

Figure 2. Vintage turquoise rough from the Sleeping Beauty mine in Arizona. Photo by Jennifer Stone-Sundberg; courtesy of Arizona Color Stones & Minerals.

Figure 1. A display case showing popular colors and materials seen this year in Tucson. Photo by Jennifer Stone-Sundberg; courtesy of Arizona Color Stones & Minerals.

GIA's Show Service Laboratory reported a solid AGTA show, with ruby, emerald, and sapphire making up the majority of the intake. Both the service lab and vendors noted movement of high-end, unusual, and rare stones, a common theme every year in Tucson.

It was hard to miss the prevalence of green to blue stones, especially in vibrant and pastel tones. They were well represented in the 2023 AGTA Spectrum and Cutting Edge Awards, and many vendors reportedly brought these colors to Tucson in response. With blues and greens leading the way, pinks and to a lesser extent purples were also highly visible (figure 1). Among the top stones spotted throughout the shows were emerald, turquoise (figure 2), opal, aquamarine, Paraíba and cuprian tourmaline (figure

Editors' note: Interested contributors should send information and illustrations to Stuart Overlin at soverlin@gia.edu.

GEMS & GEMOLOGY, VOL. 60, NO. 1, pp. 90–138.

Figure 3. A 30.26 ct blue cushion-cut cuprian tourmaline from Mozambique. Photo by Robert Weldon; courtesy of Evan Caplan.

Figure 4. A 5.34 ct vivid green modified cushion-cut Russian demantoid garnet displaying horsetail inclusions. Photo by Robert Weldon; courtesy of Tsarina Jewels.

3), green garnet (figure 4), and unheated Montana sapphire. Strong showings of unheated blue Ukrainian topaz, unheated bicolor green and blue zoisite, blue zircon, pink to purple garnets, electric pink and purple sapphire (figure 5), morganite, fluorescent "dragon" Malaya garnet, rose quartz, pink tourmaline, baroque pearls, and Oregon sunstone were also noted.

Another trend was the demand for visibly unheated stones. "Silky" sapphire and spinel with needle inclusions creating a soft, glowing appearance were extremely popular (figure 6). Also referred to as "opalescent," "hazy," "milky," and "sleepy," these stones were some of the hottest at the AGTA, Gem & Jewelry Exchange (GJX), and Pueblo shows. Dudley Blauwet Gems reported selling out of all of their opalescent milky stones by the fourth day of AGTA.

Other noted trends included the importance of geographic origin and traceability reporting for many buyers, the popularity of fancy shapes such as hearts and pears (figure 7), and the use of white metal in jewelry both in the AGTA Spectrum Award winners and throughout the shows.

Demand for American stones was evident once again, with more vendors carrying sapphire from Montana, turquoise from Nevada and Arizona, and sunstone from Oregon. In fact, one of the most often encountered materials in jewelry this year was vintage turquoise reportedly from the famed Sleeping Beauty mine in Arizona (figure 8). In the past, these various American gems were available mainly from vendors directly associated with the mining claims. The Southwestern motif, always a fixture in Tucson, was decidedly more pronounced this year, with many large silver items throughout the shows, including bangles, cuff

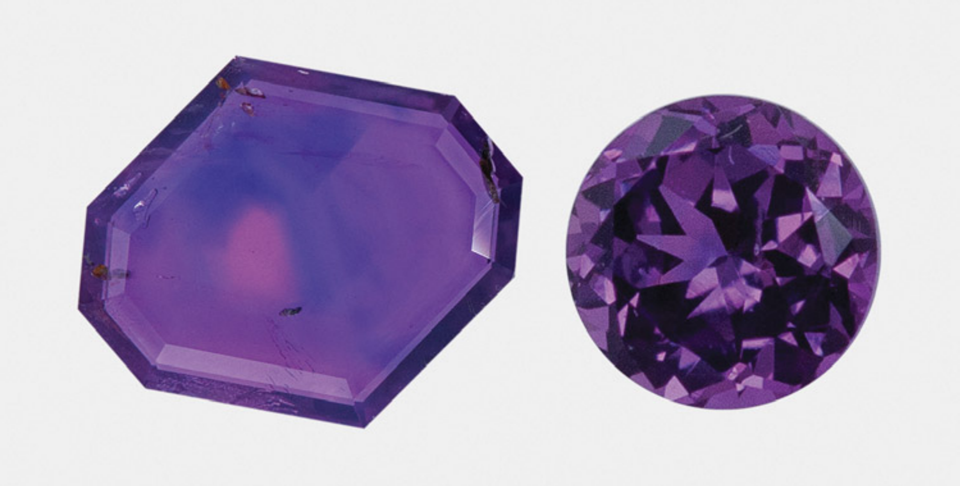

Figure 5. Pink and purple "Nebula" sapphire in both freeform faceted tablet (left; 7.77 × 9.20 mm, 0.82 ct) and brilliant-cut (right; 4 mm round, 0.73 ct) styles. This material is from a mine in Madagascar that produces very small stones ranging from hot pink to violet. Photos by Kalim Korey; courtesy of Caroline C.

Figure 6. Sapphire and spinel with a visible silky haze creating a glowing, sleepy appearance were popular throughout the shows. Left: Four emerald-cut Mahenge spinel (clockwise from top: 3.00 ct purple, 1.77 ct purple, 2.40 ct purple, and 3.71 ct hot pink). Courtesy of Bryan Lichtenstein. Right: A 4.50 ct "opalescent" unheated sapphire from Sri Lanka. Courtesy of Misfit Diamonds. Photos by Robert Weldon.

bracelets, statement earrings, necklaces, and bolo ties adorned with turquoise (figure 9), red coral, blue topaz, and opal. This observation was validated the following week when singer Post Malone performed "America the Beautiful" before Super Bowl LVIII wearing a striking silver bolo tie complete with a large bright green turquoise stone with brown matrix. The bolo was reportedly made by Navajo artist Leonard Nez of New Mexico using a piece of Royston turquoise.

In addition to the presence of vintage jewelry this year, we also found multiple examples of repurposing antiquities into jewelry. As for new finds, we report on bright blue opal from Chile, green amber from Ethiopia, high-quality orange-flash rainbow moonstone from Madagascar, and recent sapphire production from the famed Kashmir region.

We hope you enjoy our coverage of the 2024 Tucson gem shows and find the following reports informative.

Jennifer Stone-Sundberg, Tao Hsu, Eric Fritz,
Lisa Kennedy, and Cristiano Brigida

Figure 7. A 0.67 ct heart-shaped pezzottaite measuring 5.61 × 6.10 mm. The rough of this rare newer gem material was found and bought in Madagascar in December 2023. The stone was cut in New York for the Tucson show, where it sold. Photo by Kalim Corey; courtesy of Caroline C.

Figure 8. Two pairs of earrings designed and crafted by Caroline Chartouni using Sleeping Beauty turquoise rough she acquired more than 10 years ago. The left pair is 18K white gold with 64.53 carats of turquoise, two cabochon moonstones, and 4.40 carats of hot pink spinel. The right pair is 18K white gold with 107.30 carats of turquoise, 4.64 carats of tsavorite garnet, and 0.19 carats of diamond. Photos by Kalim Corey; courtesy of Caroline C.

Figure 9. Vintage Navajo silver bolo tie with turquoise reportedly from the Morenci mine in southeastern Arizona, which is not currently being mined for turquoise. This highly collectible material, known for its desirable blue color and iron pyrite matrix, dates back to 1864 and was a byproduct of copper mining. Photo by Kevin Schumacher; courtesy of Aaron Palke.

Figure 10. This clean piece of tumbled green amber from Ethiopia, measuring approximately 5.5–6.0 × 2.8–3.5 cm, displays flow structures and some inclusions. Photo by Cristiano Brigida; courtesy of Rainbow King Solomon Mines.

COLORED STONES AND ORGANIC MATERIALS

Green amber from Ethiopia. Many consumers and gem enthusiasts are most familiar with yellow and golden amber commonly found in the Baltic Sea region and the Dominican Republic. However, the gem can also be white, orange to red, or brown. In rare cases, strong fluorescence can give amber a bluish or greenish appearance.

At the Pueblo Gem & Mineral Show, Rainbow King Solomon Mines showed the authors some rare green amber said to be from the Amhara region of Ethiopia. The selection consisted mainly of large tumbled pieces with a yellowish green to greenish yellow bodycolor, visible flow structure and bubbles, moderate to heavy inclusions, and numerous brown discolorations (figure 10). A few pieces contained sizable insect inclusions as well. The exhibitor presented a limited amount of experimental faceted pieces (figure 11), but these were not for sale. The faceted pieces showed a surprisingly high luster and brilliance, as well as fiery flashes of orange and green colors. Because of the material's dark tone, prominent brown discolorations, and relative abundance of biological inclusions—no samples were tested by the GIA laboratory—the authors believe it was natural, compared to the green autoclaved copal previously described by Abduriyim et al. ("Characterization of 'green amber' with infrared and nuclear magnetic resonance spectroscopy," Fall 2009 *G&G*, pp. 158–177).

The discovery of Ethiopian amber deposits is relatively recent, with orange to yellow amber most commonly found. Compared to other amber sources, the occurrence of green amber in Ethiopia is more prevalent but still rare overall and limited to certain localities. The amber observed at the Pueblo show matches the characteristics of the highly bio-included green amber described in detail by Bouju and Perrichot ("A review of amber and copal occurrences in Africa and their paleontological significance," *BSGF - Earth Sciences Bulletin*, Vol. 191, 2020, article no. 17).

Lisa Kennedy and Cristiano Brigida
GIA, New York

An exceptional cat's-eye emerald. Those in the gem trade often recall a memorable experience, gemstone, or business connection. A Brazilian cat's-eye emerald (figure 12) presented at the AGTA show by estate dealer Doug Liebman (Scottsdale, Arizona) conjured all three.

Figure 11. Ethiopian faceted green amber, measuring approximately 18 × 18 mm. The gem looks very lively under sunlight. Photo by Cristiano Brigida; courtesy of Rainbow King Solomon Mines.

Figure 12. Double cabochon cat's-eye emerald weighing 5.11 ct and measuring 10.77 × 8.95 × 7.39 mm, from Goiás State, Brazil. Photo by Robert Weldon; courtesy of Douglas M. Liebman Estate Jeweler.

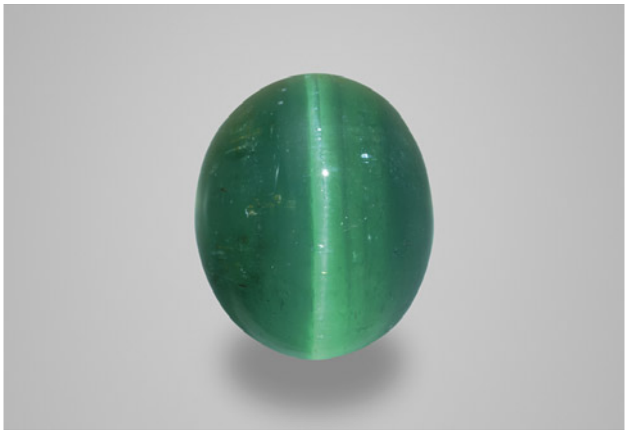

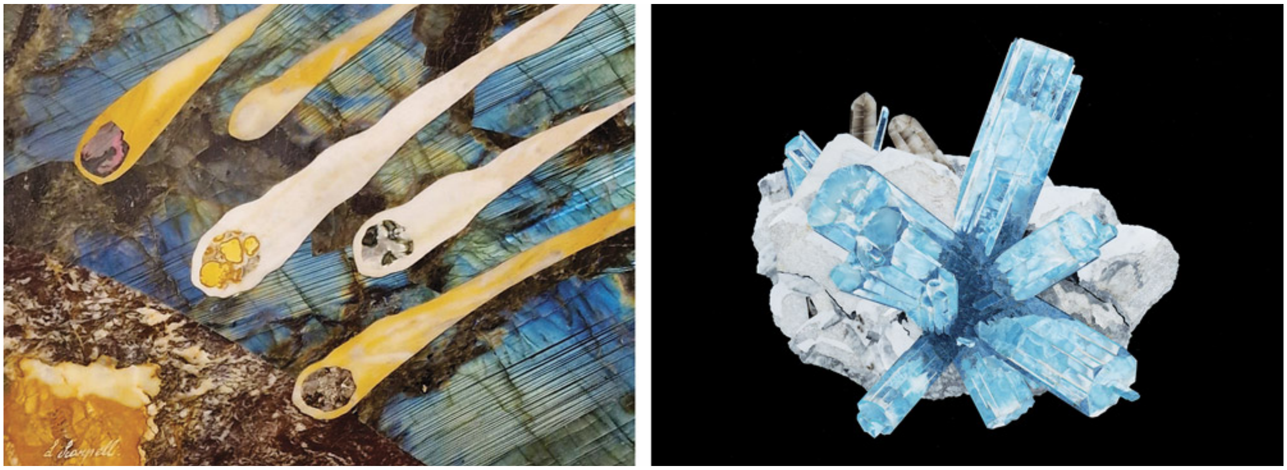

Figure 13. Left: "Meteorites," a mosaic by Leonardo Scarpelli. A labradorite background gives a strong sense of light shining in the night sky as the observer moves. Right: The "Starburst" mosaic by Leonardo Scarpelli. Larimar proved the perfect material to reproduce aquamarine's transparency and color. Photos by Cristiano Brigida; courtesy of Scarpelli Mosaici.

Liebman shared the story of how in 1983, early in his career, he forged a long-term relationship with Albert Sabbagh, cofounder of Ben Sabbagh Bros. in Brazil. Liebman's early buying trips to Brazil revealed a wide variety of gemstone offers at all price points, including the magnificent cat's-eye emerald.

Emeralds have been mined sporadically and in small quantities in the Brazilian state of Goiás for more than 100 years. In 1981, the deposits were found to produce emerald of a desirable quality. This prompted more steady mining, which has been continuous ever since. The emeralds occur in a talc schist as stubby crystals usually less than 1 cm long. Their color ranges from pale to dark green, often with a bluish overtone. The best faceted stones are rarely over one carat.

Last year, at GJX 2023, Liebman visited the Ben Sabbagh Bros. booth and spoke with Albert's sons Samuel and Clement. They showed him a cat's-eye emerald from Goiás that had been part of their late father's private collection. Liebman recalled the emerald from his early days with Sabbagh. While impressed by the stone, he left the booth without buying.

After some reflection, Liebman returned to GJX first thing the next morning. He said yes to the emerald before they even told him the price.

The 5.11 ct cat's-eye emerald is extraordinary for its color, clarity, legacy, and allure, with no additional light source needed to display the centerline cat's-eye effect. What goes around often does come back around, at the right time, in the right place: Tucson, Arizona.

Eric Fritz
GIA, Carlsbad

Gemstones and art. Exploring the Tucson Fine Mineral Gallery, the author was impressed by artistic masterpieces hanging from the walls. These exhibits ranged from stone mosaics of modern subjects to watercolor paintings of minerals. The author had the chance to speak with mosaic artists Leonardo and Catia Scarpelli (Scarpelli Mosaici, Florence) and watercolor artist Ksenia Levterova (Kyiv).

The Scarpelli family creates stunning mosaics representing contemporary subjects using the technique of *commesso fiorentino* (from the Latin *commettere*, meaning "put together"), which dates back to the Italian Renaissance. In this craft, opaque stones of different colors and textures (*pietra dura*) are finely cut into unique shapes and seamlessly joined together. This traditional art form developed and achieved a level of perfection in the late sixteenth century in Florence, under the rule of the Medici family, who wanted to depict their era in a durable, eternal medium.

Leonardo Scarpelli, the son of a *commesso fiorentino* master, began his career in 1992. Challenged by the idea of moving from traditional to more modern subjects, he experimented with the *commesso fiorentino* technique by incorporating gem materials that had never been used before, such as labradorite. Scarpelli discovered that labradorite brought depth and life to subjects where dynamism is essential, such as a splashing water drop or meteorites falling in the night sky (figure 13, left), allowing him to create unusual motion effects unexpected from a traditional mosaic.

After Scarpelli exhibited in some gem and mineral shows, the idea of reproducing mineral specimens with the proper transparency and color nuances by means of *commesso fiorentino* became a compelling challenge. When commissioned to reproduce a fine aquamarine specimen from Pakistan, the Scarpellis' extensive search for the right color landed on Larimar, the trade name for a variety of pectolite. Its light blue color and white speckles made Larimar ideal for the purpose, leading to impressive results (figure 13, right). This is one more case where the use of a gem material associated with traditional stones demonstrated all its potential in bringing into play precious effects, colors, and textures.

Figure 14. Watercolors of tourmaline with albite (left) and a diamond crystal from Kimberley, South Africa (right). Photos by Cristiano Brigida; courtesy of Ksenia Levterova.

Ksenia Levterova is a talented Ukrainian watercolor artist. Passionate about the perfection of mineral shapes and their fascinating colors, she specializes in the reproduction of mineralogical subjects at a photorealistic level.

Levterova's artworks exhibited in Tucson this year encompassed a wide range of subjects, from the captivating beauty of fine specimens such as tourmaline to the precise reproduction of mineral crystallizations (figure 14). Watercolor makes it possible to represent the most subtle variations in color and transparency effects while displaying each crystal's characteristics with remarkably high definition. The degree of realism and the fidelity to shapes and color nuances allow a rigorous mineralogical consistency. As a result, Levterova's work is becoming popular in many gem and mineral shows, and she has a gallery hosted on Mindat (https://www.mindat.org/gallery-63606.html).

Cristiano Brigida

Butterfly brooch showcasing East African gems. At the AGTA show, Andrew Rosenblatt, company spokesperson for Akiva Gil (New York City), showed us a magnificent butterfly brooch featuring colored stones from East Africa (figure 15). Notably, Akiva Gil was among the first to acquire spinel and raspberry rhodolite from Tanzania in the early 2000s. Joseph Gil collaborated with the late master jeweler Pietro DiBenedetto to develop a piece that would showcase the beautiful array of colors from this part of the world.

Figure 15. This colorful 18K gold butterfly brooch designed by Pietro DiBenedetto features 49 East African colored gems, accompanied by colorless and yellow diamonds. Photo by Robert Weldon; courtesy of Akiva Gil & Co.

The resulting brooch contains fine-quality green tsavorite (17.98 carats total), yellow grossular (0.98 carats total), and orange mandarin garnets (10.15 carats total) alongside pink spinel (15.00 carats total) and fancy-color sapphire (8.47 carats total). These are accented by 1.60 carats of yellow and colorless diamonds. This piece highlights the wide range of colored gem varieties in highly desirable hues that East Africa contributes to the gem trade today.

Jennifer Stone-Sundberg and Robert Weldon
GIA, Carlsbad

Guatemalan jadeite jade: Rough and finished. Jadeite jade is one of the most important aggregate gems in today's global marketplace, with known sources in Myanmar, Japan, Russia, and Guatemala. Among them, Myanmar is the most legendary and still dominates today's market. Guatemala, however, has recently reclaimed its status as an important jadeite jade producer (see Z. Huang et al., "'Ice jade' from Guatemala," pp. 26–41 of this issue).

At this year's 22nd Street show, Yax Tun Minerals (Denver, Colorado) offered a wide range of Guatemalan jadeite jade, including rough pieces in blue, green, and lavender (figure 16). According to owner Luke Miller, the bluish color is the most common and the most desired in the American market. All rough is covered with a "skin" resulting from weathering.

Figure 16. The rough Guatemalan jadeite jade sold by Yax Tun Minerals included blue, green, and lavender hues, with blue being the most prevalent. Photo by Tao Hsu; courtesy of Yax Tun Minerals.

The seller provided a strong flashlight for buyers to assess the quality of the rough, similar to what buyers do at the major jadeite auction in Myanmar. The blue color was quite saturated, while the green and lavender colors were not. The bluish rough showed high transparency and some had green veins running through it (figure 17, left). The green veins also exhibited high transparency (figure 17, right). The lavender rough pieces were of low transparency and had a coarser texture than the other two color varieties (figure 16).

The blue color is characteristic of Guatemalan jadeite jade, which is often called "Olmec blue" in the trade. The Olmec civilization was a Mesoamerican culture revealed by archaeological artifacts. The blue to green-blue jadeite jade mined in Guatemala was prized by the Olmecs from about 1500 to 400 BCE. Mesoamerican cultures that fol-

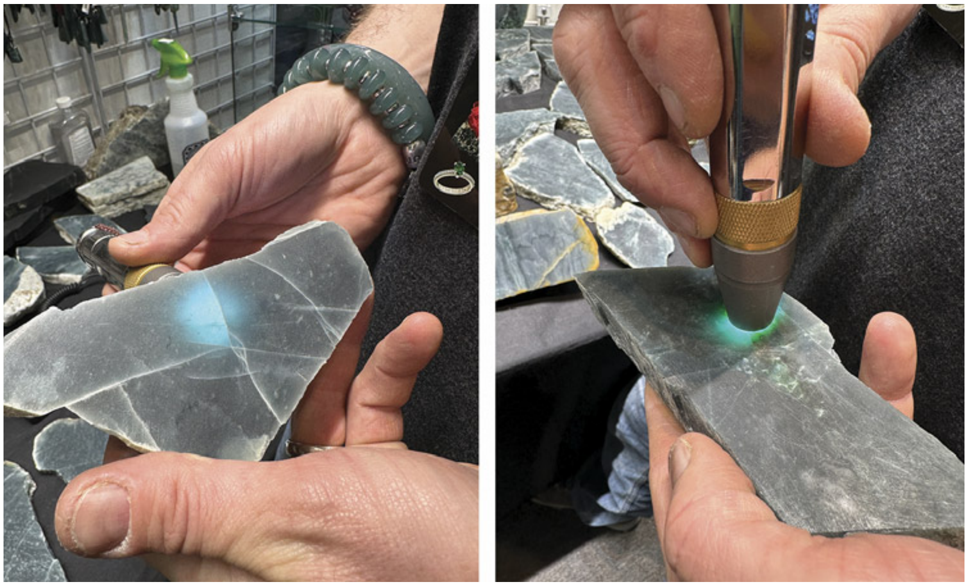

Figure 17. The bluish jadeite jade from Guatemala showed high transparency and a very fine texture (left). Some displayed green veins throughout. A flashlight revealed a slight green tint in some pieces with high transparency and fine texture (right). Photos by Tao Hsu; courtesy of Yax Tun Minerals.

Figure 18. This spectacular "Rainbow Luna" dagger features a blade of beautiful Guatemalan jadeite jade that shows the characteristic Olmec blue color and even deeper purplish blue close to the point. Courtesy of Georg Schmerholz.

Figure 19. An 18K yellow gold and blackened sterling silver shagreen wide cuff bracelet, pendant, earrings, and ring set with antique mother-of-pearl gaming counters. Courtesy of Sarosi by Timeless Gems.

lowed, such as Mayan, Zapotec, and Totonac, continued the reverence for jadeite jade. But when the Spanish conquered Mesoamerica in the sixteenth century, their appetite for gold and emeralds contributed to the fall of Guatemalan jadeite jade popularity. Mayan guards kept the jade mine locations secret, and they were not rediscovered until 1974. Since then, Guatemala has been gradually regaining recognition as an important source of jadeite jade.

Finished products offered at the Yax Tun booth included beads, beaded necklaces, bracelets, earrings, and small pendants, polished or carved. Many of the top-quality materials are processed at Miller's carving studio in Mexico.

As Guatemalan jadeite jade gains popularity among both Western and Asian consumers, more gem artists are using this material to show their creativity. World-renowned sculptor Georg Schmerholz brought an outstanding collection of jade to the Tucson Gem and Mineral Show. His latest creation, "Rainbow Luna," is second in the "Resplendent Quetzal" series, which honors a beautiful bird native to Guatemala. Completed in June 2023, the 14-inch dagger is carved from the finest Guatemalan jadeite jade with a patinated bronze handle (figure 18). Schmerholz's jade art bridges the two disciplines of sculpture and gemstone carving.

The wide range of appearance and quality of Guatemalan jadeite jade offers versatility to designers, artists, and consumers. Sufficient production and distribution are essential for this gem material to reach a wider audience.

Tao Hsu
GIA, Carlsbad

Historical relics repurposed into jewelry. One theme that emerged at the AGTA, GJX, and Pueblo shows was the repurposing of historical artifacts to produce new jewelry items. We saw the incorporation of Chinese, Greek, Viking, and medieval European artifacts into various jewelry pieces at all three shows. Many attendees were drawn to the idea of having a connection to the past in a wearable form.

At GJX, Sarosi by Timeless Gems (Los Angeles) exhibited eye-catching carved mother-of-pearl jewelry (figure 19). While the sheer beauty of the pieces initially caught the authors' attention, the craftsmanship and story behind them enabled this collection to stand out among a sea of designs. At the center of all the pieces in the collection were hand-engraved mother-of-pearl Chinese gaming counters, once used like modern-day gambling chips. The eighteenth-century counters were commissioned by British royalty and nobility during the Qing Dynasty. Most were engraved on one side with family crests or monograms, with the reverse side illustrating some aspect of Chinese life. The counters were surrounded by a combination of 18K yellow gold, polished sterling silver, and blackened sterling silver, handcrafted by jewelers in Los Angeles to evoke traditional Chinese architecture.

In the AGTA designer showroom, Zaffiro (Walla Walla, Washington) devoted a section of their case to their artifact collection, comprising sixth- to fifteenth-century Viking, Anglo-Saxon, and European medieval relics that they incorporated into jewelry (figure 20). These one-of-a-kind pendants integrate actual buried treasure purchased from a reputable auction house in the UK. Zaffiro founders Jack and Elizabeth Gualtieri explained that they

Figure 20. Three ancient artifacts repurposed by Zaffiro. Top left: Medieval silver-gilt strap end from the thirteenth to fifteenth century, set in granulated 22K yellow gold with a 0.07 ct red spinel. Center: Gilded bronze medieval mount from the twelfth to fourteenth century, set in 22K granulated and 18K yellow gold with 0.15 carats of tsavorite garnet and an 11.5 × 14.0 mm black Tahitian pearl. Bottom right: Gilded bronze belt mount from the tenth to twelfth century, set in granulated 22K yellow gold with a 0.13 ct blue sapphire. Photo by Robert Weldon; courtesy of Zaffiro.

like to use items from before the advent of the printing press. Many of the antiquities, originally used to decorate items such as belts, clothing, and horse tack, have retained their original gilding. The Gualtieris set the artifacts in 22K gold frames or rivets and decorate with granulation, sometimes accenting the pieces with colored stones. The appeal of these pieces is in the stories that they tell.

Back at the GJX show, Shans Premier (New York City) offered a large selection of antiquities, including coins in addition to colored stones and jewelry. This multi-generational business has been dealing in antiquities for more than 100 years and in the U.S. for about 40 years. This was their thirtieth year in Tucson. They typically sell more gemstones at U.S. shows, but in Tucson they have a strong following for their antiquities.

Sason Shan described a particularly intriguing pendant incorporating one of the most circulated coins from the height of classical Greek civilization: the silver Athenian owl tetradrachm (figure 21). This surprisingly heavy coin was used throughout the ancient world around the time of the Peloponnesian War. Greece minted enormous quantities of these coins using silver from Laurion. Worth several days' wages, they were too valuable for basic transactions (R.A. Augustin, "Ancient coins – The most famous coin of antiquity – The Athenian owl," *Coin Week*, 2022, accessed February 10, 2024, https://coinweek.com/ancient-coins-famous-coin-antiquity/).

Figure 21. A silver Greek Athenian owl tetradrachm from the fifth century BCE weighing approximately 17.2 g with an approximate diameter of 24 mm set in an 18K yellow gold pendant, which cleverly allows the rotation of this coin to face upward on both sides even though the two sides are not stamped in the same orientation. The left image shows the coin obverse with a profile of Athena, and the right image shows the coin tail featuring her patron animal, the owl, which was also a symbol of ancient Athens. Photos by Jennifer Stone-Sundberg; courtesy of Shans Premier.

With sustainability at the forefront of many consumers' minds, these upcycled designs extend the life of antiquities, allowing them to be displayed for many years to come.

Lisa Kennedy and Jennifer Stone-Sundberg

Intarsia jewelry box by Nicolai Medvedev and Susan Helmich. Opening day at the AGTA show was truly memorable with the premiere of "Treasure Chest II with Blue Boy" (figure 22, left), a joint collaboration between intarsia master Nicolai Medvedev and jewelry designer Susan Helmich. The exterior of the chest is adorned with Australian opal, Paraíba tourmaline from Brazil, diamonds, South African sugilite, Burmese maw-sit-sit, turquoise from the Sleeping Beauty mine (Arizona) and Nevada, gold-in-quartz from Australia and California, Utah dinosaur bone, 22K gold, and a matched pair of exquisite opal slices from Virgin Valley, Nevada. This type of Nevada opal is commonly referred to as "conk" wood, in which the cells of the original wood have been opalized. The slices featured

Figure 22. Left: The front of the "Blue Boy" chest features two wing-like "conk" wood opal slices from Nevada. Right: A 22K gold stingray adorns the top of the chest, guarding the contents within. Photo by Robert Weldon.

on the front of the box came from the Bonhams opal and phenomenal gem auction in 2021.

The stingray "Blue Boy" on top was designed and hand carved by Helmich, created from 22K gold with Paraíba tourmaline and diamonds (figure 22, right). The interior is lined with burl wood veneer, with jasper inset into the lid, malachite (Bisbee, Arizona), and an 18K gold hinge. The chest, which took two years to complete, is the second in the series from Medvedev and Helmich. Their first chest featured an octopus.

Eric Fritz

Figure 23. A 9.30 ct oval cut and a 4.12 ct triangular cut of a new type of moonstone from Madagascar featuring an orange flash effect. Photo by Robert Weldon; courtesy of Dudley Blauwet Gems.

New high-quality rainbow moonstone from Madagascar. Moonstone, a perennial favorite in Tucson, was offered both as loose stones and in jewelry throughout the shows. This year, a new type of transparent moonstone from Andilamena in the Alaotra-Mangoro region of northeastern Madagascar displayed a distinct orange flash effect in addition to strong blue adularescence. Moonstone is normally cut en cabochon, but the two moonstones in figure 23 were faceted because of their high transparency and to better display the orange flash.

Blue moonstone is a phenomenal gemstone variety of orthoclase, a mineral belonging to the alkali feldspar group. This potassium aluminum silicate gem is transparent to translucent, with a white bodycolor and blue adularescence. The blue "moonlight" is caused by light interference from moonstone's alternating microscopic layers of albite and orthoclase. Rainbow moonstone, which shows flashes of various colors that can include blue, is also a feldspar mineral but belongs to the plagioclase group and falls into the calcium-rich labradorite variety. This new material was confirmed to be plagioclase feldspar and within the labradorite variety by Bear Williams (Stone Group Laboratories, Jefferson City, Missouri) using Raman spectroscopy, making this a high-quality rainbow moonstone.

This new material was reportedly mined in 2023, and the initial supply of several kilograms of rough sold out at extraordinarily high per-carat prices. Hopefully more of this intriguing material will reach the marketplace soon.

Jennifer Stone-Sundberg

Morganite from Blue Star Gems. Morganite, a pink gem discovered in 1910 in Madagascar, was identified as a new variety of beryl by George Kunz, who named it in honor of his friend J.P. Morgan. Morganite has since been found in several other countries, most notably Brazil, Mozambique, Afghanistan, China, Russia, and the United States. The most productive mine today is in Minas Gerais, Brazil.

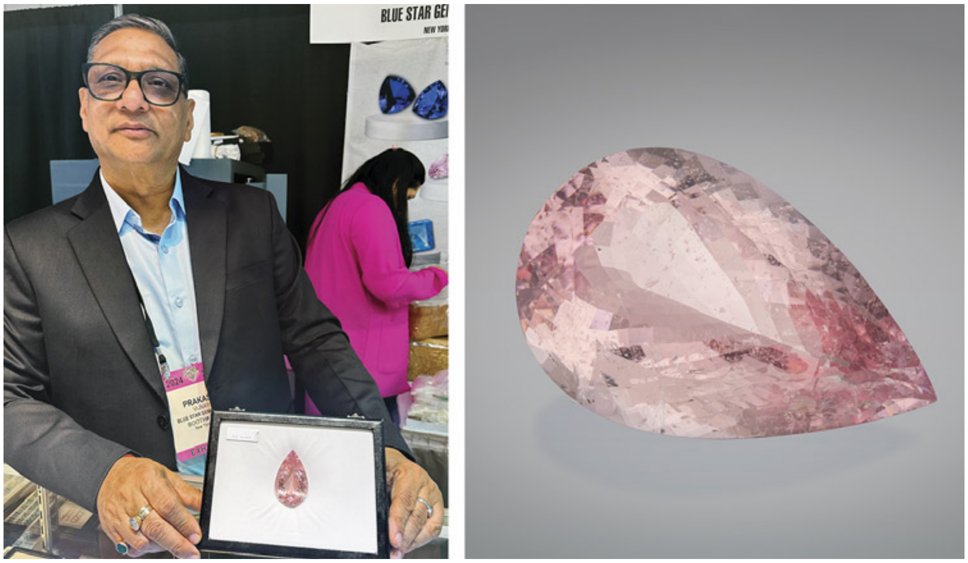

Figure 24. The 236.27 ct pear-shaped untreated morganite from old Madagascar stock was designed by Prakash Chand Vijay, who also oversaw the cutting. Photos by Jennifer Stone-Sundberg (left) and Robert Weldon (right). Courtesy of Blue Star Gems.

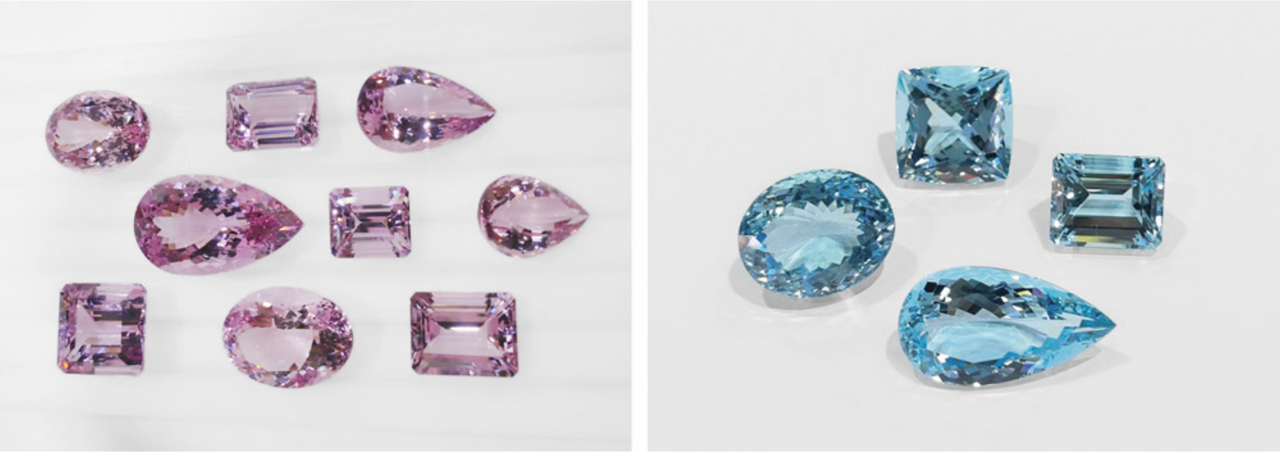

Figure 25. Left: Suite of morganite from Mozambique ranging from 27.90 ct (the center rectangular step cut) to 92.34 ct (the largest pear). These stones underwent a lengthy heating and electron radiation treatment to bring out the best color and clarity. Right: Suite of aquamarines from Madagascar. Clockwise from left: 31.88 ct oval brilliant cut, 49.08 ct cushion cut, 35.80 ct rectangular step cut, and 24.51 ct pear brilliant cut. Photos by Prateek Vijay; courtesy of Blue Star Gems.

At the GJX show, an extraordinary morganite stood out at the Blue Star Gems (New York City) booth (figure 24). Owner Prakash Chand Vijay indicated that the 236.27 ct stone was from vintage stock from the original morganite mine in Madagascar. This one-of-a-kind untreated stone had a particularly pleasing deep warm pink color and a striking constellation of small inclusions scattered throughout. With Vijay's expertise in the selection and cutting of stones from Africa, he participated in and oversaw the cutting of this exceptional gem.

Vijay's daughter, Jyoti Vijaywargi, said that this year they brought more than 100 pieces of attractively colored purplish pink morganite in sizes of over 20 carats each (figure 25, left). These stones came from Mozambique and underwent a lengthy heating and electron irradiation treatment in Germany to bring out the best color and clarity.

The enhancement of morganite color has been shifting from neutron irradiation to electron irradiation, avoiding the risk of a radioactive product (T. Stephan et al., "Irradiation treatment and gamma-ray spectroscopy of morganite," *37th International Gemmological Conference Proceedings*, Tokyo, 2023, pp. 123–125). Vijaywargi noted that due to the large sizes of their morganites, the entire process takes about five years to produce the quality seen, attesting to the value of the material and the patience of the vendor. The treatment itself takes about three and a half years, followed by an additional 18 months to let the stones cool down and be tested before they can be sold. Sometimes the stones do not respond to the treatment, and there is no color improvement at all. To date, there is no pretreatment testing to indicate whether the stones will respond to the treatment, so each run is a financial risk.

In addition to morganite, Blue Star Gems had extensive offerings of aquamarine (figure 25, right)—one of this year's most popular stones—and tanzanite. The aquamarine comes from Madagascar. Despite global business challenges, the show proved successful for Blue Star Gems, particularly for high-end stones. The company was also able to attract new buyers this year.

Vijaywargi described the recent challenges around the pricing of wholesale versus retail items. On the wholesale side, prices for all goods have increased, yet these price changes have not been reflected at the retail end. As a vendor carrying substantial inventory of rare gemstones, Vijaywargi anticipates an increase in the value of Blue Star's collection, which will require patience as a seller.

Jennifer Stone-Sundberg

Blue opal from Chile. Opal is an extremely popular stone in its many phenomenal varieties. However, the market also offers countless types of nonphenomenal opal, whose selling point is their combination of color, pattern, and degree of transparency.

At the 22nd Street show, the author came across an enchanting ocean blue variety of opal from Chile, exhibited by Chilean Rocks and Minerals. The material on view was opaque to semitranslucent with an overall color banding and greasy luster, tumbled or cut as cabochons. The most prized pieces contained slightly greenish and vivid blue colors (figure 26, left). Less valuable polished stones showed alternating blue and solid white layers or the presence of green material and sometimes brown matrix in their bands. The cutters used the natural banding to their advantage, resulting in attractive colors and patterns that often evoke pleasant seascapes (figure 26, right). After cutting, the material is polymer impregnated to create a tough and durable finished product.

Figure 26. Left: A polished Chilean blue opal pear-shaped cabochon displaying a uniform and strongly saturated medium blue color and a greasy luster. Right: An oval cabochon representative of the typical color palette and banding, varying from bluish green to slightly greenish blue and pure white, which produces a "seascape" image. Photos by Cristiano Brigida; courtesy of Chilean Rocks and Minerals.

A selection of various grades of rough material was also available, displaying a dull conchoidal fracture with the dominant textural feature being the intricate interplay of blue and green, the two main colors (figure 27).

According to the dealer, this was the debut of cut Chilean blue opal at the Tucson gem shows. This type of opal is reportedly from the Atacama region, the only known occurrence to date in Chile, where a few mining operations are actively extracting the material. Presently known to the trade is a blue opal from Peru referred to as "Andean opal," but that material is generally translucent and lower in saturation than the Chilean blue opal.

No detailed mineralogical analyses on the samples exhibited at 22nd Street have been reported. The blue color could be due to internal light scattering and dispersed chrysocolla, a mineral known for its vivid blue hue. Chrysocolla is commonly found in copper-rich deposits such as the porphyry copper deposits in the Atacama region. The analogy with Peruvian blue opal, which comes from a similar chrysocolla-rich geological setting, supports this hypothesis.

Given its vibrant color saturation, ability to take a high polish, and the desirable texture and alternating color patterns of the cut stones, this Chilean blue opal was a pleasant new addition to the gem offerings from Tucson 2024.

Cristiano Brigida

Precious opal from Pedro II, Brazil. Prime Gems, Inc. (New York City) offered a small quantity of precious opal from Brazil at this year's GJX show. As an opal source, Brazil has been underrepresented for the past four decades since a "golden age" from the 1960s to mid-1970s. The inventory of Brazilian opal from Prime Gems helped inform attendees of the fine quality available from this part of the world.

Multiple states in Brazil have opal occurrences, but the most important reserves are in the Pedro II munici-

Figure 27. Rough sample of Chilean blue opal, about 18 cm wide, displaying a dull conchoidal fracture, alternating green and blue bands, some white lenses (milky quartz), and a light brown matrix. Photo by Cristiano Brigida; courtesy of Chilean Rocks and Minerals.

Figure 28. Pedro II is the most important opal source in Brazil. The town is located in the northeast of the state of Piauí, and opal deposits are distributed in an area about 20 km in diameter around the township. The current opal mine is an open-pit operation. Photo courtesy of Prime Gems.

pality, located in the northeastern state of Piauí (figure 28). According to the local artisanal miners, the first precious opals were found near the end of the 1930s. During its peak in the 1960s and 1970s, more than 30 mining operations were active. However, by the early 1980s, over two-thirds of the mines were abandoned. Currently, opal mining in this area is still small-scale and mostly manual.

The opals in this region are found in both primary and alluvial deposits. In the primary deposits, opal occurs in veins in the host sandstones (figure 29, left). This occurrence is similar to Australian opal deposits in that both are of a sedimentary nature. The vendor displayed an interesting rough opal attached to a piece of intrusive igneous rock, creating a "salt and pepper" appearance (figure 29, right). According to the vendor, diabase dikes intruded into the sedimentary rocks in this area. Diabase is of basaltic composition, and its main constituent minerals are plagioclase feldspar and pyroxene, which are of lighter and darker colors, respectively. This rough piece shows that opal also develops

Figure 29. Opal rough from Pedro II shows that opal can occur in veins in the host sedimentary rocks (left) or as thin layers attached to intrusive dikes (right). The sedimentary rocks have a light color, while the dikes are darker. Photos by Tao Hsu (left) and Robert Weldon (right); courtesy of Prime Gems.

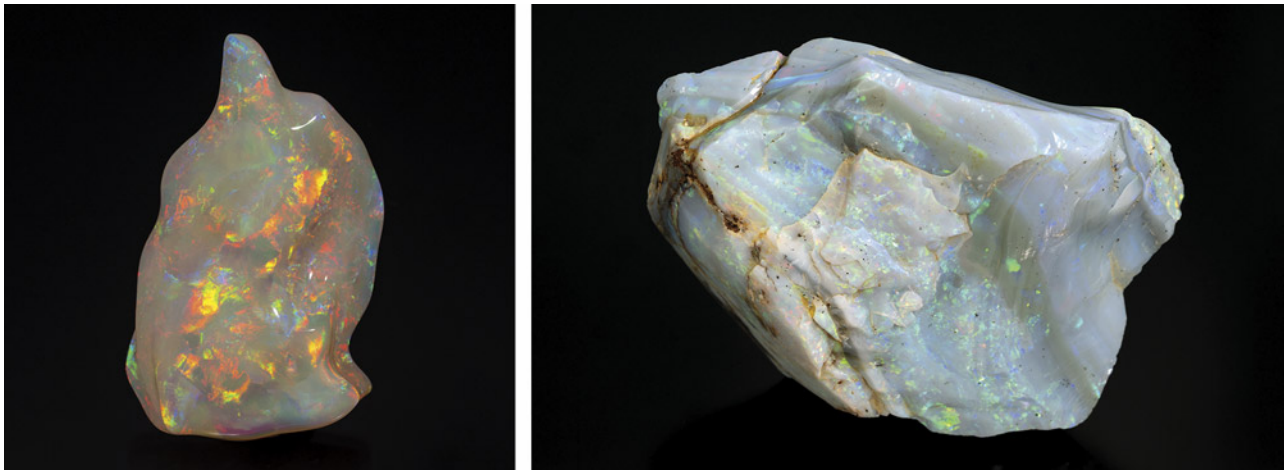

Figure 30. High-quality opal from Brazil shows extremely vivid play-of-color. Some are of transparent light gray to white bodycolor such as this 132.3 ct freeform (left), while others have darker bodycolor (right). Photos by Robert Weldon; courtesy of Prime Gems.

at the contact between the dike and the host sedimentary rocks.

At the region's alluvial deposits, miners wash and manually extract opal. This is hard work but feasible for those who cannot afford mechanical equipment. Most of the miners alternate between opal mining during the dry summer and farming in the rainy season.

Prime Gems offered Brazilian opal with transparent light gray to white bodycolor from Pedro II, similar in appearance to white opal from Australia (figure 30, left). The play-of-color was especially charming in less transparent pieces that showed colors of the whole spectrum, with bluish and greenish colors most commonly displayed. Red play-of-color is rarer and more sought after, with a higher price tag. Some pieces with darker bodycolor resembled Australian black opal (figure 30, right).

Finished products available at the show included loose opal as cabochons, freeform polished singles or pairs, doublets, and some mosaic pieces. The top-quality materials displayed a vibrant whole-spectrum play-of-color. Opal that was of good quality but too thin for freeform single pieces was used to make doublets, with the thin opal layer glued to a dark base. To support local communities, mine operators allow the local people to use very small pieces of opal from mine waste to create mosaics for sale. The supplemental income from the sales of the mosaics can reach as much as $30 per day.

The miners informed the author that Brazilian opals are sometimes sold as Australian in the marketplace. Brazilians are proud of the quality of their opal, and opal from Pedro II is one of the two products from the state of Piauí that bear the Geographical Indication certificate. The Brazilian government grants this GI label to products or services that are characteristic of a region. The aim is to ensure that Brazilian opal is properly represented and can generate revenue to further support mining and the local communities.

Tao Hsu

Patania Jewelry. At the GJX show, the Patania Jewelry booth featured striking silver jewelry, incorporating turquoise, red coral, and other gems, that stood out for its diversity in style. Some pieces had a strong Southwestern motif, while others blended in elements of modernism. A visit with the family at the booth while viewing designs from four generations of jewelers illustrated the diversity of styles.

The Patania family has been making jewelry in the southwestern United States since 1927. Frank Patania Sr. was only nine years old when he emigrated from Sicily to the United States in 1909 following a devastating earthquake. He opened the Thunderbird Shop in Santa Fe, New Mexico, after leaving New York following a bout of tuberculosis. His son Frank Jr., grandson Sam, and great-grandson Marco have all followed in his footsteps, each with his own distinct style.

The Thunderbird Shop was initially a curio shop selling Navajo and Pueblo silver jewelry along with Native American blankets, rugs, pottery, baskets, beadwork, and paintings. Frank Sr. started selling his own silver and turquoise art nouveau and Native American–inspired pieces such as jewelry, boxes, belt buckles, spoons, and letter openers out of the shop in the 1930s (figure 31). With the help of his wife, Aurora Patania, and other family members, the Thunderbird Shop grew and became a popular Santa Fe destination for prominent artists such as Georgia O'Keeffe. In fact, a 1933 Alfred Stieglitz photograph shows her wearing one of the Thunderbird Shop's ridged silver bracelets, since renamed "Georgia" in her honor. Frank Sr. was known as a jewelry artist who brought a Mediterranean influence to silver and turquoise work. A second Thunderbird Shop was opened in Tucson in 1936.

As an apprentice to his father, Frank Jr., or "Pancho," carried forward the silversmithing tradition, expanding it to incorporate modern design concepts. He began entering

Figure 31. "Cleopatra" sterling silver necklace designed by Frank Patania Sr., featuring 99 Morenci turquoise stones. Photo by Robert Weldon; courtesy of Patania Jewelry.

pieces in juried shows and developed a reputation as a top U.S. designer in the contemporary art movement. Frank Jr. was known for his meticulous craftsmanship, not only in jewelry but also in liturgical items and abstract sculptures. Two of his cuff bracelets are in the permanent collection of the Smithsonian American Art Museum. Figure 32 shows a duplicate of one—the "Asymmetry" hollow-form bracelet, also known as the "Twin Peaks" bracelet.

Sam Patania studied under Frank Jr. for 10 years starting at age 14. After this training period, Sam began branching out with his own designs featuring metal texturing and shaping methods such as repoussé. He credits Danish silversmith Georg Jensen and American artist William Spratling as his inspirations. This year at AGTA, Sam's expertise and passion for texturing was evident at his demonstration during the MJSA Journal LIVE session. Fig-

Figure 32. One of two identical silver hollow-form bracelets by Frank Patania Jr. This cuff, known as both "Asymmetry" and "Twin Peaks," was made around 1960 from six pieces of sterling silver using a small superstructure for support during the soldering process. The cuff weighs 100 g and measures 7 cm (2.75 in.) at its widest point. Photo by Robert Weldon; courtesy of Patania Jewelry.

Figure 33. Nebula series necklace by Sam Patania, featuring sterling silver and spiderweb turquoise from the Number 8 mine in Nevada used for the pendant, while the necklace consists of turquoise beads from the Sleeping Beauty mine in Arizona. Photo by Sam Patania; courtesy of Patania Jewelry.

ure 33 shows an example of his work with turquoise and silver.

Sam's son Marco Patania is continuing the storied family tradition with silver forming, texturing, and stamping. Trained by his father for six years from the age of 13, with additional training at the Haystack School of Craft in Maine, Marco draws inspiration from the mid-century modern vibe and the unique role of Los Alamos, New Mexico, in nuclear research during that era. He pays homage to these themes by incorporating vintage uranium-containing glass marbles into modern cuff designs (figure 34). These marbles fluoresce a bright yellowish green under ultraviolet light.

For nearly a century, the Patania family has followed a tradition of excellence in Southwestern and modern jewelry craftsmanship.

Jennifer Stone-Sundberg

The appeal of non-nacreous pearls. Pearls never disappoint at the AGTA and GJX shows, and this year was no exception. While quantities were lower, a good supply of Tahitian, freshwater, and South Sea pearls was available. AGTA hosted a booth sponsored by Martin Rappaport featuring nacreous natural pearls from Bahrain, complete with reports from DANAT, the Bahrain Institute for Pearls & Gemstones. Of particular interest was a wide selection of natural non-nacreous pearls.

Several vendors at GJX offered non-nacreous conch pearls, with a smaller selection available at the AGTA show. Alec Rupp-Smith of Aloha Pearls Hawaii showed a fabulous graduated, mixed-color conch pearl necklace (figure 35) at both the GJX and Pueblo shows. The necklace featured 37 conch pearls with a total weight of 179 carats. Thirty-two diamonds, 9.06 carats total, were used as accents to the suite of pearls.

Rupp-Smith also presented an interesting Melo pearl from Myanmar (figure 36). The pearl was clearly cut in half, with the other half likely fabricated into jewelry. The remaining 57 ct half was polished to display the fine concentric rings used to help separate bead-nucleated cultured pearls from their natural counterparts, without the need for X-ray tomography. The banding was visible even without a loupe.

Figure 34. Silver cuff by Marco Patania. Note the antique uranium glass marble beads that fluoresce under UV light (right) and the hand stamping on the interior. Photos by Robert Weldon; courtesy of Patania Jewelry.

Figure 35. Necklace featuring 37 conch pearls accented by 32 diamonds. Photo by Robert Weldon; courtesy of Aloha Pearls Hawaii.

Somewhere in the Rainbow returned to the AGTA show to highlight recent acquisitions to their ever-growing collection. The mission of the collection is to bring education and enjoyment of fine colored gems to museums, galleries, and facilities dedicated to preserving the rarity and beauty of these minerals, gems, and articles of jewelry. The collection features pearls and colored stones from a wide contingent of designers from around the world. This year, three non-nacreous pearl creations stood out, sourced from Carlos Chanu, owner of California-based PCD Pearls.

The first was a *Cassis* pearl suite consisting of a graduated necklace and convertible ring/brooch all fabricated in 18K gold and platinum by designer Jim Grahl of Balboa Island, California (figure 37, left). Chanu sourced the pearls from Europe over the course of one year. The layout of the necklace took a month to get just right, with a nicely

Figure 36. Melo "half pearl" weighing 57 ct. Photo by Robert Weldon; courtesy of Aloha Pearls Hawaii.

matched blend of size, shape, and color. The ring/brooch pearl is one of the finest examples of *Cassis* known.

The second is the "Golash" brooch in figure 37 (right), named after the man who purchased it at an antique store in 2000 for $14, which dates back to 1835 and was fabricated in the state of Rhode Island. Two rare quahog pearls (*Mercenaria mercenaria*) are set in the piece. At 13.5 ct and 13 mm, the larger, slightly button-shaped pearl has a glass-

Figure 37. Left: Cassis *pearl necklace and convertible ring/brooch designed by Jim Grahl. Right: "Golash" brooch featuring fine quahog pearls. Photos by Robert Weldon; courtesy of the Somewhere in the Rainbow collection.*

*Figure 38. Quahog (*Mercenaria mercenaria*) pearl suite offered at the GJX show. Photo by Robert Weldon; courtesy of Pacific Coast Pearls.*

like surface and stunning color that make it an exceptional natural quahog pearl. *Mercenaria* pearls are rare, found as a byproduct of the clam fishing industry on the East Coast of the United States. The smaller, near-perfect drop-shape pearl measures nearly 9 × 7 mm and weighs 2.89 ct. Uniform natural drop pearls are among the rarest for any mollusk. As part of an international pearls exhibition, the "Golash" brooch toured the world from 2001 to 2008.

Pacific Coast Pearls (Henderson, Nevada) brought an impressive array of natural pearls to GJX this year. After owner Wes Rankin found his first abalone pearl while diving off the coast of California, he spent the next decade collecting and purchasing pearls. This led to what has become one of the largest selections of natural pearls on the market today. At the show, co-owner Tish Rankin assembled an extraordinary suite of quahog pearls, just waiting for the right designer and inspiration to come along (figure 38). If only the humble clam had known.

Eric Fritz

Thirty years later: "The Royal Tapestry" revisited. Three generations of the Piat family gathered at the University of Arizona Alfie Norville Gem & Mineral Museum in Tucson on February 1 to see "The Royal Tapestry" (see Spring 2022 GNI, pp. 110–111) for the first time. The tapestry (figure 39) was created by French master jewelry house Cristofol Paris more than thirty years ago, with Maison Piat (Paris) procuring the gemstones and facilitating their cutting. Prior to the gathering, Daniel Piat was the only family member who had seen the completed tapestry.

The tapestry contains almost 27,000 emeralds, diamonds, rubies, and blue and yellow sapphires as well as 37.5 lbs of 18K gold. Its 122 × 71 cm (42 × 24 in.) dimensions, the same as those of an Islamic prayer rug, were specified by the royal family in the Middle East who privately commissioned it. More than 25 cutters matched the stone sizes within one-tenth of a millimeter. Cristofol Paris artisans spent more than 16,000 hours crafting the tapestry. Manufacturing a work of jewels that moved and flowed like a carpet or woven cloth required a form of prong setting, new at the time, that involved fewer "shared" prongs. Throughout the process, in a time before the advent of mobile phones and digital images, materials were shipped back and forth between Paris, Bangkok, Jaipur, and the Jura region of France.

Figure 39. Emmanuel and Daniel Piat (right) examine "The Royal Tapestry" together for the first time at the Alfie Norville Gem & Mineral Museum. Photo by Robert Weldon.

Figure 40. Left: Two Kashmir sapphire rough crystals: 77.00 ct unheated (left) and 25.20 ct heated (right). Right: Unheated Kashmir sapphires. Left to right: 1.29 ct pear shape, 2.60 ct cushion cut, 21.09 ct dragon carving, and 4.08 ct oval cut. Photos by Robert Weldon; courtesy of Eddie Cleveland of KashmirBlue and Jeffery Bergman of EighthDimensionGems.

The tapestry remained with the unnamed royal family until the early 2000s, when it was sold to a private collector. Prior to its exhibition in Tucson, it had been exhibited only in Hong Kong and London for one day each.

At the Alfie Norville Museum reception, board member Shelly Sergent touched on the origin of the tapestry concept and the process of transporting it from Zurich to Tucson. Daniel Piat shared the story of the tapestry's creation, describing the challenges presented by the design and the immense amount of work and detailed craftsmanship it required. Eric Piat noted the difficulty of sourcing the gems in a strict range of colors. Daniel said that after more than thirty years, all of the gems are still perfectly seated in more than 106,000 prongs and 26,649 seats, calling it "an engineering feat never duplicated in the jewelry world today."

Erin Hogarth
GIA, Carlsbad

New sapphire material from Kashmir. The legendary and remote sapphire mines of Kashmir, the disputed Himalayan territory between India and Pakistan, produced the finest-quality sapphires from 1890 through the 1920s. These coveted gems made their way south to Mumbai and eventually to Europe and America. Now, 100 years later, rough stones are still found, deposited through erosive processes. During the summer months, Kashmiri shepherds migrate north through the higher Himalayas, where they occasionally find sapphires in the riverbeds and on the hillsides. The glacier-tumbled rough typically exhibits rounded surfaces, affectionately referred to as "plums in pudding" by English geologist C.S. Middle in the 1930s (figure 40, left). Many in the trade believe the best available material dates back to five productive years in the 1880s.

Exhibited at the AGTA show by Jeffery Bergman (EighthDimensionGems, Bangkok) and Mayer & Watt (Maysville, Kentucky), this selection of newly found rough crystals, loose cut gems (figure 40, right), and mounted Kashmir sapphires (figure 41) was all recently faceted by lapidary artisan Eddie Cleveland of KashmirBlue, who lived in Kashmir researching the historic mines for more than a decade. Cleveland uses his heat-treating experience to turn much of the pale grayish geuda-like rough to rich, well-saturated blues through standard high-temperature heating techniques. A limited amount of new material is found each year, and only a few pieces find their way to market.

Eric Fritz

Figure 41. Two untreated Kashmir sapphire rings. Top: 1.59 ct cushion-cut cornflower blue sapphire set in white gold with VVS baguette diamonds. Bottom: 1.00 ct oval-cut medium lighter blue sapphire set in an Art Deco style diamond platinum ring. Photo by Robert Weldon; courtesy of Eddie Cleveland of KashmirBlue and Jeffery Bergman of EighthDimensionGems.

Figure 42. Untreated Montana sapphire showing a variety of cuts and the range of in-demand green to blue hues available. The stones range in size from 3.34 ct (stone on the far right) to 5.78 ct (third from the left). Photo by Jennifer Stone-Sundberg; courtesy of Obsessed Over Gems.

Montana sapphire at Obsessed Over Gems. At the AGTA show, miner and owner Don Johnson (Obsessed Over Gems, Helena, Montana) showed us an array of unheated Montana sapphires in a range of hues, cuts, and sizes (figure 42) while describing what is in demand from his customers. Pale green is particularly popular, followed by pale blue.

"Silky" stones with a soft appearance were in high demand this year, an observation echoed by other vendors. The abundance of needle inclusions in some of Johnson's silky stones rendered them translucent to virtually opaque, such as the dark green sapphire in figure 43 that he referred to as the "silk bomb."

In response to the demand for natural colors and unaltered inclusions, Johnson has moved away from heat treating any newly mined sapphires. He has many of his stones precision cut by notable cutters, resulting in clean stones with so much fire that at first glance, one could mistake them for a stone with a much higher refractive index (figure 44).

For his larger and more significant stones, Johnson has been providing mine-to-market origin and traceability reports. These certifications document both the rough and the resulting cut stone. He uses two laboratory services (GIA and AGL) for each stone he deems important enough to provide this documentation for.

Johnson, along with many other vendors, sees no softening in the Montana sapphire market; in fact, it keeps getting stronger each year. He noted that the first day of the AGTA show this year was the busiest he has ever had. On that opening day, he sold almost all of the stones with origin and traceability reports that he had brought to Tucson.

Jennifer Stone-Sundberg

Figure 43. Three Montana sapphires showing a range of silkiness, from virtually none (2.80 ct green round cut by Craig Oliveira) to moderate (10.33 ct blue cushion cut by Victor Tuzlukov) to strong (21.20 ct hazy green "silk bomb" cut by Tuzlukov). Photo by Robert Weldon; courtesy of Obsessed Over Gems.

Figure 44. A 4.44 ct grayish violetish blue modified round brilliant Montana sapphire, precision cut by Joyce Wang to maximize light return. Photo by Robert Weldon; courtesy of Obsessed Over Gems.

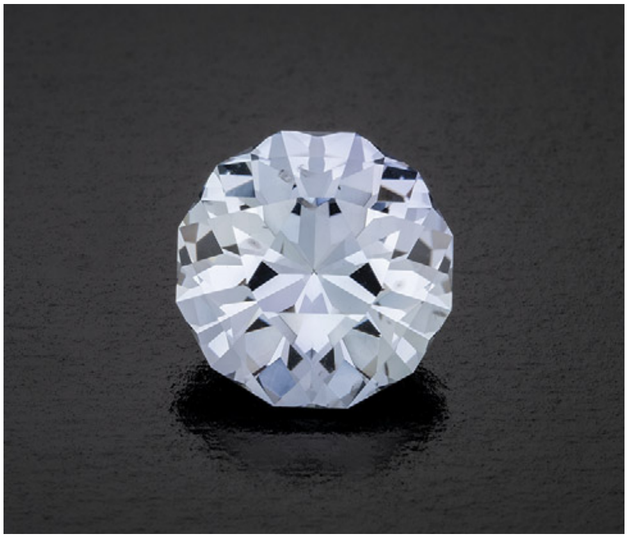

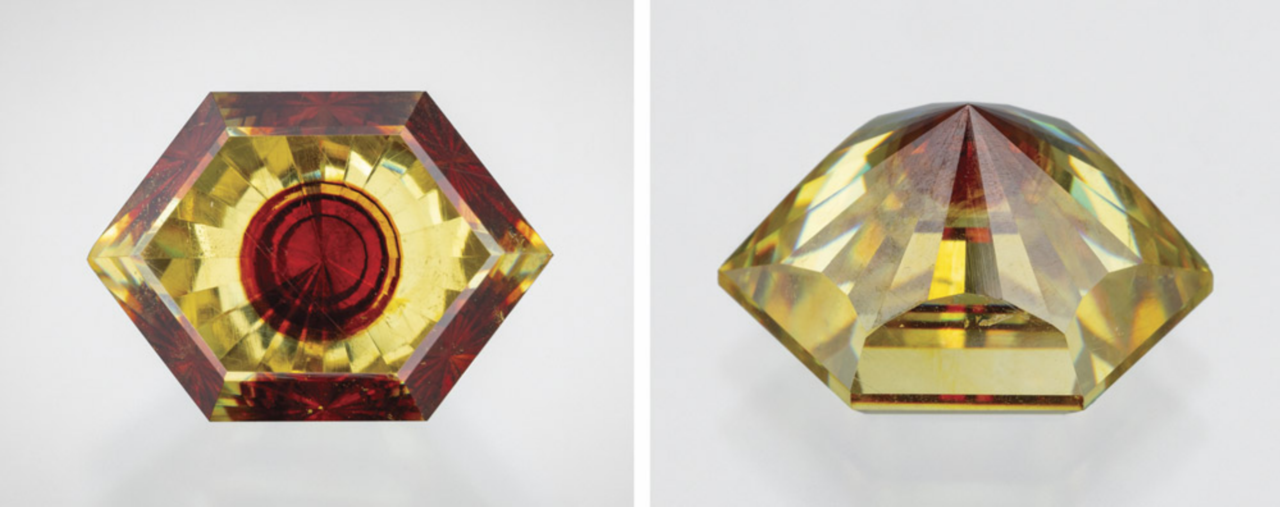

Figure 45. A 7.70 ct yellow sphalerite from Spain exhibiting a one-of-a-kind red circular center with distinct black rings. Face-up view of the pattern (left) and face-down view showing the careful placement of the red region by the cutter (right). Photos by Robert Weldon; courtesy of Dudley Blauwet Gems.

Unique sphalerite from Spain. Tucson is always full of surprises, and this year was no exception. At the AGTA show, Dudley Blauwet (Dudley Blauwet Gems, Louisville, Colorado) pulled a gem box out of his pocket to show the author a truly unique gem. This yellow sphalerite had a perfect red circle centered in the table with three sharp and distinct black rings encircling it (figure 45).

The stone was cut from material from Santander in Cantabria, Spain, a source known for producing the best facet-grade sphalerite in the world. The deposit yields orange and red stones that can be quite large, with some weighing hundreds of carats.

Sphalerite, a zinc sulfide (ZnS) mineral, is an important ore of zinc and rarely of gem quality. Colorless in its pure form, it goes from yellow to red to brown to a submetallic black color with the addition of iron. The presence of cobalt can cause a green color. Sphalerite has both an extremely high refractive index (2.37) and dispersion (>0.150), and when properly cut it can have significant brilliance. Despite these desirable gem qualities, sphalerite's softness (Mohs hardness of only 3.5 to 4.0), brittleness, and perfect cleavage make it a challenge to cut and polish (R.T. Liddicoat, *Handbook of Gem Identification*, Gemological Institute of America, Santa Monica, California, 1989).

This one-of-a-kind stone was expertly cut in Europe by an artisan who knew how to work soft, brittle stones with cleavage and how to properly center the red "dot" in the culet. The distribution of iron in this sphalerite crystal assumes distinct regions: sharply defined black rings with high iron saturation, a red circular area of medium saturation, and a surrounding area of lower saturation.

This exceptional sphalerite is proof that the combination of Mother Nature and a skilled cutter can reveal the infinite possibilities for spectacular gems.

Jennifer Stone-Sundberg

Out of Our Mines. As noted in the overview on pp. 90–93, turquoise was one of the most prolific gems in Tucson this year, found in a variety of jewelry, cut stones, and rough throughout the shows. Richard Shull and Helen Constantine-Shull of Out of Our Mines (Dyer, Nevada) reported strong sales at the AGTA show, where they had an impressive variety of mainly American stones, particularly turquoise and variscite from Nevada. They also offered other popular materials, including Oregon chalcedony, California tourmaline, Oregon sunstone, Nevada golden opal, and Arizona amethyst.

Childhood visits to trading posts during trips to the Southwest sparked Richard's fascination with turquoise and jewelry. His family's gold mining activities in California and Nevada inspired his own interest in mining. Helen similarly traveled throughout the Southwest as a child, developing a strong appreciation for the local rocks and plants. Both Shulls have extensive lapidary and jewelry-making experience. They began mining their own material in the late 1980s and became mine owners in the 1990s. Currently, they own and operate several turquoise and variscite claims in Nevada.

Helen attributed her passion for turquoise and variscite to their great variety of patterns and colors. Their highest-end turquoise is material with tight, distinct spiderweb patterning from their Black Widow and Black Web Gem mines. Only about two pounds of material has been recovered to date from the Black Web Gem mine, and it is some of the finest natural black web turquoise in the world (figure 46). Also popular are greens from the Northern Lights mine, bright greenish blue material with striking reddish brown matrix from the Double Eagle mine, blues with strongly contrasting matrix from the Nevada Blue mine, and pattern-free clear gem material from the Supernova and Aztec mines at Royston (figure 47).

Figure 46. Extremely rare Black Web Gem mine turquoise nuggets and cabochons from Nevada. These pieces are natural with no treatments except for the backings added to the cabochons. The center oval is approximately 16 × 12 mm. Photo by Richard Shull; courtesy of Out of Our Mines.

Figure 47. Natural Nevada turquoise from the Nevada Blue mine (stone farthest to the right, the pear shape on top, and the large center triangle); the Double Eagle mine (freeform triangular stone on center right and the geometric freeform below that); the Northern Lights mine (green stone); the Black Widow mine (two tight spiderweb stones on the left); and calibrated stones from the Supernova and Aztec mines at Royston (clear gem material without patterning). Sizes range from 2.12 ct to 24.62 ct. Photo by Robert Weldon; courtesy of Out of Our Mines.

Turquoise with distinct matrix patterning is a strong draw for those seeking one-of-a-kind pieces, a very popular trend in jewelry today. However, there is still solid demand for clear gem material, which the Shulls sell from both vintage sources (1950s Persian) and from their own Dyer Blue and Supernova mines in Nevada, which both produce webbed and clear turquoise (figure 48).

Variscite, a non-copper-containing aluminum phosphate mineral closely related to turquoise, is gaining popularity as consumers learn more about this mineral. Variscite comes in a range of greens and can exhibit the same fascinating matrix patterns found in turquoise (figure 49).

The Shulls described how some buyers form a personal connection with the material. For these customers, the stone they acquire is more than simply a piece of turquoise; it is a stone from a known location, uncovered by a known person, with a clear story of how it reached the final form in front of them.

Jennifer Stone-Sundberg

Figure 48. Stabilized Nevada turquoise from the Supernova mine. Sizes range from 5.61 to 13.09 ct. Photo by Robert Weldon; courtesy of Out of Our Mines.

Figure 49. Variscite with matrix (left) and clear gem variscite without patterning (right). Photos by Jennifer Stone-Sundberg; courtesy of Out of Our Mines.

Ukrainian pegmatitic heliodor and topaz. This year in Tucson, exceptionally large, clean, and attractively colored topaz and beryl from the Volodarsk-Volynskii pegmatite field in Ukraine (also known as the Volyn deposit) were very popular at multiple shows.

The Volyn deposit is in the northwestern portion of Ukraine, about 190 km from Kyiv. This deposit has been worked for more than 100 years and was initially mined for piezoelectric quartz with topaz as a byproduct. More recently it has been known for producing large and fine-quality topaz and beryl crystals as well as phenakite (Be_2SiO_4) and fluorite. The topaz ranges in color from blue to a golden-red sherry color, while the beryl ranges from mainly yellow heliodor to green beryl to greenish blue aquamarine. The large, beautifully etched heliodor crystals brought international notice to this deposit in the 1980s (G. Franz et al., "Etch pits in heliodor and green beryl from the Volyn pegmatites, northwest Ukraine: A diagnostic feature," Fall 2023 *G&G*, pp. 324–339).

At the GJX and Pueblo shows, Nomad's (New York City) had high-quality heliodor and topaz that were carefully cut to retain the beautiful rough etching patterns characteristic of this material (figure 50, left). These intricate etching patterns were retained in each gem's pavilion and visible face-up through the polished table (figure 50, right). The founders and owners are from Ukraine, and they started Nomad's in the 1990s with pegmatite minerals from Volyn.

At the AGTA and Pueblo shows, Dudley Blauwet Gems (Louisville, Colorado) featured topaz, heliodor, and phenakite from Volyn, which they have successfully been carrying for three years. This year, however, the demand for these Ukrainian gems has grown. In fact, Ukrainian topaz was one of their best sellers, with much of the material gone by the first day of AGTA. The bicolor blue to sherry topaz was a particularly strong seller, followed by blue topaz (figure 51). They noted that the miner they work with has been reworking old pockets for the last 20 years, and all of the topaz stones they offered in Tucson this year

Figure 50. Left: This 109.68 ct heliodor and 80.62 ct bicolor topaz are from the Volyn deposit in Ukraine. They are cut to leave natural etch faces on the pavilion/culet, while the crown and table are faceted. Right: A 162.22 ct pear-cut heliodor. The natural etching patterns are retained on the pavilion and are well displayed through the polished table. Photos by Robert Weldon; courtesy of Nomad's.

Figure 51. Exceptionally large and clean blue and bicolor topaz from the Volyn deposit. The blue triangular cut is 113.86 ct, the middle blue cube cut is 87.82 ct, and the blue and golden bicolor rectangular cut is 55.70 ct. Photo by Robert Weldon; courtesy of Dudley Blauwet Gems.

were from the same pocket at a depth of about 35 meters in the central part of the Volyn deposit.

The beauty, size, and availability of the gem crystals from these pegmatites bodes well for the continued presence of this material in the marketplace.

Jennifer Stone-Sundberg

Wim Vertriest
GIA, Bangkok

Gold granulation by Zaffiro. Granulation, an ancient goldsmithing technique dating back nearly five millennia to Mesopotamia, involves the joining of tiny high-karat gold or other precious metal spheres ("granules") to a metal base to create a decorative pattern (J. Wolters, "The ancient craft of granulation," *Gold Bulletin*, Vol. 14, No. 3, 1981, pp. 119–129). These patterns can be very complex, and the granulation process is one that requires a high level of precision.

In the AGTA designer showroom, we spoke with Jack and Elizabeth Gualtieri of Zaffiro (Walla Walla, Washington; figure 52), who specialize in 22K gold granulation. They occasionally incorporate platinum as well. They find the granulation technique very rewarding and meditative, as it demands extraordinary focus.

The Gualtieris formed Zaffiro in 1996 in Portland, Oregon, after meeting at the University of Kansas several years earlier. Their focus on granulation was inspired by a seminar at the university and by Elizabeth's study abroad in Florence. They chose the name "Zaffiro," which translates to sapphire in Italian. The business was a part-time venture until they could dedicate themselves to it full-time starting in 2003. They have sold their pieces through galleries, retail shows, and private clients. In 2019, they moved to Walla Walla.

Figure 52. Elizabeth and Jack Gualtieri of Zaffiro at their AGTA booth. Photo by Jennifer Stone-Sundberg.

Figure 53. "Where the Ocean Meets the Sky" is a one-of-a-kind pendant featuring a 19.51 ct Australian boulder opal and 11.37 carats of blue moonstone. The boulder opal is accented with 0.63 carats of tsavorite garnet. The granulated yellow gold is 22K, and the gold links between the elements are 18K yellow gold. Photo by Robert Weldon; courtesy of Zaffiro.

Jack and Elizabeth design and construct each piece from start to finish and consult with each other on their individual designs. They alloy their own 22K yellow, white, and rose gold and also create their own gold sheet, wire, and granulation balls. After clipping snippets of wire onto charcoal blocks, the blocks are heated to bead the metal into tiny balls of gold, which are then sorted by size through sieving. (To watch a video showing the process of fabricating granulation balls, please go to www.gia.edu/gems-gemology/spring-2024-gemnews-gold-granulation).

The Gualtieris find inspiration in the stones they purchase, the natural world around them, and architecture. In

Figure 54. Tanzanite pendant designed and fabricated by Elizabeth Gualtieri containing a 46.15 ct tanzanite crystal in a hand-fabricated setting of granulated 22K gold. Photo by Robert Weldon; courtesy of Zaffiro Jewelry.

fact, they sometimes have to negotiate over who will get to use a particular stone, as both artists may simultaneously envision designs for it.

Jack's opal, moonstone, and tsavorite garnet pendant design (figure 53) began with the Australian boulder opal. The moonstones inspired him to go larger with the design and add some movement to the piece. He said the use of green tsavorite garnet accent stones around the opal instead of blue stones was a riskier option but ultimately the right choice.

A heated rough tanzanite crystal inspired the pendant designed and built by Elizabeth in figure 54. This piece rep-

Figure 55. Suhan Wang's winning necklace design sketch for the 2023 Gianmaria Buccellati Foundation Award for Excellence in Jewelry Design, featuring platinum, emerald, ruby, diamond, and tsavorite.

resents a signature style the Gualtieris describe as "talismans," signifying the way in which collectors of the pieces connect with them. This jewelry collection features rough crystals or baroque pearls and represents some of Zaffiro's most personal pieces. The intricate caps allow for a more expressive use of granulation and accent stones.

The fusion of this ancient technique with contemporary jewelry designs is a testament to the timelessness of granulation and its endless design possibilities.

Jennifer Stone-Sundberg

ANNOUNCEMENTS

Seventh annual Gianmaria Buccellati Foundation Award winner. Suhan Wang, a graduate of GIA's Jewelry Design program in Taiwan, received the seventh annual Gianmaria Buccellati Foundation Award for Excellence in Jewelry Design. The 18 finalists and winner were announced at the GIA Alumni Collective's "Night at the Museum" event held during the AGTA GemFair in Tucson. Wang's winning design, a necklace featuring platinum coils adorned with emerald, ruby, diamond, and tsavorite, stood out to the judges for its sense of movement and skill of execution (figure 55).

Created in partnership with the Gianmaria Buccellati Foundation in 2018, the award recognizes outstanding talent in design among GIA students worldwide. Larry French, chief officer for North American strategies at the foundation, said, "On behalf of the Gianmaria Buccellati Foundation and Rosa Maria Buccellati, we want to congratulate Ms. Suhan Wang, plus all the other designers whose work has honored this competition. We also want to send our appreciation to the talented GIA design instructors whose skill and efforts helped the students on their journey to celebrate the art of jewelry design in the highest way, an art that meant so much to Gianmaria Buccellati."

As part of the award, Wang will travel to Italy and meet with a representative from the foundation.

The 2024 Gianmaria Buccellati Foundation Award for Excellence in Jewelry Design competition is underway and open to students in GIA's Jewelry Design courses who meet the eligibility requirements. Visit www.gia.edu/buccellati-foundation-award-jewelry-design for more information.

REGULAR FEATURES

COLORED STONES AND ORGANIC MATERIALS

Unusual aquamarine–white beryl. Recently, the author analyzed an interesting 41.51 ct faceted bicolor beryl (figure 1) composed of aquamarine and opaque white beryl. This gem belongs to Brazilian gem dealer Veber Leite and is part of his collection containing several similar specimens. According to Leite, the bicolor beryls were mined in Brumado, a city located in the state of Bahia, Brazil, but their geographic origin could not be confirmed.

Figure 1. A 41.51 ct freeform faceted bicolor beryl. Photo by Marina Boncompagne.

Standard gemological testing of both sections revealed a specific gravity of 2.70 and a refractive index of 1.581–1.592. Ultraviolet/visible/near-infrared (UV-Vis-NIR) spectra revealed an absorption band centered at about 810 nm, also present in both sections. In beryl, this band is associated with Fe^{2+} (D.L. Wood and K. Nassau, "The characterization of beryl and emerald by visible and infrared absorption spectroscopy," *American Mineralogist*, Vol. 53, No. 5, 1968, pp. 777–800; Y. Hu and R. Lu, "Color characteristics of blue to yellow beryl from multiple origins," Spring 2020 *G&G*, pp. 54–65) and possibly enhanced by neighboring Fe^{3+} (S. Saeseaw et al., "Geographic origin determination of emerald," Winter 2019 *G&G*, pp. 614–646). The blue section exhibited an anisotropic band around 600 nm when viewing an *e*-ray oriented absorption spectrum, typical of aquamarine (Hu and Lu, 2020). The white color was caused by an isotropic absorption band ranging from 400 to 700 nm with a nearly identical absorption coefficient through all wavelengths.

Although seemingly opaque, when exposed to the polariscope's intense light source, the white portion allowed the passage of light and showed no extinction under crossed polarizers, suggesting a polycrystalline composition.

Raman spectra were collected at room temperature using a Horiba Scientific LabRAM HR Evolution spectrometer coupled with an Olympus Scientific Solutions BX-41 microscope with a 50× magnification lens. The acquisition time was 120 seconds, grating: 500 nm. For this analysis, a 532 nm excitation laser was selected. Both sections exhibited major peaks around 321, 395, 520, 683, 1011, and 1066 cm^{-1} (figure 2). Minor peaks were observed at 448, 622, and 1141 cm^{-1}. The spectra were compatible with beryl and, although clarity treatment was not observed, displayed relatively strong absorptions at approximately 1504 and 1567 cm^{-1} (again, see figure 2) that may suggest the presence of a filling agent (M.L. Johnson et al., "On the identification of various emerald filling substances," Summer 1999

Figure 2. The Raman spectra of the blue and white sections in the 41.51 ct bicolor beryl. Spectra are offset vertically for clarity.

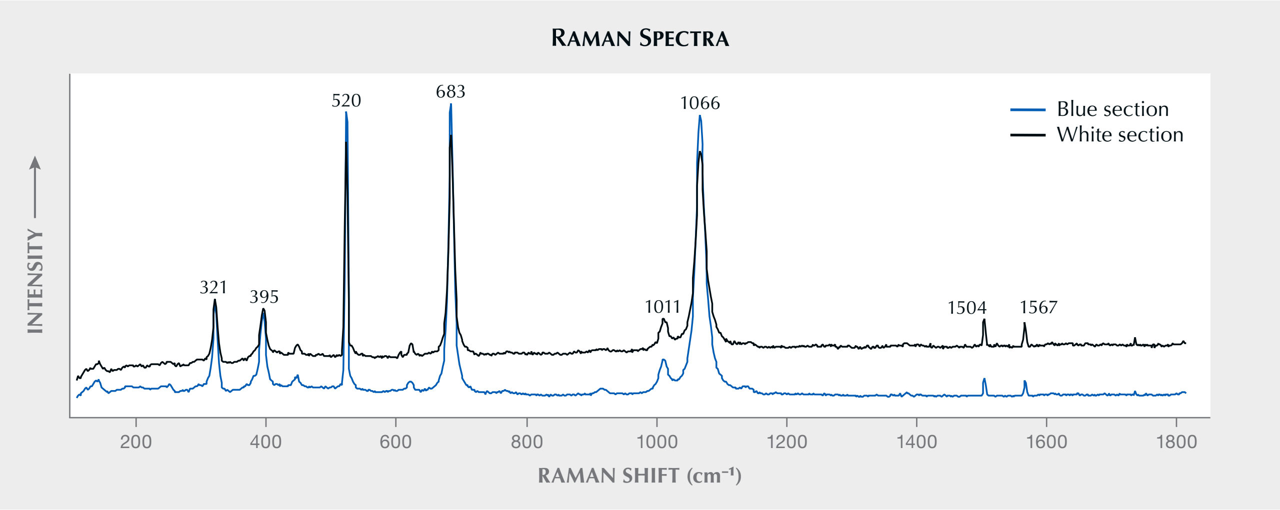

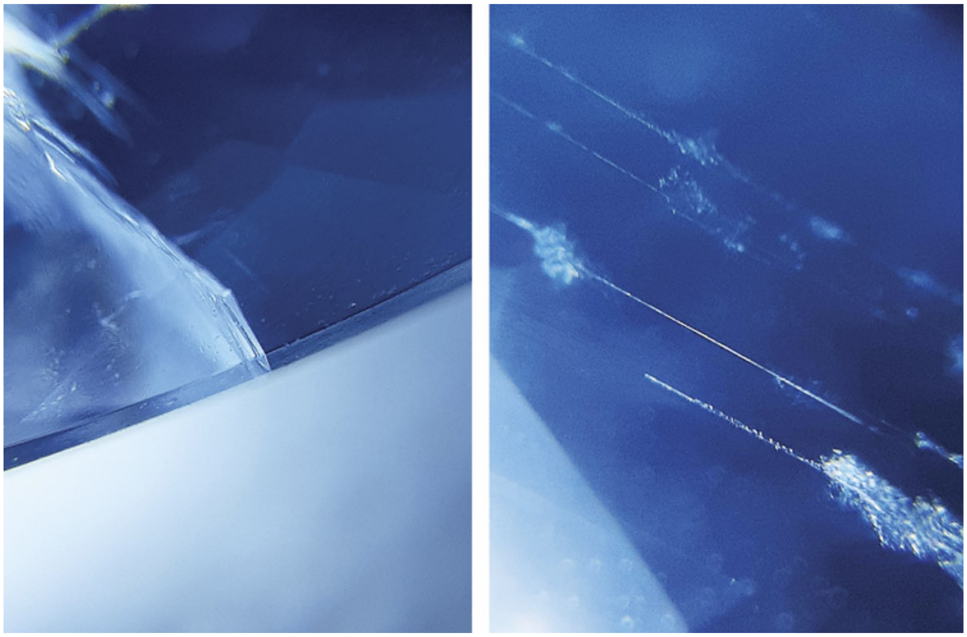

Figure 3. Left: The aquamarine–white beryl boundary. Right: Beryl channels parallel to aquamarine's c*-axis in the blue portion of the bicolor beryl. Photomicrographs by Marina Boncompagne; field of view 10.00 mm.*

G&G, pp. 82–107). Additional Raman analysis with a spectral range of 100–3500 cm^{-1} is required to determine whether the peaks are indeed related to a filling substance.

Microscopic analysis revealed a well-defined aquamarine–white beryl boundary (figure 3, left). Channels parallel to the *c*-axis were also observed (figure 3, right).

The author is aware of similar aquamarine–white bicolor beryl from the state of Minas Gerais, but this was the author's first encounter with such beryl reportedly from Brumado, Bahia.

Acknowledgments: The author thanks Professor Ariete Righi from the physics department of the Federal University of Minas Gerais (DF-UFMG) for providing the Raman analysis.

Marina Boncompagne
Federal University of Espírito Santo (UFES), Brazil

Beryl from Newfoundland, Canada. Prospectors Art Gardner and Terry Russell recently discovered concentrically zoned beryl [$Be_3Al_2(Si_6O_{18})$] in central Newfoundland, Canada, along the Bay D'Espoir Highway, and sent preliminary findings to GIA's Carlsbad laboratory. The green rims of these beryls were often sufficiently green to be considered emerald. The outer rims were bright green or pale green, and the cores were very pale green or white (figures 4 and 5). Most zones had low transparency. They formed hexagonal columns at the 1–3 cm scale, associated with mica-quartz-feldspar veins and minor tourmaline, calcite, biotite, fluorite, pyrite, and arsenopyrite. Some stones were suitable for polishing and setting in jewelry, especially as cabochons. An individual specimen may have zones that fit into the definitions of emerald and white beryl, with the brighter greens at the rims.

Canada is host to a number of gem minerals, including emerald from Yukon and the Northwest Territories (G.

Figure 4. Emerald and beryl specimens from Newfoundland, Canada. The chip on the right has a distinct green rim in this position, on its lower right edge. Photo by Emily Lane; courtesy of Art Gardner and Terry Russell.

Figure 5. In situ *emerald and beryl from Newfoundland. The primary crystal shows a lively green hue. The crystal on the lower right shows strong concentric zonation with a green rim and a white core. Photo by Emma Hutchinson Photography; courtesy of Art Gardner.*

Giuliani et al., "Emerald deposits: A review and enhanced classification," *Minerals*, Vol. 9, 2019). This beryl deposit on Newfoundland Island is within the Great Bend Complex of ophiolites. The mica-quartz-feldspar veins hosting the beryl are found within a host rock rich with scheelite [$Ca(WO_4)$]. Other pegmatitic dikes are regularly found within the bedrock, and a ~450 km belt of beryl-bearing pegmatite dikes extends across the island from east to west. This discovery adds another locality to Canada's gemological map.

The ultraviolet/visible/near-infrared (UV-Vis-NIR) absorption spectrum of the green zone in the leftmost crystal in figure 4 displayed absorption bands at 420 (Fe^{3+}), 615 (V^{3+}, Cr^{3+}), and 835 nm (Fe^{2+}) and a sharp but low absorption peak at 956 nm (H_2O) (figure 6). These are due to the combined effects of vanadium and iron, with minor influence of chromium. These features are common in emerald.

The beryls' chemistry, as determined by laser ablation–inductively coupled plasma–mass spectrometry (LA-ICP-MS), is unique from other worldwide deposits; both the white cores and green rims had elevated lithium and cesium (figure 7). The lithium and cesium values are within the range expected more of a beryl from a lithium-cesium rich pegmatite, such as many morganites or goshenites. The green coloration is primarily due to vana-

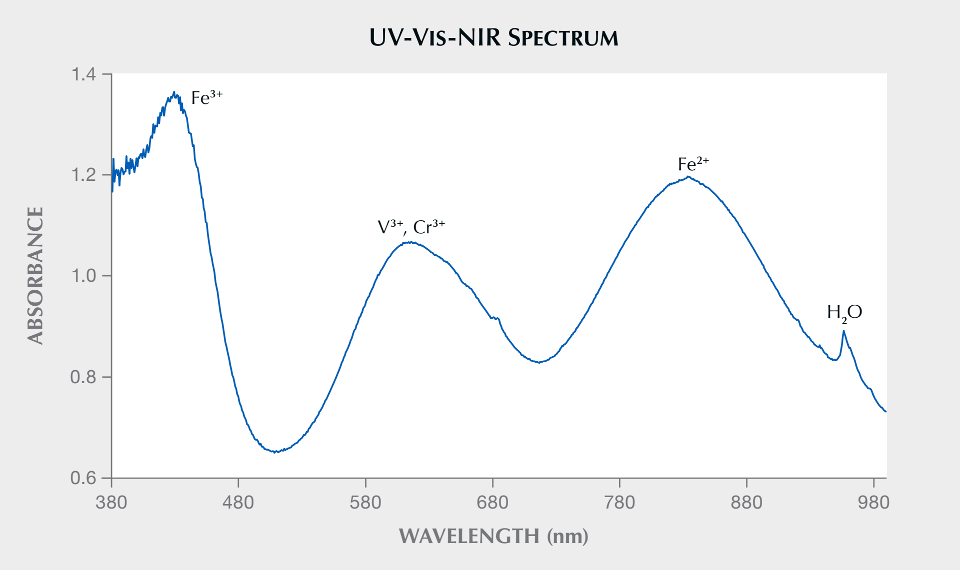

Figure 6. UV-Vis-NIR absorption spectrum of the first crystal on the left in figure 4. Absorption bands are seen at 420, 615, and 835 nm, and a low but sharp peak at 956 nm.

TABLE 1. Composition ranges (in ppm) for significant minor elements in Newfoundland emeralds, measured by LA-ICP-MS.

Sample area	Li	Na	Mg	V	Cr	Fe	Cs
Green rims	1100–1310	9980–11200	5290–8210	1000–2100	11.8–213	1500–2330	4260–5180
White cores	2000–2290	8070–9640	1630–3570	52.7–270	0.93–7.77	723–903	2630–3240
Detection limit (ppm)	0.06	2	0.05	0.01	0.3	2	0.02

dium, with minor chromium, which are both chromophores of emerald (table 1). The magnesium is consistently higher than iron, as expected for emeralds (R.E. Henry et al., "Crystal-chemical observations and the relation between sodium and H_2O in different beryl varieties," *Canadian Mineralogist*, Vol. 60, 2022, pp. 625–675). The magnesium and transition metals are higher in the green rims than in the white cores, which have higher lithium. However, the cesium is higher in the green rims. This is likely due to the near-mutual exclusivity of beryllium site and aluminum site cation substitutions, preventing significant lithium substitutions when there is a high level of magnesium and transition metals (R.E. Henry et al., "Predicting the crystal structure of beryl from the chemical composition," *Canadian Journal of Mineralogy and Petrology*, Vol. 61, No. 4, 2023, pp. 873–897). As magnesium and iron require charge balancing, sodium and cesium can serve this purpose; while cesium is associated with lithium in geologic environments, it does not have the same crystal-chemical constraints as lithium in beryl.

These beryls' formation at the intersection of an ophiolite and a pegmatite is consistent with conditions required to create emerald as it brings together a source of vanadium or chromium with a source of beryllium. The goshenite cores are a feature that have been seen in emeralds from some other localities, including Russian emeralds.

Due to their uniquely high cesium and lithium, emerald zones of beryl from this locality are easy to differentiate. Should gem-quality specimens come to the market, a method is in place to confirm their origin as Newfoundland. Efforts are underway to continue exploration for additional gem material.

Rhiana Elizabeth Henry
GIA, Carlsbad

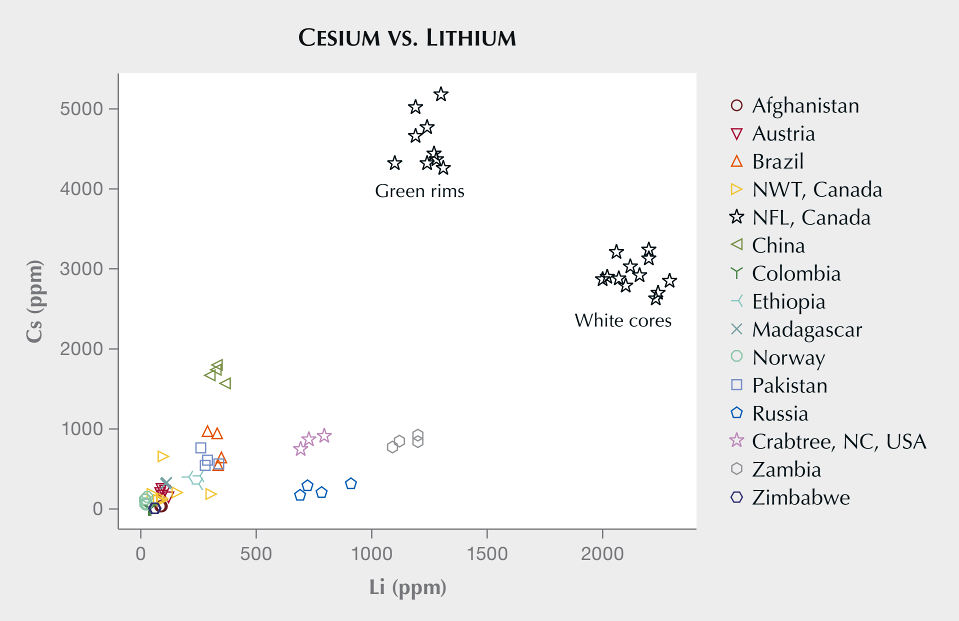

Figure 7. Cesium vs. lithium for emerald from worldwide localities, demonstrating the unique chemistry of Newfoundland (NFL) emeralds. Worldwide emerald data from GIA laboratories.

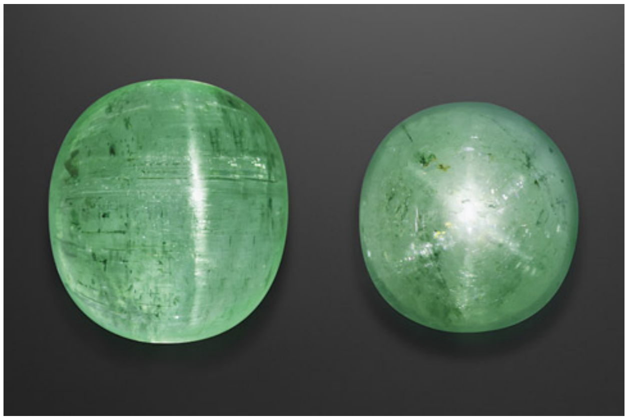

Figure 8. Cat's-eye emerald (11.31 ct) and star emerald (4.99 ct) from Chitral, Pakistan. Photo by Lhapsin Nillapat; courtesy of Mohammed Ayub (Pretty Little Gem Co, Ltd, Bangkok).

Phenomenal emeralds from Chitral, Pakistan. In November 2023, GIA researchers had the chance to study a parcel of emeralds reportedly from Chitral in Pakistan. All of the stones matched previously documented characteristics of emeralds from Chitral (C.S. Hanser et al., "Comparison of emeralds from the Chitral District, Pakistan, with other Pakistani and Afghan emeralds," *Journal of Gemmology*, Vol. 38, No. 6, 2023, pp. 582–599).

Among the stones were two cabochons that showed unusual phenomena: chatoyancy and asterism (figure 8). Both had a refractive index of 1.57 (spot reading) and a yellowish green to green color, which identified them as emerald.

Cat's-eye emeralds are found in a number of locations, most notably Brazil and Colombia. The effect is caused by large concentrations of fine parallel tubes. Proper orientation of these linear features during cutting can result in a sharp, centered cat's-eye when the tubes reflect light.

Star emeralds are even rarer, with most originating from Brazil and Madagascar. The effect is usually caused by very small thin films that reflect light. The proper orientation of the cabochon dome with respect to tiny platelets can result in a six-rayed star that moves across the curved surface of the stone. In this emerald, some of the platelets that create the lower left arm are highlighted by iridescent reflective colors.

Figure 9. A 1.59 ct red musgravite. Photo by Shunsuke Nagai.

To our knowledge, these are the first phenomenal emeralds from Chitral, and they offer prime examples of lesser-known phenomenal emeralds.

Wim Vertriest
GIA, Bangkok

Identification of chromium-bearing red gemstones using photoluminescence: A red musgravite case study. Photoluminescence (PL) provides us with useful information to understand physical properties of gem materials and can also be used for gem identification and treatment detection. For example, a 1.59 ct red musgravite (figure 9) that had previously been examined by the Central Gem Laboratory in Japan (Z. Zhenghao et al., "A remarkable Cr-bearing red musgravite," *Journal of Gemmology*, Vol. 38, No. 6, 2023, pp. 548–551) was also submitted to GIA's Tokyo laboratory for identification. Its standard gemological properties (refractive index, specific gravity, dichroism, and UV fluorescence reaction), Raman spectrum, and ultraviolet/visible spectrum were consistent with musgravite. The chemical formula was measured as $Be_{1.21}(Mg_{1.95}, Fe_{0.01}, Zn_{0.02})Al_{5.86}O_{12}$ by laser ablation–inductively coupled plasma–mass spectrometry (LA-ICP-MS) with a chromium concentration of 1360–1840 ppm (table 1). A PL spectrum for musgravite (figure 10) was also collected with a 532 nm laser and consisted of two strong

TABLE 1. Trace-element concentrations (in ppmw) of the red musgravite sample, measured by LA-ICP-MS.

	Ti	V	Fe	Cr	Zn
Concentration	50.4–160	120–275	366–473	1360–1840	2440–2800
Detection limit (ppmw)	0.7	0.07	5	0.6	0.2

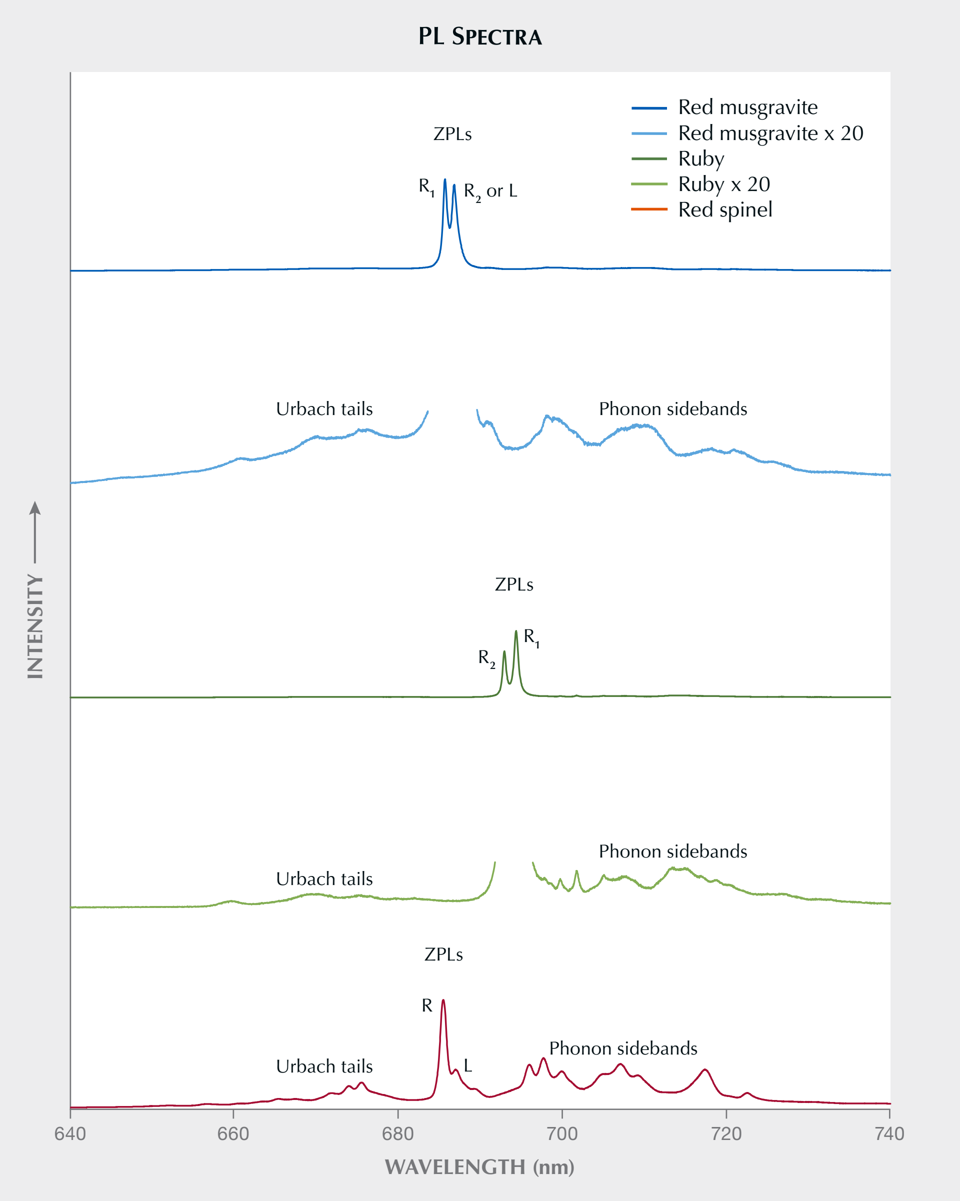

Figure 10. The PL spectrum of the red musgravite consisted of two very strong peaks at 685.7 nm (R_1) and 686.8 nm (R_2 or L). In the spectrum below that, its weak side peaks are expanded by multiplying the intensity by 20. They are partially similar to those of ruby (692.9 (R_2) and 694.4 (R_1) nm), its expanded weak side bands, and a red spinel (685.5 (R) and 687.1 (L) nm). Spectra are offset vertically for clarity.

peaks and weak side bands. Interestingly, the positions of the strong peaks were close to those caused by chromium in spinel, but the overall pattern was similar to that caused by chromium in ruby or sapphire. PL emission spectra are collected by exposing a material to strong short wavelength light, creating excited energy states in the material. These excited energy states then relax and return to a ground state by emitting light at a longer wavelength than the excitation wavelengths. The light collected during this relaxation is the PL spectrum. Trace amounts of chromium in many materials can easily enter these excited energy states and produce characteristic PL spectra in different gems such as ruby, spinel, and musgravite.

In this report, we investigated the reasons why these PL spectra differ between red musgravite, ruby, and spinel. The two strong peaks at 685.7 and 686.8 nm of the red musgravite are referred to as zero-phonon lines (ZPLs) that do not contain the energy of "lattice vibrations," which are the motions of atoms around their equilibrium positions. These peaks result from the transition from the lowest excited state to the ground state of three 3d orbital electrons of the Cr^{3+} ion replacing the Al^{3+} ion at the center of oxygen polyhedra, as in ruby and red spinel. The crystal structure of musgravite includes one type of AlO_4 tetrahedron and three types of AlO_6 octahedron: one undistorted and two differently distorted; see figure 11A, drawn using VESTA software (K. Momma and F. Izumi, "VESTA 3 for three-dimensional visualization of crystal, volumetric and morphology data," *Journal of Applied Crystallography*, Vol. 44, 2011, pp. 1272–1276) and the reported crystal structure

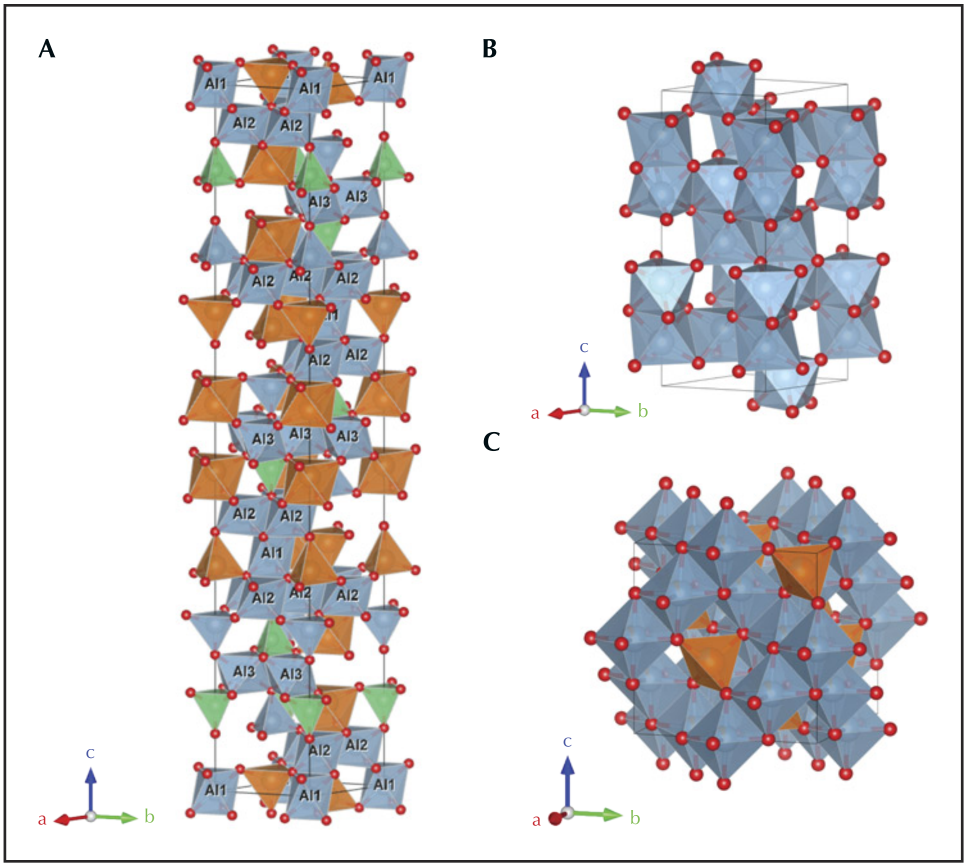

Figure 11. Polyhedral representations of the crystal structures of (A) reported musgravite, $BeMg_{1.63}Fe_{0.37}Al_6O_{12}$ (Nuber and Schmetzer, 1983); (B) typical corundum, Al_2O_3; and (C) normal spinel, $MgAl_2O_4$. Thin black lines depict the unit cells. The green tetrahedra are BeO_4. The orange tetrahedra and octahedra are MgO_4 and MgO_6, respectively. The blue tetrahedra and octahedra are AlO_4 and AlO_6, respectively. In musgravite, the AlO_6 octahedra have three types: one undistorted (Al1) and two differently distorted (Al2 and Al3).

data (B. Nuber and K. Schmetzer, "Crystal structure of ternary Be-Mg-Al oxides: taaffeite, $BeMg_3Al_8O_{16}$, and musgravite, $BeMg_2Al_6O_{12}$," *Neues Jahrbuch fur Mineralogie, Monatshefte*, 1983, pp. 393–402). The chromium PL emission is split into two strong lines, due to either the distortion of the AlO_6 octahedron as in ruby and sapphire, or the occupation of multiple crystal sites by chromium. The position of the red musgravite is shorter in wavelength than in ruby and sapphire but almost equal to that of red spinel. This means the energy difference between the excited and ground states is greater than that in ruby and close to that in red spinel.

The chromium PL spectrum for musgravite shows additional small peaks at longer and shorter wavelengths, termed "phonon sidebands" and "Urbach tails," respectively (again, see figure 10). If the intensity of the main ZPLs is a large proportion of the total luminescence intensity, it indicates that the Debye-Waller factor, representing the magnitude of atomic vibrations in a crystal structure, is small. The weak sidebands on both sides of the red musgravite indicate that the Debye-Waller factor is smaller than that of red spinel but similar to ruby.

PL spectroscopy on chromium-bearing gemstones is not only one of the most powerful tools for quick and nondestructive identification but also a means to obtain interesting physical properties of rare gemstones by comparing with the PL spectra of familiar gems. Furthermore, the difference in degree of the Debye-Waller factor may be one of the reasons why the presence or absence of heat treatment can be detected by PL in spinel (S. Saeseaw et al., "Distinguishing heated spinels from unheated natural spinels and from synthetic spinels: A short review of on-going research," https://www.gia.edu/doc/distinguishing-heated-spinels-from-unheated-natural-spinels.pdf, April 2, 2009), but not in corundum.

Taku Okada and Makoto Miura
GIA, Tokyo

Challenges in identifying drilled keshi pearls. Distinguishing natural pearls from non-bead cultured (NBC) pearls, commonly referred to as "keshi" in the industry, has become increasingly complex. While traditional methods such as radiomicrography were once reliable for the identification of South Sea keshi NBC pearls, recent advances in pearl drilling techniques have rendered these conventional approaches less foolproof. As a result, there is a growing need for advanced data analysis to study the internal structure, chemistry, and other spectral features associated with the mollusk origin to enable reliable separation of natural from NBC pearls.

To further examine challenging structures, GIA's Mumbai laboratory borrowed pearls represented as natural from a known source. The lot consisted of 40 white to light cream drop and oval pearls (28 undrilled, 7 drilled, and 5 partially drilled). The smallest weighed 0.62 ct and measured 5.17 × 4.16 mm, and the largest weighed 2.95 ct and measured 9.53 × 6.65 mm (figure 12). The pearls all looked new, with smooth, high-luster surfaces that were free of blemishes. Under 40× magnification, the surfaces showed well-defined overlapping fine aragonite platy structures that accounted for their silky surface sheen.

Energy-dispersive X-ray fluorescence revealed manganese levels ranging from below detection level to 33.80 ppm and higher strontium levels ranging from 1756 ppm to 3364 ppm. Most of the pearls showed an inert reaction under X-ray fluorescence, while some had a weak yellowish green reaction. The latter reaction accounts for the higher manganese levels recorded. The pearls emitted medium to strong yellowish green fluorescence under long-wave ultraviolet light and a similar weaker reaction under short-wave UV. Based on these analyses, a saltwater origin was confirmed for all of the pearls.

Examined with real-time X-ray microradiography (RTX), most of the pearls showed minimal growth arcs, and some revealed faint linear-looking features visible only in certain directions. External and internal features aroused suspicion that these pearls were NBC. Another important observation was related to the size and length of the drill holes. Given the importance of maintaining weight, it is customary to drill drop and oval pearls to approximately one-third of their length. These pearls, however, were drilled to a depth that covered more than two-thirds of their length, while others were fully drilled with oversized drill holes. This indicated the pearls were drilled with the specific intention of concealing internal structures (Summer 2023 Lab Notes, pp. 218–220).

RTX imaging was performed for all the pearls in three directions, with careful alignment along their lengths to detect the presence of any linear feature or its remnants resulting from the drilling process. In most cases, proving a cultured origin only through RTX imaging was challenging. Consequently, the structures were studied using X-ray computed microtomography (μ-CT) analysis, as shown in table 1. In pearls 1 and 2, both undrilled, RTX imaging revealed a few distinct growth arcs, but not much was visible at their centers. Pearl 1 exhibited a small suspicious linear feature along its length, while pearl 2 did not. Interestingly, μ-CT analysis revealed an elongated linear feature running along the length of both pearls, accompanied by a few growth arcs, with the outer nacre lacking many growth features.

Pearls 3 and 4 were partially drilled, and both exhibited drill holes of unusual length and size compared to those observed in natural pearls. RTX imaging showed a few growth arcs toward the outer nacre and minimal growth at the center around the drill hole area. When aligned along their lengths, remnants of a linear feature crossing the drill hole were clearly visible in pearl 3, whereas pearl 4 did not show any evidence of the linear feature. Similarly, μ-CT analysis on both pearls revealed remnants of the linear feature toward the end of their drill holes, indicating an unsuccessful attempt to remove the linear features. Pearl 5, which was fully drilled, had fine growth arcs along its

Figure 12. Lot of 40 drop and oval pearls, with the smallest weighing 0.62 ct and measuring 5.17 × 4.16 mm and the largest weighing 2.95 ct and measuring 9.53 × 6.65 mm. Photo by Gaurav Bera.

TABLE 1. Surface appearance and internal structures of the pearl samples.

Sample	Macro	RTX	μ-CT
Pearl 1 1.44 ct 6.98 × 5.28 mm		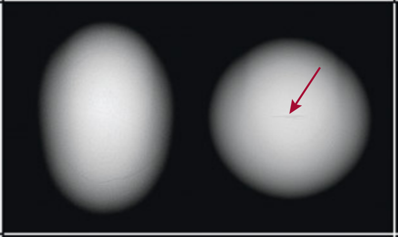	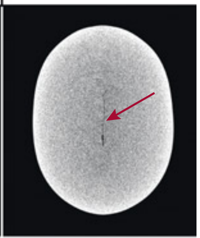
Pearl 2 1.79 ct 6.66 × 6.00 mm	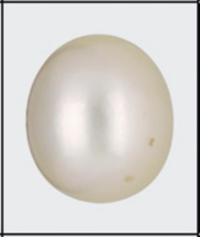	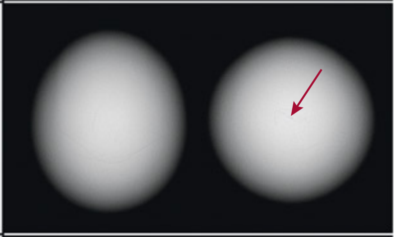	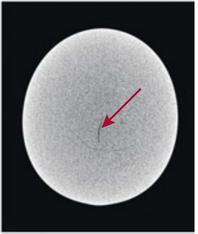
Pearl 3 1.70 ct 9.27 × 6.49 mm	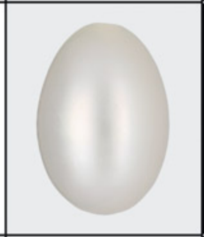	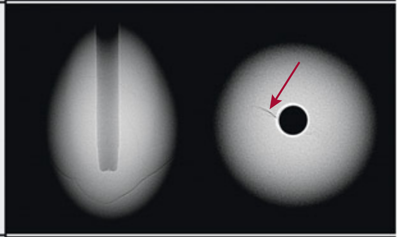	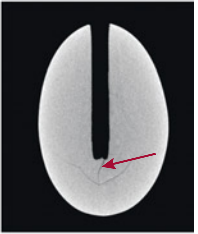
Pearl 4 2.04 ct 7.53 × 6.21 mm		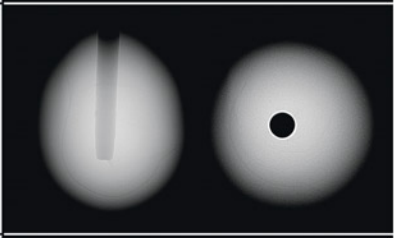	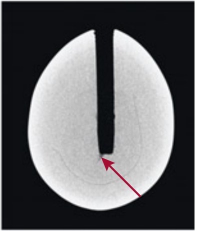
Pearl 5 1.43 ct 7.79 × 6.26 mm		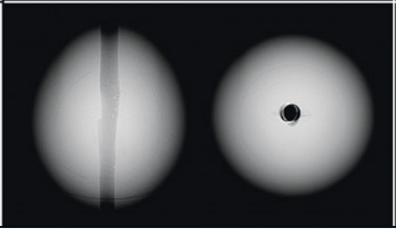	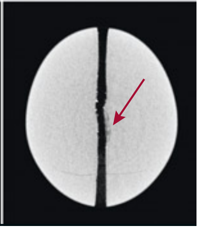

shape in RTX imaging, with a faint shadow feature running parallel to the drill hole. Through μ-CT analysis, a linear feature near the drill hole area was clearly visible.

As observed, structures from the samples closely resembled those observed in South Sea NBC pearls from the *Pinctada maxima* mollusk (A. Homkrajae et al., "Internal structures of known *Pinctada maxima* pearls: Cultured pearls from operated marine mollusks," Fall 2021 *G&G*, pp. 186–205). In particular, drop and oval pearls from this mollusk should be carefully examined to avoid misidentification as natural due to the absence of structure if only examined under RTX imaging.

Natural drop and oval pearls are highly valued, and those with exceptional appearance and size are not easy to find. In recent decades, some members of the trade have attempted to conceal the linear features visible in South Sea keshi pearls using film or dental X-ray machines and subsequent drilling to remove any evidence. This often results in remnants of the linear features being left behind, as observed in these samples. These remnants can only be identified by carefully aligning the pearls in RTX imaging and through μ-CT analysis. Such subtle features can be easily overlooked during testing, potentially leading to their misinterpretation and misidentification as natural pearls.

It is therefore essential for the trade to remain alert and informed about these increasingly frequent practices.

Roxane Bhot Jain, Abeer Al-Alawi, Anukul Belanke, and Lubna Sahani
GIA, Mumbai

Two pen pearls from Bahrain. Pen or pinna pearls, also known as the "fan clam," originate from the marine bivalve mollusk belonging to the genus *Pinna* or *Atrina*. They are commonly found across the Indo-West Pacific region, from southeastern Africa to Melanesia and New Zealand, extending north to Japan and south to New South Wales. Additionally, they can be found in the Mediterranean Sea, the Red Sea, and the Arabian (Persian) Gulf. Typically, the shell size ranges from 10 to 60 cm, producing pearls measuring up to 11 mm and rarely even 16 mm. Most of these pearls are non-nacreous, displaying colors ranging from yellowish orange to brown and black, while the nacreous pearls exhibit a silvery surface (*CIBJO Guide for Classifying Natural Pearls and Cultured Pearls*, 2021).

GIA's Mumbai laboratory recently received two pen pearls for scientific examination. They were recovered by a renowned Bahraini diver from the shallow waters off Bahrain, fished at a depth of 2 meters in October 2023. Pearl A was a bicolor yellowish brown and black button shape, weighing 0.65 ct and measuring 4.65 × 4.25 mm, while pearl B was a yellowish brown near-button, weighing 0.73 ct and measuring 4.86 × 4.34 mm (figure 13). Visual observation showed significant surface-reaching cracks on pearl A (figure 14A) and a network of crazing or cracking due to the columnar structure on pearl B (figure 14C). When viewed under 40× magnification with a fiber-optic light, both exhibited a translucent non-nacreous surface with a columnar calcite structure, displaying a pseudohexagonal cellular outline (N. Sturman et al., "Observations on pearls reportedly from the Pinnidae family (pen pearls)," Fall 2014 *G&G*, pp. 202–215).

Figure 13. Two pen pearls from Bahrain displayed on a pen shell originating from the same waters. Both the shell and the pearls exhibit a similar color pattern. Pearl A measures 4.65 × 4.25 mm and weighs 0.65 ct (left); Pearl B measures 4.86 × 4.34 mm and weighs 0.73 ct (right). Photo by Gaurav Bera.

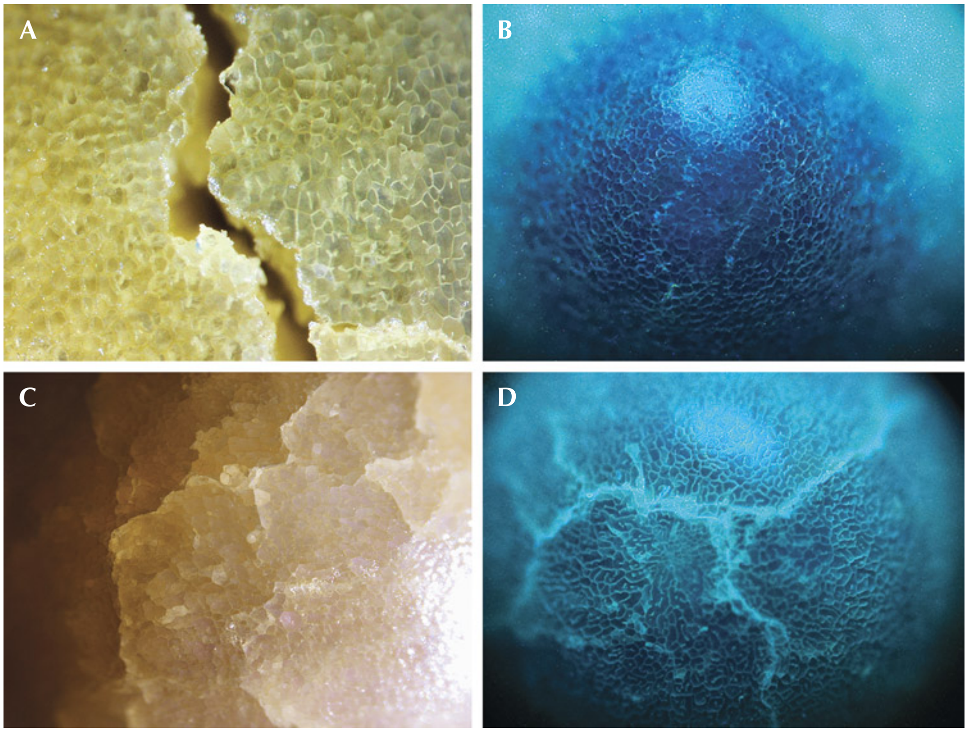

Figure 14. A: Non-nacreous cellular structure with a significant surface-reaching crack in pearl A; field of view 0.5 mm. B: DiamondView image of the cellular structure on the black area on pearl A. C: Cellular structure with a network of subsurface cracking on pearl B; field of view 1.6 mm. D: DiamondView image of a spectacular greenish blue reaction of the cellular structure and the subsurface cracks on pearl B. Images by Karan Rajguru (A, B, and D) and Pfokreni Nipuni (C).

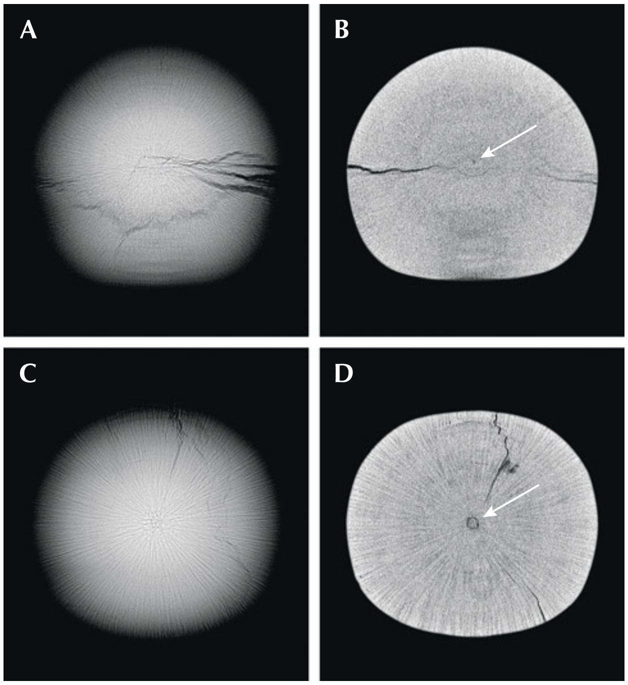

Figure 15. Top: RTX imaging of pearl A shows an acicular structure with significant surface-reaching cracks (A), and µ-CT imaging reveals a minute core (B). Bottom: RTX imaging of pearl B shows an acicular structure with a few subsurface cracks (C), and µ-CT imaging reveals a small central core (D).

The pearls showed an inert reaction when exposed to X-ray fluorescence. Energy-dispersive X-ray fluorescence spectrometry on both revealed manganese levels below detection limits and 45 ppm and higher strontium levels of 1183 ppm and 1303 ppm, respectively, confirming their saltwater origin. Under long-wave ultraviolet radiation, the black area on pearl A was inert, while the yellowish brown area showed a moderate yellowish green reaction similar to that of pearl B. Faint patchy reddish areas were also observed under the translucent surface of pearl B, a reaction linked to a type of porphyrin pigment. When exposed to short-wave UV, pearl A was almost inert and pearl B showed a weaker yellowish green reaction. When examined by the deep-UV wavelength (<230 nm) of the DiamondView, both revealed a greenish blue reaction with a mosaic of fine cellular features of the columnar calcite structure (figure 14, B and D).

Real-time X-ray microradiography (RTX) and X-ray computed microtomography (µ-CT) were conducted to study the internal structures. RTX imaging of pearl A revealed a fine acicular (radial) structure with significant surface-reaching cracks (figure 15A). A minute core was visible in µ-CT imaging (figure 15B). Pearl B also exhibited an acicular structure but with broader radiating lines than those observed in pearl A (figure 15C). Similarly, µ-CT imaging revealed a small central core with a few minor cracks (figure 15D). These structures corresponded with the columnar structure observed on their surfaces (Fall 2009 GNI, pp. 69–71).

Raman spectroscopy using 514 and 830 nm laser excitation revealed peaks for both pearls at 280 and 712 cm^{-1} as well as 1085 cm^{-1}, indicative of calcite. The surface of pearl B was ground down, exposing a dark brown ring along with the acicular structure (figure 16, left). This ring was not visible in RTX or µ-CT imaging. Raman analysis on different spots of the ground pearl showed similar calcite peaks with a weak polyenic pigment peak at around 1437 cm^{-1}. Photoluminescence analysis for both pearls revealed very weak bands at 620, 650, and 680 nm, indicating natural coloration. These bands were more distinct on the cross-sectional areas of pearl B. In addition, the dark brown central core and ring exhibited a brownish red reaction when viewed under long-wave UV radiation (figure 16, right), linked to a type of porphyrin pigment previously recorded in partially non-nacreous and nacreous pearls from the *Pteria* species (S. Karampelas and H. Abdulla, "Black non-nacreous natural pearls from *Pteria* sp.," *Journal of Gemmology*, Vol. 35, No. 7, 2017, pp. 590–592) and in a *Pinctada radiata* shell with a partially non-nacreous blister pearl (Winter 2023 GNI, pp. 527–529).

Non-nacreous pen pearls are often priced lower than their nacreous counterparts from the *Pinctada* species,

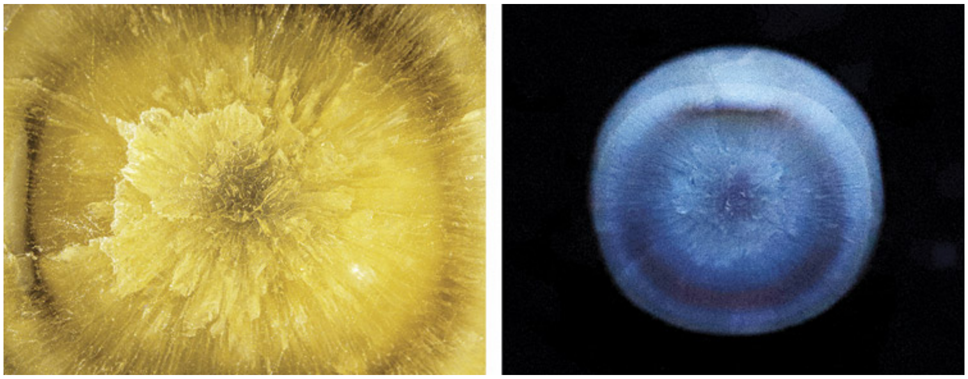

Figure 16. Left: Cross section of pearl B after grinding, revealing an acicular structure with a dark inner ring and a small central core; field of view 2.1 mm. Right: Long-wave UV image of the cross section with the dark ring and core showing a brownish red reaction. Photos by Karan Rajguru.

Figure 17. A rare 7.38 ct orangy red rhodonite. Photo by Chunyan Wang.

Figure 18. Many long tube inclusions were observed in the rhodonite sample. Photomicrograph by Chunyan Wang; field of view 2.36 mm.

mainly due to their durability issues related to surface cracks. Although not desirable for jewelry purposes, they have been used as nuclei for producing atypical bead cultured pearls. In such cases, identification becomes very challenging due to their internal structure composed of natural acicular growth features. This submission provided an interesting opportunity to study these known pen pearl samples from Bahrain, a habitat shared with the popular *Pinctada radiata* mollusk species.

Abeer Al-Alawi, Karan Rajguru, Pfokreni Nipuni, and Roxane Bhot Jain
GIA, Mumbai

Cummingtonite needles encased by quartz in a rhodonite. Recently, the authors examined a 7.38 ct gem-quality rhodonite exhibiting a vivid orangy red color and good transparency (figure 17). Gemological testing, Fourier-transform infrared spectroscopy, and Raman spectroscopy identified it as rhodonite. This gemstone had a refractive index of 1.733–1.747 and specific gravity of 3.46. Most rhodonite is opaque and is used as an ornamental stone, and transparent facet-grade material is very rare. Microscopic observation revealed an abundance of long, curved needles scattered randomly throughout the gem host (figure 18), consistent with previous studies. Occasional fluid inclusions were also seen.

A previous publication suggests that these curved needles are cummingtonite, an amphibole group mineral with a chemical formula of $(Mg, Fe^{2+})_2(Mg,Fe^{2+})_5Si_8O_{22}(OH)_2$ (P. Leverett et al., "Ca-Mg-Fe-rich rhodonite from the Morro da Mina mine, Conselheiro Lafaiete, Minas Gerais, Brazil," *Mineralogical Record*, Vol. 39, 2008, pp. 125–130). Raman spectroscopy confirmed the identity of one needle as cummingtonite, displaying characteristic peaks at 190, 667, and 1036 cm^{-1} when the laser beam was focused on the center of it. However, several new peaks appeared when the laser beam moved to the boundary between the needle and the rhodonite, including a 208 cm^{-1} peak that matched with quartz. Such a finding is new to the authors, since needle inclusions encased in another mineral have rarely been reported. To further investigate this finding, more than 10 points were selected, and the results identified quartz between the cummingtonite needle and the rhodonite host. All the tested Raman spectra were compared to the Raman online database.

To further explore the relationship between rhodonite, quartz, and cummingtonite needles, a 3D Raman map was performed on a selected area of 3 × 14 × 12 μm with a step size of 2 μm. After running for 17.25 hours, more than 500 spectra were recorded. Three feature peaks were selected for image reconstruction: 3658 cm^{-1} for cummingtonite, 113 cm^{-1} for rhodonite, and 208 cm^{-1} for quartz (figure 19). Due to the similarity between the Raman spectra of cummingtonite and rhodonite, the main peaks were not chosen for mapping. The OH-related peak at 3658 cm^{-1} was only observed in cummingtonite, enabling us to distinguish the two minerals. The Raman mapping image is shown in figure 20, with blue indicating the host, green for quartz, and red for cummingtonite. These images revealed that the detection of quartz between rhodonite and cummingtonite was not by accident but indicated a considerable presence of quartz inclusions. Previous studies have reported quartz as an isolated and random mineral inclusion in rhodonite from Australia (e.g., P. Millsteed et al., "Inclusions in transparent gem rhodonite from Broken Hill, New South Wales, Australia," Fall 2005 *G&G*, pp. 246–254). Based on our observation of the position of the

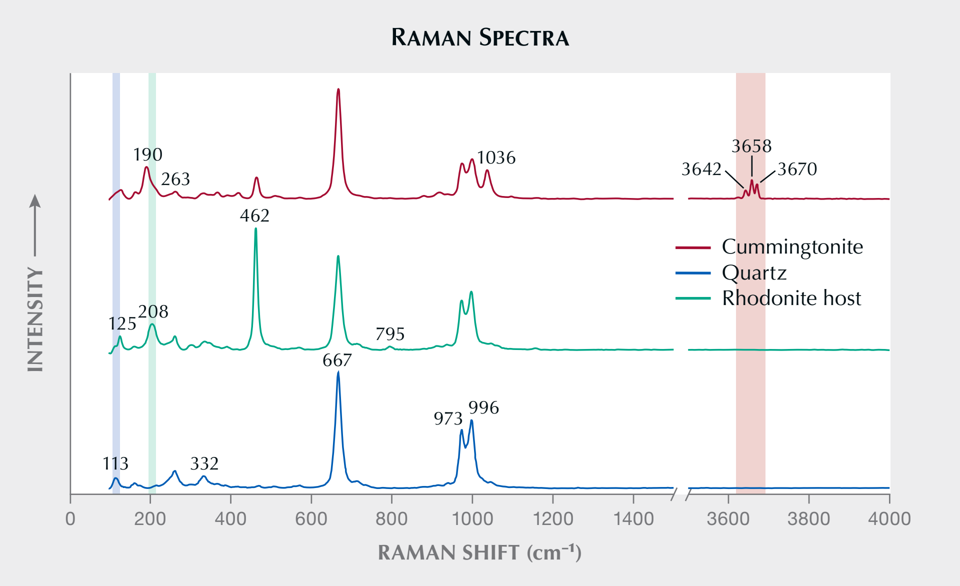

Figure 19. The Raman spectra of cummingtonite, quartz, and rhodonite. While the long tube was identified as cummingtonite, quartz was detected between the tube and the rhodonite host. Spectra are offset vertically for clarity.

quartz, we speculate that it may be the product of the decomposition of cummingtonite under certain temperatures and pressures.

This intricate inclusion association pattern may offer a new perspective on the origin of curved needles in rhodonite. This case also highlights the usefulness of Raman mapping as a tool for nondestructive analysis of inclusions.

Yujie Gao, Xueying Sun (shirley.sun@guildgemlab.com), and Ziyun Zhang
Guild Gem Laboratories, Shenzhen, China

Ruobin Tang
Chengdu, China

Update on Liberian ruby. Liberian rubies were reported more than a decade ago (L. Kiefert and M. Douman, "Ruby from Liberia," Summer 2011 *G&G*, p. 138). These rubies were found in two diamond mines located along the Mano River and in Nimba Province close to the Guinean border. GIA's Tokyo laboratory recently received 10 Liberian corundum samples (figure 21) from the Japan-based NGO Diamonds for Peace. These samples were collected at Weasua, Liberia, the same locality recently reported in *G&G* (Spring 2023 GNI, pp. 149–150).

Most of the rough corundum pebbles recovered from Weasua showed weakly saturated purplish red, pink, pale yellow, and green colors; most fall in the color range of sapphire, except for a few red ones. Three of the ruby sam-

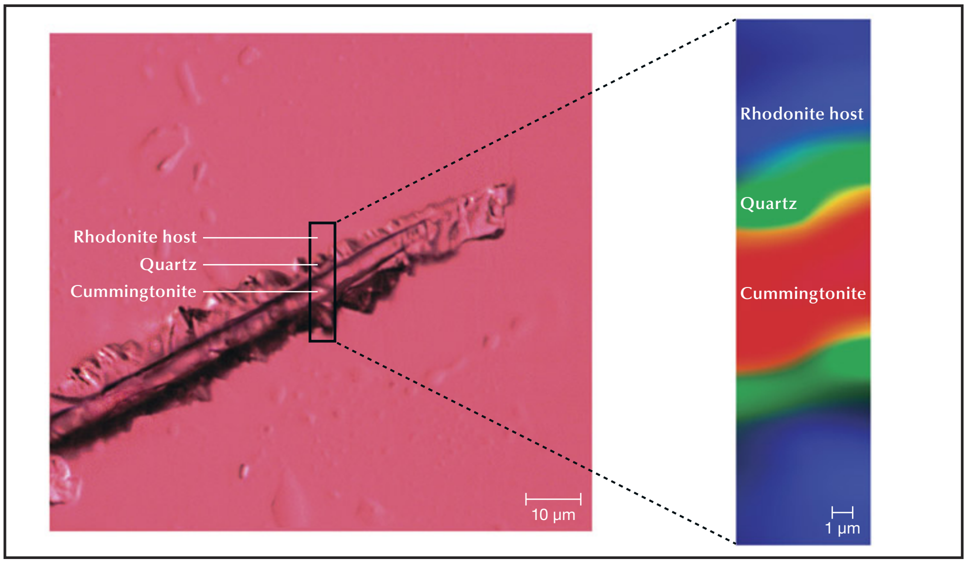

Figure 20. 3D false-color Raman mapping of one of the encased needle inclusions with the surrounding host. The rectangle shows the mapping area. The blue area indicates the existence of the rhodonite host, the green area the quartz, and the red area indicates the cummingtonite.

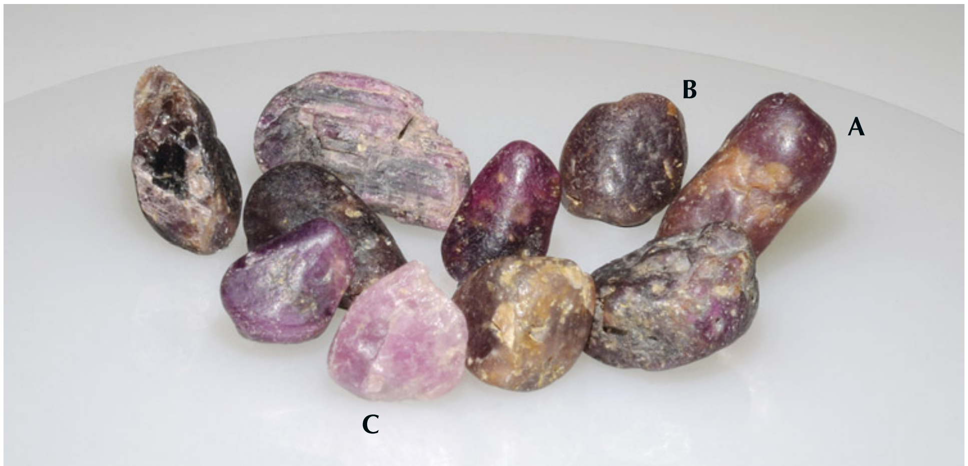

Figure 21. Ten corundum samples from the Lofa River in Weasua, Liberia. Photo by Shunsuke Nagai.

ples—11.65 ct purplish red (A), 6.52 ct dark purplish red (B), and 5.37 ct light purplish red (C)—were cut and polished for observation and advanced testing. Standard gemological testing yielded a refractive index of 1.762–1.770, a uniaxial interference pattern, and a hydrostatic specific gravity of 3.85–3.99. Except for the specific gravity, which is slightly low presumably due to the inclusions, the gemological characteristics were consistent with corundum.

The rounded surfaces of the rough stones suggested weathering. Most were semitransparent to translucent, heavily included, and displayed lamellar twinning structures in two orientations (figure 22). The twinning planes were filled with orange secondary minerals. Other internal features included irregularly shaped reflective particles

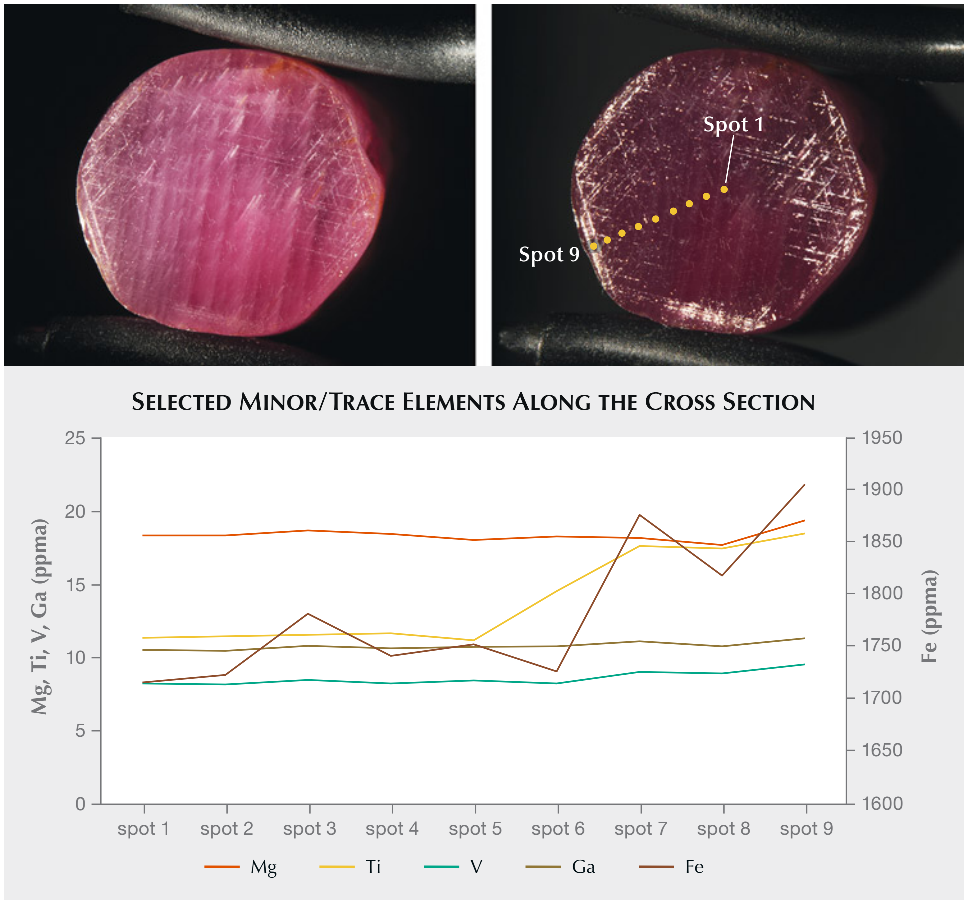

Figure 22. Sample A shows strong two-direction lamellar twinning structures (top left) and contains numerous reflective inclusions near the rim (top right). Both photos are under fiber-optic illumination; the light source of the top right photo is in a specific direction to show the reflective inclusions. Photomicrographs by Yuxiao Li; field of view 19.5 mm. The plot at the bottom shows the minor/trace element concentrations of each spot. The spot position is shown in the top right photo.

TABLE 1. Minor and trace element concentrations (in ppma) of rubies from Liberia.

	Mg	Ti	V	Fe	Ga
Sample A	17.70–19.38	11.2–18.5	8.17–9.57	1716–1906	10.47–11.32
Sample B	14.78–21.14	21.4–28.8	16.25–16.53	1340–1347	24.39–25.77
Sample C	21.39–25.51	23.3–84.4	4.36–5.20	968–997	8.80–9.62
Total	14.78–25.51	11.2–84.4	4.36–16.53	968–1906	8.80–25.77
Detection limit (ppma)	0.04	0.1	0.01	2	0.01

aligned in three directions, iridescent small particles, and fine needles (figure 23). Sample A showed a less-included core and particle-rich rim, and sample B was heavily included with large whitish aggregate inclusions and some small black minerals along the twinning planes. These black minerals were identified by Raman spectroscopy as vonsenite ($Fe^{2+}{}_2Fe^{3+}(BO_3)O_2$).

Laser ablation–inductively coupled plasma–mass spectrometry (LA-ICP-MS) was carried out to analyze trace element compositions. On sample A, we measured nine spots from center to edge. The rim area (spots 7–9) yielded higher iron and titanium, and similar levels of magnesium, vanadium, and gallium compared with the less-included core area (spots 1–6) (figure 22). We measured three spots on each of the remaining two samples. The results are presented in table 1, showing the wide range of concentrations of titanium, vanadium, iron, and gallium. (Spot 1 of sample B shows high titanium (84.3 ppma) with zirconium (0.054 ppma), likely caused by the contamination of small inclusions.)

Kongsomart et al. (Winter 2017 GNI, pp. 472–473) summarized the trace element concentrations in rubies from East African deposits. Samples A and C of the Liberian rubies in this study showed trace element concentrations similar to those from Mozambique. Sample B had a high gallium concentration, overlapping with rubies from the Zahamena deposit in Madagascar. Considering the wide range of trace element concentrations of Liberian rubies and those from East African deposits, these chemistry components are not helpful in separating the Liberian ruby

Figure 23. Black inclusions, identified as vonsenite by Raman spectroscopy, were observed with twinning planes (left) and reflective particles aligned in three directions with fine needles (right). Photomicrographs by Yuxiao Li; fields of view 2.4 mm (left) and 2.9 mm (right).

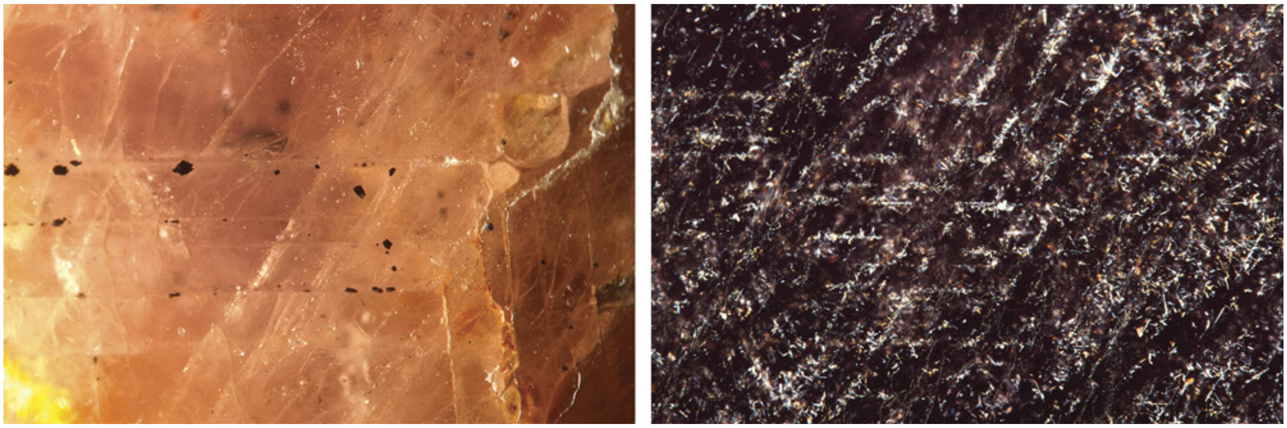

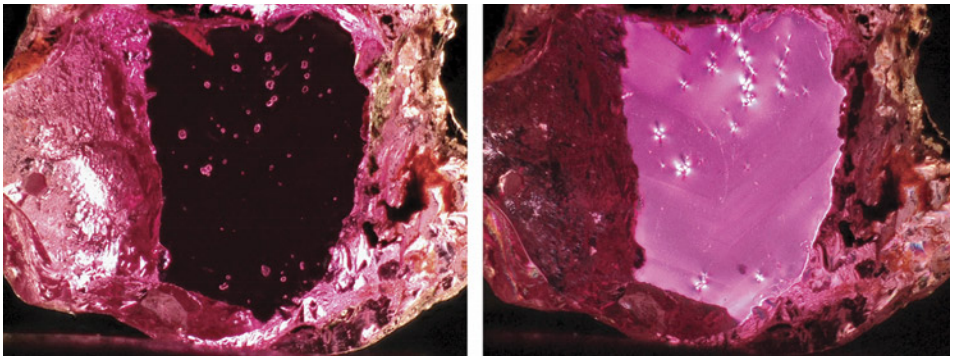

Figure 24. Colorless crystals with high relief (left) in a ruby mined near Caraia in the Montepuez region. Placing the ruby between crossed polarizers (right) revealed a stress halo caused by low-dose radiation emitted by the zircon inclusion. Photomicrographs by Wim Vertriest; field of view 3.6 mm.

from other origins. The ruby samples from these East African origins are less included than the Liberian samples in this study. For identification services, we are able to determine the origin not only by trace elements but also by microscopic observations (A.C. Palke et al., "Geographic origin determination of ruby," Winter 2019 *G&G*, pp. 580–613). If it is necessary to separate Liberian rubies from other highly included low-quality rubies, comprehensive study on such included samples is needed.

Recently, some low-quality rubies reportedly mined from Guinea have been sold on the market. These materials are often heat treated and filled with lead glass, with some cabochons displaying six-rayed asterism after treatment. Both rough samples of Guinean ruby in the GIA colored stone reference collection and the studied Liberian rubies show a classic weathered "barrel" shape, semitransparent to translucent transparency, pinkish color, and most are heavily included. Given that the deposit of Guinea ruby is located upstream, north of Liberia, these rubies presumably originated from the same or closely related geological condition. With proper treatment, Liberian rubies could show asterism and be used as jewelry material.

Yuxiao Li and Yusuke Katsurada
GIA, Tokyo

Chie Murakami and Mai Suzuki
Diamonds for Peace, Yokohama

Update on inclusion scenes in Mozambican rubies. In August 2022, a team of GIA gemologists visited the ruby mines near Montepuez in the Cabo Delgado province of northern Mozambique (Fall 2022 GNI, pp. 383–386). This included a visit to the deposits farther west in the region, near the village of Caraia. This mining area is north of the N14 road, while most of the previously known productive ruby deposits are southeast of this highway.

Ruby mining near Caraia has been ongoing for more than a decade but was mostly limited to artisanal mining activity until 2017. In the last few years, the ruby deposits have been developed on a larger scale by Fura Gems. The first official sale of this material took place in late 2021, and regular auctions have been organized since then (Fall 2021 GNI, pp. 276–277).

During GIA's visit in August 2022, gemologists collected a large suite of rough rubies directly from the wash plant and sort house at the mine site. The samples ranged from 0.1 to 1.2 g and were transparent and fracture-free. The vast majority contained some crystal inclusions, and an extensive inclusion study of this material matched well with the known data from Mozambican ruby, with one exception. The most common inclusions are bands of fine silk, short needles, and particles, including reflective platelets. Mozambican rubies typically show three distinctive types of solid crystals: transparent greenish amphibole crystals with a stubby to elongated shape; pseudohexagonal frosty mica crystals with small expansion fractures; and black opaque sulfide crystals with a metallic luster. All of these features were prevalent in the rubies mined near Caraia.

However, one observation stood out: In 8 of the 85 studied samples, zircon crystal inclusions were found. While zircon crystals are also transparent, their relief is higher than that of the more common amphibole crystals. They also tend to be smaller and are rarely elongated in rubies. The most efficient way to identify them is by viewing the stones between crossed polarizers, which highlights the obvious stress halos around the slightly radioactive zircon crystals (figure 24). In all of GIA's samples, the identification was also confirmed by confocal Raman spectroscopy.

To our knowledge, zircon crystals have not been previously documented in rubies from Mozambique. They are, however, a hallmark for rubies from Madagascar (A.C. Palke et al., "Geographic origin determination of ruby," Winter 2019 *G&G*, pp. 580–612). The presence of zircon crystal inclusions is often a decisive discriminator in the origin determination of rubies. The inclusion scenes of high-quality Mozambican and Malagasy rubies can look very similar, but only the latter were known to have abundant zircon inclusions. This is no longer true now that zircon inclusions have also been identified in rubies from Mozambique.

Trace element analysis can often assist in separating rubies from East African sources. But even there, some overlap occurs between Mozambique and Madagascar, especially for stones with higher iron concentrations. All the Mozambican rubies with zircon inclusions showed a trace element signature that matched completely with other Mozambican rubies when analyzed with both energy-dis-

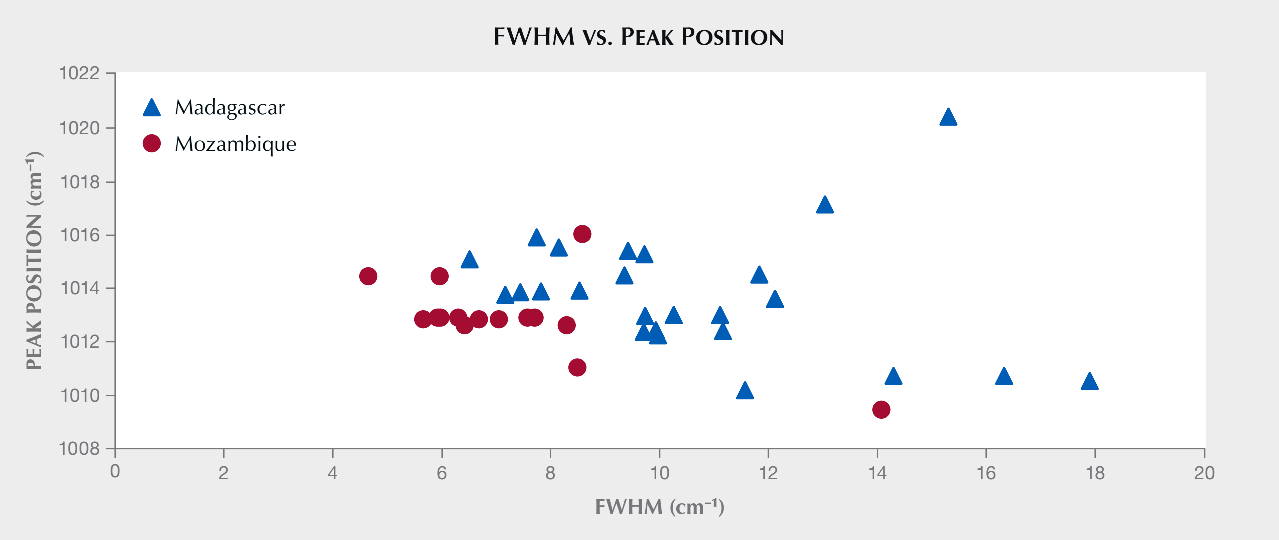

Figure 25. This chart shows the FWHM vs. the peak position of the most important peak (1015 cm^{-1}) in the Raman spectrum of zircon inclusions in Mozambican and Malagasy rubies.

persive X-ray fluorescence and laser ablation–inductively coupled plasma–mass spectrometry. Fortunately, the rubies from Caraia tend to have a low iron concentration, reducing the likelihood that their trace chemistry composition will match with Malagasy rubies, which tend to have higher iron concentrations.

Raman spectra of the zircons in rubies from Mozambique (15 inclusions in 6 different stones) and Madagascar (27 inclusions in 13 different stones) showed that the main peak (1015 cm^{-1}) in Mozambican zircon inclusions tends to have lower full width at half maximum (FWHM), but there is no clear separation between the two populations based on the Raman spectra of the zircon inclusions (figure 25).

The discovery of zircon inclusions in Mozambican rubies has a potentially major impact on the origin determination criteria used for the two most common sources of East African ruby. These new discoveries also highlight two important aspects of origin determination research: the critical need to keep collecting samples from known deposits to identify new features in current production, and the power of the microscope as an identification tool in a gemological laboratory.

Wim Vertriest

ANNOUNCEMENTS

William Ruser: The Jeweler Who Charmed Hollywood. A new book by Judy Colbert and Peggy Tsiamis chronicles the life of "Jeweler to the Stars" William Ruser, best known for his whimsical figural jewelry with freshwater pearls. Ruser's celebrity clientele included Frank Sinatra, Elizabeth Taylor, Joan Crawford, and Ronald Reagan during Hollywood's golden age. With little published about Ruser, the research and interviews conducted for the book reveal personal and professional details about the jeweler and his business on Rodeo Drive in Beverly Hills. The book (figure 26) also features more than 100 images. *William Ruser: The Jeweler Who Charmed Hollywood* is available through the GIA store (https://store.gia.edu/collections/history-lore).

Figure 26. Jeweler William Ruser owned a prestigious store on Rodeo Drive in Beverly Hills during Hollywood's golden age.

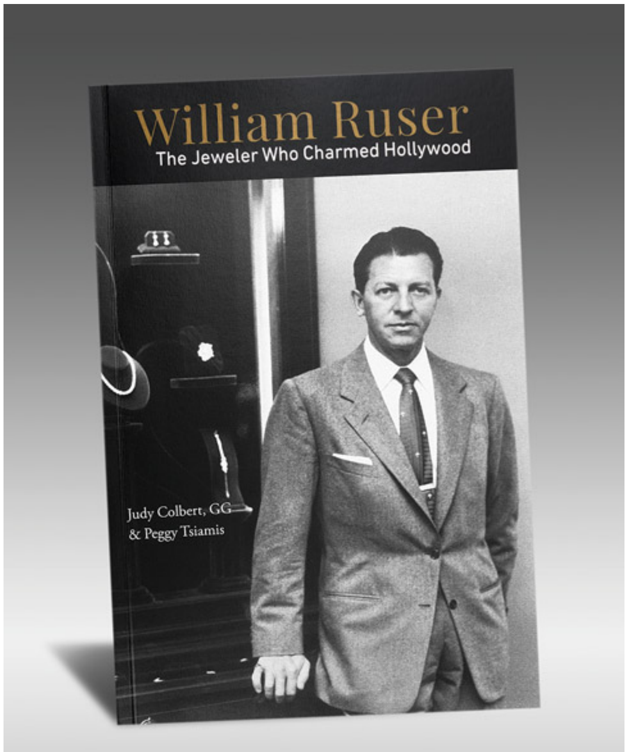

Beyond Beauty: A Garnet Necklace Decoded

Erin Hogarth | GIA, Carlsbad

Two 2023 AGTA Spectrum Awards—Best Use of Platinum and Color and Best Use of Platinum and Color Men's Wear—were recently awarded to "Garanatus: From Rough to Cut," a 29-inch platinum necklace set with more than 77 total carats of rare garnets. "Garanatus" is a play on the origin of garnet's name—*granatus*, Latin for "seed-like," because of its resemblance to pomegranate seeds. The necklace was designed and fabricated by Mary van der Aa (Mary van der Aa Fine Jewels, Detroit) using 28 garnets that gem cutter Todd Wacks (Tucson Todd's Gems, Arizona) collected and hand-faceted over a span of 13 years; van der Aa collaborates with Wacks (figure 1) on all of her jewelry. These are her fourth and fifth Spectrum awards.

The necklace design (figure 2) symbolizes the transformation from rough to faceted garnet. "Garanatus" actually consists of two necklaces that connect with tiny neodymium magnets to form 22 rhombic dodecahedrons—the shape of a rough garnet crystal. Each of these magnetic links encases a garnet (figure 3), and detaching the two pieces reveals the gems inside. The garnet's type and locality are imprinted on the back of each link. A QR code on the necklace leads to a website detailing the stones and the necklace's creation.

Figure 1. Jewelry designer Mary van der Aa and gem cutter Todd Wacks. Courtesy of Mary van der Aa Fine Jewels and Tucson Todd's Gems.

"We wanted the necklace to be educational because many people don't know what an incredible stone garnet is," van der Aa said. "Everyone's seen every color of sapphire and tourmaline. Garnet doesn't get the attention it deserves. It can come in any color, even colorless or color change."

The necklace's garnet varieties span the color spectrum and localities (figure 4). Perhaps the most impressive is a 1.69 ct pink garnet from the Dora Maira locality in Italy, one of the largest of its type. Five of the garnets show color change. Other highlights include a 5.15 ct "grape jelly" pyrope-almandine from Mozambique; a 3.00 ct yellow grossular of a type reportedly produced by only one deposit in Tanzania in the 1980s; a 2.47 ct red "anthill" garnet that is exceptionally large for its Arizona locale; a 2.70 ct chromium grossular from Ethiopia; and a 2.86 ct Lindi garnet from Tanzania that reacts to UV light. The final addition was a 3.05 ct Russian demantoid with a horsetail inclusion, acquired in 2023, that van der Aa considered necessary to complete the collection.

Wacks acquired the first stone, a 2.75 ct blue color-change garnet from Bekily, Madagascar, while he was a student at GIA (van der Aa is also a GIA graduate). These are even rarer than alexandrite and are easily mistaken for them. "My love for garnet started there," he said. "After the fifth stone, I realized it was a decent little rainbow." His search focused on high clarity, color, and dispersion more than size (the sizes range from under a carat to 5.63 ct). "We used the rarest garnets I've been able to find," he said. "Every time I found a strange deposit or an exceptional example of the known localities, I added it to my collection. I don't know how many thousands of stones I saw."

"Nine out of ten of them, if I wasn't a gemologist, I would never guess it was a garnet," van der Aa said. "Especially because of the sparkle. A lot of them look almost like green diamonds or yellow sapphires." Wacks added, "There are a few secrets used for cutting these garnets to produce really nice dispersive stones."

The idea for the necklace came to Wacks in 2020, when he realized the garnets would "really rock" in a necklace and asked van der Aa to design one. She told him it would take some time to develop something amazing. More than 450 hours went into crafting the piece. "It was quite a challenge technically," she said, noting the uniqueness of the magnetic jacket design and the QR code.

"Garanatus" contains 2.5 lbs (more than 1 kg) of platinum. "These were the best of the best garnets he could find, so I thought platinum was what they deserved," van der Aa said. The half of the link that features the QR code is 18K gold because the highly reflec-

Figure 2. "Garanatus: From Rough to Cut," a platinum necklace featuring 28 rare garnets, won two 2023 AGTA Spectrum Awards. Photo by Robert Weldon; courtesy of Mary van der Aa Fine Jewels and Tucson Todd's Gems.

Figure 3. The 18K gold half link features a QR code that leads to a website with details about the garnets and the necklace's creation. Photo by Robert Weldon; courtesy of Mary van der Aa Fine Jewels and Tucson Todd's Gems.

tive platinum didn't display the QR code well. "The 18K gives a luxe two-tone look," she said. The 18K gold portion also indicates the back of the necklace and contains a cluster of seven colorless ("leuco") garnets from Sri Lanka (1.40 carats total) rather than one stone.

Based on GIA researchers' analysis, these garnets demonstrate the entire range of garnet chemistry in the natural world. Their chemical compositions also shed light on their color origins. Many have color caused by essential chemical components, such as iron in the Namibian demantoid and the purple pyrope-almandine from Mozambique. Some are colored by trace impurity elements, including vanadium in the color-change garnets from East Africa and chromium in the Russian demantoid and the "anthill" garnet.

"You get really sentimental holding on to something like this," Wacks said. Initially he planned to keep the necklace, but as it neared completion, van der Aa suggested he consider parting with the garnets because it had become so extraordinary.

"To go from saying, 'Just make a necklace,' to this—it turned out beyond anything I could have ever thought of," he said. "It's likely the most impressive necklace in history displaying the beauty of the garnet group. I've done a fair amount of research but haven't found anything that compares."

"Our dream is for it to go somewhere people could learn from it and see it and leave with a huge smile, knowing that garnet is such an incredible gemstone," van der Aa said. "Now he's okay with parting with them."

"Garanatus" will be on display in the GIA Museum beginning this spring.

Figure 4. "Garanatus: From Rough to Cut" is set with more than 77 total carats of rare garnets. Photo by Robert Weldon; courtesy of Mary van der Aa Fine Jewels and Tucson Todd's Gems.

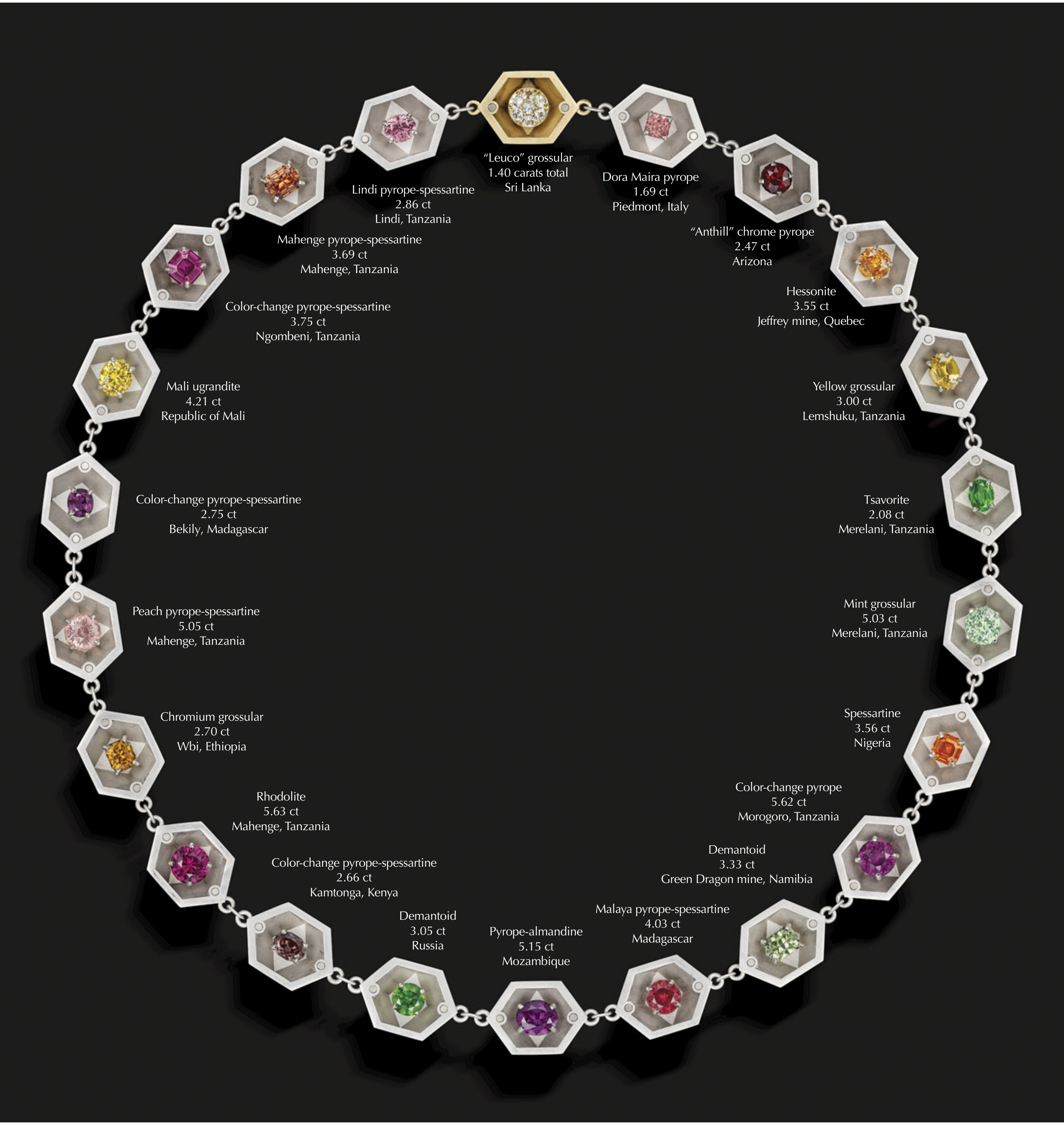
"Leuco" grossular
1.40 carats total
Sri Lanka
Dora Maira pyrope
1.69 ct
Piedmont, Italy
"Anthill" chrome pyrope
2.47 ct
Arizona
Hessonite
3.55 ct
Jeffrey mine, Quebec
Yellow grossular
3.00 ct
Lemshuku, Tanzania
Tsavorite
2.08 ct
Merelani, Tanzania
Mint grossular
5.03 ct
Merelani, Tanzania
Spessartine
3.56 ct
Nigeria
Color-change pyrope
5.62 ct
Morogoro, Tanzania
Demantoid
3.33 ct
Green Dragon mine, Namibia
Malaya pyrope-spessartine
4.03 ct
Madagascar
Pyrope-almandine
5.15 ct
Mozambique
Demantoid
3.05 ct
Russia
Color-change pyrope-spessartine
2.66 ct
Kamtonga, Kenya
Rhodolite
5.63 ct
Mahenge, Tanzania
Chromium grossular
2.70 ct
Wbi, Ethiopia
Peach pyrope-spessartine
5.05 ct
Mahenge, Tanzania
Color-change pyrope-spessartine
2.75 ct
Bekily, Madagascar
Mali ugrandite
4.21 ct
Republic of Mali
Color-change pyrope-spessartine
3.75 ct
Ngombeni, Tanzania
Mahenge pyrope-spessartine
3.69 ct
Mahenge, Tanzania
Lindi pyrope-spessartine
2.86 ct
Lindi, Tanzania